

Aus dem Institut für Molekular- und Zellbiologie der Hochschule Mannheim

Leiter: Prof. Dr. rer. nat. Mathias Hafner

Complex binding and elution behavior of therapeutic proteins under
column overloading conditions

Inauguraldissertation
zur Erlangung des Doctor scientiarum humanarum (Dr. sc. hum.)
der
Medizinischen Fakultät Mannheim
der Ruprecht-Karls-Universität
zu
Heidelberg

vorgelegt von
Felix Seelinger

aus
Speyer

2022

Dekan: Prof. Dr. med. Sergij Goerd
Referent: Prof. Dr. rer. nat. Mathias Hafner

TABLE OF CONTENTS

LIST OF ABBREVIATIONS.....	1
LIST OF SYMBOLS	4
1 INTRODUCTION.....	9
1.1 Therapeutic proteins – bispecific monoclonal antibodies.....	9
1.2 Modeling and simulation of preparative chromatography processes.....	11
1.3 Theoretical considerations.....	16
1.4 Aim of the work.....	25
2 MATERIAL AND METHODS	27
2.1 Materials.....	27
2.2 Methods.....	39
3 RESULTS.....	56
3.1 Determined dead volumes, column parameters, resin parameters, exclusion factors (k_d, i) and axial dispersion coefficient (D_{ax})	56
3.2 Characterization of the bsAb samples.....	57
3.3 Modeling in the linear range of the adsorption isotherm	63
3.4 Investigation and comparison of the elution behavior under high loading and overloading conditions of the samples bsAbY and bsAbX	66
3.5 Modeling the binding and elution behavior of bsAbY under high loading and overloading conditions by applying the Steric Mass Action (SMA) model	68
3.6 Investigation of complex high loading and column overloading phenomena when using bsAbY.....	81
3.7 Modeling the binding and elution behavior of bsAbX under high loading and overloading conditions using the Self-Association-SMA (SAS-SMA) model.....	94

3.8 Investigation of complex high loading and overloading phenomena when using bsAbX	107
4 DISCUSSION	110
4.1 Size variants and charge variants heterogeneity of the bsAb samples.....	110
4.2 Modeling in the linear range of the adsorption isotherm	113
4.3 Langmuir and anti-Langmuir elution behavior under high loading and column overloading conditions.....	115
4.4 Modeling the binding and elution behavior of bsAbY in the non-linear range of the adsorption isotherm using a modified SMA model	116
4.5 Complex high loading and overloading phenomena when using bsAbY ...	122
4.6 Modeling the binding and elution behavior of bsAbX in the non-linear range of the adsorption isotherm using a modified SAS-SMA model	132
4.7 Complex high loading and overloading phenomena when using bsAbX ...	137
4.8 Conclusion.....	138
5 SUMMARY	142
6 REFERENCES.....	144
7 TABULAR APPENDIX.....	158
8 FIGURE APPENDIX.....	177
9 LIST OF TABLES	184
10 LIST OF FIGURES	187
11 CURRICULUM VITAE	190
12 ACKNOWLEDGEMENT	192

LIST OF ABBREVIATIONS

AEX	anion exchange
AL-L	anti-Langmuir to Langmuir
BiTE	bispecific T-cell engager
BSA	bovine serum albumin
bsAb	bispecific monoclonal antibody
CEX	cation exchange
CEX-HPLC	cation exchange-high-performance liquid chromatography
CHES	2-(Cyclohexylamino)ethane-1-sulfonic acid
CIP	cleaning in place
CPA	colloidal particle adsorption
CV	column volume
DBC	dynamic binding capacity
DNA	deoxyribonucleic acid
EI	empiric interpolation
EMG	exponentially modified Gaussian function
Fab	fragment antigen binding
Fc	fragment crystallizable
FDA	Food and Drug Administration
GLP-1	glucagon-like peptide-1
GRM	general rate model
HCl	hydrochloric acid
HEPES	2-[4-(2-Hydroxyethyl)piperazin-1-yl]ethane-1-sulfonic acid
ID	inner diameter

LIST OF ABBREVIATIONS

IEC	ion exchange chromatography
kDa	kilodalton
IEP	isoelectric point
IgG	immunoglobulin G
LGE	linear gradient elution
mAb	monoclonal antibody
MES·H ₂ O	2-morpholin-4-ylethanesulfonic acid monohydrate
MOPSO	2-Hydroxy-3-(morpholin-4-yl)propane-1-sulfonic acid
MP	main variants
N_{AA}	number of amino acids
NaCl	sodium chloride
NaH ₂ PO ₄ ·H ₂ O	sodium dihydrogen phosphate monohydrate
NaN ₃	sodium azide
NaOH	sodium hydroxide
n.s.	not specified
ODE	ordinary differential equations
p.A.	pro analysi
pH	<i>potential of hydrogen / negative logarithm of the hydrogen ion concentration</i>
Ph.Eur.	pharmacopoeia europaea
pK_a	negative logarithm of the acid dissociation constant
PV	pre-variants
QSPR	Quantitative structure–property relationship
RNA	ribonucleic acid
SAS-SMA	Self-Association Steric Mass Action

LIST OF ABBREVIATIONS

SD	Stoichiometric Displacement
SE-HPLC	size exclusion-high-performance liquid chromatography
SMA	Steric Mass Action
TAPS	[tris(hydroxymethyl)methylamino]propanesulfonic acid
UV	ultraviolet
v/v	volume per volume

LIST OF SYMBOLS

Symbols

A_i	distribution coefficient
c	molar concentration of pure water
c_i	protein concentration in the liquid phase
c_1	counterion concentration in the liquid phase
$c_{1,init}$	initial salt concentration in the liquid phase
$c_{1,final}$	final salt concentration in the liquid phase
$c_{1,elu}$	eluting salt concentration in the liquid phase
$Comp$	compression
D_{ax}	axial dispersion coefficient
d_p	particle diameter
d_c	diameter of the column
ΔG_1^0	standard Gibbs energy change of association of the counterion
ΔG_i^0	standard Gibbs energy change of adsorption of component i
$\Delta G_{IEC,i}^0$	standard Gibbs energy change of the ion exchange equilibrium of component i
g_{pH}	slope of the linear pH gradient
g_1	slope of the linear salt gradient
GH_{pH}	normalized slope of the linear pH gradient
GH_1	normalized slope of the linear salt gradient
$K_{eq,i}$	equilibrium constant of the ion exchange reaction
$K_{eq,2,i}$	equilibrium constant of the self-association equilibrium
$K_{eq,2,i}^*/c$	constant of the equilibrium constant of the self-association equilibrium

$k_{d,i}$	exclusion factor
$k_{eff,i}$	effective mass transfer coefficient
$K_{p,i}$	protein-specific constant of the asymmetric activity coefficient for the protein in solution
$K_{p,i}^*$	constant of the protein-specific constant of the asymmetric activity coefficient for the protein in solution
$K_{1,i}$	counterion-specific constant of the asymmetric activity coefficient for the protein in solution
L	charged ligands
L_c	column length
L_{Bed}	bed length
M_1	first central peak moment
M_2	second central peak moment
m_i	constant of the pH-dependent steric shielding factor
N_{-i}	number of acidic amino acids
N_{+i}	number of basic amino acids
P_i	charged protein molecules
$P_{1,i}$	charged monomeric protein molecules
$P_{2,i}$	charged dimeric protein molecules
pH_{init}	initial pH in the liquid phase
pH_{final}	final pH in the liquid phase
pH_{elu}	eluting pH in the liquid phase
pK_{a_i}	pK_a value of the individual amino acids
q_1	concentration of bound counterion
q_1^*	averaged salt concentration in the stationary phase
\bar{q}_1	concentration of bound counterion accessible for exchange with the protein

LIST OF SYMBOLS

$q_{1,i}$	concentration of bound monomeric protein
$q_{2,i}$	concentration of bound dimeric protein
q_i	concentration of bound protein
q_i^*	averaged protein concentration in the stationary phase
$q_{eq,i}^*$	averaged concentration in the stationary phase in equilibrium
$q_{max,1,i}$	theoretical maximal binding capacity of the monomer
$q_{max,2,i}$	theoretical maximal binding capacity of the dimer
$q_{max,i}$	theoretical maximal binding capacity
$\bar{q}_{max,i}$	mean value of the theoretical maximal binding capacity
R	universal gas constant
S	salt counter ions
T	temperature
t	time
u_{int}	interstitial mobile phase velocity
\dot{V}	volumetric flow rate
V_0	void volume of the column
$V_{bsAb,i}$	volume between the injection valve and the UV sensor with the column mounted, measured with bsAb solutions
V_c	total column volume
V_{cond}	volume between the injection valve and the conductivity sensor with the column mounted, measured with a high salt solution
$V_{cond,system}$	dead volume for the conductivity sensor
V_{dex}	volume between the injection valve and the UV sensor with the column mounted, measured with a DextranBlue solution
V_g	gradient volume
$V_{pH,system}$	dead volume for the pH sensor

V_t	total liquid volume of the column
$V_{UV,system}$	dead volume for the UV sensor
x	axial position in the column
z_i	charge number of a protein
z_1	charge number of a salt ion

Greek Letters

a_1	activity of the counterion in solution
\hat{a}_1	activity of the counterion in the adsorbate state
$\hat{a}_{1,i}$	activity of the monomeric protein in the adsorbate state
$\hat{a}_{2,i}$	activity of the dimeric protein in the adsorbate state
a_i	activity of the protein in solution
\hat{a}_i	activity of the protein in the adsorbate state
γ_1	activity coefficient of the counterion in solution
$\hat{\gamma}_1$	activity coefficient of the counterion in the adsorbate state
$\hat{\gamma}_{1,i}$	activity coefficient of the monomeric protein in the adsorbate state
$\hat{\gamma}_{2,i}$	activity coefficient of the dimeric protein in the adsorbate state
γ_i	activity coefficient of the protein in solution
$\hat{\gamma}_i$	activity coefficient of the protein in the adsorbate state
$\tilde{\gamma}_i$	asymmetric activity coefficient of the protein in solution
γ_i^∞	activity coefficient of the protein in solution at infinite dilution
ϵ	dielectric constant of water at 298.15 K
ϵ_{280nm}	extinction coefficient at 280 nm
ϵ	interstitial porosity
ϵ_p	intraparticle porosity

ε_t	total porosity
Λ	ionic capacity of the pore volume
Λ_{packed}	ionic capacity of the packed resin bed
$\Lambda_{settled}$	ionic capacity of the settled resin
μ_1	reference state chemical potential of the counterion in solution
$\hat{\mu}_1$	reference state chemical potential of the counterion in the adsorbate state
μ_i	reference state chemical potential of the protein in solution
$\hat{\mu}_i$	reference state chemical potential of the protein in the adsorbate state
v_i	characteristic protein binding charge
v_{MV}	characteristic protein binding charge of the main variants
$v_{pH=0,i}$	theoretical protein binding charge at pH = 0
v_{PV}	characteristic protein binding charge of the pre-variants
$\sigma_{1,i}$	steric shielding factor of the monomeric protein
$\sigma_{2,i}$	steric shielding factor of the dimeric protein
σ_i	steric shielding factor
$\bar{\sigma}_i$	mean value of the steric shielding factors
x_1	mole fraction of the counterion in solution
\hat{x}_1	mole fraction of the counterion in the adsorbate state
$\hat{x}_{1,i}$	mole fraction of the monomeric protein in the adsorbate state
$\hat{x}_{2,i}$	mole fraction of the dimeric protein in the adsorbate state
x_i	mole fraction of the protein in solution
\hat{x}_i	mole fraction of the protein in the adsorbate state

1 INTRODUCTION

Parts of this section (1 INTRODUCTION) have already been published in a similar or identical form in Seelinger et al.¹ (Part 1, 2022) and in Seelinger et al.² (Part 2, 2022). Parts of this section (1 INTRODUCTION) are also included in a similar or identical form in Seelinger et al.³ (DRAFT (submitted)).

1.1 Therapeutic proteins – bispecific monoclonal antibodies

1.1.1 Therapeutic proteins in modern medicine

Therapeutic proteins, also known as biopharmaceuticals or simply biologics, are biotechnologically produced recombinant proteins used as medicinal drugs.^{4,5} They include a large group of various therapeutically active proteins such as proteohormones, monoclonal antibodies (mAbs), growth factors, enzymes, vaccines, and blood clotting factors etcetera.^{6,7} Therapeutic proteins are now well-established in modern medicine⁵ and are used to treat several major diseases, including autoimmune, cardiovascular and infectious diseases, diabetes mellitus, cancer and inflammation.⁸⁻¹⁰ The greatest benefits of therapeutic proteins are their high specificity and potency.⁵ Therefore, new therapeutic proteins and especially therapeutic mAbs are continuously being developed to improve the treatment of a variety of diseases.⁴ This has led to tremendous progress in the last decades, resulting in the development of bispecific monoclonal antibodies (bsAbs).¹¹

A bsAb is a single molecule designed to bind to two different targets or epitopes and thus exert two different functions.^{7,11} The simultaneous binding of two targets or epitopes allows unique mechanisms of action not possible with mAbs, like for example T cell localization or clotting factor replacement.¹¹⁻¹⁴ Consequently, a higher therapeutic efficacy for bsAbs over combinations of mAbs was observed for a wide range of indications.^{11,15,16} Currently, bsAbs are used to treat infectious, inflammatory and malignant diseases.⁷ In nature, antibodies are usually monospecific, so bispecific antibodies are generally artificial proteins that have to be produced by biochemical, molecular and genetic methods.¹⁷ The concept of bsAbs was first proposed in the 1960s by Nisonoff and his co-workers.^{18,19} However, it has taken decades for the first market approvals for bsAbs. In 2014, the bispecific T-cell engager (BiTE) Blinatumomab, sold under the brand name Blynicyto[®] (Amgen), was the first bsAb

which gained FDA (Food and Drug Administration) approval that is still in clinical use today.^{7,20,21} It was approved for the treatment of relapsed or refractory B-cell acute lymphoblastic leukemia.^{7,20,21} Inspired by the success of Blincyto[®], a significant number of new clinical trials have been registered since 2014.⁷ To date, according to Passariello et al.²² and other publications,^{7,23–25} more than 100 bsAb formats have been developed and more than 50 bsAbs have been studied in clinical trials.

1.1.2 Purification of therapeutic proteins by chromatography

An industrial production process for therapeutic proteins usually comprises four main steps which take place in the following order: preparation of the cell culture media, production of the target protein by fermentation (upstream processing), purification of the target protein (downstream processing) and formulation.^{26,27} Thereby, the downstream processing has the main goal to efficiently isolate the target protein from the cell culture media and to purify it to a final product quality.²⁷ An industrial purification process includes many different unit operations like cell disruption (not always required), centrifugation, virus inactivation, ultrafiltration, column chromatography, membrane chromatography, etcetera.^{4,27} Thereby, these unit operations aim to remove cells, cell fragments, viruses, host cell deoxyribonucleic acid (DNA), host cell ribonucleic acid (RNA), host cell proteins, endotoxins and product related impurities like protein fragments and aggregates.⁴ In this work, the main focus is on chromatography, which is the predominant technique for purification and analysis of therapeutic proteins.^{27,28} According to Hanke and Ottens,²⁸ a purification process for therapeutic protein usually includes three chromatography purification steps. According to Kimerer et al.¹¹, downstream processing of a bsAb generally utilizes the same process strategies used for common mAbs. Thereby, capture with Protein A chromatography is usually the first step, followed by polishing with ion exchange or hydroxyapatite columns.¹¹ A polishing step with hydrophobic interaction chromatography columns is also frequently applied.^{29,30} In this work, the focus is on ion exchange chromatography (IEC), which is very often used in particular for challenging polishing steps such as the removal of unwanted isoforms, fragments and aggregates.^{4,31}

Thereby, important to mention is that chromatographic purification steps like IEC account for a large proportion of the total manufacturing costs in biopharmaceutical production.^{1,32,33} As a consequence, the development of highly optimized and

efficient chromatography processes gained particular importance for the biotech industry.¹ For the development of such processes, empirical methods are still mostly used, but the application of mechanistic models for process development is increasingly attracting the interest of pharmaceutical companies.^{1,34–37}

1.2 Modeling and simulation of preparative chromatography processes

In industrial IEC processes are usually operated under high loading conditions, in order to make them as cost-effective and efficient as possible. In the development of such processes, the application of mechanistic modeling for industrial process development is gaining more and more attention from medicinal product manufacturers.^{1,34–37} Numerous models have been developed that provide adequate descriptions of protein elution at high column loadings. Upon examination of these models, it is noticeable that retention times are generally well predicted at high column loadings, however, discrepancies are often observed in the description of peak shapes.^{1,38} Both salt and pH gradients are difficult to describe under high column load conditions, with the latter including challenging complex peak shapes such as double-peak formation.^{1,2,36,39} If protein elution within salt and pH gradients have to be precisely described under high loading conditions, IEC models are needed that are provided with parameters and formalisms capable of describing the influences of column load, salt concentrations and pH properly.^{1,2,39–41}

1.2.1 Overview and comparison of different binding models

Creasy et al.^{39,41,42} published a systematic empiric interpolation (EI) method based on batch adsorption isotherms that can predict protein elution over broad ranges of column load, pH, and salt concentrations. However, the EI method requires a high number of model parameters for method calibration⁴¹ and a reliable description of elution behavior outside the parameter window used for calibration is impossible due to its empirical nature.³⁹ A more straightforward method for describing protein elution behavior is the use of mechanistic models. Particularly notable is that mechanistic models can be predictive with a relatively small number of model parameters, regardless of how extensive the applied data set is.¹

For IEC, mechanistic models are usually distinguished between stoichiometric and non-stoichiometric models.⁴³

Stoichiometric models such as the Steric Mass Action (SMA) model⁴⁴ are based on the principle that interactions between proteins and a stationary phase can be described by reversible stoichiometric displacement and coverage of counterions bound to the stationary phase by charged proteins.⁴³ Stoichiometric models are generally known for their simplicity, although it is often reported that they do not always provide an accurate representation of non-linear adsorption behavior.^{45–47}

Colloidal isotherm models belong to the class of non-stoichiometric models and use the colloidal nature of proteins as a theoretical basis. These models consider the accessible adsorber surface as a limiting factor and not its ionic capacity.^{36,43} In recent years, some papers presented colloidal isotherm models that were modified to provide the capability of describing elution behavior within the linear and also the non-linear adsorption range.^{36,38,43,48,49} Briskot et al.^{36,43} introduced a so called colloidal particle adsorption (CPA) model where elution behavior under high loading conditions is described by a combination of steric surface blocking effects and interactions between proteins that are adsorbed to the stationary phase. Protein elution over broad ranges of pH, salt concentrations, and column loadings could be successfully described.^{36,43}

For this work, stoichiometric mechanistic models are used, since these models are still the most widely applied in both academia and industry.³⁶ For low loading conditions, the Stoichiometric Displacement (SD) model is used.^{50,51} In the SD model, adsorption is mainly described by the number of binding sites and the equilibrium constant which are both linear isotherm parameters.¹ Description of enhanced load conditions can be done by using the SMA model proposed by Brooks and Cramer, which is able to describe Langmuir elution behavior under high loading conditions.⁴⁴ The SMA model is an extension of the SD model that uses the same model parameters as the SD model and contains only the steric shielding factor as additional non-linear parameter.¹ If anti-Langmuir binding and elution behavior under high loading conditions needs to be described, the Self-Association-SMA (SAS-SMA) model introduced by Mollerup can be used.^{3,52,53} This model is an extension of the SMA model and describes self-association of the protein on the stationary phase in the form of self-dimerization.^{52,53}

1.2.2 pH-dependence of the model parameters in stoichiometric models

To ensure the proper functioning of the applied mass action models, the model parameters need to adapt appropriately as a function of pH, because the mobile phase pH has a strong impact on protein adsorption in IEC.⁵⁴ Description of protein binding and elution over broad ranges of pH and protein concentrations is only possible with pH-dependent linear and non-linear model parameters.¹ There are already a few publications that have investigated the pH-dependence of the SD/SMA/SAS-SMA model parameters and some of them have also included it in their models.^{1-3,32,40,54-61} Yang et al.⁶⁰ modified their SMA model by describing the pH-dependence of the model parameters by taking into account protein structure properties.⁶⁰ Bosma and Wesselingh extended their SMA model with a pH-dependent equilibrium constant.⁶¹ They described the pH-dependence of the equilibrium constant via the electrokinetic charge of the protein, however, neglected a pH-dependence of the binding charge.⁶¹ Schmidt et al.⁵⁹ and Kluters et al.⁴⁰ applied a protein net charge-based model^{62,63} to describe the pH-dependence of the protein binding charge. By using Mollerup's thermodynamic model,⁶⁴ they were able to describe the pH-dependence of the equilibrium constant with the pH-dependence of the binding charge.^{40,59} Saleh et al.⁵⁷ also used an SMA model that takes into account the pH-dependence of the linear isotherm parameters, but assumed that the shielding factor is pH-independent. However, Saleh and co-workers hypothesized that the introduction of a pH-dependent shielding factor could further improve the ability of their model to describe high loading experiments with changing pH.⁵⁷ Koch et al.⁶⁵ used a modified SAS-SMA model to describe complex anti-Langmuir to Langmuir behavior (AL-L) of a polypeptide under high loading conditions. The AL-L behavior is characterized by the peaks initially exhibiting an anti-Langmuir shape as the loading increases and then suddenly beginning to exhibit Langmuir shapes when a certain loading is exceeded.^{65,66} Koch et al.⁶⁵ extended the SAS-SMA model with two activity coefficients for the protein and salt in solution. By implementing pH-dependent empirical descriptions for the activity coefficient of the protein in solution, the complex AL-L elution behavior of a polypeptide within a range of pH 3.3 to pH 4.3 could be precisely predicted.⁶⁵ However, Koch and colleagues did not describe the steric shielding factor in a pH-dependent manner and, furthermore, they also did not describe the model parameters for describing self-dimerization in a pH-dependent manner.^{3,65} Shi et al.⁵⁵ investigated the effects of pH and ionic strength on the model

parameters of the SMA model around the isoelectric point (IEP) of a protein. They used anion exchange (AEX) chromatography and investigated, among other things, the pH-dependence of the steric shielding factor. As the pH decreased, the characteristic charge decreased while the shielding factor increased. They concluded that an increase of the steric shielding factor at lower pH values might be attributed to the decreased adsorption capacity of the protein.⁵⁵ Furthermore, Shi and co-workers demonstrated that the SMA model describes the IEC equilibrium of proteins more accurately when the influences of pH and salt concentration on the model parameters are taken into account.⁵⁵

1.2.3 Modeling and simulation under high loading and overloading conditions

When a chromatography column is overloaded with proteins, complex elution profiles can be observed.² As a result, phenomena such as complex peak shapes and unexpected sample breakthroughs can occur under high loading and overloading conditions,² as has already been shown in other scientific studies.^{36,38,65–68}

Recently published works showed that in preparative cation exchange (CEX) chromatography run in bind-elute mode, the elution profiles can be influenced by the charge variants of the protein.^{58,69–71} Rischawy et al.⁵⁸ and Saleh et al.⁵⁷ described the complex elution behavior of antibody samples by including individual variants into their SMA modeling-based approach. Saleh et al.⁵⁷ determined individual shielding factor values for each charge isoform of their mAb sample. The estimated shielding factor values of the individual charge variants differed significantly (e.g., because of repulsive effects⁷²), resulting in a good agreement between simulated and experimental elution profiles.⁵⁷

Diedrich et al.⁶⁷ observed complex peak shapes with a shoulder in the peak front and sample breakthrough under high loading conditions. They hypothesized that multiple binding orientations of a protein can lead to these kinds of peak shapes under overloading conditions. While the classical SMA model failed in describing these peaks, their multi-state SMA model successfully predicted the resulted elution profiles.⁶⁷ Huuk et al.⁶⁸ observed similar phenomena and hypothesized that non-ideal behavior of the protein in the mobile phase is responsible for these complex peak shapes. By extension of the SMA model with an asymmetric activity coefficient initially introduced by Mollerup⁵², retention of the peaks could be well described, however, deviations in the description of the peak shapes remain unsolved.⁶⁸

Some researchers have used other binding models than the SMA model to describe complex high loading behavior. Briskot et al.³⁶ applied a non-stoichiometric CPA model that considered protein-protein interactions in the bound state. The CPA model can predict these elution profiles for the most part.^{36,43} Khalaf et al.⁶⁶ observed complex AL-L behavior of some proteins on polyelectrolyte brush type cation exchangers under high loading conditions because of multi-layer binding. An AL-L adsorption isotherm was developed capable of describing multi-layer binding. Using this AL-L model, flow through experiments performed under enhanced column loading could be successfully described.⁶⁶

Some publications indicate that the kinetics of the protein adsorption on the ion exchanger might explain overloading effects like unforeseen sample breakthrough.⁷³⁻⁷⁵ Intraparticle diffusional mass transport is often the rate limiting factor in protein adsorption.⁷³ According to Wesselingh and Bosma, both the surface and pore diffusion will decrease when the binding strength increases⁷⁵ and thus may result in sample breakthrough before saturation of the resin beads.^{73,76,77} Potential mass transfer limitations may also be amplified by the relatively large size of the bsAb samples used in this work (molecular mass of ~ 147 kDa (bsAbX) and ~ 239 kDa (bsAbY)).^{1-3,78} An advanced mass transfer model that accounts for surface and pore diffusion is needed to describe salt- and pH-dependent sample breakthrough.⁷⁹ In line with this conclusion, Kumar et al.³⁸ combined their colloidal isotherm model with an extended mass transport model, which was able to describe surface diffusivity as a function of ionic strength or binding affinity. Thus, their model-based approach was able to simulate overloading effects like breakthrough as well.

Recently, an uncommon adsorption and elution behavior of bsAbs was reported to occur even at low loading conditions. Kimerer et al.^{11,78,80,81} reported that bsAbs tend to have more conformational flexibility than normal mAbs, leading to the formation of multiple binding forms with different binding affinities. Consequently, these conformational forms led to complex patterns of bound proteins within the particles dependent on pH and salt concentration⁷⁸ and the formation of multiple peaks dependent on the residence time,¹¹ on the hold time,¹¹ and on the salt concentration during loading⁸⁰ was observed. Kimerer et al. developed multi-state SD¹¹ and SMA⁷⁸ models suitable for modeling of multiple peak formations, which was verified at low loading conditions.¹¹ The above-mentioned multi-state SMA model established by

Diedrich et al.⁶⁷ could also be used to describe multi-state binding under high loading conditions.

1.3 Theoretical considerations

The following subsections of this chapter present and summarize the theoretical foundations and the models used for modeling and simulation of IEC experiments.

1.3.1 IEC adsorption equilibrium

The ion exchange process can be described based on the competition between charged protein molecules P_i and salt counterions S for binding to the oppositely charged ligands L of the stationary phase. The stoichiometric exchange of proteins with the binding charge number z_i and exchangeable salt counterions with the charge number z_1 can be described as follows⁶⁴:



For monovalent counterions like Na^+ , z_i is identical to the stoichiometric coefficient or characteristic binding charge $v_i = z_i/z_1$. The index 1 refers to the salt, since in this work the salt is always considered as component 1 for the calculation of IEC adsorption equilibria. The index i refers to the proteins. In this work, the proteins are considered as components 2, 3, ..., $n + 1$. The thermodynamic equilibrium constant $K_{eq,i}$ for the exchange reaction is defined as⁶⁴:

$$K_{eq,i} = \frac{\hat{a}_i a_1^{v_i}}{a_i \hat{a}_1^{v_i}} = \frac{\hat{x}_i x_1^{v_i} \hat{\gamma}_i \gamma_1^{v_i}}{x_i \hat{x}_1^{v_i} \gamma_i \hat{\gamma}_1^{v_i}} = \frac{q_i (c_1)^{v_i}}{c_i (\bar{q}_1)^{v_i}} \frac{\hat{\gamma}_i \gamma_1^{v_i}}{\gamma_i \hat{\gamma}_1^{v_i}} \quad (2)$$

With the activity a , the mole fraction x and the activity coefficient γ . The circumflex above a , x and γ indicates the corresponding parameters for the adsorbed species. Multiplying the mole fractions with the molar density c in the pore volume gives the molar concentration for the adsorbed protein q_i and adsorbed salt q_1 , as well as the respective molar concentration in the liquid phase given by c_i and c_1 .⁶⁴ The bar above q_1 indicates that only adsorbed counterions accessible for exchange with the protein are involved in the equilibrium.^{1,44,82}

Activity coefficients are able to express the deviations from the ideal behavior of the solution.⁶⁴ Thereby, it is convenient to normalize the activity coefficient of a species

dissolved in solvent to the activity coefficient of the corresponding species at infinite dilution in solvent, thus introducing a so-called asymmetric activity coefficient.^{3,4} Mollerup et al.^{52,64,68,83,84} normalized the activity coefficient for the protein in solution γ_i to the activity coefficient for the protein in solution at infinite dilution γ_i^∞ resulting in the asymmetric activity coefficient for the protein in solution $\tilde{\gamma}_i$ which is given as follows:

$$\tilde{\gamma}_i = \frac{\gamma_i}{\gamma_i^\infty} \quad (3)$$

Furthermore, it is quite common to assume ideal behavior of the species in IEC which is expressed by activity coefficients that are set to unity.^{44,85} To simplify the modeling approach, the activity coefficients for the bound species ($\hat{\gamma}_i$ and $\hat{\gamma}_1$) were set to one. The activity coefficient for the protein in solution at infinite dilution γ_i^∞ was also set to one. Hence, the calculation of $K_{eq,i}$ changes as follows⁶⁴:

$$K_{eq,i} = \frac{q_i}{c_i} \left(\frac{c_1}{\bar{q}_1} \right)^{v_i} \frac{\gamma_1^{v_i}}{\tilde{\gamma}_i} \quad (4)$$

The asymmetric activity coefficient $\tilde{\gamma}_i$ was always set to one when the elution behavior of bsAbY was described with the SMA model (see section 1.3.2), which further simplifies equation (4). For the calculation of the elution behavior of bsAbX with the SAS-SMA model (see section 1.3.3), $\tilde{\gamma}_i$ was calculated with equation (23), according to the constraints formulated in section 1.3.4.

According to Gerstner et al.,⁸⁶ $K_{eq,i}$ can also be calculated from the alteration in the standard Gibbs energy change of the ion exchange equilibrium of component i ($\Delta G_{IEC,i}^0$), which is given as follows:

$$-RT \ln K_{eq,i} = \Delta G_{IEC,i}^0 = \hat{\mu}_i^0 + v_i \mu_1^0 - \mu_i^0 - v_i \hat{\mu}_1^0 = \Delta G_i^0 - v_i \Delta G_1^0 \quad (5)$$

Here μ_i^0 and μ_1^0 are the reference state chemical potentials of the protein and the counterion, respectively, while the circumflex above $\hat{\mu}_i^0$ and $\hat{\mu}_1^0$ indicates the corresponding parameters for the bound species, with the universal gas constant R , the absolute temperature T and the Gibbs energy change of adsorption of component i (ΔG_i^0) and the Gibbs energy change of association of the counterion (ΔG_1^0).

The linear model parameters v_i and $K_{eq,i}$ both depend on the pH of the mobile phase.^{1,59} The pH-dependence of v_i was introduced based on a protein net charge model^{59,62,63}:

$$v_i = \sum_i -\frac{N_{-i}}{1 + 10^{pK_{a_i} - pH}} + \sum_i \frac{N_{+i}}{1 + 10^{pH - pK_{a_i}}} \quad (6)$$

Here, N_{-i} stands for the number of acidic amino acids that are involved in the binding of the protein to the ligand, N_{+i} stands for the number of basic amino acids that are involved in the binding of the protein to the ligand (see Table 19), and pK_{a_i} stands for the pK_a (negative logarithm of the acid dissociation constant) values of the individual amino acids (see Table 17). Here, the assumption is made that the pK_{a_i} value of the individual amino acids is not influenced by their positions within the amino acid sequence of the protein.⁵⁹ With changing pH, v_i usually follows the titration curve of the protein.⁵⁹ However, v_i is typically not identical with the net charge of the protein, since not all charged amino acids within the amino acid sequence of the protein are available for interactions with the oppositely charged ligands of the stationary phase.⁵⁹ Equation (5) defines the pH-dependence of $K_{eq,i}$. Here it can be clearly seen that the pH-dependence of $K_{eq,i}$ is given by v_i .

1.3.2 Steric Mass Action (SMA) model

In 1992, Brooks and Cramer have proposed to use the SMA model for describing the protein adsorption equilibrium in IEC.⁴⁴ The SMA model introduces the steric shielding factor σ_i which depicts the shielding of salt counterions upon protein binding by, among other things, steric hindrance.^{1,44} In the SMA model, adsorption of the protein to the stationary phase leads to a reduction of adsorbed and accessible salt counterions which is given by the following expression⁴⁴:

$$\bar{q}_1 = \Lambda - \sum_{i=2}^{n+1} (\sigma_i + v_i) q_i \quad (7)$$

Where Λ is the ionic capacity (mol/L_{pore volume}) in the pore volume. In this work, the asymmetric activity coefficient $\tilde{\gamma}_i$ is set to one when the SMA model is used. Substituting equation (7) into equation (4), setting $\tilde{\gamma}_i$ to one and doing some rearrangements leads to the following multi-component SMA isotherm^{1,44}:

$$\frac{q_i}{c_i} = K_{eq,i} \frac{1}{\gamma_1^{v_i}} \left(\frac{\Lambda}{c_1} \right)^{v_i} \left(1 - \sum_{j=2}^{n+1} \frac{(\sigma_j + v_j) q_j}{\Lambda} \right)^{v_i} = K_{eq,i} \frac{1}{\gamma_1^{v_i}} \left(\frac{\Lambda}{c_1} \right)^{v_i} \left(1 - \sum_{j=2}^{n+1} \frac{q_j}{q_{max,j}} \right)^{v_i} \quad (8)$$

With the theoretical maximal binding capacity $q_{max,i}$. At very low protein concentrations ($q_i \rightarrow 0$ and $c_i \rightarrow 0$) the distribution coefficient A_i giving the initial slope of the isotherm can be approximated by⁸⁷:

$$A_i = \frac{q_i}{c_i} = K_{eq,i} \frac{1}{\gamma_1^{v_i}} \left(\frac{\Lambda}{c_1} \right)^{v_i} \quad (9)$$

Equation (9) is the linear isotherm of the SD model, which demonstrates that the SMA model and the SD model are identical under low loading conditions ($q_i \rightarrow 0$ and $c_i \rightarrow 0$).⁴⁰ Likewise, in the case of the SD model, $\tilde{\gamma}_i$ was always set to one.

1.3.3 Self-Association Steric Mass Action (SAS-SMA) model

Many proteins self-associate, which means that they associate with other proteins of the same type.^{52,53} Insulin is a well-known example for self-association.⁵² Mollerup et al.^{52,53} established an extended version of the SMA model which is called Self-Association Steric Mass Action (SAS-SMA) model. The SAS-SMA model assumes that self-association occurs on the stationary phase surface in the form of self-dimerization, resulting in a dimer that has the same binding charge v_i as the monomer.^{52,53} In this work, the SAS-SMA model was extended by Mollerup's asymmetric activity coefficient for the protein in solution $\tilde{\gamma}_i$ ^{52,53,64,68,83,84} to describe additionally protein-protein interactions in the mobile phase.

When a protein binds to another protein of the same species, the association scheme is⁵²:



The index $1, i$ represents the monomeric protein and the index $2, i$ represents the dimeric protein. The equilibrium constant of the self-association equilibrium $K_{eq,2,i}$ is given as follows^{52,64}:

$$K_{eq,2,i} = \frac{\hat{a}_{2,i}}{a_i \hat{a}_{1,i}} = \frac{\hat{x}_{2,i}}{x_i \hat{x}_{1,i}} \frac{\hat{\gamma}_{2,i}}{\gamma_i \hat{\gamma}_{1,i}} = \frac{q_{2,i} c}{c_i q_{1,i} \gamma_i \hat{\gamma}_{1,i}} \quad (11)$$

with the activity of bound dimer $\hat{a}_{2,i}$ and of bound monomer $\hat{a}_{1,i}$, with the mole fraction of bound dimer $\hat{x}_{2,i}$ and of bound monomer $\hat{x}_{1,i}$, as well as with the concentration of bound dimer $q_{2,i}$ and of bound monomer $q_{1,i}$. As mentioned above, an ideal behavior of the adsorbed species was assumed in this work. This simplification applies to both the adsorbed monomer layer ($\hat{\gamma}_{1,i} = 1$) and the adsorbed dimer layer ($\hat{\gamma}_{2,i} = 1$). Together with the other assumptions already mentioned, the equilibrium constant of the self-association equilibrium $K_{eq,2,i}$ is given by⁵²:

$$K_{eq,2,i} = \frac{q_{2,i} c}{c_i q_{1,i} \tilde{\gamma}_i} \quad (12)$$

The reduction of bound and accessible salt counterions \bar{q}_1 due to protein binding and self-dimerization is given by⁵²:

$$\bar{q}_1 = \Lambda - \sum_{i=2}^{n+1} \left((\sigma_{1,i} + v_i) q_{1,i} + (\sigma_{2,i} + v_i) q_{2,i} \right) \quad (13)$$

with the shielding factor for the monomer $\sigma_{1,i}$ and the dimer $\sigma_{2,i}$. The isotherm for the monomer is⁵²:

$$\begin{aligned} \frac{q_{1,i}}{c_i} &= K_{eq,i} \frac{\tilde{\gamma}_i}{\gamma_1^{v_i}} \left(\frac{\Lambda}{c_1} \right)^{v_i} \left(1 - \sum_{j=2}^{n+1} \left(\frac{(\sigma_{1,j} + v_j) q_{1,j}}{\Lambda} - \frac{(\sigma_{2,j} + v_j) q_{2,j}}{\Lambda} \right) \right)^{v_i} \\ &= K_{eq,i} \frac{\tilde{\gamma}_i}{\gamma_1^{v_i}} \left(\frac{\Lambda}{c_1} \right)^{v_i} \left(1 - \sum_{j=2}^{n+1} \left(\frac{q_{1,j}}{q_{max,1,j}} - \frac{q_{2,j}}{q_{max,2,j}} \right) \right)^{v_i} \end{aligned} \quad (14)$$

with the theoretical maximal binding capacity of the monomer $q_{max,1,i}$ and the theoretical maximal binding capacity of the dimer $q_{max,2,i}$. By rearranging equation (12) one can calculate the concentration of bound dimer⁵²:

$$q_{2,i} = q_{1,i} \frac{K_{eq,2,i}}{c} c_i \tilde{\gamma}_i \quad (15)$$

whereby the total concentration of bound protein q_i can be calculated by⁵²:

$$q_i = q_{1,i} + 2q_{2,i} = q_{1,i} \left(1 + 2 \frac{K_{eq,2,i}}{c} c_i \tilde{\gamma}_i \right) \quad (16)$$

For simplification it is assumed that⁵²:

$$(\sigma_{2,i} + v_i) = 2(\sigma_{1,i} + v_i) = 2(\sigma_i + v_i) \quad (17)$$

This gives the following isotherm for the monomer⁵²:

$$\begin{aligned} \frac{q_{1,i}}{c_i} &= K_{eq,i} \frac{\tilde{\gamma}_i}{\gamma_1^{v_i}} \left(\frac{\Lambda}{c_1} \right)^{v_i} \left(1 - \sum_{j=2}^{n+1} \left(\frac{(\sigma_j + v_j) q_{1,j}}{\Lambda} - \frac{(\sigma_j + v_j) 2q_{2,j}}{\Lambda} \right) \right)^{v_i} \\ &= K_{eq,i} \frac{\tilde{\gamma}_i}{\gamma_1^{v_i}} \left(\frac{\Lambda}{c_1} \right)^{v_i} \left(1 - \sum_{j=2}^{n+1} \left(\frac{(\sigma_j + v_j) q_j}{\Lambda} \right) \right)^{v_i} \end{aligned} \quad (18)$$

and the following isotherm for the dimer⁵²:

$$\frac{q_{2,i}}{c_i} = \frac{q_{1,i}}{c_i} \frac{K_{eq,2,i}}{c} c_i \tilde{\gamma}_i = K_{eq,i} \left(\frac{\Lambda}{c_1} \right)^{v_i} \left(1 - \sum_{j=2}^{n+1} \left(\frac{(\sigma_j + v_j) q_j}{\Lambda} \right) \right)^{v_i} \frac{K_{eq,2,i}}{c} c_i \frac{\tilde{\gamma}_i^2}{\gamma_1^{v_i}} \quad (19)$$

Based on equation (15), the resulting multi-component isotherm of the total protein is given by:

$$\begin{aligned} \frac{q_i}{c_i} &= K_{eq,i} \frac{\tilde{\gamma}_i}{\gamma_1^{v_i}} \left(\frac{\Lambda}{c_1} \right)^{v_i} \left(1 - \sum_{j=2}^{n+1} \left(\frac{(\sigma_j + v_j) q_j}{\Lambda} \right) \right)^{v_i} \left(1 + 2 \frac{K_{eq,2,i}}{c} c_i \tilde{\gamma}_i \right) \\ &= K_{eq,i} \frac{\tilde{\gamma}_i}{\gamma_1^{v_i}} \left(\frac{\Lambda}{c_1} \right)^{v_i} \left(1 - \sum_{j=2}^{n+1} \left(\frac{q_j}{q_{max,j}} \right) \right)^{v_i} \left(1 + 2 \frac{K_{eq,2,i}}{c} c_i \tilde{\gamma}_i \right) \end{aligned} \quad (20)$$

Since it is well-known that protein oligomerization like dimerization depends on pH,^{88,89} the parameter $K_{eq,2,i}/c$ was assumed to be pH-dependent. In the course of the project an empirical description of the pH-dependence of $K_{eq,2,i}/c$ was found, which is shown and explained in section 3.7.1.2 (see equation (43)).

At very low protein concentrations ($q_i \rightarrow 0$ and $c_i \rightarrow 0$ (and thus $\tilde{\gamma}_i = 1$, see section 1.3.4)), equation (20) simplifies to the linear SD isotherm or respectively to the distribution coefficient A_i giving the initial slope of the isotherm (see equation (9)). This demonstrates that the applied SAS-SMA model and the SD model are identical under low loading conditions ($q_i \rightarrow 0$ and $c_i \rightarrow 0$).

1.3.4 Activity coefficients for salt and protein in solution

The activity coefficient for salt in solution γ_1 was used in combination with the SD model, the SMA model, and the SAS-SMA model. Thereby, γ_1 was calculated by using a Davies equation⁹⁰ which is extended with a temperature-dependent term introduced by Debye and Hückel⁹¹:

$$\log \gamma_1 = -1.82 \cdot 10^6 (\epsilon T)^{-3/2} z_1^2 \left(\frac{\sqrt{c_1}}{1 + \sqrt{c_1}} - 0.3 \cdot c_1 \right) \quad (21)$$

Here, T is the temperature at 298.15 K and ϵ is the dielectric constant of water at 298.15 K. A value of 78.38 was used for ϵ .⁹² The Davies equation is suitable to predict the behavior of an electrolytic solution up to an ion concentration of 0.5 mol/L.^{93,94}

In this work, the asymmetric activity coefficient for the protein in solution $\tilde{\gamma}_i$ was always set to one in the case of the SD model and the SMA model. The asymmetric activity coefficient $\tilde{\gamma}_i$ was only used in combination with the SAS-SMA model. Thereby, $\tilde{\gamma}_i$ was calculated as previously introduced by Mollerup⁵² and already successfully applied by Huuk et al.⁶⁸:

$$\ln \tilde{\gamma}_i = K_{p,i} c_i + K_{1,i} c_1 \quad (22)$$

with the parameter $K_{p,i}$ that is specific for the protein and the parameter $K_{1,i}$ that is specific for the counterion. In the complete work, no correlation was found where $K_{1,i}$ was needed. $K_{1,i}$ was therefore always set to zero, which simplified the formula for calculating $\tilde{\gamma}_i$ as follows:

$$\ln \tilde{\gamma}_i = K_{p,i} c_i \quad (23)$$

The relationship shown in equation (23) is then only relevant at high loading conditions, since the relationship does not matter at low loading conditions or at

diluted conditions ($c_i \rightarrow 0$). This means that at low loading conditions $\tilde{\gamma}_i$ has a value of one. Furthermore, the parameter $K_{p,i}$ relates to the difference of water-protein and protein-protein interactions.^{68,95} According to Mollerup,⁸³ $K_{p,i}$ depends on the charge of the protein and thus on pH. In the course of the project an empirical description of the pH-dependence of $K_{p,i}$ was found, which is shown and explained in section 3.7.1.2 (see equation (42)).

1.3.5 Linear gradient elution (LGE)

In the 1980s, Yamamoto and co-workers developed a mathematical model to describe the elution of proteins in IEC using linear gradient elution (LGE) experiments.^{96–98} Since Yamamoto's LGE approach applies only to low loading or diluted conditions ($c_i \rightarrow 0$), $\tilde{\gamma}_i$ has a value of one (see equation (23) in section 1.3.4). In this work, linear salt gradient elution experiments at fixed pH, as well as linear pH gradient elution experiments at constant counterion concentrations were used for determination of linear model parameters. Thus, the correlation of the normalized gradient slope and A_i is given by^{40,59}:

$$\begin{aligned} \frac{dGH_1}{dc_{1,elu}} &= \frac{dGH_{pH}}{dpH_{elu}} = \left[k_{d,i} \cdot \left(K_{eq,i} \frac{1}{\gamma_1^{v_i}} \left(\frac{\Lambda}{c_{1,elu}} \right)^{v_i} \right) + k_{d,i} - 1 \right]^{-1} \\ &= \frac{1}{k_{d,i} \cdot A_i + k_{d,i} - 1} \end{aligned} \quad (24)$$

with the eluting salt concentration in the liquid phase $c_{1,elu}$, the eluting pH in the liquid phase pH_{elu} , the normalized salt gradient slope GH_1 , the normalized pH gradient slope GH_{pH} and the exclusion factor of the protein $k_{d,i}$. In equation (24), $K_{eq,i}$ is calculated as shown in equation (5), with the model parameters ΔG_i^0 and ΔG_1^0 . Furthermore, v_i is calculated as shown in equation (6), using of course the determined pH_{elu} values. The normalized slope of the linear salt gradient is given by⁴⁰:

$$GH_1 = g_1(V_c(1 - \varepsilon)\varepsilon_p) = \frac{c_{1,final} - c_{1,init}}{V_g} (V_c(1 - \varepsilon)\varepsilon_p) \quad (25)$$

V_c is the column volume (CV), g_1 is the slope of the linear salt gradient, and V_g is the gradient volume with the initial salt concentration $c_{1,init}$ and the final salt

concentration $c_{1,final}$. The gradient slope is normalized to the pore volume. The pore volume can be calculated by using the interstitial porosity of the packed column ε and the intraparticle porosity ε_p .⁸⁷ Similar to the definition of the normalized salt gradient slope, the normalized slope of the linear pH gradient GH_{pH} is⁵⁹:

$$GH_{pH} = g_{pH}(V_c(1 - \varepsilon)\varepsilon_p) = \frac{pH_{final} - pH_{init}}{V_g} (V_c(1 - \varepsilon)\varepsilon_p) \quad (26)$$

The initial pH in the linear pH gradient is given by pH_{init} and the final pH in the linear pH gradient is given by pH_{final} . The slope of the linear pH gradient is given by g_{pH} .

1.3.6 Column simulation model

A lumped rate model was used for simulation of protein elution profiles, salt concentration in solution c_1 , and mobile phase pH. The lumped rate model for calculation of the protein elution curves consists of the following differential material balance⁹⁹:

$$\frac{\partial c_i}{\partial t} + u_{int} \frac{\partial c_i}{\partial x} + \frac{(1 - \varepsilon)\varepsilon_p k_{d,i}}{\varepsilon} \frac{\partial q_i^*}{\partial t} = D_{ax} \frac{\partial^2 c_i}{\partial x^2} \quad (27)$$

Thereby, the averaged concentration of adsorbed protein in the accessible pore volume is given by q_i^* , the axial dispersion is given by D_{ax} , the axial position in the column is given by x and the interstitial mobile phase velocity is given by u_{int} . Equation (27) was also used for calculation of c_1 , with the assumption that the salt is treated as an inert modulator with $D_{ax} = 0$, $k_{d,1} = 1$, and local equilibrium between c_1 and q_1^* exists. Here, q_1^* is the averaged concentration of adsorbed counterion in the accessible pore volume. The mobile phase pH was treated like a common mobile phase modulator and hence also calculated using equation (27) with the same assumptions as for c_1 .

A linear driving force approximation was used to describe mass transfer for the protein in the column. Thereby, the mass transfer resistance in the solid phase is considered to be dominant^{99,100}:

$$\frac{\partial q_i^*}{\partial t} = k_{eff,i} \frac{6}{d_p} (q_{eq,i}^* - q_i^*) \quad (28)$$

In this equation, d_p denotes the particle diameter of the resin and $q_{eq,i}^*$ is the averaged concentration of adsorbed protein in the accessible pore volume that is in equilibrium with the mobile phase.⁴⁰ The effective mass transfer coefficient $k_{eff,i}$ is a lumped rate parameter. $k_{eff,i}$ describes the transfer between q_i^* and $q_{eq,i}^*$.⁹⁹ Equation (27) and equation (28) are discretized by a first-order central finite-difference method as shown by Ingham et al.¹⁰¹ and the resulting system of ordinary differential equations (ODE) was solved using the fourth-order Rosenbrock (stiff) method in Berkeley Madonna™. The computation was done using a number of at least thirty increments.

For the SAS-SMA model, the IEC adsorption equilibrium was modeled by using the following equation, which is similar to the SMA formalism^{44,82}:

$$q_{eq,i}^* = \frac{\Lambda K_{eq,i} \frac{\tilde{Y}_i}{\gamma_1^{v_i}} \left(\frac{\bar{q}_1}{c_1}\right)^{v_i-1} c_i \left(1 + 2 \frac{K_{eq,2,i}}{c} c_i \tilde{Y}_i\right)}{c_1 + \sum_{i=2}^{n+1} (\sigma_i + v_i) K_{eq,i} \frac{\tilde{Y}_i}{\gamma_1^{v_i}} \left(\frac{\bar{q}_1}{c_1}\right)^{v_i-1} c_i \left(1 + 2 \frac{K_{eq,2,i}}{c} c_i \tilde{Y}_i\right)} \quad (29)$$

If no protein-protein interactions are expected to be present ($K_p = 0$ and $K_{eq,2,i}/c = 0$), then the SAS-SMA isotherm (equation (29)) simplifies to the following SMA isotherm¹:

$$q_{eq,i}^* = \frac{\Lambda K_{eq,i} \frac{1}{\gamma_1^{v_i}} \left(\frac{\bar{q}_1}{c_1}\right)^{v_i-1} c_i}{c_1 + \sum_{i=2}^{n+1} (\sigma_i + v_i) K_{eq,i} \frac{1}{\gamma_1^{v_i}} \left(\frac{\bar{q}_1}{c_1}\right)^{v_i-1} c_i} \quad (30)$$

Both, the SMA formalism (equation (30)) and the SAS-SMA formalism (equation (29)) were solved by using a Newton iteration like shown in the doctoral thesis of Frederiksen.⁸²

1.4 Aim of the work

The objective of the work was to investigate, to describe, to model, and to simulate the complex binding and elution behavior of two therapeutically active bsAbs under high loading and column overloading conditions on the strong cation exchange resin POROS™ XS.

Therefore, the binding and elution behavior of the bsAbs used must be investigated and specified in order to select appropriate stoichiometric binding models for each

bsAb. Subsequently, these models have to be modified and further developed accordingly, whereby two main requirements in particular have to be fulfilled:

First, the usage of comparatively simple models that require only a limited number of model parameters to ensure the simplicity and applicability of the applied model-based approaches.

Second, the ability to predict protein elution over wide ranges of pH and salt concentrations when high loading and even overloading conditions are applied.

To achieve these goals, the stoichiometric binding models used should be modified to include activity coefficients (e.g. for the description of salt in solution) and to include pH-dependent descriptions of the model parameters. The unique aspect here is that not only the linear model parameters will be described in a pH-dependent manner, but also the pH-dependence of the non-linear model parameters like the steric shielding factor will be described. Hence, the stoichiometric binding models should each be described in a fully pH-dependent manner. The functionality of these pH-dependent models should be verified with linear salt, pH, and dual gradient elution experiments performed under high loading and overloading conditions. The pH-dependent linear and non-linear model parameters, which adjust their values as the pH changes, should enable precise prediction of the resulting peak retentions and peak shapes in particular. The ability of the models to describe complex elution profiles due to high column loadings must be thoroughly tested. The causes must be found if discrepancies between simulated and experimental data are observed as a consequence of complex high loading and overloading phenomena. Possible solutions for eliminating these discrepancies must be presented or at least logical suggestions for their elimination must be made (e.g. suggestions for further model modifications). Complex high loading and overloading phenomena such as sample breakthrough during loading or pre-shoulder formation must be investigated in detail for these purposes.

2 MATERIAL AND METHODS

2.1 Materials

Some of the materials and related information listed in this section (2.1 Materials) have already been shown, listed and described in the publications Seelinger et al.¹ (Part 1, 2022) and Seelinger et al.² (Part 2, 2022). Some of the materials and related information listed in this section (2.1 Materials) are also shown, listed and described in Seelinger et al.³ (DRAFT (submitted)).

2.1.1 Chemicals

Table 1: List of chemicals

Name	Grade/Purity	Manufacturer
Acetic acid 100 %	p.A.	AppliChem GmbH
CHES	≥ 99.0 %	Sigma-Aldrich
DextranBlue	n.s.	Sigma-Aldrich
Ethanol	≥ 99.0 %	Berkel AHK
HEPES	≥ 99.5 %	AppliChem GmbH
Hydrochloric acid (HCl)	Titripur [®]	Merck KGaA
MES·H ₂ O	≥ 99.0 %	AppliChem GmbH
MOPSO	≥ 99.0 %	Sigma-Aldrich
Sodium azide (NaN ₃)	≥ 99.0 %	AppliChem GmbH
Sodium chloride (NaCl)	≥ 95.0 %	Carl Roth
Sodium dihydrogen phosphate monohydrate (NaH ₂ PO ₄ ·H ₂ O)	Ph.Eur.	AppliChem GmbH
Sodium hydroxide (NaOH)	≥ 98.0 %	Carl Roth
Succinic acid	≥ 99.0 %	abcr GmbH
TAPS	≥ 99.0 %	AppliChem GmbH

2.1.2 Electronic devices

Table 2: List of electronic devices

Devices	Name / Model	Manufacturer
Analytical balance	R160P-*D1	Sartorius
Autosampler for ÄKTAmicro	A-905	Cytiva
Fraction collector used for 5 mL tubes	Frac-920	Cytiva
Heating bath	IKA [®] HBR4 digital	IKA
Liquid chromatography system for protein analysis	ÄKTA™ micro	Cytiva
Liquid chromatography system for protein purification	ÄKTA™ purifier 100	Cytiva
Magnetic stirrer	COMBIMAG RCT	IKA
Microplate reader	GENios Pro	Tecan Group
pH electrode	SenTix [®] 980	WTW
pH/Conductivity meter	inoLab_IDS Multi 9420	WTW
Spectroscopy system	Agilent 8453	Agilent Technologies
Ultrapure water production system	Milli-Q [®] Gradient	Merck KGaA
Ultrasonic bath	Sonorex Super 10 P	Bandelin

2.1.3 Miscellaneous items

Miscellaneous item	Name / Model	Manufacturer
Bottle Top Filters	Bottle Top Filters 500 mL	Thermo Fisher Scientific Inc.
Membran filters 0.45 μm for bottle top filtration	Cellulose acetate mebrane filters	Sartorius
Piston-stroke pipettes	PIPETMAN Pipettes, P2 – P1000	Gilson, Inc.
96 well plate for UV absorption measurement in microplate reader	UV-Star [®] plate, 96 well, flat bottom	Greiner Bio- One GmbH

2.1.4 Software

Table 3: List of software

Software	Provider	Application
Berkley Madonna [™]	R. Macey and G. Oster, University of California (Berkeley, USA)	Mathematical modeling software for numerical solving of ordinary differential equations and difference equations.
UNICORN [™] 5.31	Cytiva	Controlling of ÄKTA Protein Purification Systems.
PeakFit [®] v4.12	SeaSolve Software	Automated nonlinear peak separation and analysis software

2.1.5 Column and resin used for preparative chromatography

The strong cation exchange resin POROS™ XS (Thermo Fisher Scientific Inc.) with the charge number XS-101 was used. The resin was used in a prepacked OPUS® MiniChrom® column with an inner diameter (ID) of 5 mm and a length of 50 mm (volume of the column $V_c = 1.0$ mL) purchased from Repligen.

The pore size distribution of the POROS™ XS resin was recently determined by Steinebach et al.¹⁰² using inverse size exclusion chromatography. The published results of Steinebach et al.¹⁰² show that the pore radii of POROS™ XS are generally smaller than 20 nm, with an average pore radius of about 8.5 nm. The pore radii of POROS™ XS reported in Steinebach et al.¹⁰² clearly demonstrate that POROS™ XS does not have a bimodal pore structure, does not have macropores and is therefore not a perfusion resin, unlike, for example, other POROS™ resins such as POROS™ 50 HS.^{103–106}

All other column and resin parameters that are relevant for this work are either based on manufacturer's data or were determined using the methods listed in section 2.2.2. A summary of the column and resin parameters is shown in Table 18, which is listed in section 3.1.

2.1.6 Desalting column for buffer exchange

PD-10 desalting columns prepacked with the gel filtration medium Sephadex G-25 purchased from Cytiva were used for rapid buffer exchange of protein samples.

2.1.7 Columns used for analytical chromatography

Table 4: List of columns used for analytical chromatography

Analytical column	Dimension	Manufacturer	Method
BioSep™ SEC s3000	ID = 7.8 mm, $L_c = 300.0$ mm	Phenomenex Inc.	SE-HPLC
YMC-BioPro SP-F	ID = 4.6 mm, $L_c = 50.0$ mm	YMC Europe GmbH	CEX-HPLC

2.1.8 Protein samples

Two bispecific monoclonal antibody (bsAb) samples were used in this work. The bsAbs were provided by Roche Diagnostics GmbH. Both bsAb samples were produced by CrossMAb technology.^{107,108} One sample was designated as bsAbY and the other as bsAbX.

The bsAbY is a so called tetravalent (2 + 2) bispecific antibody with a molar mass of 239 kDa. Therefore, two CrossFab fragments, both of which have a size of ~ 48 kDa, were fused to the C-terminus of the Fc-domain of an immunoglobulin G (IgG) antibody.¹⁰⁷ The protein bsAbY has a theoretical IEP of ~ 9.3. The extinction coefficient at 280 nm of the bsAb is 1.400 mL/(mg·cm).

The bsAbX is a so called bivalent (1 + 1) bispecific antibody with a molar mass of 147 kDa and a theoretical IEP of ~ 8.6. The extinction coefficient at 280 nm of the bsAb is 1.648 mL/(mg·cm).

The bsAb samples were pre-purified from the supernatant of the cell-free culture to a research purity of $\geq 85\%$.

2.1.9 Buffer solutions

All buffer solutions were vacuum filtrated through a 0.45 μm cellulose nitrate filter (Satorious). Afterwards they were degassed for 20 min in an ultrasonic bath (Bandelin) at room temperature.

2.1.9.1 Buffer solutions for determination of dead volumes, porosities and axial dispersion coefficient (D_{ax})

2.1.9.1.1 Buffer solution used as running buffer for determination of dead volumes, porosities and axial dispersion coefficient (D_{ax}).

Table 5: Composition of buffer solution used as running buffer for determination of dead volumes, porosities and axial dispersion coefficient (D_{ax}).

Ingredients	Concentrations
MES·H ₂ O	20 mmol/L
NaCl	150 mmol/L
In ultrapure water, pH 6.0	

2.1.9.1.2 *Buffer solution used as high salt solution for determination of dead volumes and porosities*

Table 6: Composition of buffer solution used as salt tracer for determination of dead volumes and porosities

Ingredients	Concentrations
MES·H ₂ O	20 mmol/L
NaCl	1000 mmol/L
In ultrapure water, pH 6.0	

2.1.9.2 Buffer solution for determination of the exclusion factor $k_{d,i}$

Table 7: Composition of buffer solution for determination of the exclusion factors $k_{d,i}$

Ingredients	Concentrations
NaH ₂ PO ₄	20 mmol/L
NaCl	1000 mmol/L
In ultrapure water, pH 7.0	

2.1.9.3 Buffer solutions for preparative CEX chromatography experiments applying linear salt gradient elution

2.1.9.3.1 *Buffer solutions for the application of linear salt gradients from 50 to 500 mmol/L Na⁺ at pH 4.5*

The composition of the buffer solutions for the application of linear salt gradients from 50 to 500 mmol/L Na⁺ at pH 4.5 is shown in Table 25 in the tabular appendix (see section 7).

2.1.9.3.2 *Buffer solutions for the application of linear salt gradients from 50 to 500 mmol/L Na⁺ at pH 5.3*

The composition of the buffer solutions for the application of linear salt gradients from 50 to 500 mmol/L Na⁺ at pH 5.3 is shown in Table 26 in the tabular appendix (see section 7).

2.1.9.3.3 Buffer solutions for the application of linear salt gradients from 50 to 500 mmol/L Na⁺ at pH 6.3

The composition of the buffer solutions for the application of linear salt gradients from 50 to 500 mmol/L Na⁺ at pH 6.3 is shown in Table 27 in the tabular appendix (see section 7).

2.1.9.3.4 Buffer solutions for the application of linear salt gradients from 35 to 500 mmol/L Na⁺ at pH 7.0

The composition of the buffer solutions for the application of linear salt gradients from 35 to 500 mmol/L Na⁺ at pH 7.0 is shown in Table 28 in the tabular appendix (see section 7).

2.1.9.3.5 Buffer solutions for the application of linear salt gradients from 25 to 500 mmol/L Na⁺ at pH 8.0

The composition of the buffer solutions for the application of linear salt gradients from 25 to 500 mmol/L Na⁺ at pH 8.0 is shown in Table 29 in the tabular appendix (see section 7).

2.1.9.3.6 Buffer solutions for the application of linear salt gradients from 25 to 500 mmol/L Na⁺ at pH 8.5

The composition of the buffer solutions for the application of linear salt gradients from 25 to 500 mmol/L Na⁺ at pH 8.5 is shown in Table 30 in the tabular appendix (see section 7).

2.1.9.3.7 Buffer solutions for the application of linear salt gradients from 25 to 500 mmol/L Na⁺ at pH 8.9

The composition of the buffer solutions for the application of linear salt gradients from 25 to 500 mmol/L Na⁺ at pH 8.9 is shown in Table 31 in the tabular appendix (see section 7).

2.1.9.4 Buffer solutions for preparative CEX chromatography experiments applying linear pH gradient elution

2.1.9.4.1 Buffer solutions for the application of linear pH gradients from pH 4.50 to 8.25 at 50 mmol/L Na⁺

The composition of the buffer solutions for the application of linear pH gradients from pH 4.50 to 8.25 at 50 mmol/L Na⁺ is shown in Table 32 in the tabular appendix (see section 7).

2.1.9.4.2 Buffer solutions for the application of linear pH gradients from pH 4.50 to 8.25 at 75 mmol/L Na⁺

The composition of the buffer solutions for the application of linear pH gradients from pH 4.50 to 8.25 at 75 mmol/L Na⁺ is shown in Table 33 in the tabular appendix (see section 7).

2.1.9.4.3 Buffer solutions for the application of linear pH gradients from pH 4.50 to 9.30 at 75 mmol/L Na⁺

The composition of the buffer solutions for the application of linear pH gradients from pH 4.50 to 9.30 at 75 mmol/L Na⁺ is shown in Table 34 in the tabular appendix (see section 7).

2.1.9.4.4 Buffer solutions for the application of linear pH gradients from pH 4.50 to 8.25 at 100 mmol/L Na⁺

The composition of the buffer solutions for the application of linear pH gradients from pH 4.50 to 8.25 at 100 mmol/L Na⁺ is shown in Table 35 in the tabular appendix (see section 7).

2.1.9.4.5 Buffer solutions for the application of linear pH gradients from pH 4.50 to 9.30 at 100 mmol/L Na⁺

The composition of the buffer solutions for the application of linear pH gradients from pH 4.50 to 9.30 at 100 mmol/L Na⁺ is shown in Table 36 in the tabular appendix (see section 7).

2.1.9.4.6 Buffer solutions for the application of linear pH gradients from pH 4.50 to 8.25 at 120 mmol/L Na⁺

The composition of the buffer solutions for the application of linear pH gradients from pH 4.50 to 8.25 at 120 mmol/L Na⁺ is shown in Table 37 in the tabular appendix (see section 7).

2.1.9.4.7 Buffer solutions for the application of linear pH gradients from pH 4.50 to 8.25 at 150 mmol/L Na⁺

The composition of the buffer solutions for the application of linear pH gradients from pH 4.50 to 8.25 at 150 mmol/L Na⁺ is shown in Table 38 in the tabular appendix (see section 7).

2.1.9.4.8 Buffer solutions for the application of linear pH gradients from pH 4.50 to 8.25 at 200 mmol/L Na⁺

The composition of the buffer solutions for the application of linear pH gradients from pH 4.50 to 8.25 at 200 mmol/L Na⁺ is shown in Table 39 in the tabular appendix (see section 7).

2.1.9.4.9 Buffer solutions for the application of linear pH gradients from pH 4.50 to 8.25 at 250 mmol/L Na⁺

The composition of the buffer solutions for the application of linear pH gradients from pH 4.50 to 8.25 at 250 mmol/L Na⁺ is shown in Table 40 in the tabular appendix (see section 7).

2.1.9.4.10 Buffer solutions for the application of linear pH gradients from pH 4.50 to 8.25 at 300 mmol/L Na⁺

The composition of the buffer solutions for the application of linear pH gradients from pH 4.50 to 8.25 at 300 mmol/L Na⁺ is shown in Table 41 in the tabular appendix (see section 7).

2.1.9.5 Buffer solutions for preparative CEX chromatography experiments applying linear dual gradient elution

2.1.9.5.1 Buffer solutions for the application of linear anti-parallel dual gradients with increasing linear salt gradient from 50 to 350 mmol/L Na⁺ and decreasing linear pH gradient from pH 6.30 to 5.10

The composition of the buffer solutions for the application of linear anti-parallel dual gradients with increasing linear salt gradient from 50 to 350 mmol/L Na⁺ and decreasing linear pH gradient from pH 6.30 to 5.10 is shown in Table 42 in the tabular appendix (see section 7).

2.1.9.5.2 Buffer solutions for the application of linear parallel dual gradients with increasing linear salt gradient from 80 to 300 mmol/L Na⁺ and increasing linear pH gradient from pH 5.20 to 7.50

The composition of the buffer solutions for the application of linear parallel dual gradients with increasing linear salt gradient from 80 to 300 mmol/L Na⁺ and increasing linear pH gradient from pH 5.20 to 7.50 is shown in Table 43 in the tabular appendix (see section 7).

2.1.9.6 Buffer solution at pH 4.5 with 7.5 mmol/L Na⁺ used for dilution of the bsAbY sample with 140 mmol/L Na⁺ to a Na⁺ concentration of 14.3 mmol/L

Table 8: Buffer solution at pH 4.5 with 7.5 mmol/L Na⁺ used for dilution of the bsAbY sample with 140 mmol/L Na⁺ to a Na⁺ concentration of 14.3 mmol/L

Buffer	Ingredients	Concentrations
Buffer solution for dilution to 14.3 mmol/L Na ⁺	Acetic acid	20.0 mmol/L
	NaOH	7.5 mmol/L
	In ultrapure water, pH 4.50	

2.1.9.7 Buffer solution for analytical size exclusion-high-performance liquid chromatography (SE-HPLC)

Table 9: Composition of buffer solution for analytical SE-HPLC

Buffer	Ingredients	Concentrations
Buffer solution for SE-HPLC	NaH ₂ PO ₄	100 mmol/L
	NaCl	300 mmol/L
	NaN ₃	0.02 %
	In ultrapure water, pH 7.00	

2.1.9.8 Buffer solutions for analytical cation exchange-high-performance liquid chromatography (CEX-HPLC)

2.1.9.8.1 Buffer solutions for the application of a linear pH gradient at 30 mmol/L Na⁺ in CEX-HPLC

Table 10: Composition of buffer solutions for the application of linear pH gradients at 30 mmol/L Na⁺ in CEX-HPLC

Buffer	Ingredients	Concentrations
Buffer A for analytical CEX-HPLC at 30 mmol/L Na⁺ (pH 5.00)	Acetic acid	8.8 mmol/L
	MES H ₂ O	10.0 mmol/L
	MOPSO	15.5 mmol/L
	NaOH	7.5 mmol/L
	NaCl	22.5 mmol/L
	In ultrapure water, pH 5.00	
Buffer B for analytical CEX-HPLC at 30 mmol/L Na⁺ (pH 9.50)	HEPES	18.4 mmol/L
	TAPS	7.2 mmol/L
	CHES	7.7 mmol/L
	NaOH	30.0 mmol/L
	In ultrapure water, pH 9.50	

2.1.9.8.2 *Buffer solutions for the application of a linear pH gradient at 60 mmol/L Na⁺ in CEX-HPLC*

Table 11: Composition of buffer solutions for the application of linear pH gradients at 60 mmol/L Na⁺ in CEX-HPLC

Buffer	Ingredients	Concentrations
Buffer A for analytical CEX-HPLC at 60 mmol/L Na⁺ (pH 5.00)	Acetic acid	10.9 mmol/L
	MES H ₂ O	11.2 mmol/L
	MOPSO	12.2 mmol/L
	NaOH	9.0 mmol/L
	NaCl	51.0 mmol/L
	In ultrapure water, pH 5.00	
Buffer B for analytical CEX-HPLC at 60 mmol/L Na⁺ (pH 9.50)	HEPES	20.4 mmol/L
	TAPS	6.1 mmol/L
	CHES	8.2 mmol/L
	NaOH	31.4 mmol/L
	NaCl	28.6 mmol/L
	In ultrapure water, pH 9.50	

2.1.9.9 *Cleaning in Place (CIP) Solutions*

2.1.9.9.1 *CIP solution using a high NaCl concentration*

Table 12: Composition of CIP solution using a high NaCl concentration

Buffer	Ingredients	Concentrations
High NaCl CIP	NaCl	1000 mmol/L
	TAPS	10 mmol/L
	In ultrapure water, pH 8.00	

2.1.9.9.2 *CIP solution using a NaOH concentration of 200 mmol/L Na⁺*

Table 13: Composition of CIP solution using a NaOH concentration of 200 mmol/L

Buffer	Ingredients	Concentrations
High NaOH CIP (200 mmol/L NaOH)	NaOH	200 mmol/L
	In ultrapure water	

2.1.9.9.3 CIP solution using a high NaOH concentration of 1000 mmol/L Na⁺**Table 14: Composition of CIP solution using a high NaOH concentration of 1000 mmol/L**

Buffer	Ingredients	Concentrations
High NaOH CIP (1000 mmol/L NaOH)	NaOH In ultrapure water	1000 mmol/L

2.1.9.10 Storage solution

Table 15: Composition of storage solution used for storage of preparative CEX and analytical CEX-HPLC columns

Buffer	Ingredients	Concentrations
Storage Solution	NaCl	150 mmol/L
	Ethanol	20 % (v/v)
	In ultrapure water.	

2.2 Methods

Parts of this section (2.2 Methods) have already been published in a similar or identical form in Seelinger et al.¹ (Part 1, 2022) and in Seelinger et al.² (Part 2, 2022). Parts of this section (2.2 Methods) are also included in a similar or identical form in Seelinger et al.³ (DRAFT (submitted)).

2.2.1 Experimental procedures for analytical chromatography

An ÄKTAmicro chromatography system (Cytiva) in combination with the control software UNICORN 5.31 (Cytiva) was used for analytical size exclusion-high-performance liquid chromatography (SE-HPLC) and cation exchange-high-performance liquid chromatography (CEX-HPLC). The UV signal at 280 nm was recorded.

2.2.1.1 Analytical SE-HPLC

SE-HPLC was applied for identification and quantification of size variants like dimers and multimers or fragments. A BioSep™ SEC s3000 column (7.8 mm ID × 300.0 mm length, Phenomenex Inc.) was used. The column was operated at a volumetric flow

rate of 0.5 mL/min. The buffer solution used for analytical SE-HPLC at pH 7.0 contained 100 mmol/L NaH_2PO_4 and 300 mmol/L NaCl (see Table 9, section 2.1.9.7).

2.2.1.2 Analytical CEX-HPLC

Charge variant analysis of the bsAb samples was carried out by CEX-HPLC. An YMC-BioPro SP-F column (4.6 mm ID × 50.0 mm length, YMC Europe GmbH) was used. The column was operated at a volumetric flow rate of 0.8 mL/min.

The bsAbY sample was eluted with a linear pH gradient from pH 5.0 to 9.5 at 60 mmol/L Na^+ . The recipe of the buffer system is shown in Table 11 (see section 2.1.9.8.2). The analytical CEX-HPLC column was equilibrated with buffer A. After sample injection the column was washed with 5 CV of 20 % buffer B. The elution of the target bsAb was initiated by a linear pH gradient from 20 % to 90 % buffer B. The gradient volume was set to 31.5 CV.

The bsAbX sample was eluted with a linear pH gradient from pH 5.0 to 9.5 at 30 mmol/L Na^+ . The recipe of the buffer system is shown in Table 10 (see section 2.1.9.8.1). The analytical CEX column was equilibrated with buffer A. After sample injection the column was washed with 5 CV of 0 % buffer B. The elution of the target bsAb was initiated by a linear pH gradient from 0 % to 100 % buffer B. The gradient volume was set to 45.0 CV.

2.2.1.3 Cleaning in place (CIP) procedure for analytical CEX-HPLC column

The analytical CEX-HPLC column was always cleaned before storage. For cleaning, the column was rinsed in the reverse direction at a flow rate of 0.3 mL/min. The column was always cleaned using two methods, whereby the column was first cleaned using a high salt cleaning in place (CIP) procedure. For the high salt CIP procedure, the column was rinsed with 5 CV high salt buffer with 1000 mmol/L NaCl at pH 8 (see Table 12, section 2.1.9.9.1). The column was then rinsed with 5 CV of the respective binding buffer (Buffer A). In a second step, a high pH CIP procedure was applied, whereby the column was rinsed with 5 CV high pH solution with 200 mmol/L NaOH (see Table 13, section 2.1.9.9.2). Afterwards, the column was again rinsed with 5 CV of the respective binding buffer (Buffer A).

2.2.1.4 Storage procedure for analytical columns

2.2.1.4.1 Storage procedure for analytical SE-HPLC column

No CIP procedure was performed for the SE-HPLC column. After the analyses, the column was stored directly. For this purpose, the column was simply rinsed for 5 CV with the running buffer (see Table 9, section 2.1.9.7) at a flow rate of 0.5 mL/min and then stored at room temperature.

2.2.1.4.2 Storage procedure for analytical CEX-HPLC column

For storage, the column was rinsed in the normal direction at a flow rate of 0.5 mL/min. The column was rinsed with 5 CV storage solution (Table 15, section 2.1.9.10). Subsequently, the column was stored at room temperature.

2.2.2 Experimental procedures for preparative chromatography

Preparative pulse experiments and preparative LGE experiments were performed on an ÄKTApurifier 100 liquid chromatography system (Cytiva) controlled by the software UNICORN 5.31 (Cytiva). For pulse experiments and LGE experiments at a load of $0.5 \text{ mg}_{\text{bsAb}}/\text{mL}_{\text{resin}}$, the UV signal at 280 nm was recorded. For LGE experiments at a load of $\geq 1.0 \text{ mg}_{\text{bsAb}}/\text{mL}_{\text{resin}}$, the UV signal was recorded at 280 nm and at 254 nm. The strong cation exchange resin POROS™ XS (Thermo Fisher Scientific Inc.) was used in a prepacked OPUS® MiniChrom® column with an inner diameter of 5 mm and a length of 50 mm (volume of the column $V_c = 1.0 \text{ mL}$) purchased from Repligen.

2.2.2.1 Determination of dead volumes

Pulse experiments were used to determine the dead volumes of the preparative chromatography system. In contrast to all other experiments, the chromatography column was not mounted on the system for the determination of the dead volumes. The volume between the injection valve and the respective sensors for UV, conductivity and pH measurement was determined. The recipe of the applied running buffer which had a pH of 6.0 and a NaCl concentration of 150 mmol/L is given in Table 5 (see section 2.1.9.1.1). A flow rate of 0.68 mL/min (207.79 cm/h) was used. Samples were injected using a 10 μL sample loop.

To determine the dead volume between the injection valve and the UV sensor ($V_{UV,system}$), a 1 mg/mL DextranBlue solution was used. Therefore, 40 mg

DextranBlue were dissolved in 40 mL running buffer. Three measurements, each with an injection of 10 μL DextranBlue solution, were performed.

To determine the dead volume between the injection valve and the conductivity sensor ($V_{cond,system}$), a high salt solution with a NaCl concentration of 1000 mmol/L (see Table 6, section 2.1.9.1.2) was used. Three measurements, each with an injection of 10 μL high salt solution, were performed.

To determine the dead volume between the injection valve and the pH sensor ($V_{pH,system}$), a high pH solution was used. This high pH solution was prepared by mixing a solution containing 1 mol/L NaOH 1:1 with the running buffer. Three measurements, each with an injection of 10 μL high pH solution, were performed.

The evaluation of the resulting peaks was performed by applying the PeakFit[®] v4.12 software (SeaSolve Software), with the use of the exponentially modified gaussian (EMG) model. Thereby, the volume between the injection valve and the peaks was determined, which corresponds to the volume between the injection valve and the sensor. The mean values of the respective three measurements were taken to determine the dead volume for each sensor.

In order to include the dead volume of the pre-packed 1 mL OPUS[®] MiniChrom[®] column, an additional volume of 30.4 μL is added to each dead volume of the system. This volume was determined by Schweiger and Jungbauer¹⁰⁹ as the dead volume of the top and bottom adapters for the column type used. This gives the total dead volume of the system and the column adapters, which was then always subtracted from the experimentally determined signals for UV, conductivity and pH. The dead volume for the UV sensor will be denoted as $V_{UV,system}$ in the following, the dead volume for the conductivity sensor as $V_{cond,system}$ and the dead volume for the pH sensor as $V_{pH,system}$.

2.2.2.2 Determination of column and resin parameters

Pulse experiments were applied to determine the column and resin parameters. The recipe of the used running buffer which had a pH of 6.0 and a NaCl concentration of 150 mmol/L is listed in Table 5 (see section 2.1.9.1.1). A flow rate of 0.68 mL/min (207.79 cm/h) was applied. Samples were injected using a 10 μL sample loop.

2.2.2.2.1 Determination of the theoretical plate height ($HETP$), plates/meter (N/m), and asymmetry (A_s)

The quality of the column packing is determined by the parameters $HETP$ (theoretical plate height), N/m (plates/meter), and A_s (asymmetry). Thereby, the parameters $HETP$ and N/m determine the peak broadening across the column and the parameter A_s determines the symmetry of the resulting peak.

Therefore, a high salt solution with a NaCl concentration of 1000 mmol/L (see Table 6, section 2.1.9.1.2) was used. Three measurements, each with an injection of 10 μ L high salt solution, were performed.

The resulting peaks were evaluated using the software UNICORN 5.31 (Cytiva). This software is able to automatically determine the values for $HETP$, N/m , and A_s after integration of the peaks.

2.2.2.2.2 Determination of interstitial porosity ε

For this purpose, the volume between the injection valve and the UV sensor with the column mounted must be first determined (V_{dex}). Therefore, a 1 mg/mL DextranBlue solution was used, which was prepared by dissolving 40 mg DextranBlue in 40 mL running buffer. Three measurements were performed with one injection of 10 μ L DextranBlue solution each.

The PeakFit[®] v4.12 software (SeaSolve Software) was used, applying the EMG function, to determine the volume between injection valve and UV sensor for each DextranBlue pulse (V_{dex}). This now allows the void volume of the column (V_0) to be determined using the following formula:

$$V_0 = V_{dex} - V_{UV,system} \quad (31)$$

The interstitial porosity ε can now be determined as follows:

$$\varepsilon = \frac{V_0}{V_c} \quad (32)$$

With the column volume V_c .

2.2.2.2.3 Determination of total porosity ε_t

For this purpose, the volume between the injection valve and the conductivity sensor with the column mounted must be determined (V_{cond}). Therefore, a high salt solution with a NaCl concentration of 1000 mmol/L (see Table 6, section 2.1.9.1.2) was used. Three measurements, each with an injection of 10 μ L high salt solution, were performed.

The PeakFit[®] v4.12 software (SeaSolve Software) was used, applying the EMG function, to determine the volume between injection valve and conductivity sensor for each salt pulse (V_{cond}). This now allows the total liquid volume of the column (V_t) to be determined using the following formula:

$$V_t = V_{cond} - V_{cond,system} \quad (33)$$

The total porosity ε_t can now be determined as follows:

$$\varepsilon_t = \frac{V_t}{V_c} \quad (34)$$

2.2.2.2.4 Determination of intraparticle porosity ε_p

The intraparticle porosity ε_p can be determined as follows:

$$\varepsilon_p = \frac{\varepsilon_t - \varepsilon}{1 - \varepsilon} \quad (35)$$

2.2.2.2.5 Determination of the ionic capacity of the packed resin Λ_{packed}

The ionic capacity of the packed resin Λ_{packed} is given by:

$$\Lambda_{packed} = \Lambda_{settled} - \frac{1}{1 - Comp} \quad (36)$$

With the ionic capacity of the settled resin $\Lambda_{settled}$ and the compression $Comp$ of the resin bed. Both the value for $\Lambda_{settled}$ and the value for $Comp$ used in this work are manufacturer information (Table 18).

2.2.2.2.6 Determination of the ionic capacity of the pore volume Λ

The ionic capacity of the pore volume Λ is given by:

$$\Lambda = \frac{\Lambda_{packed}}{(1 - \varepsilon) \cdot \varepsilon_p} \quad (37)$$

2.2.2.3 Determination of the of the exclusion factors $k_{d,i}$

Pulse experiments were applied to determine the exclusion factors $k_{d,i}$ of the protein samples bsAbY and bsAbX. For these pulse experiments, the chromatography column was mounted on the system and high salt conditions (~ 1 mol/L Na^+) were used so that the protein could not bind to the stationary phase of the resin. The recipe of the applied running buffer which had a pH of 7.0 and a NaCl concentration of 1000 mmol/L is listed in Table 7 (see section 2.1.9.2). For the antibody pulse injections bsAb solutions with a concentration of 0.50 mg/mL were used. Furthermore, it was important that the proteins were dissolved in the corresponding running buffer and that the protein samples had exactly the same pH and especially the same salt concentrations as the running buffer used, in order to avoid incorrect or

falsified measurement results. For this purpose, the protein samples first had to be prepared properly. The protein samples were buffer-exchanged into the running buffer used. Therefore, the PD-10 desalting columns prepacked with Sephadex G-25 resin (Cytiva) were applied for rapid buffer exchange using gravity flow. After the buffer exchange, the concentrations of the protein solutions were determined. Therefore, the UV absorption at 280 nm was measured by using the spectroscopy system Agilent 8453 (Agilent Technologies). Using the measured UV absorptions, the protein concentration was then calculated by applying the Beer's law. The protein solutions were then diluted with the running buffer to a final concentration of 0.50 mg/mL.

For the pulse experiments, a flow rate of 0.68 mL/min (207.79 cm/h) was applied. Samples were injected using a 10 μ L sample loop. For each protein, three measurements were performed with an injection of 10 μ L of the prepared high salt protein samples.

The PeakFit[®] v4.12 software (SeaSolve Software) was used, applying the EMG function, to determine the volume between injection valve and UV sensor for each protein pulse ($V_{bsAb,i}$). The exclusion factor $k_{d,i}$ for each protein was then calculated by using the following equation:

$$k_{d,i} = \frac{\left(\frac{V_{bsAb,i} - V_{UV,system}}{V_c} \right) - \varepsilon}{(1 - \varepsilon) \cdot \varepsilon_p} \quad (38)$$

2.2.2.4 Determination of the axial dispersion coefficient (D_{ax})

Pulse experiments with BlueDextran were applied to determine the axial dispersion coefficient (D_{ax}). For these pulse experiments, the column was mounted on the chromatography system. The recipe of the running buffer which had a pH of 6.0 and a NaCl concentration of 150 mmol/L is listed in Table 5 (see section 2.1.9.1.1). A flow rate of 0.68 mL/min (207.79 cm/h) was applied. Therefore, a 1 mg/mL DextranBlue solution was used, which was prepared by dissolving 40 mg DextranBlue in 40 mL running buffer. Three measurements were performed with one injection of 10 μ L DextranBlue solution each.

The evaluation of the generated DextranBlue peak was performed with the software PeakFit[®] v4.12 (SeaSolve Software) by using the EMG model. With EMG fit of the DextranBlue injection peak, the first central moment M_1 and the second central

moment M_2 can be determined. The second central moment is also called variance and is already squared. With M_1 and M_2 , the determination of D_{ax} can be done by applying the following equation³²:

$$D_{ax} = \frac{M_2}{M_1^2} \times \frac{\left(L_{Bed} \left(\frac{\dot{V}}{\varepsilon \pi (d_c^2 / 4)} \right) \right)}{2} \quad (39)$$

Here, L_{Bed} is the bed length of the column, \dot{V} stands for the volumetric flow rate and d_c is the diameter of the column.

2.2.2.5 Linear gradient elution (LGE) experiments

The preparative LGE experiments were always set up the same way: First the column was equilibrated with 10 column volumes (CV) of equilibration buffer. Then the sample was loaded onto the column with the appropriate loading volume. Subsequently, the column was washed with 10 CV of equilibration buffer and then the linear gradient was performed. After that, the column was washed with 10 CV of elution buffer. After each experiment, the column was cleaned with CIP solutions as explained in section 2.2.2.7.

2.2.2.5.1 LGE experiments performed under low loading conditions using a column loading of 0.5 mg_{bsAb}/mL_{resin}

Linear pH gradient and linear salt gradient elution experiments were performed with a column loading of 0.5 mg_{bsAb}/mL_{resin}. These LGE experiments were used for modeling and simulation of the antibodies' elution behavior at low loading conditions and thus for the determination of the the linear model parameters $\Delta G_1^0/RT$, $\Delta G_i^0/RT$, N_{-1} (N_{carb} and N_{tyr}), N_{+1} (N_{amine} , N_{his} and N_{nterm}) and the respective $k_{eff,i}$ values. A flow rate of 0.68 mL/min (207.79 cm/h) was always applied under low loading conditions. The sample was loaded with a feed concentration of 0.1 mg/mL by using a 50 mL Superloop (Cytiva).

For the linear pH gradients buffer systems with 0.050, 0.075, 0.100, 0.120, 0.150, 0.200, 0.250, 0.300 mol/L Na⁺ were used. The linear pH gradients were performed with four different gradient slopes. Thereby, the gradient volumes were adjusted to achieve the following gradient slopes: 0.0938, 0.0625, 0.0469 and 0.0313 CV⁻¹. Linear pH gradients were achieved by using complex buffer mixtures consisting of multiple buffer substances (acetic acid, succinic acid, MES·H₂O, MOPSO, HEPES,

TAPS and CHES) with overlapping pK_a values.^{110,111} Urbansky et al.¹¹¹ and Kröner et al.¹¹⁰ described already models which predict the composition of initial and final buffers that lead to the formation of linear pH gradients with constant buffer capacity when the buffers are mixed externally. Following their models,^{110,111} discontinuous buffer systems were calculated in this work for the generation of linear pH gradients. The individual buffer systems of the linear pH gradients are enumerated in section 2.1.9.4 and the recipes for the respective buffer systems are presented in tables in the tabular appendix (see section 7) of this dissertation.

For the linear salt gradients buffer systems with pH 4.5, 5.3, 6.3, 7.0 and 8.9 were used. The linear salt gradients were performed with four different gradient slopes. Thereby, the gradient volumes were adjusted to achieve the following gradient slopes: 0.0113, 0.0075, 0.0056, 0.0038 mol/CV. The individual buffer systems of the linear salt gradients are enumerated in section 2.1.9.3 and the recipes for the respective buffer systems are presented in tables in the tabular appendix (see section 7) of this dissertation.

A detailed list of the LGE experiments used to model bsAbY elution and bsAbX elution under low loading conditions using column loadings of $0.5 \text{ mg}_{\text{bsAb}}/\text{mL}_{\text{resin}}$ is given in Table 16.

For modeling of bsAbY elution using column loadings of $0.5 \text{ mg}_{\text{bsAb}}/\text{mL}_{\text{resin}}$, a number of 48 LGE experiments were performed, consisting of 20 linear salt gradient elution experiments and 28 linear pH gradient elution experiments (see Table 16).

For modeling of bsAbX elution using column loadings of $0.5 \text{ mg}_{\text{bsAb}}/\text{mL}_{\text{resin}}$, a number of 48 LGE experiments were performed, consisting of 16 linear salt gradient elution experiments and 32 linear pH gradient elution experiments (see Table 16).

Table 16: Set of experiments used for modeling of bsAbY elution and bsAbX elution at low loading conditions (load = 0.5 mg_{bsAb}/mL_{resin}).

pH / -	Na ⁺ / mmol·L ⁻¹	Gradient volume, given in column volumes / CV	Used bsAb sample
4.50 – 8.25	50	40.0, 60.0, 80.0 and 120.0	only bsAbX
4.50 – 8.25	75	40.0, 60.0, 80.0 and 120.0	only bsAbX
4.50 – 9.30	75	51.2, 76.8, 102.4 and 153.6	only bsAbY
4.50 – 8.25	100	40.0, 60.0, 80.0 and 120.0	only bsAbX
4.50 – 9.30	100	51.2, 76.8, 102.4 and 153.6	only bsAbY
4.50 – 8.25	120	40.0, 60.0, 80.0 and 120.0	bsAbY and bsAbX
4.50 – 8.25	150	40.0, 60.0, 80.0 and 120.0	bsAbY and bsAbX
4.50 – 8.25	200	40.0, 60.0, 80.0 and 120.0	bsAbY and bsAbX
4.50 – 8.25	250	40.0, 60.0, 80.0 and 120.0	bsAbY and bsAbX
4.50 – 8.25	300	40.0, 60.0, 80.0 and 120.0	bsAbY and bsAbX
4.50	50 – 500	40.0, 60.0, 80.0 and 120.0	bsAbY and bsAbX
5.30	50 – 500	40.0, 60.0, 80.0 and 120.0	bsAbY and bsAbX
6.30	50 – 500	40.0, 60.0, 80.0 and 120.0	bsAbY and bsAbX
7.00	35 – 500	41.3, 62.0, 82.7 and 124.0	bsAbY and bsAbX
8.90	25 – 500	42.2, 63.3, 84.4 and 126.7	only bsAbY

2.2.2.5.2 Linear salt gradient elution experiments performed under low loading, high loading and column overloading conditions using column loadings of 1 to 90 mg_{bsAb}/mL_{resin}

Linear salt gradient elution experiments were performed with increasing column loadings of 1 to 90 mg_{bsAb}/mL_{resin}. These LGE experiments were mainly used for modeling and simulation of the elution behavior at low loading, high loading, and column overloading conditions and were thus used, among other things, to determine and verify the non-linear model parameters (σ_i , $K_{p,i}$, and $K_{eq,2,i}/c$) and the respective $k_{eff,i}$ values. A flow rate of 0.68 mL/min (207.79 cm/h) was generally applied. The

samples were injected with a feed concentration of $1 \text{ mg}_{\text{bsAb}}/\text{mL}_{\text{resin}}$. The sample was loaded with a 1 mL sample loop and with 50 or 150 mL Superloops (Cytiva).

For both antibody samples (bsAbY and bsAbX), linear salt gradients with pH 4.5 (50 – 500 mmol/L Na^+), pH 5.3 (50 – 500 mmol/L Na^+), pH 6.3 (50 – 500 mmol/L Na^+) and pH 7.0 (35 – 500 mmol/L Na^+) were applied. Only for bsAbY, additional experiments with pH 8.0 (25 – 500 mmol/L Na^+), pH 8.5 (25 – 500 mmol/L Na^+) and pH 8.9 (25 – 500 mmol/L Na^+) were applied. The individual buffer systems of the linear salt gradients are enumerated in section 2.1.9.3 and the recipes for the respective buffer systems are presented in tables in the tabular appendix (see section 7) of this dissertation. These linear salt gradients were all performed with column loadings of 1, 5, 12 and $25 \text{ mg}_{\text{bsAb}}/\text{mL}_{\text{resin}}$. For the linear salt gradients performed with pH values of pH 4.5, 5.3, 6.3, 7.0, 8.0 and 8.5 additional experiments using column loadings of 50 and $75 \text{ mg}_{\text{bsAb}}/\text{mL}_{\text{resin}}$ were applied. For the linear salt gradients performed with pH values of pH 4.5, 5.3 and 8.0 additional experiments using a column loading of $90 \text{ mg}_{\text{bsAb}}/\text{mL}_{\text{resin}}$ were applied.

With the linear salt gradient at pH 4.5, additional experiments with the sample bsAbY were performed where the Na^+ concentrations during sample loading were varied. In these experiments, the column was always equilibrated with 50 mmol/L Na^+ before sample loading and washed with 50 mmol/L Na^+ after sample loading. However, the sample was loaded onto the column with different Na^+ concentrations of 14.3, 50.0, 120.0, 200.0 and 250.0 mmol/L. These additional experiments were performed with column loadings of 1, 25, 50 and $75 \text{ mg}_{\text{bsAb}}/\text{mL}_{\text{resin}}$. To prepare the antibody samples with Na^+ concentrations ranging from 50 to 250 mmol/L Na^+ , the bsAbY sample which had a protein concentration of 19.48 mg/mL and a Na^+ concentration of 140 mmol/L was used. This sample was diluted to a protein concentration of 1 mg/mL with the respective binding buffers with Na^+ concentrations of 50 mmol/L (see Table 25), 120 mmol/L (see Table 37), 200 mmol/L (see Table 39), and 250 mmol/L (see Table 40). Thus, Na^+ concentrations were adjusted to an accuracy of $\pm 5 \text{ mmol/L}$. It was decided that this was accurate enough. To obtain a Na^+ concentration of 14.3 mmol/L, the sample was diluted with a specially prepared dilution buffer with a concentration of 7.5 mmol/L Na^+ (see Table 8, section 2.1.9.6).

With the linear salt gradient at pH 4.5, further additional experiments were performed with the sample bsAbY, where the time for loading the sample, called the loading time,² was varied. Therefore, at a pH of 4.5 using 50 mmol/L Na^+ for loading of 75 mg

bsAbY onto the 1 mL column, the bsAbY sample was injected once at a lower flow rate of 103.9 cm/h (0.34 mL/min), once at the normal flow rate of 207.79 cm/h (0.68 mL/min) and once at a higher flow rate of 415.59 cm/h (1.36 mL/min) to vary the loading time. Before sample loading and after sample loading, the normal flow rate of 207.79 cm/h (0.68 mL/min) was always set.

Since pH has a significant influence on the estimation of the pH-dependent non-linear model parameters (e.g. the shielding factor σ_i), slight differences in pH of the individual batches of salt gradient buffer systems were compensated by pH corrections. These pH corrections should avoid falsification of the estimated values of the model parameters. Whenever a freshly prepared buffer system was used for salt gradient experiments with column loadings of $\geq 5 \text{ mg}_{\text{bsAb}}/\text{mL}_{\text{resin}}$, an initial run was performed with a loading of $1 \text{ mg}_{\text{bsAb}}/\text{mL}_{\text{resin}}$. A pH correction was then determined for this freshly prepared salt gradient buffer system by performing a chromatogram simulation of this initial run with a loading of $1 \text{ mg}_{\text{bsAb}}/\text{mL}_{\text{resin}}$. Thereby, the simulated peak was shifted to the position of the experimental peak by adjusting the applied pH. This corrected pH value was then used for the following simulations of high loading experiments (load $\geq 5 \text{ mg}_{\text{bsAb}}/\text{mL}_{\text{resin}}$) performed with the appropriate buffer system. These pH corrections were applied to both the linear salt gradient elution experiments of the bsAbY sample and the bsAbX sample.

2.2.2.5.3 Linear pH gradient elution experiments performed under low loading, high loading and column overloading conditions using column loadings of 1 to 90 $\text{mg}_{\text{bsAb}}/\text{mL}_{\text{resin}}$

Linear pH gradient elution experiments were performed with increasing column loadings of 1 to $90 \text{ mg}_{\text{bsAb}}/\text{mL}_{\text{resin}}$. These LGE experiments were used to model and to simulate the elution behavior at low loading, high loading and column overloading conditions. Thereby, these LGE runs were mainly used, among other things, for the determination of their respective $k_{\text{eff},i}$ values and especially for the verification of the pH-dependent descriptions of the non-linear model parameters (σ_i , $K_{p,i}$, and $K_{\text{eq},2,i}/c$). A flow rate of 0.68 mL/min (207.79 cm/h) was generally applied. The samples were injected with a feed concentration of 1 mg/mL. The sample was loaded with a 1 mL sample loop and with 50 or 150 mL Superloops (Cytiva).

For both antibody samples (bsAbY and bsAbX), linear pH gradient elution experiments with 75 mmol/L Na^+ (pH 4.50 to 9.30), 120 mmol/L Na^+ (pH 4.50 to 8.25) and 200 mmol/L Na^+ (pH 4.5 to 8.25) were applied. The individual buffer systems of

the linear pH gradients are enumerated in section 2.1.9.4 and the recipes for the respective buffer systems are presented in tables in the tabular appendix (see section 7) of this dissertation. These linear pH gradients were all performed with column loadings of 1, 25, 50 and 75 mg_{bsAb}/mL_{resin}. For the linear pH gradients performed with Na⁺ concentrations of 75 and 120 mmol/L additional experiments using a column load of 90 mg_{bsAb}/mL_{resin} were applied.

With the linear pH gradient (pH 4.5 to 9.3) at 75 mmol/L Na⁺, additional experiments with the sample bsAbX were applied where one time the Na⁺ concentration during sample loading and one time the flow rate during loading were varied. The pH value during loading was always set to pH 4.5. These additional experiments were performed with column loadings of 75 mg_{bsAb}/mL_{resin}. Before the sample loadings, the column was equilibrated using a flow rate of 207.79 cm/h (0.68 mL/min) and a Na⁺ concentration of 75 mmol/L, and after the loadings, the column was washed using a flow rate of 207.79 cm/h (0.68 mL/min) and a Na⁺ concentration of 75 mmol/L. In addition to the standard experiment with a normal loading at 207.79 cm/h (0.68 mL/min) and 75 mmol/L Na⁺, another experiment was performed with a loading at 75 mmol/L Na⁺ and a decreased flow rate of 103.9 cm/h (0.34 mL/min) to test a loading time that is twice as long as normal. Furthermore, another experiment was performed where the sample bsAbX was loaded onto the column at a flow rate of 207.79 cm/h (0.68 mL/min) with an increased Na⁺ concentration of 175 mmol/L Na⁺. To achieve a concentration of ~ 175 mmol/L Na⁺, the sample was diluted to a protein concentration of 1 mg/mL in a buffer containing 175 mmol/L Na⁺, which was accurate enough for this experiment. The buffer at pH 4.5 containing 175 mmol/L Na⁺ was prepared by mixing four parts of buffer containing 200 mmol/L Na⁺ (see Table 39, section 7, buffer A) with one part of buffer containing 75 mmol/L Na⁺ (see Table 33, section 7, buffer A).

2.2.2.5.4 Linear dual gradient elution experiments performed under low loading and high loading conditions using column loadings of 1 to 50 mg_{bsAb}/mL_{resin}

Only for the antibody sample bsAbY, linear dual gradient elution experiments were performed with increasing column loadings of 1 to 50 mg_{bsAb}/mL_{resin}. These LGE experiments were used for determination of the respective $k_{eff,i}$ values and especially for the verification of the pH-dependent descriptions of the steric shielding factor σ_i . A flow rate of 0.68 mL/min (207.79 cm/h) was generally applied. The

samples were injected with a feed concentration of 1 mg/mL. The sample was loaded with a 1 mL sample loop and with 50 or 150 mL Superloops (Cytiva).

A parallel dual gradient and an antiparallel dual gradient were applied, both performed with column loadings of 1, 25 and 50 mg_{bsAb}/mL_{resin}. The parallel dual gradient was composed of an increasing linear salt gradient from 0.08 to 0.30 mol/L Na⁺ and an increasing linear pH gradient going up from pH 5.2 to 7.5. The gradient volume was set to 23.00 CV. The antiparallel dual gradient was composed of an increasing linear salt gradient going up from 0.05 to 0.35 mol/L Na⁺ and a decreasing linear pH gradient going down from pH 6.3 to 5.1. The gradient volume was set to 26.67 CV. The individual buffer systems of the linear dual gradients are enumerated in section 2.1.9.5 and the recipes for the respective buffer systems are presented in tables in the tabular appendix (see section 7) of this dissertation.

2.2.2.6 Display of elution profiles from preparative LGE experiments

For displaying the protein elution curves from the LGE runs performed at column loadings of 0.5 mg_{bsAb}/mL_{resin} and 1.0 mg_{bsAb}/mL_{resin}, the UV signal at 280 nm was converted into the protein concentration curves using an extinction coefficient ϵ_{280nm} 1.400 mL/(mg·cm) for bsAbY and an ϵ_{280nm} of 1.648 mL/(mg·cm) for bsAbX. For the runs performed at loadings of ≥ 5.0 mg_{bsAb}/mL_{resin}, the UV signal at 254 nm was recorded and converted into the UV signal at 280 nm using detector-specific conversion factors. Subsequently, this UV signal at 280 nm was also converted into the protein concentration curves with the respective ϵ_{280nm} values.

For a small collection of high loading experiments, the charge variant and size variant distribution of the bsAb samples during elution was investigated. During these high loading experiments, fractions were collected using a Frac-920 fraction collector (Cytiva). The fractions were collected in 5 mL tubes (VWR International). The total amount of protein in these fractions was determined by photometric analysis (see section 2.2.3). Some of the fractions were additionally analyzed by CEX-HPLC (see section 2.2.1.2) to check the distribution of the individual charge variants in these collected fractions. Some of the fractions were additionally analyzed by SE-HPLC (see section 2.2.1.1) to check the distribution of size variants in these collected fractions.

2.2.2.7 Cleaning in place (CIP) procedure for preparative chromatography column

After each preparative LGE experiment, the column was cleaned first with a high salt CIP and subsequently with a high pH CIP. The preparative column was rinsed in the normal direction at a flow rate of 0.5 mL/min. For the high salt CIP, the column was rinsed with 5 CV of a high salt solution with 1000 mmol/L NaCl at pH 8 (see Table 12, section 2.1.9.9.1). The column was then rinsed with 5 CV of the respective binding buffer (buffer A) that was used for the previous LGE experiment. In a second step, a high pH CIP procedure was applied, whereby the column was rinsed with 5 CV of a high pH solution with 1000 mmol/L NaOH (see Table 14, section 2.1.9.9.3). Afterwards, the column was again rinsed with 5 CV of the respective binding buffer (Buffer A).

2.2.2.8 Storage procedure for preparative chromatography columns

For storage, the column was rinsed in reverse direction with 5 CV storage solution with 150 mmol/L NaCl and 20 % (v/v) ethanol (see Table 15, section 2.1.9.10). The volumetric flow rate was set to 0.5 mL/min. Afterwards the column was stored at 4 °C.

2.2.3 Quantitative analysis

Quantitative analysis was carried out by photometric measurement utilizing a GENios™ Pro microplate reader (TECAN) and 96 well UV-STAR® micro titer plates (Greiner Bio-One GmbH). The fill volume per well was 150 µL. The wavelength was set to 280 nm during the measurements. The determined adsorption was converted into protein concentration by a linear calibration curve.

2.2.4 Determination of linear model parameters at low loading conditions

The elution data derived from the LGE experiments at low loading conditions (load = 0.5 mg_{bsAb}/mL_{resin}) were used to determine the linear model parameters $\Delta G_1^0/RT$, $\Delta G_i^0/RT$, N_{-1} (N_{carb} and N_{tyr}), and N_{+1} (N_{amine} , N_{his} and N_{nterm}). Equation (25) and equation (26) were used to calculate for each linear salt and pH gradient elution experiment the normalized gradient slope, respectively. The data points from the linear salt and pH gradients, where the eluting Na⁺ concentration and the eluting pH correlate with the normalized gradient slope, respectively, were transferred to Berkeley Madonna™. Then, the elution data were simultaneously fitted

to equations (5), (6), and (24). Therefore, the fourth-order Runge-Kutta method was used as an ODE solver here. The curve fit function of Berkeley Madonna™ that is based on a Nelder-Mead Simplex method^{112,113} was used for curve fitting by simultaneously varying the linear model parameters $\Delta G_1^0/RT$, $\Delta G_i^0/RT$, N_{-1} (N_{carb} and N_{tyr}) and N_{+1} (N_{amine} , N_{his} and N_{nterm}). The pK_{a_i} values of the amino acids are listed in Table 17.

The $k_{eff,i}$ values were estimated only for the LGE experiments with the steepest gradient slopes of 0.0938 CV^{-1} and 0.0113 mol/CV for the linear pH and salt gradients, respectively. An inverse peak fitting method was used for estimation of the individual $k_{eff,i}$ values applying the fourth-order Rosenbrock stiff ODE solver and the integrated curve fit function in Berkeley Madonna™.

Table 17: pK_{a_i} values of amino acids used for modeling

	Carboxyl	Amines	Histidine	N-term	Tyrosine
pK_{a_i}	4.45	10.40	6.00	7.50	9.50

2.2.5 Determination of non-linear model parameters at high loading and column overloading conditions

The SMA model was used to describe the binding and elution behavior of the therapeutic protein bsAbY under high loading and overloading conditions. Therefore, only the pH-dependent shielding factor σ_i had to be determined. Linear salt gradient elution experiments with fixed pH values of 4.5, 5.3, 6.3, 7.0, 8.0, 8.5 and 8.9 were used to determine the pH-dependence of σ_i at high loading conditions (load $\geq 5 \text{ mg}_{bsAb}/\text{mL}_{resin}$). The shielding factor σ_i was simultaneously estimated with $k_{eff,i}$ with an inverse peak fitting method. The values for σ_i and $k_{eff,i}$ were estimated for each experiment individually. This means, at one pH, for each experiment performed at that pH, an individual σ_i value as well as an individual $k_{eff,i}$ value were estimated. Therefore, in Berkeley Madonna™, the fourth-order Rosenbrock stiff ODE solver and the integrated curve fit function were used. Table 21 shows the parameters determined by this procedure. For the linear pH and dual gradients only $k_{eff,i}$ was adjusted to the individual elution profiles since σ_i was calculated with a pH-dependent function (see section 3.5.2, equation (40)).

The SAS-SMA model was used to describe the binding and elution behavior of the therapeutic protein bsAbX under high loading and overloading conditions. In addition to the pH-dependent shielding factors σ_i , the pH-dependent non-linear parameters $K_{p,i}$ and $K_{eq,2,i}/c$ had to be determined here. Since the estimation of several parameters from only one experiment can lead to so-called overestimations,³ multi-chromatogram fits were performed here. This means that the non-linear model parameters were not determined from single experiments, but from several experiments simultaneously. Therefore, the linear salt gradient elution experiments at pH 4.5, 5.3, 6.3, and 7.0, which were carried out with column loadings of 5, 12, 25, and 50 mg_{bsAb}/mL_{resin}, were used to determine the pH-dependent non-linear model parameters $K_{p,i}$, $K_{eq,2,i}/c$ and σ_i . The runs at 75 and 90 mg_{bsAb}/mL_{resin} were not used for the determination of the non-linear parameters, however, they were used for their verification. An inverse peak fitting method by using the integrated curve fit function in Berkeley Madonna™ was used for parameter estimation. The fourth-order Rosenbrock (stiff) method was used as an ODE solver. As already mentioned, multi-chromatogram fits were conducted. Thus, for one pH value, all runs with loadings from 5 to 50 mg_{bsAb}/mL_{resin} were fitted simultaneously by varying the parameters $K_{p,i}$, $K_{eq,2,i}/c$, σ_i , and $k_{eff,i}$. Thereby, for the parameters $K_{p,i}$, $K_{eq,2,i}/c$ and σ_i , one value each was estimated globally for all runs at one pH value, and for the $k_{eff,i}$ values, an individual $k_{eff,i}$ value was estimated for each individual experiment. Numerous fits were performed for each pH value, and the mean values were calculated from the model parameters of the five best fits and used as the final result. Table 23 shows the parameters determined by this procedure and the corresponding standard deviations. For the linear pH gradients only $k_{eff,i}$ was adjusted to the individual elution profiles since $K_{p,i}$, $K_{eq,2,i}/c$, and σ_i were calculated with empirical pH-dependent functions. The empirical equations for calculating the pH-dependent $K_{p,i}$ and the pH-dependent $K_{eq,2,i}/c$ are shown in section 3.7.1.2 (equations (42) and (43), respectively), and the empirical equation for calculating the pH-dependent σ_i is shown in section 3.7.1.3 (equation (44)).

3 RESULTS

3.1 Determined dead volumes, column parameters, resin parameters, exclusion factors ($k_{d,i}$) and axial dispersion coefficient (D_{ax})

Parts of section 3.1 have already been published in a similar or identical form in Seelinger et al.¹ (Part 1, 2022) and in Seelinger et al.² (Part 2, 2022). Parts of this section 3.1 are also included in a similar or identical form in Seelinger et al.³ (DRAFT (submitted)).

The determined dead volumes, column parameters, resin parameters, exclusion factors ($k_{d,i}$) and axial dispersion coefficient (D_{ax}) are listed in Table 18.

Table 18: Dead volumes, column parameters, resin parameters, exclusion factors ($k_{d,i}$) and axial dispersion coefficient (D_{ax})

Parameter	Symbol	Value	Unit	Approach
Dead volume, UV sensor	$V_{UV,system}$	0.339	mL	see section 2.2.2.1
Dead volume, conductivity sensor	$V_{cond,system}$	0.669	mL	see section 2.2.2.1
Dead volume, pH sensor	$V_{pH,system}$	0.748	mL	see section 2.2.2.1
Column length	L_c	5.0	cm	Manufacturer info.
Inner diameter	ID	0.5	cm	Manufacturer info.
Column volume	V_c	1.0	mL	Manufacturer info.
Particle diameter	d_p	0.005	cm	Manufacturer info.
Theoretical plate height	$HETP$	0.042	cm	see section 2.2.2.2.3
Plates/meter	N/m	2390	N/m	see section 2.2.2.2.3
Asymmetry	A_s	1.03	---	see section 2.2.2.2.3
Void volume of the column	V_0	0.350	mL	see section 2.2.2.2.2
Total column liquid volume	V_t	0.800	mL	see section 2.2.2.2.3
Interstitial porosity	ε	0.350	---	see section 2.2.2.2.2
Total porosity	ε_t	0.800	---	see section 2.2.2.2.3
Intraparticle porosity	ε_p	0.692	---	see section 2.2.2.2.4
Exclusion factor, bsAbY	$k_{d,bsAbY}$	0.645	---	see section 2.2.2.3

Exclusion factor, bsAbX	$k_{d,bsAbX}$	0.672	---	see section 2.2.2.3
Axial dispersion coefficient	D_{ax}	$5.42 \cdot 10^{-3}$	$\text{cm}^2 \cdot \text{s}^{-1}$	see section 2.2.2.4
Compression	$Comp$	0.09	---	Manufacturer info.
Ionic capacity of the gravity settled resin	$\Lambda_{settled}$	0.111	mol/L	Manufacturer info.
Ionic capacity of the packed bed	Λ_{packed}	0.122	mol/L	see section 2.2.2.2.5
Ionic capacity of the pore volume	Λ	0.270	mol/L	see section 2.2.2.2.6

3.2 Characterization of the bsAb samples

The bsAb samples were analyzed by analytical SE-HPLC, analytical CEX-HPLC, and by preparative CEX experiments performed under low loading conditions.

3.2.1 Characterization of the bsAbY sample

Parts of the section 3.2.1 have already been published in a similar or identical form in Seelinger et al.¹ (Part 1, 2022) and in Seelinger et al.² (Part 2, 2022).

Only one batch of bsAbY sample was used in this work. The results of the SE-HPLC and CEX-HPLC analyses are shown in Figure 1 and the results of the preparative CEX runs at low loading conditions are shown in Figure 2.

As can be seen in Figure 1A, the analysis by SE-HPLC revealed that the applied bsAbY sample consists almost entirely of monomeric variants ($\geq 90\%$). Separated size variants like dimers and multimers ($\leq 1\%$), as well as fragments ($\leq 9\%$) are only slightly detectable.

The analysis by high-resolution CEX-HPLC (Figure 1B) revealed that the bsAbY sample consists of several different variants. It can be seen that within an elution volume of 22.2 to 25.0 mL, several strongly distinct charge variants elute close together, while at lower elution volumes (≤ 22.2 mL) there is a group of quite weakly distinct charge variants that form a noticeable fronting. Therefore, it was decided to divide the sample into two parts or, rather, into two groups of charge variant species. The subdivision into the so-called pre-variants and main variants is shown in Figure 1B and explained in the corresponding figure caption. This partitioning was done to investigate the distribution of charge variants during preparative high loading and

column overloading runs and, in particular, to investigate the influence of the earlier eluting pre-variants.

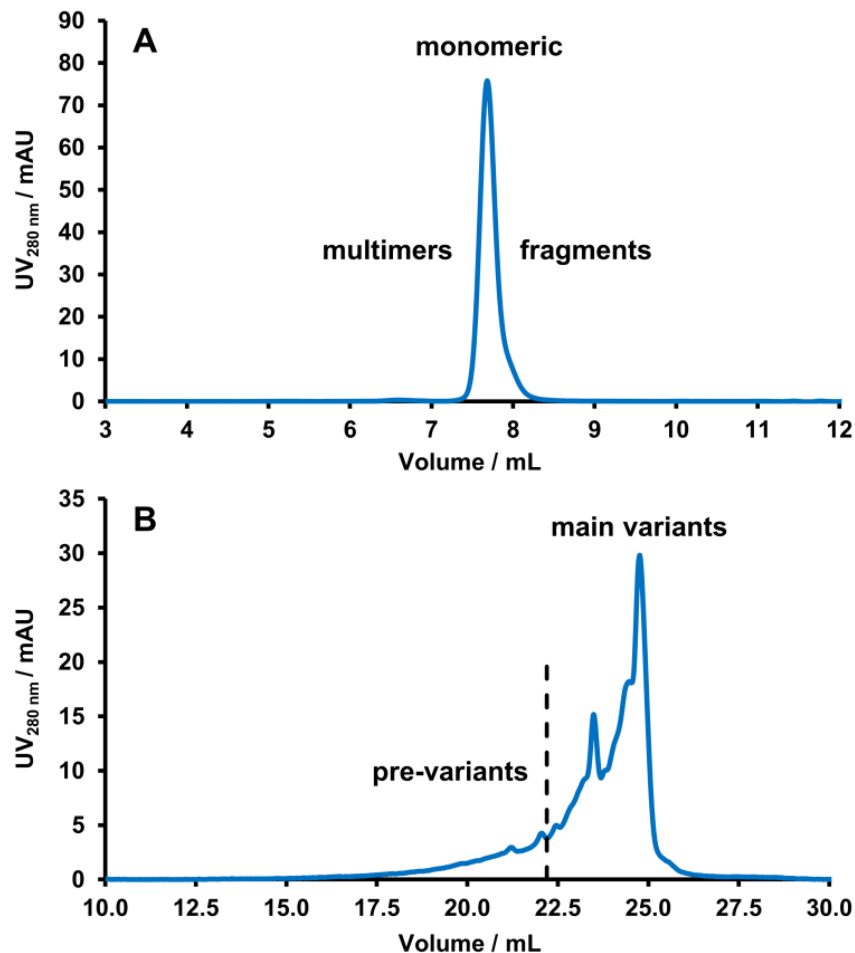


Figure 1. Analysis of the bsAbY sample by SE-HPLC and CEX-HPLC. (A) Analytical SE-HPLC chromatogram of the bsAbY sample. The analysis revealed that bsAbY consists almost completely of monomeric variants ($\geq 90\%$). Separated size variants like dimers and multimers ($\leq 1\%$), as well as fragments ($\leq 9\%$), are only slightly recognizable. (B) Analytical CEX-HPLC chromatogram of the bsAbY sample. The bsAbY was divided into two charge variant species. The black dashed line indicates the border between the individual species. The peak area from 15.00 mL to 22.20 mL is related to one species which accounts for $\sim 19\%$ of the total peak area. Thereby, all protein signals in this area are classified as pre-variants. The peak area from 22.20 mL to 30.00 mL was related to one species and made up $\sim 81\%$ of the total peak area. All protein signals in this area are classified as main variants. Parts of this figure are already published in Seelinger et al.¹ (Part 1, 2022) and in Seelinger et al.² (Part 2, 2022).

In Figure 2, preparative CEX experiments performed under low loading conditions (load $\leq 1 \text{ mg}_{\text{bsAb}}/\text{mL}_{\text{resin}}$) are shown and compared with corresponding single-component simulations. The model parameters for these simulations are listed in

Table 19 and Table 20. Thereby, Figure 2A shows a salt gradient run at pH 5.3 and Figure 2B shows a salt gradient run at pH 8.0. These two experiments are representative for all other LGE experiments performed at loadings of $\leq 1 \text{ mg}_{\text{bsAb}}/\text{mL}_{\text{resin}}$ where the protein sample bsAbY was used. It can be seen, that the resulted peaks are predominately symmetrical with only weakly distinct pre-shoulders. At a higher pH of 8.0, the pre-variants appear to be better separated from the main variants than at pH 5.3. The elution profiles at column loadings of $\leq 1 \text{ mg}_{\text{bsAb}}/\text{mL}_{\text{resin}}$ could be predicted with sufficient agreement using only one simulated variant (see Figure 2A/B).

Based on these analyses, it was decided to describe the elution of the bsAbY sample with only one simulated variant. The detailed explanation of this decision is presented in section 4.1.1.

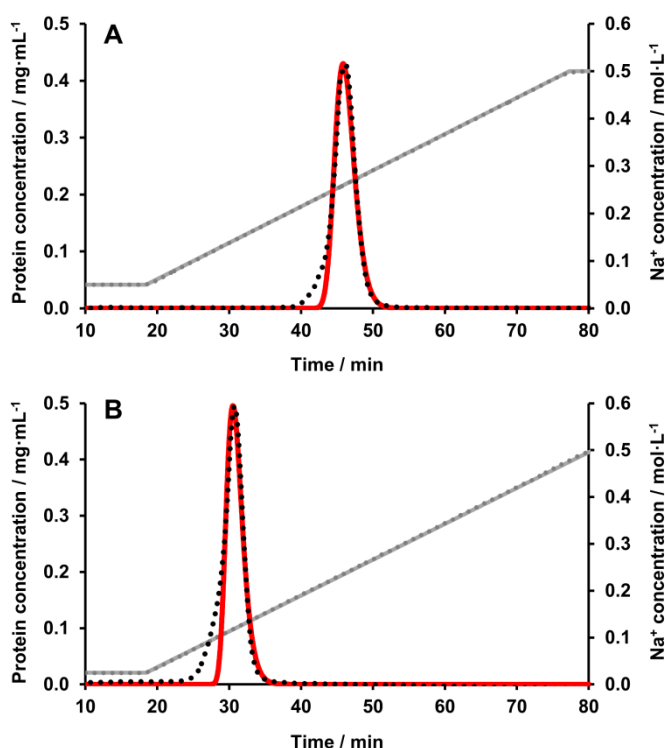


Figure 2. Linear salt gradient elution experiments with the sample bsAbY performed under low loading conditions. A column load of $1 \text{ mg}_{\text{bsAb}}/\text{mL}_{\text{resin}}$ was used. The runs were conducted at fixed pH values of pH 5.3 (A) and pH 8.0 (B). The black dots represent experimental data and the red lines represent simulated data. This figure is already published in an identical form in Seelinger et al.¹ (Part 1, 2022).

3.2.2 Characterization of the bsAbX sample

Parts of this section 3.2.2 are also included in a similar or identical form in Seelinger et al.³ (DRAFT (submitted)).

In this work, three different batches of bsAbX samples were used, whereby the comparability of the three batches had to be checked in particular. The results of the

SE-HPLC and CEX-HPLC analyses are shown in Figure 3 (and Figure 4) and the results of the preparative CEX runs at low loading conditions are shown in Figure 5.

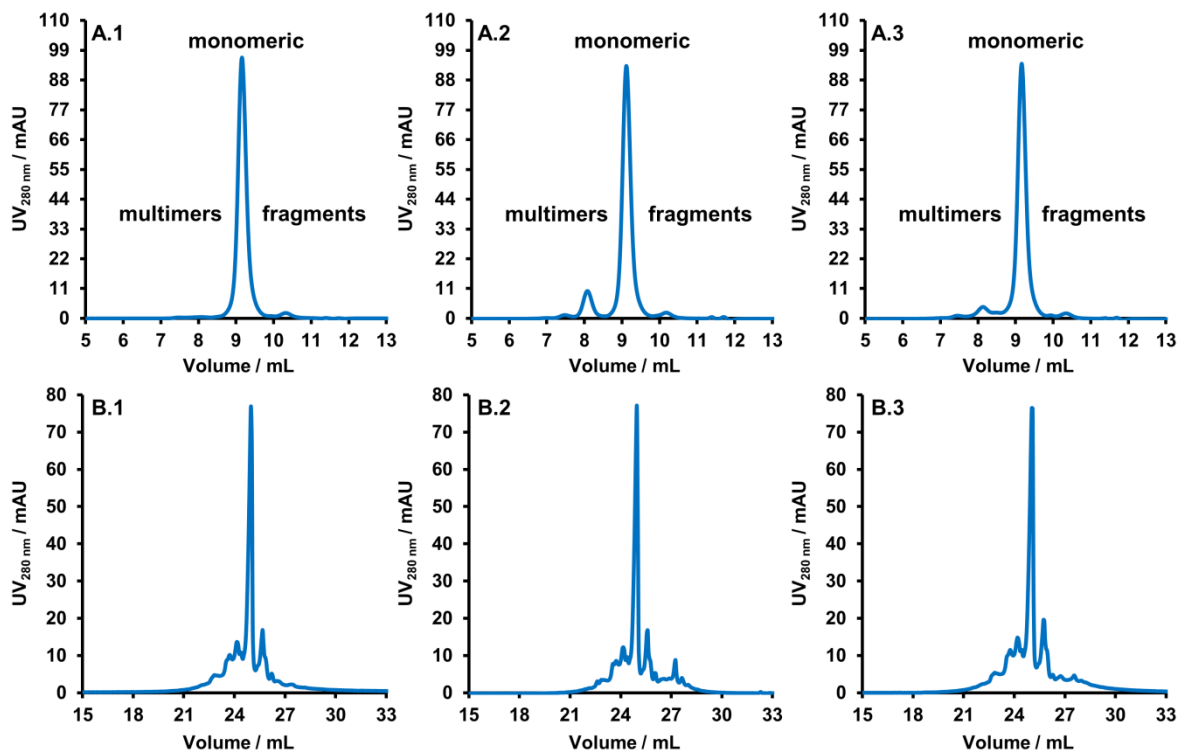


Figure 3. Analysis of the bsAbX sample by SE-HPLC and CEX-HPLC. The bsAbX samples batch 1, batch 2, and batch 3 were analyzed by SE-HPLC and CEX-HPLC. (A.1) SE-HPLC revealed that batch 1 consists of 2 % fragments, 98 % monomers and 0 % dimers/multimers. (A.2) SE-HPLC revealed that batch 2 consists of 3 % fragments, 86 % monomers and 11 % dimers/multimers. (A.3) SE-HPLC revealed that batch 3 consists of 3 % fragments, 89 % monomers and 8 % dimers/multimers. (B.1-3) Analytical CEX-HPLC shows that batch 1 (B.1), batch 2 (B.2), and batch 3 (B.3) all have a very similar distribution of charge variants, with a very strong major variant in the center surrounded by several smaller variants. This figure is also included in a similar or identical form in Seelinger et al.³ (DRAFT (submitted)).

As can be seen in Figure 3A.1-3, SE-HPLC analysis revealed that the different bsAbX batches differ significantly in their composition of size variants. Batch 1 consists of 2 % fragments, 98 % monomers and 0 % dimers/multimers (see Figure 3A.1). Batch 2 consists of 3 % fragments, 86 % monomers and 11 % dimers/multimers (see Figure 3A.2). Batch 3 consists of 3 % fragments, 89 % monomers and 8 % dimers/multimers (see Figure 3A.3). It is noticeable that batch 2 and batch 3 contain different types of dimers and multimers, which may also have an impact on preparative CEX elution profiles. While batch 1 was used only for the

modeling runs at low loading conditions (see section 3.3), batch 2 was used for the salt gradient runs at high loading and overloading conditions (see section 3.7.1) and batch 3 was used for the salt gradient and pH gradient runs at high loading and overloading conditions (see sections 3.7.1 and 3.7.2.2).

As can be seen in Figure 3B.1-3, analytical CEX-HPLC shows that all batches have a similar distribution of charge variants, with a very strong major variant in the center surrounded by several smaller variants. Similar to the bsAbY sample, it was decided to divide the bsAbX sample into two parts or, rather, into two groups of charge variant species. The subdivision into the so-called pre-variants and main variants is shown in Figure 4 with the sample bsAbX batch 3 and explained in the corresponding figure caption. This partitioning was done to investigate the distribution of charge variants during preparative high loading and column overloading runs and, in particular, to investigate the influence of the earlier eluting pre-variants.

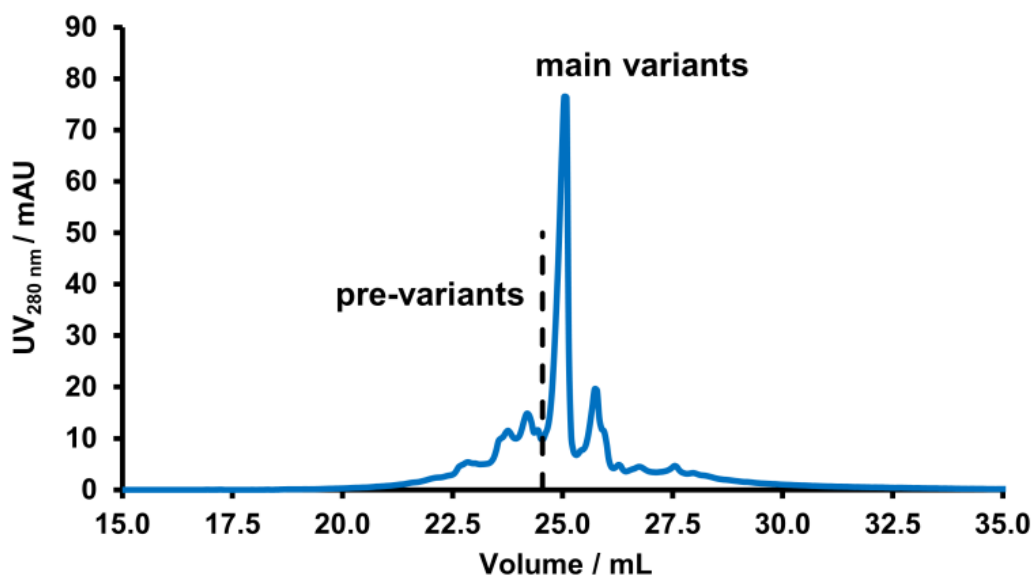


Figure 4. Analysis of sample bsAbX batch 3 by CEX-HPLC and subdivision of the sample into pre-variants and main variants. The bsAbX was divided into two charge variant species. The black dashed line indicates the border between the individual species. The peak area from 15.00 mL to 24.54 mL is related to one species which accounts for ~ 29 % of the total peak area. Thereby, all protein signals in this area are classified as pre-variants. The peak area from 24.54 mL to 35.00 mL was related to one species and made up ~ 71 % of the total peak area. All protein signals in this area are classified as main variants. This figure may be included in a similar or identical form in Seelinger et al.³ (DRAFT (submitted)).

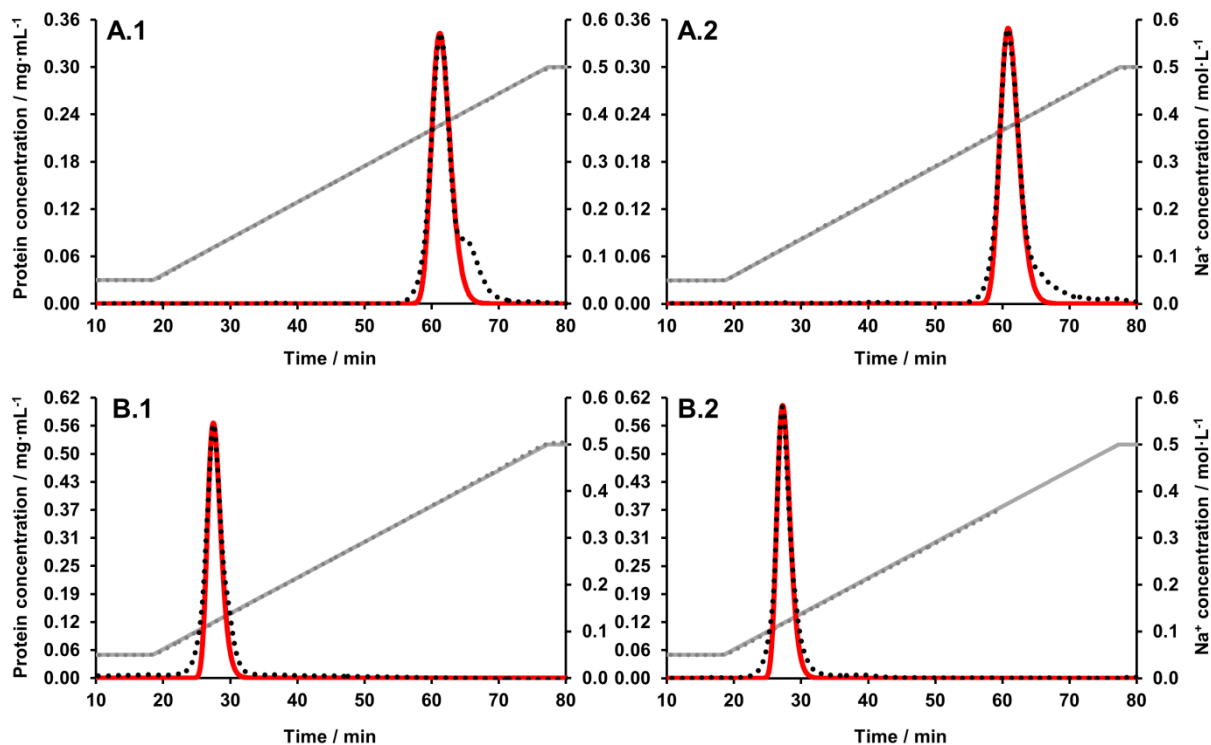


Figure 5. Linear salt gradient elution experiments with the sample bsAbX performed under low loading conditions. A column load of $1 \text{ mg}_{\text{bsAb}}/\text{mL}_{\text{resin}}$ was used. The runs were conducted with the bsAbX sample batch 2 at fixed pH values of pH 4.5 (A.1) and pH 6.3 (B.1), as well as with batch 3 at fixed pH values of pH 4.5 (A.2) and pH 6.3 (B.2). The black dots represent experimental data and the red lines represent simulated data. This figure or parts of it may be included in a similar or identical form in Seelinger et al.³ (DRAFT (submitted)).

In Figure 5, preparative CEX runs performed under low loading conditions (load $\leq 1 \text{ mg}_{\text{bsAb}}/\text{mL}_{\text{resin}}$) are shown and compared with corresponding single-component simulations. The model parameters for these simulations are listed in Table 19 and Table 20. Only LGE experiments of the bsAbX samples batch 2 (Figure 5A.1 and B.1) and batch 3 (Figure 5A.2 and B.2) are shown, since only these two samples were used for high loading and overloading experiments and only these two batches contained an increased amount of dimers/multimers. Thereby, Figure 5A.1 and A.2 show salt gradient runs at pH 4.5 with batch 2 (A.1) and with batch 3 (A.2). Figure 5B.1 and B.2 show salt gradient runs at pH 6.3 with batch 2 (B.1) and with batch 3 (B.2). These four experiments are representative for all other LGE experiments performed at loadings of $\leq 1 \text{ mg}_{\text{bsAb}}/\text{mL}_{\text{resin}}$ where the protein sample bsAbX was used. It can be seen that the resulting main elution peaks are predominantly symmetrical. Interestingly, at pH 4.5 peak shoulders in the rear parts of the main elution peaks can be seen while at a pH of 6.3 no peak shoulders can be

seen. However, by subtracting the mass of dimers/multimers from the set load, the main elution peaks at column loads of $\leq 1 \text{ mg}_{\text{bsAb}}/\text{mL}_{\text{resin}}$ could be predicted at all pH values with sufficient agreement using only one simulated variant (see Figure 5).

Based on these analyses, it was decided to describe the elution of the bsAbX sample with only one simulated variant. The detailed explanation of this decision is presented in section 4.1.2.

3.3 Modeling in the linear range of the adsorption isotherm

Parts of the section 3.3 have already been published in a similar or identical form in Seelinger et al.¹ (Part 1, 2022). Some of the results shown in section 3.3 were also used for the publication Seelinger et al.² (Part 2, 2022). Parts of this section 3.3 are included in a similar or identical form in Seelinger et al.³ (DRAFT (submitted)).

Under low loading conditions, no uncommon elution behavior was observed for both antibodies. Therefore, the same approach (see section 2.2.4) was used for the two bsAbs to determine their linear model parameters.

The modeling of $GH_{\text{pH-pH}_{\text{elu}}}$ data and $GH_1\text{-}C_{1,\text{elu}}$ data is shown in Figure 6. The data points in Figure 6A, Figure 6B, Figure 6D, and Figure 6E are the eluting Na^+ concentrations and pH values from the individual linear salt and pH gradient elution experiments plotted over their corresponding normalized gradient slopes calculated with equations (25) and (26), respectively. It can be seen, that the dataset for bsAbY covers protein elution over a pH range from pH 4.5 to 8.9 and within a Na^+ concentration range from 59.8 to 402.8 mmol/L. The dataset for bsAbX covers protein elution over a pH range from pH 4.5 to 7.3 and within a Na^+ concentration range from 50.0 to 375.0 mmol/L. The solid lines show the fitted $GH_{\text{pH-pH}_{\text{elu}}}$ and $GH_1\text{-}C_{1,\text{elu}}$ correlation according to equations (5), (6) and (24) with the model parameters given in Table 19. Figure 6C and Figure 6F show the pH-dependence of the characteristic protein charge v_i and the logarithmic equilibrium constant $\ln K_{\text{eq},i}$ calculated by using equation (6) and (5), respectively, by using the amino acids involved in binding listed in Table 19. The calculated v_i curve as well as the $\ln K_{\text{eq},i}$ curve both decrease with increasing pH.

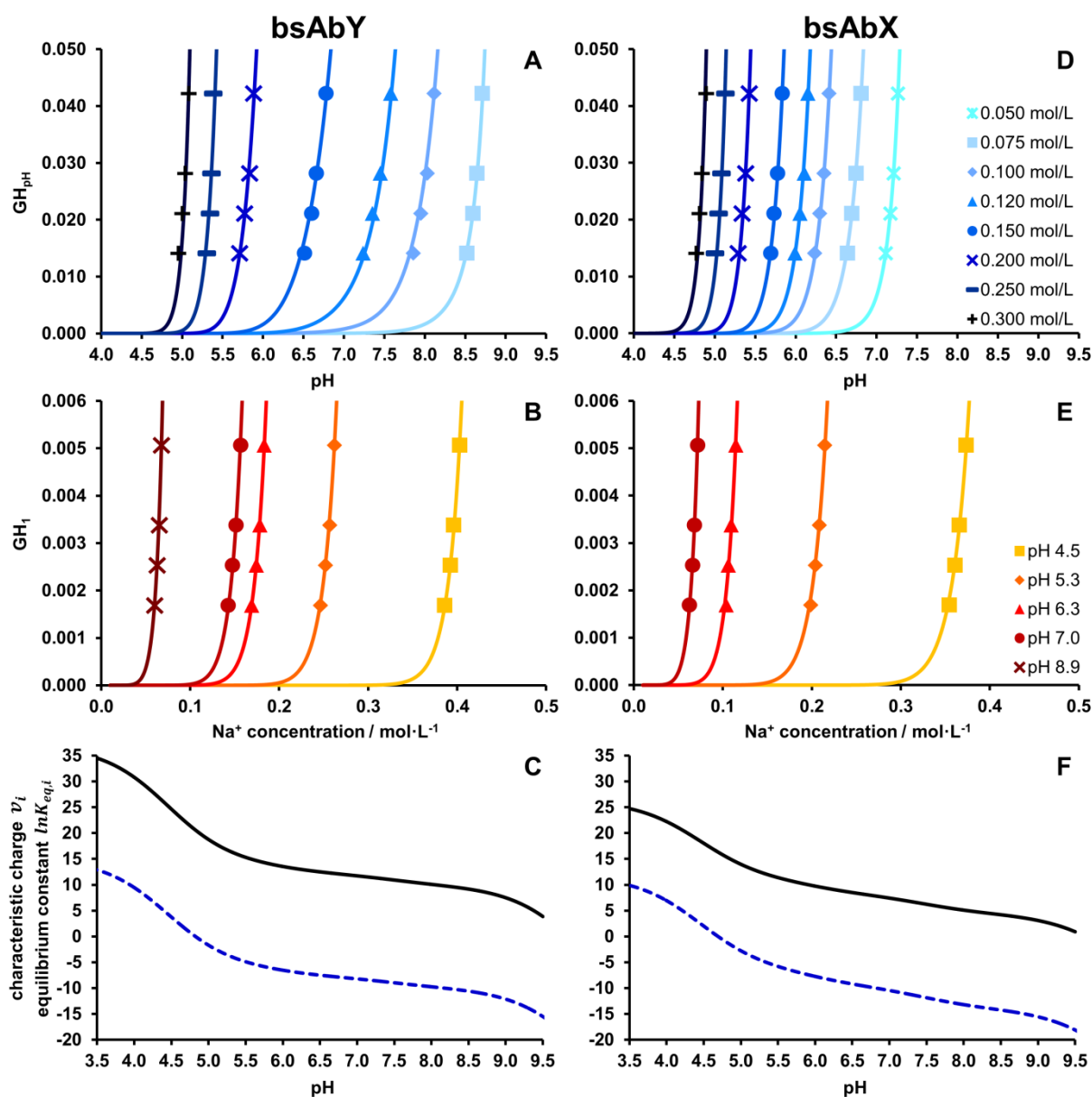


Figure 6. Modeling in the linear range of the adsorption isotherm. Eluting pH of bsAbY (A) and eluting pH of bsAbX (D) as a function of the normalized pH gradient slope (GH_{pH}) for different Na^+ concentrations. Eluting Na^+ concentration of bsAbY (B) and eluting Na^+ concentration of bsAbX (E) as a function of the normalized salt gradient slope (GH_1) for different pH values. In these graphs (A, B, D, and E), the solid lines show the correlation according to equations (5), (6), and (24) with the model parameters given in Table 19. In the graphs (C and F), the black solid lines show the characteristic charge v_i of the bsAbY and bsAbX as a function of pH according to equation (6). The blue dashed lines show the equilibrium constant $\ln K_{eq,i}$ as a function of pH according to equation (5). Parts of this figure are already published in Seelinger et al.¹ (Part 1, 2022). Parts of this figure are also included in a similar or identical form in Seelinger et al.³ (DRAFT (submitted)).

Table 19: Determined thermodynamic model parameters and determined number of amino acids N_{AA}

	$\frac{\Delta G_1^0}{RT}$	$\frac{\Delta G_i^0}{RT}$	N_{carb}	N_{amine}	N_{his}	N_{nterm}	N_{tyr}
bsAbY	0.93	19.08	22.94	32.71	1.81	2.31	4.56
bsAbX	1.17	19.18	15.48	19.81	2.80	3.71	2.47

The $k_{eff,i}$ values for the linear gradient elution experiments estimated under low loading conditions ($\leq 1 \text{ mg}_{bsAb}/\text{mL}_{resin}$) are listed in Table 20.

Table 20: Determined $k_{eff,i}$ values for low loading conditions (load $\leq 1 \text{ mg}_{bsAb}/\text{mL}_{resin}$)

pH / -	$\text{Na}^+ / \text{mmol}\cdot\text{L}^{-1}$	$k_{eff,i} / \text{cm}\cdot\text{s}^{-1}$	
		bsAbY	bsAbX
4.50 – 9.30	50	---	$1.42\cdot 10^{-5}$
4.50 – 8.25(9.30)	75	$1.26\cdot 10^{-5}$	$1.61\cdot 10^{-5}$
4.50 – 9.30	100	$1.07\cdot 10^{-5}$	$1.80\cdot 10^{-5}$
4.50 – 8.25	120	$9.24\cdot 10^{-6}$	$2.01\cdot 10^{-5}$
4.50 – 8.25	150	$1.46\cdot 10^{-5}$	$2.17\cdot 10^{-5}$
4.50 – 8.25	200	$1.66\cdot 10^{-5}$	$2.46\cdot 10^{-5}$
4.50 – 8.25	250	$1.76\cdot 10^{-5}$	$2.60\cdot 10^{-5}$
4.50 – 8.25	300	$1.77\cdot 10^{-5}$	$2.42\cdot 10^{-5}$
4.50	50 – 500	$1.61\cdot 10^{-5}$	$2.23\cdot 10^{-5}$
5.30	50 – 500	$1.75\cdot 10^{-5}$	$2.28\cdot 10^{-5}$
6.30	50 – 500	$1.91\cdot 10^{-5}$	$2.83\cdot 10^{-5}$
7.00	35 – 500	$2.08\cdot 10^{-5}$	$2.50\cdot 10^{-5}$
8.00	25 – 500	$1.87\cdot 10^{-5}$	---
8.50	25 – 500	$1.79\cdot 10^{-5}$	---
8.90	25 – 500	$1.73\cdot 10^{-5}$	---
6.30 – 5.10	50 – 350	$1.84\cdot 10^{-5}$	---
5.20 – 7.50	80 – 300	$2.35\cdot 10^{-5}$	---

The determined linear model parameters N_{AA} , $\Delta G_1^0/RT$, $\Delta G_i^0/RT$ (see Table 19) and the $k_{eff,i}$ values for low loading conditions (see Table 20) allow *in silico* chromatogram simulation of low loading experiments.

3.4 Investigation and comparison of the elution behavior under high loading and overloading conditions of the samples bsAbY and bsAbX

Parts of this section 3.4 have already been published in a similar or identical form in Seelinger et al.¹ (Part 1, 2022) and in Seelinger et al.² (Part 2, 2022). Parts of this section 3.4 are also included in a similar or identical form in Seelinger et al.³ (DRAFT (submitted)).

The elution behavior of the two bsAb samples under high loading and overloading conditions was investigated and compared by using different column loadings (1, 5, 12, 25, 50, 75, and 90 mg_{bsAb}/mL_{resin}). Representative of all linear gradients used in this work, the elution behavior of the two bsAbs is shown in overlay plots for the linear salt gradients at pH 4.5 and for the linear pH gradients at 120 mmol/L Na⁺. These overlay plots are shown in Figure 7.

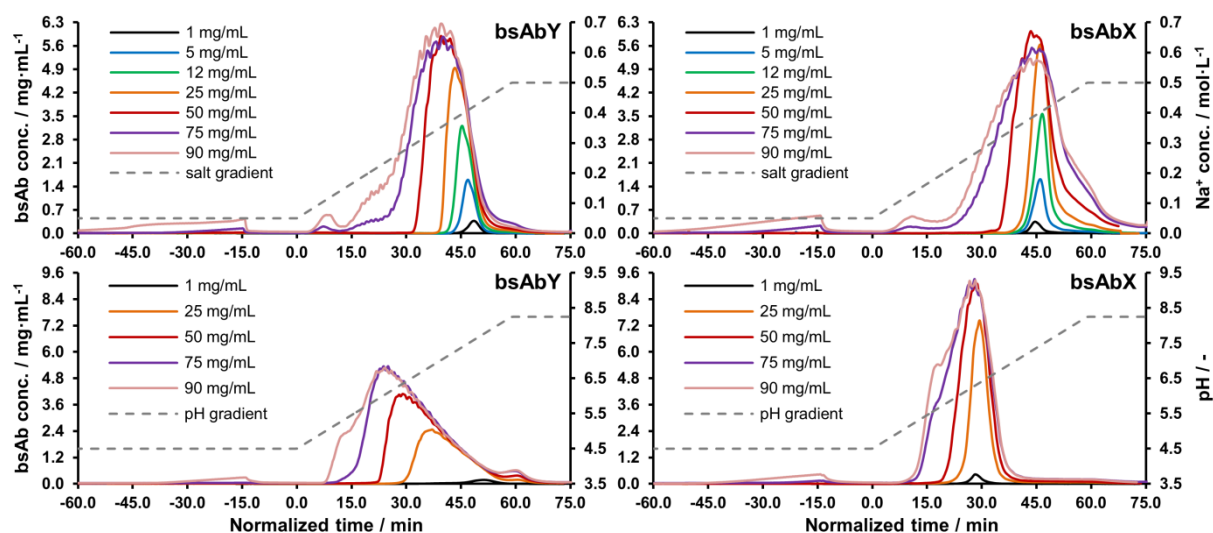


Figure 7. Elution behavior of bsAbY and bsAbX (batch 3) under high loading and overloading conditions. Overlay plots of the linear salt gradients at pH 4.5 and the linear pH gradients at 120 mmol/L Na⁺ with increasing column loadings from 1 to 90 mg_{bsAb}/mL_{resin}. The time in minutes is normalized to the gradient start. The upper two overlay plots show the linear salt gradients and the lower two overlay plots show the linear pH gradients. Some of the data illustrated in this figure are already shown in Seelinger et al.¹ (Part 1, 2022) and in Seelinger et al.² (Part 2, 2022). Parts of this figure are also included in a similar or identical form in Seelinger et al.³ (DRAFT (submitted)).

Figure 7 illustrates that the antibody sample bsAbY showed up to a loading of $50 \text{ mg}_{\text{bsAb}}/\text{mL}_{\text{resin}}$ a common Langmuir elution behavior.^{44,66} As the loading increases from 1 to $50 \text{ mg}_{\text{bsAb}}/\text{mL}_{\text{resin}}$, the peaks increase in height and the maxima and fronts of the peaks shift to lower retention times. From 5 to $50 \text{ mg}_{\text{bsAb}}/\text{mL}_{\text{resin}}$, the elution peaks of the antibody bsAbY have a trapezoidal shape and the peak maxima are located in the front region of the peaks. As already mentioned, this type of elution behavior is called Langmuir behavior which can be described by the SMA model.^{1,2,44} However, from a loading of $\geq 50 \text{ mg}_{\text{bsAb}}/\text{mL}_{\text{resin}}$, clear overloading phenomena were observed. As shown in Figure 7, the peaks in the salt gradients do not continue to increase in height from a loading of $\geq 50 \text{ mg}_{\text{bsAb}}/\text{mL}_{\text{resin}}$. For the pH gradients, the peaks do not increase further in height from a loading of $\geq 75 \text{ mg}_{\text{bsAb}}/\text{mL}_{\text{resin}}$. In addition, at column loadings of 75 and $90 \text{ mg}_{\text{bsAb}}/\text{mL}_{\text{resin}}$, significant overloading effects such as breakthrough, formation of additional peaks, peak fronting, as well as shoulders in the peak front and back of the peaks can be observed. In the further course of the project, it was examined why these overloading phenomena occurred. Moreover, it was investigated whether the applied SMA model is able to describe these overloading effects. Additionally, if discrepancies were found between the simulations and the experimental elution profiles, it was investigated whether these deviations were a consequence of limitations of the applied SMA model or if there were other reasons behind them.

The antibody sample bsAbX, on the other hand, showed a completely different binding and elution behavior. The sample bsAbX showed an uncommon and complex anti-Langmuir elution behavior under high loading conditions.^{52,64–66,114,115} Up to a column loading of $50 \text{ mg}_{\text{bsAb}}/\text{mL}_{\text{resin}}$, the elution peaks of the antibody bsAbX have a backward inclined asymmetric peak shape with peak maxima in the posterior region of the peaks. As the loading increases from 1 to $50 \text{ mg}_{\text{bsAb}}/\text{mL}_{\text{resin}}$, the peaks increase in height and the rears of the peaks and the peak maxima move to higher retention times. Since the SMA model is not able to represent such load-dependent shifts towards higher retentions, a modified stoichiometric binding model had to be used. For this purpose, a modified SAS-SMA model^{3,52} was used in this work, which is able to describe anti-Langmuirian binding and elution behavior. Moreover, from a loading of $\geq 50 \text{ mg}_{\text{bsAb}}/\text{mL}_{\text{resin}}$, the peaks do not increase further in height. In addition, at column loadings of 75 and $90 \text{ mg}_{\text{bsAb}}/\text{mL}_{\text{resin}}$, significant overloading effects such as breakthrough, formation of additional peaks, peak fronting and shoulders in the

peak front and back of the peaks can be observed. In the further course of the project, it was partially examined why these overloading phenomena occurred. Furthermore, it was examined to what extent the applied SAS-SMA model is able to describe binding and elution of the protein bsAbX under high loading and overloading conditions. To some extent, when discrepancies were found between the simulations and the experimental elution profiles, it was investigated whether these discrepancies were a consequence of the limitations of the SAS-SMA model used or whether there were other reasons behind them.

3.5 Modeling the binding and elution behavior of bsAbY under high loading and overloading conditions by applying the Steric Mass Action (SMA) model

3.5.1 Determination of pH-dependent shielding factor σ_i values and $k_{eff,i}$ values under high loading and overloading conditions

Parts of section 3.5.1 have already been published in a similar or identical form in Seelinger et al.¹ (Part 1, 2022) and in Seelinger et al.² (Part 2, 2022).

A modified SMA model with a pH-dependent shielding factor σ_i was used to describe binding and elution behavior of the sample bsAbY under high loading and overloading conditions. In this work, only linear salt gradient elution experiments at fixed pH values were used for the determination of the σ_i values. The σ_i and $k_{eff,i}$ values leading to the best fit for the individual linear salt gradient elution experiments performed under high loading and column overloading conditions (load $\geq 5 \text{ mg}_{bsAb}/\text{mL}_{resin}$) are listed in Table 21.

As can be seen in Table 21, the $k_{eff,i}$ values for all linear salt gradients are decreasing with increasing column loadings.

For each pH value highly similar values for σ_i were determined by inverse peak fitting for column loads of 5, 12, and 25 $\text{mg}_{bsAb}/\text{mL}_{resin}$ (up to 50 $\text{mg}_{bsAb}/\text{mL}_{resin}$ at pH 5.3).

The chromatogram simulations of the runs performed at pH 5.3 and pH 8.0 are shown in Figure 8 and in Figure 9, respectively, which are presented as examples in this section.

Table 21: Determined SMA model parameters and $k_{eff,i}$ values for high loading and overloading conditions for the sample bsAbY

pH / -	Corrected pH / -	v_i / -	Load / mg·mL ⁻¹	$k_{eff,i}$ / cm·s ⁻¹	Individual values		Mean values	
					σ_i / -	$q_{max,i}$ / mol·L ⁻¹	$\bar{\sigma}_i$ / -	$\bar{q}_{max,i}$ / mol·L ⁻¹
4.5	4.50	24.64	5	$1.46 \cdot 10^{-5}$	38.50	$4.26 \cdot 10^{-3}$	38.56	$4.25 \cdot 10^{-3}$
	4.50	24.64	12	$1.36 \cdot 10^{-5}$	38.72	$4.25 \cdot 10^{-3}$		
	4.48	24.85	25	$1.25 \cdot 10^{-5}$	38.45	$4.23 \cdot 10^{-3}$		
	4.48	24.85	50	$8.44 \cdot 10^{-6}$ / b)	--- / a)	--- / a)		
	4.46	25.18	75	$7.74 \cdot 10^{-6}$ / b)	--- / a)	--- / a)		
	4.48	24.85	90	$6.82 \cdot 10^{-6}$ / b)	--- / a)	--- / a)		
5.3	5.27	16.59	5	$1.65 \cdot 10^{-5}$	69.13	$3.15 \cdot 10^{-3}$	68.90	$3.16 \cdot 10^{-3}$
	5.27	16.59	12	$1.52 \cdot 10^{-5}$	68.00	$3.19 \cdot 10^{-3}$		
	5.30	16.44	25	$1.37 \cdot 10^{-5}$	69.27	$3.15 \cdot 10^{-3}$		
	5.30	16.44	50	$1.17 \cdot 10^{-5}$	69.21	$3.15 \cdot 10^{-3}$		
	5.27	16.60	75	$8.75 \cdot 10^{-6}$ / b)	--- / a)	--- / a)		
	5.30	16.44	90	$8.40 \cdot 10^{-6}$ / b)	--- / a)	--- / a)		
6.3	6.26	12.95	5	$1.85 \cdot 10^{-5}$	86.56	$2.71 \cdot 10^{-3}$	87.29	$2.69 \cdot 10^{-3}$
	6.26	12.95	12	$1.74 \cdot 10^{-5}$	87.50	$2.69 \cdot 10^{-3}$		
	6.24	12.99	25	$1.62 \cdot 10^{-5}$	87.81	$2.68 \cdot 10^{-3}$		
	6.24	12.99	50	$1.58 \cdot 10^{-5}$ / b)	--- / a)	--- / a)		
	6.24	12.99	75	$1.55 \cdot 10^{-5}$ / b)	--- / a)	--- / a)		
	7.0	6.94	11.83	5	$2.02 \cdot 10^{-5}$	100.50		
6.94		11.83	12	$1.92 \cdot 10^{-5}$	103.71	$2.34 \cdot 10^{-3}$		
6.94		11.83	25	$1.83 \cdot 10^{-5}$	103.50	$2.34 \cdot 10^{-3}$		
6.92		11.82	25	$1.85 \cdot 10^{-5}$	103.36	$2.34 \cdot 10^{-3}$		
6.92		11.82	50	$1.81 \cdot 10^{-5}$ / b)	--- / a)	--- / a)		
6.92		11.82	75	$1.76 \cdot 10^{-5}$ / b)	--- / a)	--- / a)		
8.0	7.93	10.19	5	$1.82 \cdot 10^{-5}$	121.00	$2.06 \cdot 10^{-3}$	120.13	$2.07 \cdot 10^{-3}$
	7.93	10.19	12	$1.72 \cdot 10^{-5}$	118.63	$2.10 \cdot 10^{-3}$		
	7.93	10.19	25	$1.64 \cdot 10^{-5}$	120.24	$2.07 \cdot 10^{-3}$		
	7.90	10.25	25	$1.64 \cdot 10^{-5}$	120.65	$2.06 \cdot 10^{-3}$		
	7.90	10.25	50	$1.52 \cdot 10^{-5}$ / b)	--- / a)	--- / a)		
	7.90	10.25	75	$1.40 \cdot 10^{-5}$ / b)	--- / a)	--- / a)		
	7.90	10.25	90	$1.29 \cdot 10^{-5}$ / b)	--- / a)	--- / a)		
8.5	8.54	9.09	5	$1.72 \cdot 10^{-5}$	129.00	$1.95 \cdot 10^{-3}$	129.78	$1.94 \cdot 10^{-3}$
	8.54	9.09	12	$1.68 \cdot 10^{-5}$	129.63	$1.95 \cdot 10^{-3}$		
	8.54	9.09	25	$1.59 \cdot 10^{-5}$	131.00	$1.93 \cdot 10^{-3}$		
	8.49	9.19	25	$1.60 \cdot 10^{-5}$	129.50	$1.95 \cdot 10^{-3}$		
	8.49	9.19	50	$1.54 \cdot 10^{-5}$ / b)	--- / a)	--- / a)		
	8.49	9.19	75	$1.48 \cdot 10^{-5}$ / b)	--- / a)	--- / a)		
8.9	8.85	8.15	5	$1.66 \cdot 10^{-5}$	139.50	$1.83 \cdot 10^{-3}$	139.85	$1.83 \cdot 10^{-3}$
	8.90	7.95	5	$1.68 \cdot 10^{-5}$	139.75	$1.83 \cdot 10^{-3}$		
	8.85	8.15	12	$1.64 \cdot 10^{-5}$	141.00	$1.81 \cdot 10^{-3}$		
	8.90	7.95	12	$1.64 \cdot 10^{-5}$	140.00	$1.82 \cdot 10^{-3}$		
	8.90	7.95	25	$1.56 \cdot 10^{-5}$	139.00	$1.84 \cdot 10^{-3}$		

a) Estimation of σ_i and $q_{max,i}$ was unfeasible because of overloading phenomena.

b) Estimated using the mean value $\bar{\sigma}_i$.

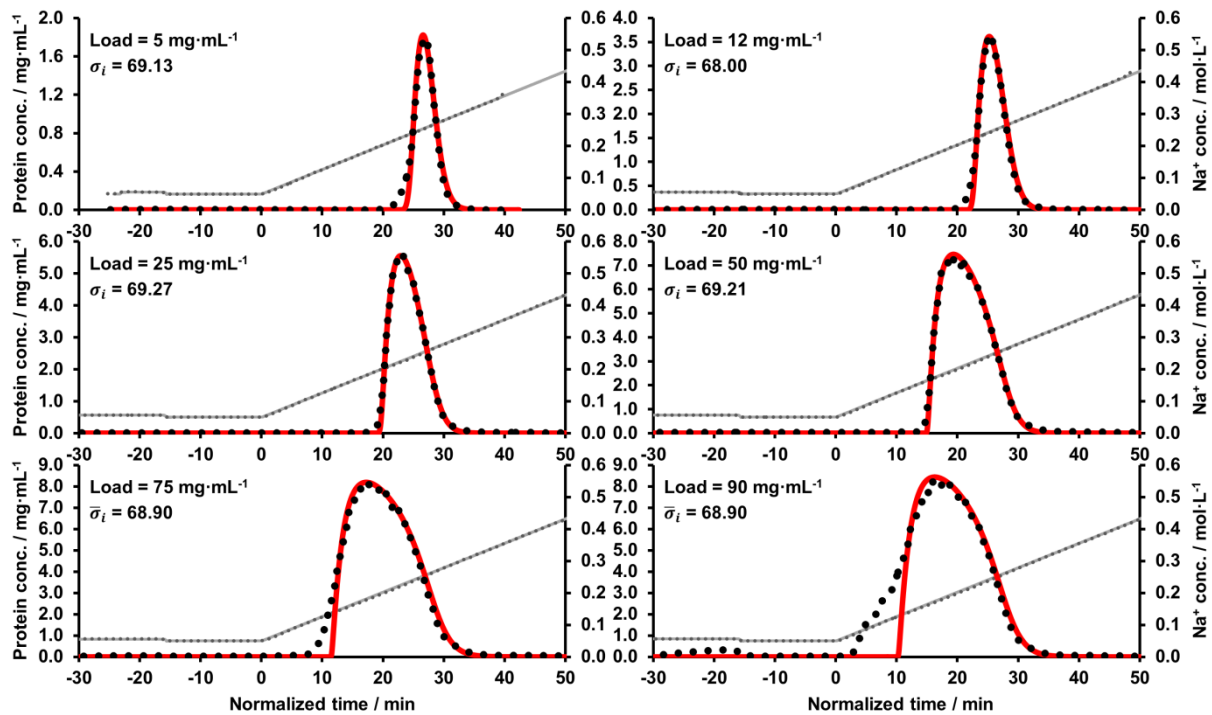


Figure 8. Salt gradient elutions of bsAbY at pH 5.3 used for estimation and verification of the steric shielding factor (σ_i) values by applying the SMA model. The black dots are experimental data and the red lines are simulated data. The time in minutes is normalized to the gradient start. At pH 5.3, highly similar values for σ_i were determined by inverse peak fitting for column loads of 5, 12, 25, and 50 $\text{mg}_{\text{bsAb}}/\text{mL}_{\text{resin}}$. At column loads of 75 and 90 $\text{mg}_{\text{bsAb}}/\text{mL}_{\text{resin}}$, a mean value $\bar{\sigma}_i$ was used for the chromatogram simulations. The applied fitted σ_i values, the mean values $\bar{\sigma}_i$ and the $k_{\text{eff},i}$ values are listed in Table 21. Some of the data shown and illustrated in this figure are already published in Seelinger et al.¹ (Part 1, 2022) and in Seelinger et al.² (Part 2, 2022).

The experimental and the corresponding simulated chromatograms shown for pH 5.3 are comparable to the corresponding chromatograms for pH 4.5. The experimental and simulated chromatograms for pH 4.5 are shown in Figure 30 in the figure appendix (see section 8). Similarly, the results shown for pH 8.0 are representative of the chromatograms for pH 6.3, 7.0, 8.5, and 8.9. The experimental and simulated chromatograms for the salt gradients at pH 6.3, 7.0, 8.5, and 8.9 are shown in Figure 31, Figure 32, Figure 33, and Figure 34, respectively, in the figure appendix (see section 8).

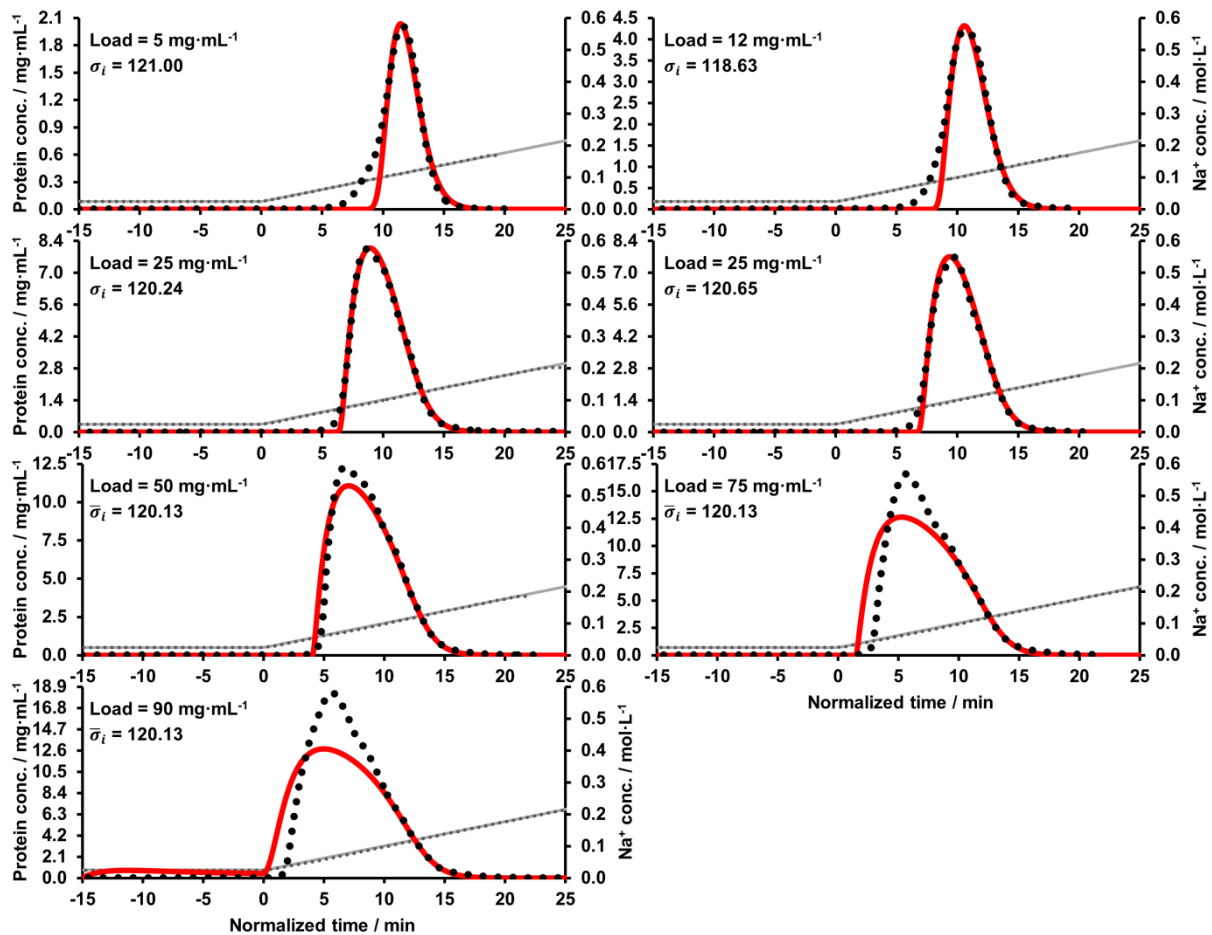


Figure 9. Salt gradient elutions of bsAbY at pH 8.0 used for estimation and verification of the steric shielding factor (σ_i) values by applying the SMA model. The black dots are experimental data and the red lines are simulated data. The time in minutes is normalized to the gradient start. At pH 8.0, highly similar values for σ_i were determined by inverse peak fitting for column loads of 5, 12, and 25 $\text{mg}_{\text{bsAb}}/\text{mL}_{\text{resin}}$. At column loads of 50, 75, and 90 $\text{mg}_{\text{bsAb}}/\text{mL}_{\text{resin}}$, a mean value $\bar{\sigma}_i$ was used for the chromatogram simulations. The applied fitted σ_i values, the mean values $\bar{\sigma}_i$ and the $k_{\text{eff},i}$ values are listed in Table 21. Some of the data shown and illustrated in this figure are already published in Seelinger et al.¹ (Part 1, 2022) and in Seelinger et al.² (Part 2, 2022).

The elution peaks of the salt gradient runs performed with column loads of 5, 12, and 25 $\text{mg}_{\text{bsAb}}/\text{mL}_{\text{resin}}$ (up to 50 $\text{mg}_{\text{bsAb}}/\text{mL}_{\text{resin}}$ at pH 5.3) could be precisely described by the simulation for all pH values tested. Furthermore, as already mentioned, very similar σ_i values were determined in this loading range for each pH value. However, starting at a load of 50 $\text{mg}_{\text{bsAb}}/\text{mL}_{\text{resin}}$ (75 $\text{mg}_{\text{bsAb}}/\text{mL}_{\text{resin}}$ at pH 5.3) complex high loading and overloading effects made estimation of σ_i by inverse peak fitting unfeasible or led to deviating and thus falsified values, which were consequently discarded. Thereby, the observed overloading phenomena at lower pH values of pH

4.5 and pH 5.3 differed from the high loading phenomena observed at pH values of $\text{pH} \geq 6.3$.

At lower pH ($\text{pH} \leq 5.3$), unexpected peak shapes like more dome-shaped peaks instead of more trapezoidal peaks are observed at column loadings of $\geq 50 \text{ mg}_{\text{bsAb}}/\text{mL}_{\text{resin}}$ ($\geq 75 \text{ mg}_{\text{bsAb}}/\text{mL}_{\text{resin}}$ at pH 5.3). In addition, peak fronting is noticeable and in some cases, even shoulders on the peak front have formed. At pH 4.5, additional peaks at the gradient start are visible (see Figure 30). Although strong binding affinities are expected at these low pH values, a breakthrough was observed at loadings of 75 and 90 $\text{mg}_{\text{bsAb}}/\text{mL}_{\text{resin}}$ at pH 4.5, while breakthrough is only observed at a loading of 90 $\text{mg}_{\text{bsAb}}/\text{mL}_{\text{resin}}$ at pH 5.3. The simulation was not able to predict these kinds of overloading effects and peak shapes and therefore no values for σ_i were fitted at these high column loadings. Instead, the mean of the σ_i values estimated at column loadings of 5, 12, and 25 $\text{mg}_{\text{bsAb}}/\text{mL}_{\text{resin}}$ (and 50 $\text{mg}_{\text{bsAb}}/\text{mL}_{\text{resin}}$ at pH 5.3) was used for the simulations at column loadings of $\geq 50 \text{ mg}_{\text{bsAb}}/\text{mL}_{\text{resin}}$ at pH 4.5 and $\geq 75 \text{ mg}_{\text{bsAb}}/\text{mL}_{\text{resin}}$ at pH 5.3. These mean values, which were determined for each pH tested, are denoted in the following as $\bar{\sigma}_i$. By using these $\bar{\sigma}_i$ values, only $k_{\text{eff},i}$ was determined for the respective runs with column loadings of $\geq 50 \text{ mg}_{\text{bsAb}}/\text{mL}_{\text{resin}}$ at pH 4.5 and $\geq 75 \text{ mg}_{\text{bsAb}}/\text{mL}_{\text{resin}}$ at pH 5.3. In Figure 8, it can be seen, that by using a mean value $\bar{\sigma}_i$ of 68.90 at pH 5.3 the main elution peaks at column loads of 75 and 90 $\text{mg}_{\text{bsAb}}/\text{mL}_{\text{resin}}$ could be well described by the simulation. By using a $\bar{\sigma}_i$ of 38.56 at pH 4.5, the main elution peaks at column loads of 50 to 90 $\text{mg}_{\text{bsAb}}/\text{mL}_{\text{resin}}$ (see Figure 30) could be partially predicted by the simulation, although it is noticeable that the peak tip is not completely described. For these simulations where the mean values $\bar{\sigma}_i$ were used, the mass of protein that formed the peak shoulders and the breakthroughs were subtracted from the set loading used for the simulation to get good descriptions of the main elution peaks.

At higher pH values ($\text{pH} \geq 6.3$), unexpected peak shapes were observed at column loadings of $\geq 50 \text{ mg}_{\text{bsAb}}/\text{mL}_{\text{resin}}$. Unexpected peak shapes here means that the peaks became relatively narrow and tall. In fact, the peak fronts here did not move much towards lower retentions with increasing loadings, but instead the elution peaks simply became higher, which resulted in these unexpected narrow and tall elution peaks. Estimation of the σ_i values using the inverse peak fitting method resulted in smaller σ_i values for the runs with loadings of $\geq 50 \text{ mg}_{\text{bsAb}}/\text{mL}_{\text{resin}}$ compared to the runs with loadings of $\leq 25 \text{ mg}_{\text{bsAb}}/\text{mL}_{\text{resin}}$. Furthermore, while at loadings of

$\leq 25 \text{ mg}_{\text{bsAb}}/\text{mL}_{\text{resin}}$ always very good agreement between experimental and simulated data was achieved with the chromatogram fits, at loadings of $\geq 50 \text{ mg}_{\text{bsAb}}/\text{mL}_{\text{resin}}$, poor agreement between experimental and simulated data was observed in some cases. Therefore, the σ_i values estimated at $\text{pH} \geq 6.3$ and $\geq 50 \text{ mg}_{\text{bsAb}}/\text{mL}_{\text{resin}}$ (values not shown) were assumed to be biased and were thus discarded. Instead, the mean values $\bar{\sigma}_i$ determined with the runs with column loadings of 5 to $25 \text{ mg}_{\text{bsAb}}/\text{mL}_{\text{resin}}$ were used here. By using these $\bar{\sigma}_i$ values, only $k_{\text{eff},i}$ was determined for the respective runs with column loadings of $\geq 50 \text{ mg}_{\text{bsAb}}/\text{mL}_{\text{resin}}$ at pH 6.3, 7.0, 8.0, and 8.5. By applying the respective mean values $\bar{\sigma}_i$, the runs at pH 6.3 with column loadings of 50 and $75 \text{ mg}_{\text{bsAb}}/\text{mL}_{\text{resin}}$ (see Figure 31) and at pH 7.0 with a loading of $50 \text{ mg}_{\text{bsAb}}/\text{mL}_{\text{resin}}$ (see Figure 32) could be simulated with acceptable agreement. At pH 8.0 the elution peaks at column loadings of 50, 75, and $90 \text{ mg}_{\text{bsAb}}/\text{mL}_{\text{resin}}$ could only be partially described by the simulation using a mean value $\bar{\sigma}_i$ of 120.13 (see Figure 9). The same is the case for the experiments at pH 7.0 with a loading of $75 \text{ mg}_{\text{bsAb}}/\text{mL}_{\text{resin}}$ (see Figure 32) and at pH 8.5 (see Figure 33) with loadings of $\geq 50 \text{ mg}_{\text{bsAb}}/\text{mL}_{\text{resin}}$. These experiments at pH 7.0 and 8.5 could also only be partially described with the respective mean values $\bar{\sigma}_i$ for these pH values (see Figure 32 and Figure 33). As described briefly before, an altered elution pattern was observed at column loadings of $\geq 50 \text{ mg}_{\text{bsAb}}/\text{mL}_{\text{resin}}$ and pH values of ≥ 6.3 , resulting in unexpectedly narrow and tall elution peaks. Thereby, the deviation between experimental and simulated peaks using the mean values $\bar{\sigma}_i$ became more pronounced with increasing pH and with increasing column loadings. Here, the rear part of the elution peaks could always be described with the applied mean values $\bar{\sigma}_i$. However, the start of peak elution and peak height is not predicted correctly, especially at pH 7.0 with a column loading of $75 \text{ mg}_{\text{bsAb}}/\text{mL}_{\text{resin}}$, at pH 8.0 with $\geq 50 \text{ mg}_{\text{bsAb}}/\text{mL}_{\text{resin}}$, and at pH 8.5 with $\geq 50 \text{ mg}_{\text{bsAb}}/\text{mL}_{\text{resin}}$. This shows that at higher pH values of ≥ 6.3 a mean value $\bar{\sigma}_i$ did not always work adequately to predict the main elution peaks. The reasons for the observed deviations and the reasons why no reliable σ_i values could be determined at pH 6.3 and $\geq 50 \text{ mg}_{\text{bsAb}}/\text{mL}_{\text{resin}}$ are shown (see section 3.6) and discussed (see section 4.5.1.1) in later sections.

3.5.2 Semi-empirical description of the steric shielding factor's pH-dependence when using the SMA model

Parts of Section 3.5.2 have already been published in a similar or identical form in Seelinger et al.¹ (Part 1, 2022) and have been used for the publication Seelinger et al.² (Part 2, 2022).

To describe the pH-dependence of σ_i , the values for σ_i estimated using the runs with column loadings up to 50 mg_{bsAb}/mL_{resin} were plotted against their corresponding pH values, as displayed in Figure 10A. These values are listed in Table 21. In Figure 10A, it can be seen that the shielding factors σ_i are strongly increasing with increasing pH.

A semi-empirical description of σ_i as a function of pH and v_i was found and ultimately used in this work.¹

$$\sigma_i = \frac{\Delta G_1^0}{RT} \cdot \frac{1}{\ln(10)} \cdot pH \cdot (v_{pH=0,i} - v_{pH,i}) \quad (40)$$

Equation (40) describes σ_i as a function of pH and of the difference between a theoretical protein binding charge $v_{pH=0,i}$ at pH = 0 and the pH-dependent protein binding charge v_i . The pH-dependent variable v_i is calculated by using equation (6). The constant $v_{pH=0,i}$ is the only adjustable parameter and was fitted using the experimental data shown in Figure 10 and Table 21. Equation (40) was used to determine the value for $v_{pH=0,i}$ of 47.54. The semi-empirical function describes the change of the experimental values for σ_i over their respective pH values (see Figure 10A) and their respective v_i values (see Figure 10B) very well, as can be seen in Figure 10.

The model parameters σ_i and v_i strongly influence the theoretical maximal binding capacity $q_{max,i}$ which is given by^{1,44}:

$$q_{max,i} = \frac{\Lambda}{(\sigma_i + v_i)} \quad (41)$$

Since the sum of σ_i and v_i ($\sigma_i + v_i$) increases with increasing pH (see Figure 10A), as a consequence, the theoretical maximum binding capacity $q_{max,i}$ decreases with increasing pH.

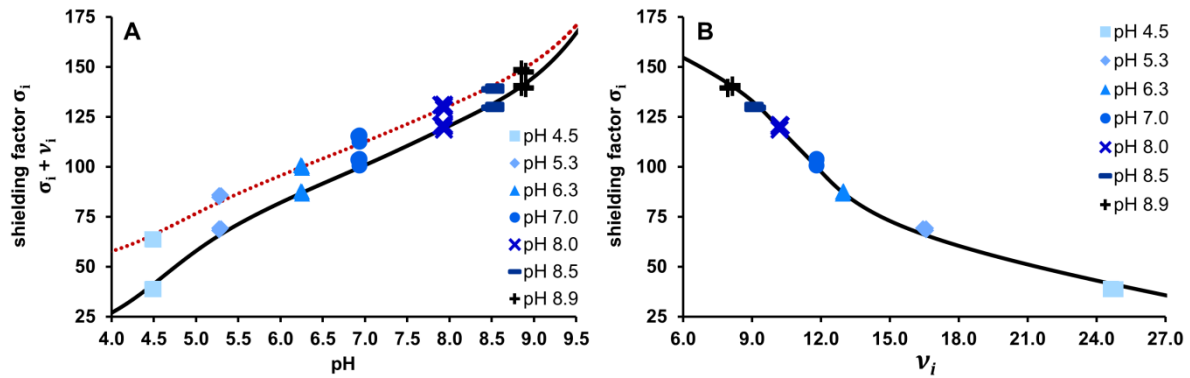


Figure 10. pH-dependence of σ_i and $\sigma_i + v_i$ (bsAbY). (A) Semi-empirical description of the pH-dependence of σ_i . The data points display the estimated values for σ_i plotted over their corresponding pH values, as well as the sum of the estimated values for σ_i and their respective values for v_i plotted over their corresponding pH values. These values are listed in Table 21. The black solid line represents the change of σ_i over mobile phase pH calculated by equation (40). The red dotted line represents the change of $\sigma_i + v_i$ over mobile phase pH determined by adding up the calculations with equation (40) and (6). (B) σ_i as a function of v_i . The data points display the estimated values for σ_i plotted over their corresponding v_i values that are listed in Table 21. The black solid line represents the change of σ_i over v_i calculated by equation (40) and (6). This figure is already published in Seelinger et al.¹ (Part 1, 2022).

3.5.3 Verification of the pH-dependent SMA model

3.5.3.1 Calculated change of pH-dependent model parameters over a linear pH gradient

Parts of Section 3.5.3.1 have already been published in a similar or identical form in Seelinger et al.¹ (Part 1, 2022).

The SMA model was modified by adding the semi-empirical equation (40) into the SMA formalism. With this extension, the SMA model includes the pH-dependent linear model parameter v_i as well as the pH-dependent non-linear model parameters σ_i and thus also $q_{max,i}$. The extended model is now capable of predicting non-linear adsorption and elution behavior when the pH value changes during the experiment, like in linear pH gradients.

A linear pH gradient from pH 4.5 to 9.3 in 51.2 CV was used as an example to visualize the change of the pH-dependent SMA model parameters v_i , σ_i and $q_{max,i}$. Figure 11 shows that the modified SMA model predicts a decreasing v_i over the applied linear pH gradient. The simulated pH-dependent shielding factor σ_i increases with increasing pH and the simulated $q_{max,i}$ decreases over the applied pH gradient,

as expected. In Figure 11, the data points for v_i , σ_i and $q_{max,i}$ are the individual values listed in Table 21. The data points were plotted at their respective pH values (see Table 21) into the linear pH gradient to confirm the simulation approach using the modified pH-dependent SMA model and underlying parameter set.

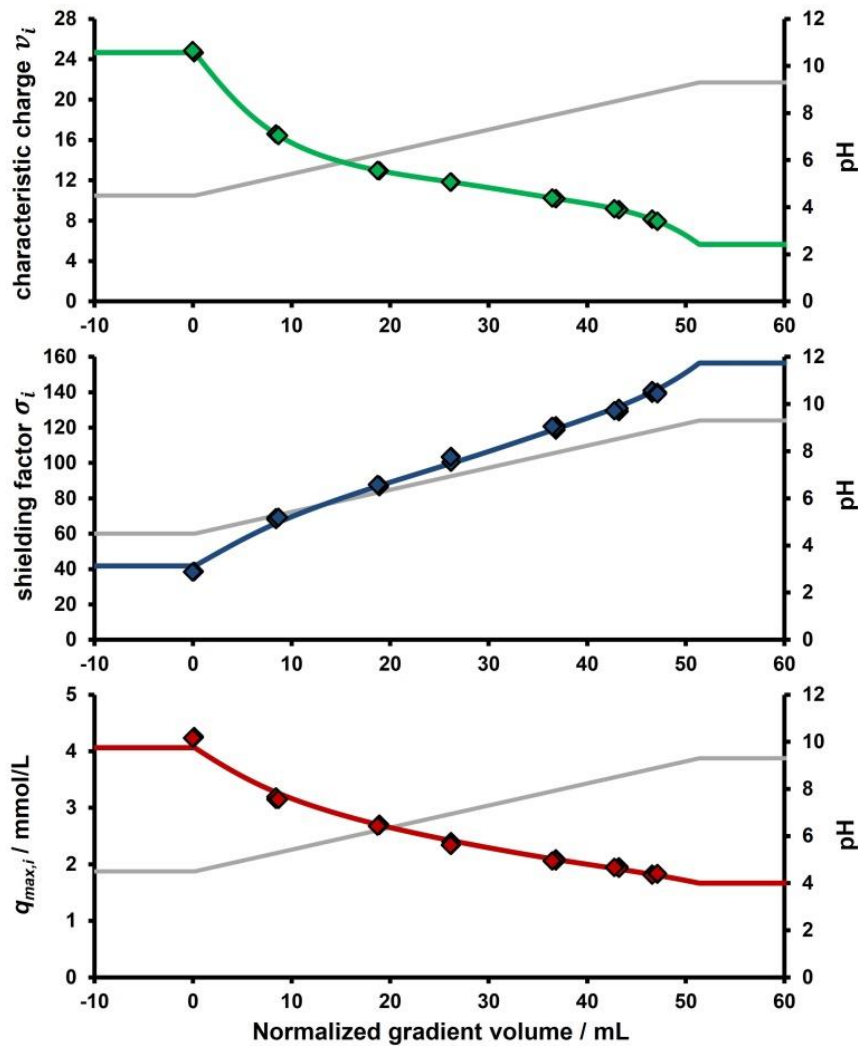


Figure 11. Simulated changes of v_i , σ_i and $q_{max,i}$ for bsAbY over a linear pH gradient (pH 4.5 – 9.3) calculated by the pH-dependent SMA model. The SMA model modified with the pH-dependent σ_i simulates a change of v_i (green line) which decreases with increasing pH. σ_i (blue line) increases with increasing pH whereas $q_{max,i}$ (red line) decreases with increasing pH. The data points for v_i , σ_i and $q_{max,i}$ are the values listed in Table 21, plotted at their corresponding pH values. The gradient volume in milliliters is normalized to the gradient start. This figure is already published in Seelinger et al.¹ (Part 1, 2022).

3.5.3.2 Simulation of linear pH gradient elution experiments performed under high loading and column overloading conditions

Parts of Section 3.5.3.2 have already been published in a similar or identical form in Seelinger et al.¹ (Part 1, 2022) and in Seelinger et al.² (Part 2, 2022).

The pH-dependent SMA model was further verified by simulation of linear pH gradient elution experiments performed under high loading and column overloading conditions. Therefore, linear pH gradient elution experiments at three different fixed counterion concentrations (75, 120, and 200 mmol/L Na⁺) and four different column loadings (25, 50, 75, and 90 mg_{bsAb}/mL_{resin}) were applied. The $k_{eff,i}$ values for the individual linear pH gradient elution experiments are listed in Table 22. The comparison between simulated and experimental data is shown in Figure 12. Increasing fixed Na⁺ concentrations in the linear pH gradients shift the elution peaks to lower elution pH values. Increasing protein loadings shift the front of the elution peaks to lower elution pH values resulting in broader peaks or overlapping peaks. The pH-dependent SMA model predicts the retention and the peak shape of the main elution peaks very well. This particularly applies to the experiments carried out with Na⁺ concentrations of 120 and 200 mmol/L and up to a column load of 75 mg_{bsAb}/mL_{resin}.

At a fixed counterion concentration of 75 mmol/L Na⁺, where the protein bsAbY elutes within a pH range of pH 6 to pH 9, the retention of the main elution peaks is well described for all column loadings. However, slight deviations between the experimental and simulated peak shapes are observed. At column loadings of 75 and 90 mg_{bsAb}/mL_{resin}, bsAbY elutes as a clear double-peak. Interestingly, the simulation can predict this complex double-peak formation. Overloading phenomena such as breakthrough, pre-peaks, and pre-shoulders are noticeable starting at a column loading of 75 mg_{bsAb}/mL_{resin} and particularly pronounced at 90 mg_{bsAb}/mL_{resin} for Na⁺ concentrations of 120 and especially 75 mmol/L Na⁺. The pH-dependent SMA model was not able to predict these overloading effects. However, when the amount of protein in the breakthrough, the pre-peaks, and the pre-shoulders was subtracted from the mass of protein used in the simulation, the single-component simulation could predict the elution of the main elution peaks quite well. As already mentioned, the pH-dependent model was even capable of predicting the complex double-peak formation observed at 75 mmol/L Na⁺. Thereby, the simulation predicts maxima of the double peaks that are located on the left side, while the experimental elution

profiles each show a maximum on the right side. The underlying reasons for these slight deviations were investigated and the corresponding results and findings are presented in section 3.6.

Table 22: $k_{eff,i}$ values for sample bsAbY estimated with linear pH and dual gradient elution experiments at high loading and overloading conditions

pH / -	$c(\text{Na}^+) / \text{mmol}\cdot\text{L}^{-1}$	Load / $\text{mg}\cdot\text{mL}^{-1}$	$k_{eff,i} / \text{cm}\cdot\text{s}^{-1}$
4.50 – 9.30	75	25	$1.21\cdot 10^{-5}$
4.50 – 9.30	75	50	$1.12\cdot 10^{-5}$
4.50 – 9.30	75	75	$6.67\cdot 10^{-6}$
4.50 – 9.30	75	90	$5.46\cdot 10^{-6}$
4.50 – 8.25	120	25	$7.20\cdot 10^{-6}$
4.50 – 8.25	120	50	$6.87\cdot 10^{-6}$
4.50 – 8.25	120	75	$6.54\cdot 10^{-6}$
4.50 – 8.25	120	90	$5.82\cdot 10^{-6}$
4.50 – 8.25	200	25	$1.59\cdot 10^{-5}$
4.50 – 8.25	200	50	$1.52\cdot 10^{-5}$
4.50 – 8.25	200	75	$1.31\cdot 10^{-5}$
6.30 – 5.10	50 – 350	25	$1.33\cdot 10^{-5}$
6.30 – 5.10	50 – 350	50	$1.31\cdot 10^{-5}$
5.20 – 7.50	80 – 300	25	$1.90\cdot 10^{-5}$
5.20 – 7.50	80 – 300	50	$1.83\cdot 10^{-5}$

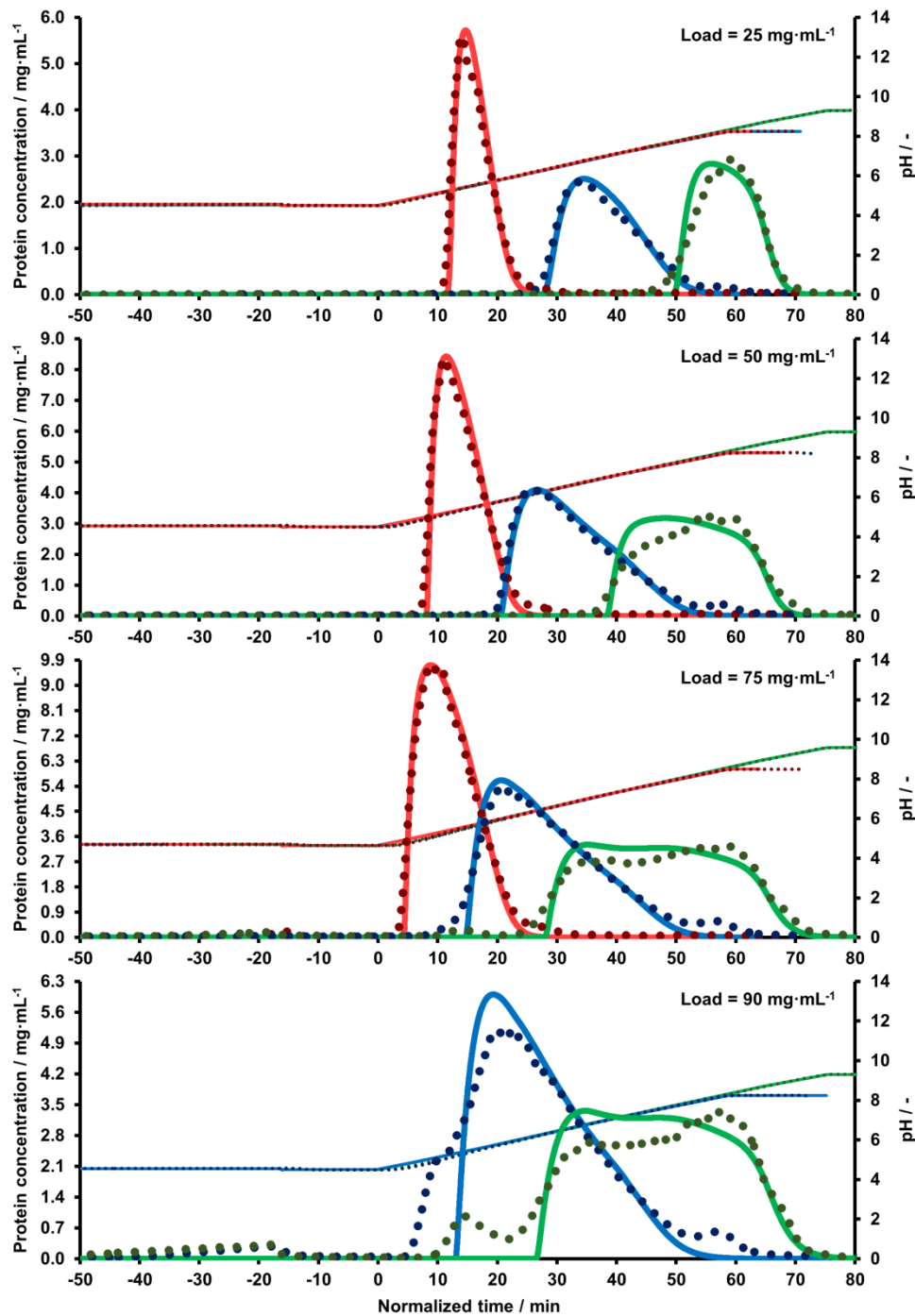


Figure 12. Linear pH gradient elution experiments performed at 75, 120 and 200 mmol/L Na⁺ with increasing loadings from 25 to 90 mg_{bsAb}/mL_{resin}, performed with the sample bsAbY and simulated by the pH-dependent SMA model. The time in minutes is normalized to the gradient start. The dots display experimental data. The lines represent simulated data. The green data represents the pH gradient (pH 4.50 – 9.30) runs performed at 75 mmol/L Na⁺. The blue data pertains to the pH gradient (pH 4.50 – 8.25) runs performed at 120 mmol/L Na⁺. The red data represents the pH gradient (pH 4.50 – 8.25) runs performed at 200 mmol/L Na⁺. This figure is already shown in a similar form in the publication Seelinger et al.¹ (Part 1, 2022). Some data of this figure are also shown in a similar form in the publication Seelinger et al.² (Part 2, 2022).

3.5.3.3 Simulation of linear dual gradient elution experiments performed under high loading conditions

Parts of Section 3.5.3.3 have already been published in a similar or identical form in Seelinger et al.¹ (Part 1, 2022).

The pH-dependent SMA model was further verified with linear dual pH and salt gradient elution experiments. A parallel dual gradient and an antiparallel dual gradient were conducted under high loading conditions (25 and 50 mg_{bsAb}/mL_{resin}). The $k_{eff,i}$ values for the individual linear dual gradient elution runs are listed in Table 22. The comparison between simulated and experimental data is shown in Figure 13. It can be seen that peak retention and peak shapes of the applied dual gradient elution experiments could be described very well in all cases.

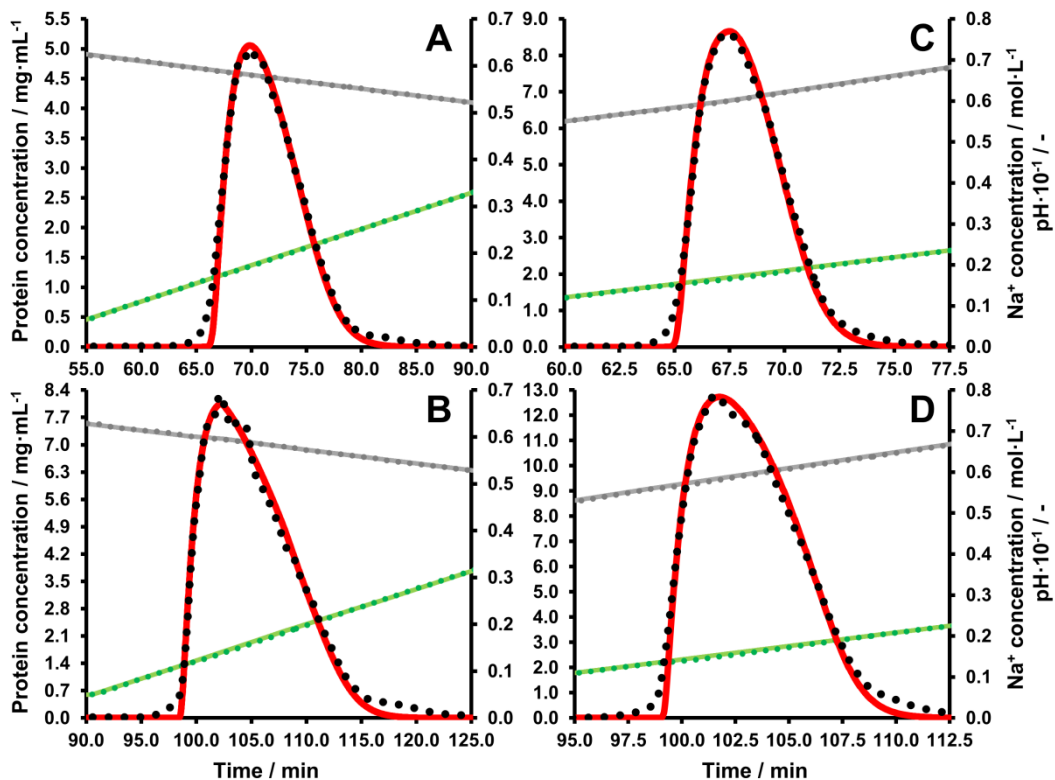


Figure 13. Dual gradient elution experiments with high column loads of 25 and 50 mg_{bsAb}/mL_{resin}, performed with sample bsAbY and simulated by the pH-dependent SMA model. The dots represent the experimental courses of the bsAb concentration (black), the pH (grey) and the Na⁺ concentration (green). The lines represent the simulated courses of the bsAb concentration (red), the pH (gray) and the Na⁺ concentration (green). The different chromatograms represent antiparallel dual gradient experiments performed at loads of 25 mg_{bsAb}/mL_{resin} (A) and 50 mg_{bsAb}/mL_{resin} (B), as well as parallel dual gradient experiments performed at loads of 25 mg_{bsAb}/mL_{resin} (C) and 50 mg_{bsAb}/mL_{resin} (D). This figure is already shown in an identical form in the publication Seelinger et al.¹ (Part 1, 2022).

3.6 Investigation of complex high loading and column overloading phenomena when using bsAbY

3.6.1 High loading and column overloading phenomena at pH \geq 6.0

Parts of section 3.6.1, including the subsections 3.6.1.1 and 3.6.1.2, have already been published in a similar or identical form in Seelinger et al.² (Part 2, 2022). Some of the data described and shown in section 3.6.1 are also published in Seelinger et al.¹ (Part 1, 2022).

In section 3.5.1 and in section 3.5.3.2, it was shown that estimation of reliable σ_i values by inverse peak fitting was unfeasible when pH values of pH \geq 6.3 and column loadings of \geq 50 mg_{bsAb}/mL_{resin} were used. Furthermore, it was even observed that the applied model-based approach was partially unable to precisely predict protein elution at high loading and column overloading conditions when pH values of pH \geq 6.0 were used. This included the simulations of the pH gradients at 75 mmol/L Na⁺ with column loadings of \geq 25 mg_{bsAb}/mL_{resin}, where the protein eluted within a pH range of pH 6 to pH 9, and the simulations of the salt gradients at pH \geq 6.3 with column loadings of \geq 50 mg_{bsAb}/mL_{resin}. Analyses of the charge variant distribution of selected experiments showed that the elution of the individual charge variants plays a key role here. The corresponding investigations and results are presented in the following subsections 3.6.1.1 and 3.6.1.2.

3.6.1.1 Charge variants elution during linear salt gradients at pH 8.0 performed under high loading conditions

To investigate the elution behavior of the bsAbY charge variants, linear salt gradient elution experiments at pH 8.0 were performed with column loads of 5 and 75 mg_{bsAb}/mL_{resin} (see Figure 14). Fractions were taken during the experiments to determine the distribution of pre-variants and main variants throughout the elution. For this purpose, the total antibody concentration in the fractions was first determined as described in section 2.2.3. Subsequently, the fractions were analyzed by CEX-HPLC, as described in section 2.2.1.2, to determine the species and proportions of the bsAbY charge variants in each fraction. Therefore, the charge variants of bsAbY were subdivided and classified into pre-variants and main variants, as shown in Figure 1B. With the determined antibody concentrations and the determined proportions of pre-variants and main variants, the concentrations of the pre-variants and the main variants in the individual fractions could then be determined. The

determined elution profiles of the bsAbY charge variants and corresponding simulations of the salt gradient elution experiments at pH 8 are shown in Figure 14. Figure 14A/C demonstrates that the pre-variants are well separated from the other charge variants of bsAbY when a column load of $5 \text{ mg}_{\text{bsAb}}/\text{mL}_{\text{resin}}$ was used. The pre-variants make up most of the observed frontal peak shoulder at lower column loads. The main elution peak is dominated by the main variant species. When using the total amount of bsAbY for simulation, the simulated peak is slightly too high compared to the main elution peak of bsAbY (see Figure 14A). If the amount of the pre-variants is subtracted from the total column loading, the elution peak of the main variants is well described by the simulation (see Figure 14C) using the determined mean value $\bar{\sigma}_i$ for pH 8.0 listed in Table 21.

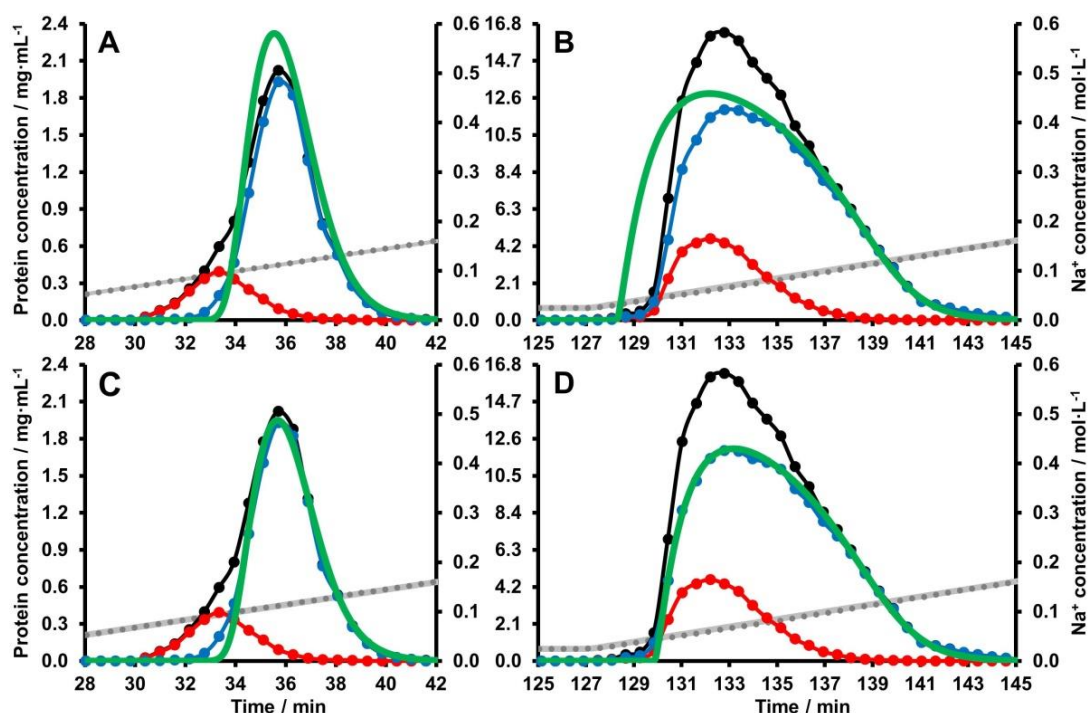


Figure 14. Elution of bsAbY charge variants in linear salt gradients at pH 8.0. The experiments were performed at column loads of $5 \text{ mg}_{\text{bsAb}}/\text{mL}_{\text{resin}}$ (A/C) and $75 \text{ mg}_{\text{bsAb}}/\text{mL}_{\text{resin}}$ (B/D). The sample bsAbY was divided into two charge variant species that were subdivided and classified as shown in Figure 1. In the displayed chromatograms, the connected dots represent the concentration of the total bsAb (black), the concentrations of the pre-variant species (red) and of the main variant species (blue). The green line represents simulated data. In (A) and (B), the elution of the complete bsAbY was predicted. In (C) and (D), the elution of the bsAb without the amount of pre-variant species was predicted. The gray data represents the experimental (dots) and simulated (lines) salt gradients (0.025 to 0.500 mol/L Na^+). For the simulations, the determined mean value $\bar{\sigma}_i$ for pH 8.0 with a value of 120.13 (see Table 21) was used. Figure 14 is already shown in an identical form in the publication Seelinger et al.² (Part 2, 2022).

At a column load of $75 \text{ mg}_{\text{bsAb}}/\text{mL}_{\text{resin}}$, the pre-variants co-elute with the main variants (see Figure 14B/D). Due to this overlapping, the shape of the main elution peak is no longer dominated by the main variants only but is influenced by all charge variants, resulting in a tall and narrow peak. When $\bar{\sigma}_i$ for pH 8.0 with a value of 120.13 (see Table 21) and the total amount of bsAbY is used for simulation, the tip of the simulated peak is much too low and the front of the simulated peak elutes too early compared to the experimental main elution peak of bsAbY (see Figure 14B). Interestingly, if the mass of pre-variants is subtracted from the total column load, the elution peak of the main variants is again well described by the simulation by using a $\bar{\sigma}_i$ of 120.13 for pH 8.0 (see Figure 14D). This shows that the applied model-based approach can describe the elution of the main variants very well, if only the mass of the main variants is used for the simulation, regardless of the loading.

3.6.1.2 Charge variants elution during linear pH gradients at 75 mmol/L Na^+ performed under high loading and overloading conditions

For the linear pH gradient elution experiments with fixed Na^+ concentrations of 75 mmol/L , where the protein eluted within a pH range of approximately pH 6 to pH 9, discrepancies in the description of the peak shapes were observed under high loading and column overloading conditions ($\geq 25 \text{ mg}_{\text{bsAb}}/\text{mL}_{\text{resin}}$). As already shown in Figure 12, single-component simulations of these runs using the pH-dependent SMA model are compared with the experimentally determined bsAb concentration curves in Figure 15. Thereby, it can be seen, that the experimental peaks (black dots) at column loadings of 25 and $50 \text{ mg}_{\text{bsAb}}/\text{mL}_{\text{resin}}$ have an asymmetric shape, with peak fronting and with maxima on the right side. The single-component simulations (green lines, Figure 15) differ in shape and predict the maxima on the left side. At column loadings of 75 and $90 \text{ mg}_{\text{bsAb}}/\text{mL}_{\text{resin}}$, sample breakthrough is observed and the main part of the protein elutes as clear double-peaks. When the amount of protein in the breakthrough and the pre-peaks was subtracted from the mass of protein used in the simulation, the single-component simulation (green line, Figure 15) could predict the elution of the main elution peaks quite well. The single-component simulation was even capable of predicting the double-peak formation. However, the maxima of the simulated double peaks are on the left side, while the experimental elution profiles each show a maximum on the right side.

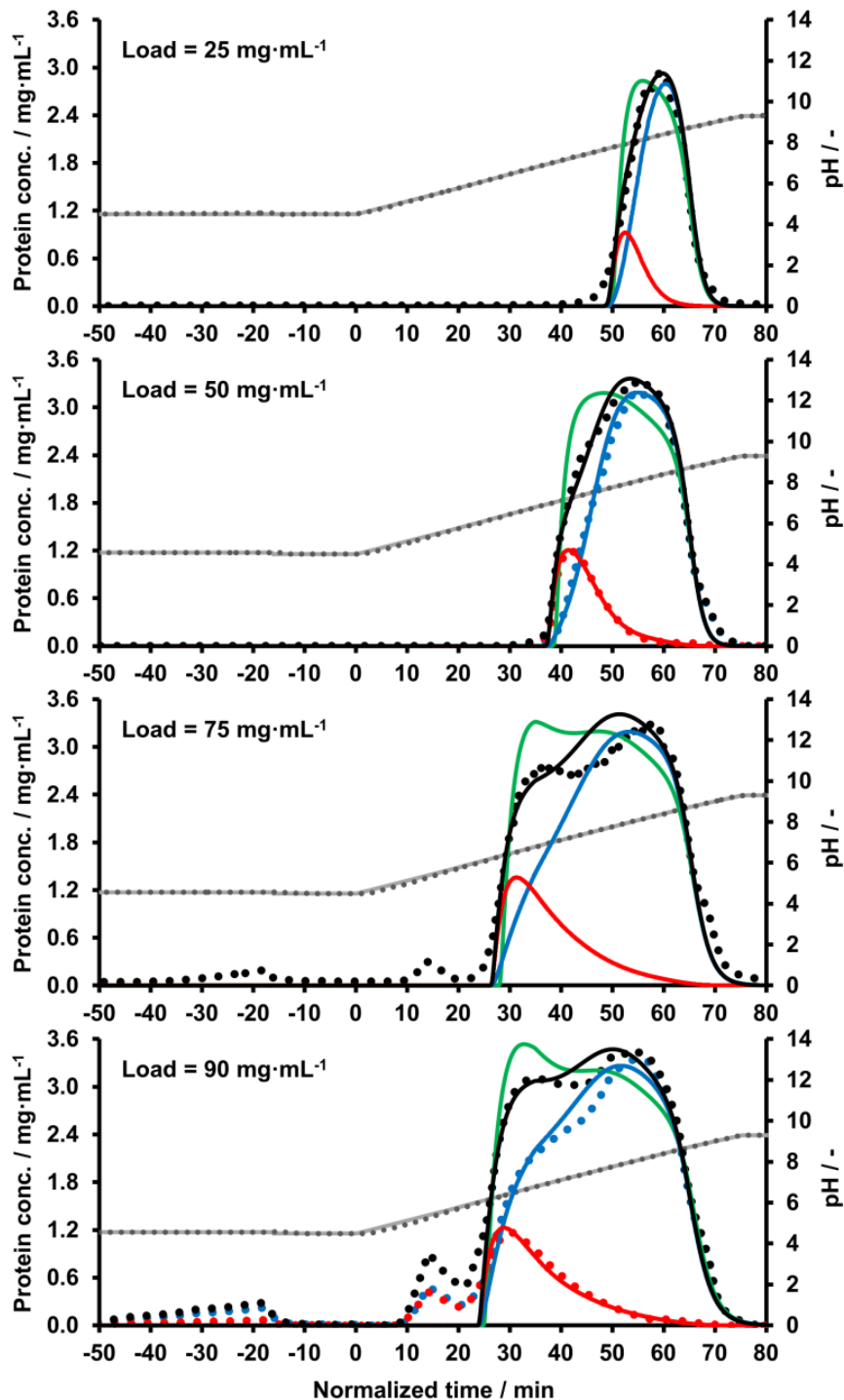


Figure 15 Comparison between single- and multi-component simulations of the pH gradient runs at 75 mmol/L Na^+ performed under high loading and overloading conditions using the sample bsAbY. The experimentally determined concentration curves of the total bsAb (black dots), the pre-variant species (red dots) and the main variant species (blue dots) are presented as overlays. For the runs with a loading of 25 and 75 $\text{mg}_{\text{bsAb}}/\text{mL}_{\text{resin}}$, no concentration curves of the pre-variants and the main variants were experimentally determined. The simulated concentration curves of the total bsAb predicted with the single-component simulation are represented by green lines. The simulated concentration curves predicted with the multi-component simulation of the total bsAb (black lines), the pre-variant species (red lines) and the main variant species (blue lines) are also presented as overlays. The grey data represents the

experimental (dots) and simulated (lines) pH gradients (pH 4.5 to 9.3). For the simulations, the pH-dependent SMA model with the pH-dependent shielding factor σ_i was used (see section 3.5.2, equation (40)). The time in minutes is normalized to the gradient start. Figure 15 is already shown in an identical form in the publication Seelinger et al.² (Part 2, 2022).

Like for the salt gradient elution's at $\text{pH} \geq 6.3$, it is reasonable to assume that multi-component elution plays an essential role here, especially on the shaping of the elution peaks. Therefore, the elution of the pre-variants and the main variants during the linear pH gradients was investigated for the runs with column loadings of 50 and 90 $\text{mg}_{\text{bsAb}}/\text{mL}_{\text{resin}}$. The elution curves of the pre-variants and main variants were determined by quantitative analysis (see section 2.2.3) and by analytical CEX-HPLC (see section 2.2.1.2), as already described in detail in section 3.6.1.1. As shown in Figure 15, the pre-variants and the main variants are well separated, and even at overloading conditions, there is no complete overlap as seen in the salt gradient at pH 8 and 75 $\text{mg}_{\text{bsAb}}/\text{mL}_{\text{resin}}$ (Figure 14B/D). For the pH gradients at 75 mmol/L Na^+ , the pre-variants always elute predominantly before the main variants and play a crucial role in the position of the double peak maxima at overloading conditions (see the runs with loadings of 75 and 90 $\text{mg}_{\text{bsAb}}/\text{mL}_{\text{resin}}$ shown in Figure 15).

Subsequently, a multi-component simulation with two bsAb species was applied to predict the elution of the pre-variants and main variants (see Figure 15). The pH-dependent v_i and σ_i correlations calculated by equation (6) and equation (40), respectively, were used for these multi-component simulations. To obtain individual pH-dependent values for the pre-variants and main variants, the pH-dependent v_i and σ_i values were modified by empirical species-specific factors. Therefore v_i and σ_i were simply multiplied by these factors. By fitting of the individual charge variant elution profiles at 50 and 90 $\text{mg}_{\text{bsAb}}/\text{mL}_{\text{resin}}$, a factor of 2.0 for σ_{PV} and of 0.98 for v_{PV} was determined for the pre-variants. For the main variants, a factor for σ_{MV} of 0.8 and a factor for v_{MV} of 1.00 were estimated. As can be seen in Figure 15, the multi-component simulations computed with these values led to very good descriptions of the individual elution profiles of the pre-variants (red dots and lines) and main variants (blue dots and lines). For all column loadings from 25 to 90 $\text{mg}_{\text{bsAb}}/\text{mL}_{\text{resin}}$, the agreement between the experimental bsAbY elution profiles (black dots) and the bsAbY elution profiles calculated by the multi-component simulation (black lines) was excellent. While the single-component simulation (green lines) can already predict

the double-peak formation, the description of the elution profiles of the total bsAb is significantly improved by the multi-component simulation (black lines). The maxima of the multi-component simulation correctly match the maxima of the experimental elution profiles (see Figure 15).

3.6.2 High loading and column overloading phenomena at $\text{pH} \leq 5.3$

Parts of section 3.6.2, including the subsections 3.6.2.1, 3.6.2.2, and 3.6.2.3, have already been published in a similar or identical form in Seelinger et al.² (Part 2, 2022). Some of the data shown in section 3.6.2 are also published in Seelinger et al.¹ (Part 1, 2022).

In section 3.5.1, it was shown that complex elution behavior like peak fronting, peak shoulders, additional peaks, and unexpected sample breakthrough was seen at $\text{pH} \leq 5.3$. These overloading phenomena are even more pronounced at $\text{pH} 4.5$ than at $\text{pH} 5.3$. These overloading effects occurred primarily at high column loadings of $\geq 50 \text{ mg}_{\text{bsAb}}/\text{mL}_{\text{resin}}$ ($\geq 75 \text{ mg}_{\text{bsAb}}/\text{mL}_{\text{resin}}$ at $\text{pH} 5.3$), and these effects became stronger with increasing column loading.

In Figure 16, the linear salt gradient elution experiments performed at $\text{pH} 4.5$ with loadings ranging from 5 to $90 \text{ mg}_{\text{bsAb}}/\text{mL}_{\text{resin}}$ are compared with the respective single-component simulations.

Figure 16 shows that up to a loading of $50 \text{ mg}_{\text{bsAb}}/\text{mL}_{\text{resin}}$, the experimental elution profiles are well predicted by the applied model. At column loadings of 75 and $90 \text{ mg}_{\text{bsAb}}/\text{mL}_{\text{resin}}$, peak fronting, peak shoulders, additional peaks at the gradient start, and breakthrough during sample loading are observed. The model cannot predict these peak shapes, pre-peaks, and breakthroughs, which occurred at $\geq 75 \text{ mg}_{\text{bsAb}}/\text{mL}_{\text{resin}}$, but calculates the expected trapezoidal-shaped peaks for a single-component Langmuirian-type adsorption isotherm.²

Fractions were taken from these experiments and analyzed by CEX-HPLC. The analyses revealed that the distribution and proportions of charge variants in the fractions from the breakthroughs, pre-peaks, and peak shoulders compare very well with the analyzed bsAbY sample used for loading (data not shown). Thus, separation of charge variants due to competitive binding and displacement effects¹¹⁶ can be excluded as a reason for the described overloading effects.

In the following, it was investigated whether different Na^+ concentrations during sample loading and different flow rates used for sample loading influence the binding

and elution behavior of bsAbY. The results are presented in the subsequent subsections 3.6.2.1, 3.6.2.2, and 3.6.2.3.

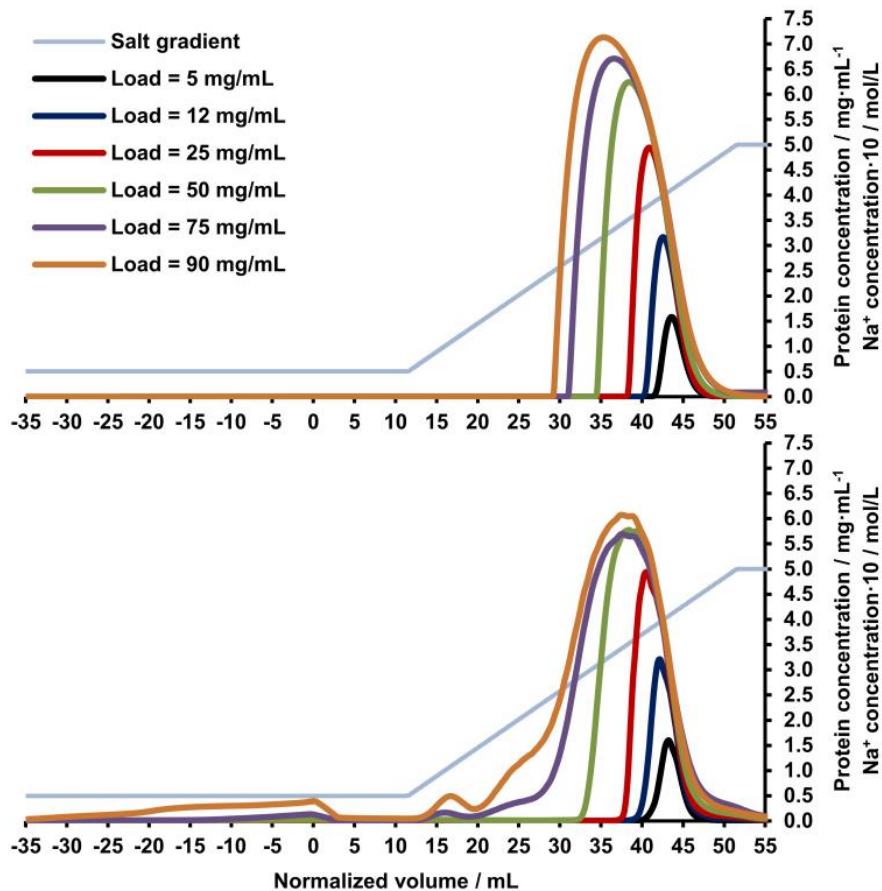


Figure 16. Comparison between experimental and simulated data from the salt gradient runs at pH 4.5 performed with increasing loadings from 5 to 90 $\text{mg}_{\text{bsAb}}/\text{mL}_{\text{resin}}$ using sample bsAbY. The upper overlay chromatogram shows the simulated data, while the lower overlay chromatogram shows the experimental data. In all experiments, the sample was loaded onto the column at a feed concentration of 1 mg/mL . The different column loads were achieved by changing the load volume. The volume in milliliters is normalized to the end of the sample loading. This figure is already shown in an identical form in the publication Seelinger et al.² (Part 2, 2022).

3.6.2.1 Influence of different Na^+ concentrations during loading on the sample breakthrough

To investigate the influence of different Na^+ concentrations during loading on the sample breakthrough, experiments were performed where 75 mg of bsAbY were loaded onto the 1 mL column at pH 4.5 in the presence of 14.3, 50.0, 120.0, 200.0, or 250.0 mmol/L Na^+ .

In this section, only the load phase will be considered. The corresponding gradient elutions will be discussed in the following section 3.6.2.2.

Loading up to 50 mg bsAb onto the 1 mL column showed no significant breakthrough with Na^+ concentrations of ≥ 50.0 mmol/L (see Figure 17). When the bsAb was injected with 14.3 mmol/L Na^+ , breakthrough is visible from the beginning and markedly increases after 50 mg bsAb were loaded onto the column. The onset of breakthrough starts later with increasing Na^+ concentration with an optimum between 120.0 mmol/L and 200.0 mmol/L Na^+ . A further increase to 250.0 mmol/L Na^+ lowers the dynamic binding capacity (DBC).

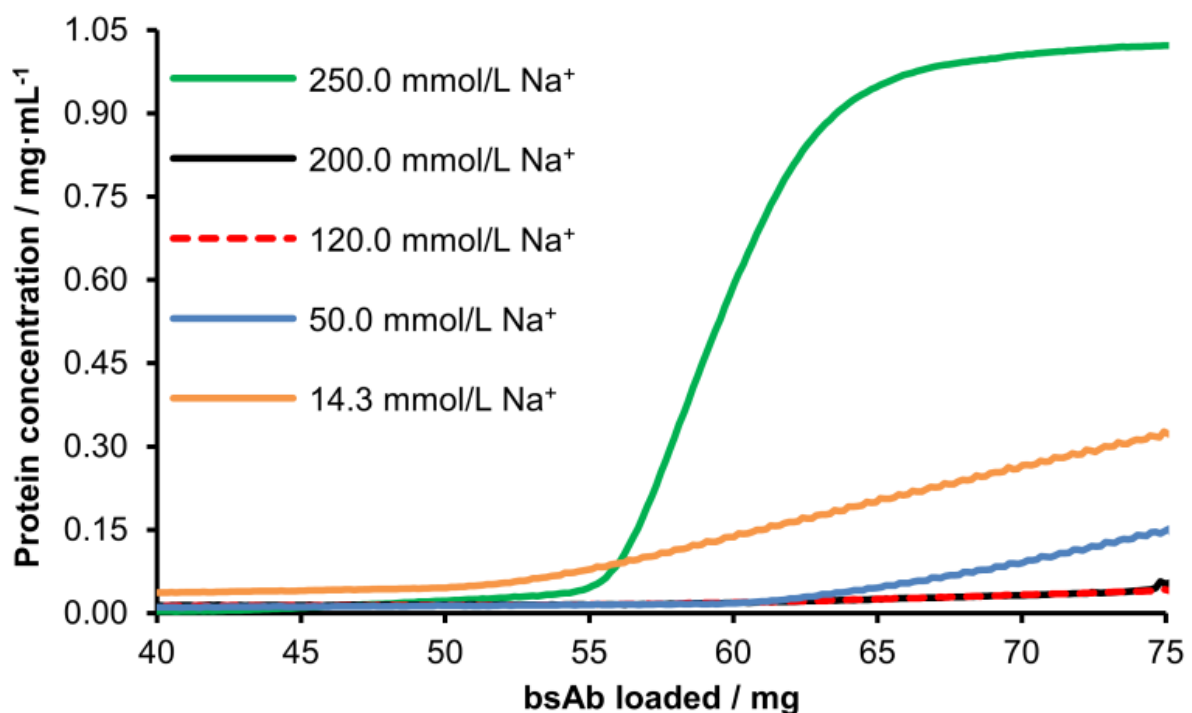


Figure 17. Overlay plot of different sample loadings performed at different Na^+ concentrations using sample bsAbY. 75 mg of bsAbY were loaded onto the 1 mL column at pH 4.5 with 14.3, 50.0, 120.0, 200.0, and 250.0 mmol/L Na^+ . The lines represent the protein concentrations. The solid black line is almost completely covered by the dashed red line, showing that the protein binds equally well at 120 and 200 mmol/L Na^+ . This figure is already shown in an identical form in the publication Seelinger et al.² (Part 2, 2022).

3.6.2.2 Influence of different Na^+ concentrations during loading on the gradient elution

In this section, it will be clarified to what extent different Na^+ concentrations during sample loading affect the elution profiles. Therefore, linear salt gradient elution

experiments at pH 4.5 with column loadings of 25, 50, and 75 mg_{bsAb}/mL_{resin} were performed where the sample was loaded onto the column with 14.3, 50.0, 120.0, 200.0, or 250.0 mmol/L Na⁺. The wash and elution steps are identical for all the runs and allow a direct comparison of the LGE chromatograms. After sample loading, the column was always washed with 50 mmol/L Na⁺ at pH 4.5 for 10 CV, and the sample was eluted with a 40 CV linear gradient from 50 to 500 mmol/L Na⁺. The gradient elution runs conducted at 75 mg_{bsAb}/mL_{resin} correspond to the respective breakthrough curves shown in Figure 17.

In Figure 18, the experimentally determined elution profiles from all these experiments are compared individually with simulated elution profiles. For the simulations, the mean value $\bar{\sigma}_i$ for pH 4.5 and the respective $k_{eff,i}$ values listed in Table 21 were used.

The experimental elution profiles of the runs with a load of 25 mg bsAbY and with ≥ 50.0 mmol/L Na⁺ are all nearly identical and are well predicted by the model (see A.2-5 in Figure 18). When the sample was loaded with 14.3 mmol/L Na⁺, the separation of a peak that elutes after the main peak is visible. This later eluting peak resulted in a main elution peak that is about 13 % smaller in area than the main peak predicted by the simulation. Analysis by SE-HPLC revealed that this later eluting peak is composed of monomeric variants and not dimers/multimers (data not shown). At a loading of 50 mg_{bsAb}/mL_{resin}, the broadest elution peak was obtained when the sample was injected with 50 mmol/L Na⁺. Compared to the elution peaks for the 120 to 250 mmol/L Na⁺ loadings, a narrow but relatively high peak shoulder on the front side of the peak is observed. The simulation predicts the peak profiles well with minor discrepancies for the peak-shoulders (see B.2-5 in Figure 18).

Loading 50 mg bsAbY sample in the presence of 14.3 mmol/L Na⁺ resulted in an increased level of later eluting monomeric variants with a proportion of ~ 17 %. The main elution peak is well described by the single-component simulation. However, the total peak area of the simulated peak is too large because the mass of later eluting variants was not subtracted from the sample load (B.1 Figure 18).

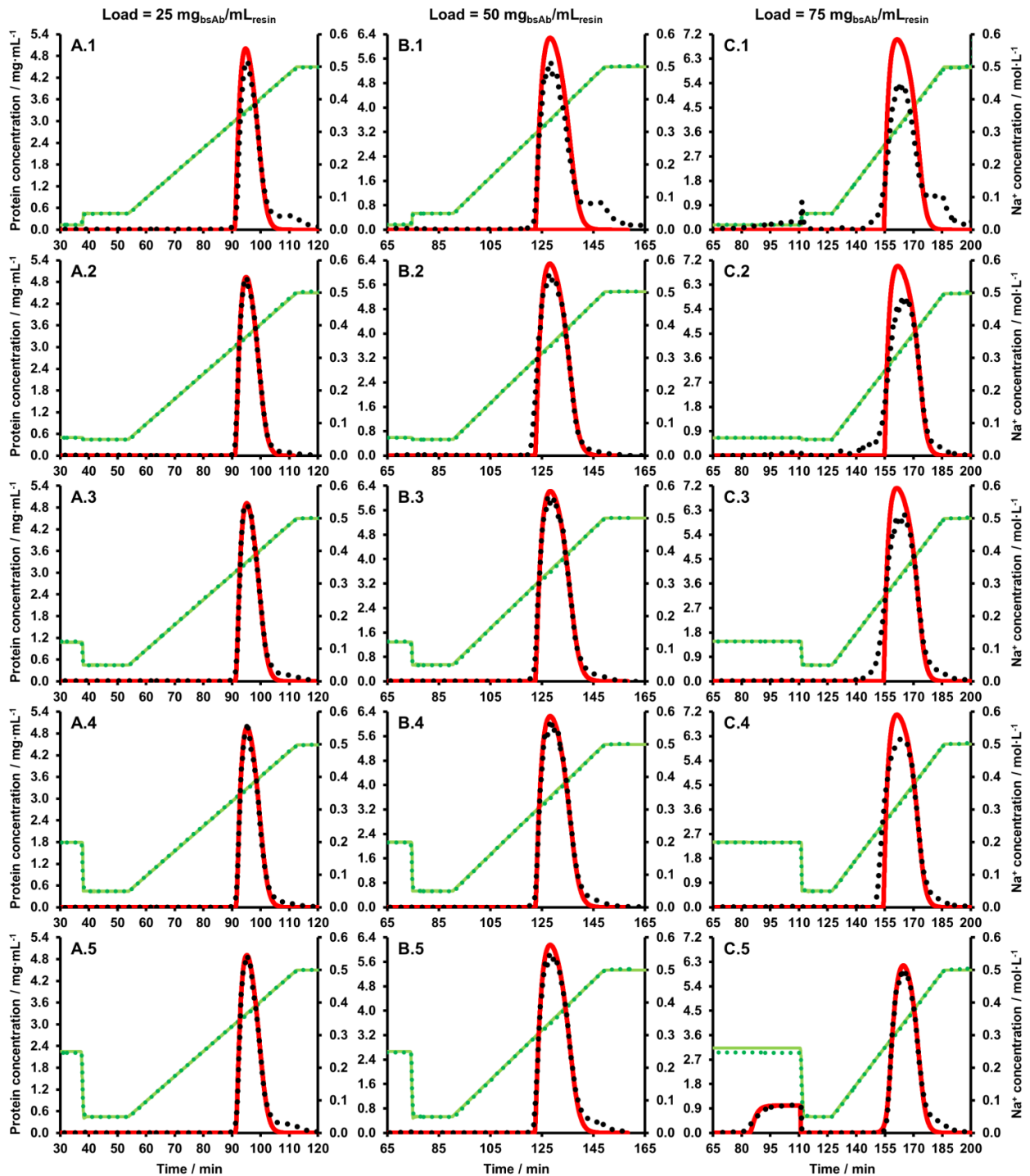


Figure 18. Comparison between experimental and simulated data of the salt gradient runs performed at pH 4.5 where the sample bsAbY was injected at different Na^+ concentrations. The sample bsAbY was injected with 14.3 mmol/L Na^+ using column loadings of 25 (A.1), 50 (B.1), and 75 $\text{mg}_{\text{bsAb}}/\text{mL}_{\text{resin}}$ (C.1), with 50 mmol/L Na^+ using column loadings of 25 (A.2), 50 (B.2), and 75 $\text{mg}_{\text{bsAb}}/\text{mL}_{\text{resin}}$ (C.2), with 120 mmol/L Na^+ using column loadings of 25 (A.3), 50 (B.3), and 75 $\text{mg}_{\text{bsAb}}/\text{mL}_{\text{resin}}$ (C.3), with 200 mmol/L Na^+ using column loadings of 25 (A.4), 50 (B.4) and 75 $\text{mg}_{\text{bsAb}}/\text{mL}_{\text{resin}}$ (C.4), and with 250 mmol/L Na^+ using column loadings of 25 (A.5), 50 (B.5), and 75 $\text{mg}_{\text{bsAb}}/\text{mL}_{\text{resin}}$ (C.5). The experimental and simulated salt gradients are represented by green dots and lines, respectively. The experimental and simulated bsAb concentrations are represented by black dots and red lines, respectively. For the simulations, the mean value $\bar{\sigma}_i$

for pH 4.5 and the respective $k_{eff,i}$ values listed in Table 21 were used. Figure 18 is already shown in an identical form in the publication Seelinger et al.² (Part 2, 2022).

At a column loading of 75 mg_{bsAb}/mL_{resin}, significant differences can be seen between the individual elution profiles (see C.1-5 in Figure 18). Breakthrough during sample loading occurred in all cases, as mentioned in section 3.6.2.1. When the sample was injected with ≤ 50 mmol/L Na⁺, an additional peak at the gradient start and a strong peak shoulder in front of the main elution peak are recognizable. When the Na⁺ concentration was increased to 120 mmol/L Na⁺ during injection, the peak at the gradient start disappeared, and the peak shoulder at the peak front became much smaller and almost disappeared with 200 mmol/L Na⁺ during loading. When the sample was loaded with 250 mmol/L Na⁺, strong sample breakthrough is seen. No additional peak or peak shoulder can be recognized, and the main elution peak is comparable to the peaks from the experiments with a load of 50 mg_{bsAb}/mL_{resin}. After a minor correction of the sample Na⁺ concentration in the simulation from 250 to 261 mmol/L Na⁺, the model was able to describe the complete elution profile very well. Both the breakthrough and the main peak were described with good agreement (see Figure 18C.5).

For the simulations with ≤ 200 mmol/L Na⁺ used for sample loading (see C.1-4 in Figure 18), the simulated peaks are too high compared to the experimental main peaks because a part of the protein could not bind or eluted as pre-peaks, peak shoulders, and post-peaks.

When 75 mg bsAbY were loaded onto the 1 mL column with 14.3 mmol/L Na⁺ (see C.1 in Figure 18), the experimental main peak is significantly smaller compared to the simulated peak. The retention of the main elution peak is well predicted by the simulation. However, the area of the simulated main peak is too large because the mass of later eluting variants with a proportion of about 20 % and protein in the breakthrough was not subtracted from the sample load used for simulation.

To get a better description of the runs, where a Na⁺ concentration of 14.3 mmol/L was used for loading, the later eluting variants are considered as an additional monomeric species. Therefore, *in silico* chromatogram simulations were performed using the corresponding runs with loadings of 25, 50 and 75 mg_{bsAb}/mL_{resin} (see Figure 19). Compared to the main peak variant, the same σ_i value and a 1.23-fold higher v_i value were used for the later eluting variants. By subtracting the amount of

protein in the breakthrough from the set load, the elution profiles could be well predicted (see Figure 19). In particular, the main elution peaks are now described with good agreement.

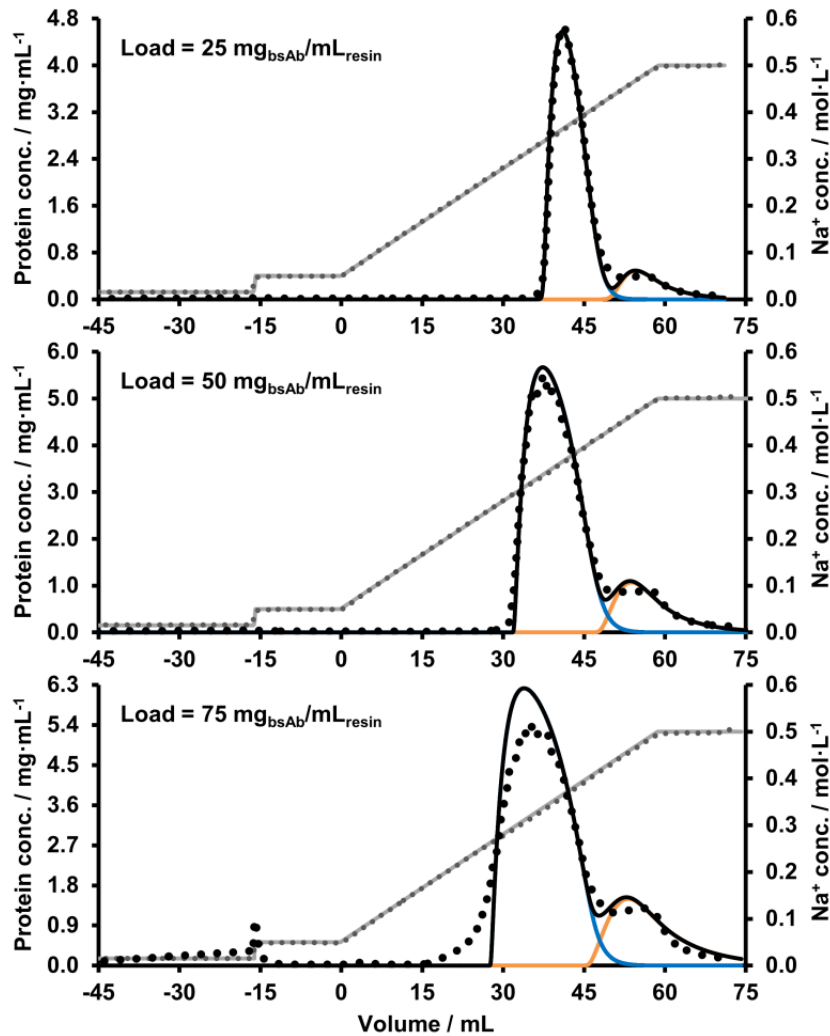


Figure 19. Multi-component simulations of the linear salt gradient runs at pH 4.5 where the sample bsAbY was injected with 14.3 mmol/L Na⁺. Experimental data are represented by dots whereby gray stands for the salt gradients and black for the total bsAbY concentration. The simulated salt gradients are represented by gray lines. The simulated protein concentration curves are represented by black lines for the total bsAbY, blue lines for the main peak and orange lines for the post-peak. For the later eluting variants, $k_{eff,i}$ values of $2.80 \cdot 10^{-6}$, $2.30 \cdot 10^{-6}$ and $1.74 \cdot 10^{-6}$ cm/s for the runs with column loads of 25, 50 and 75 mg_{bsAb}/mL_{resin} respectively were used. As the loading increased, the proportion of later eluting variants increased, with proportions of 13 %, 17 %, and 20 % used for the simulations at loads of 25, 50, and 75 mg_{bsAb}/mL_{resin}, respectively. This figure is already shown in an identical form in the publication Seelinger et al.² (Part 2, 2022).

3.6.2.3 Influence of different flow rates (loading times) during loading on the sample breakthrough and gradient elution

In this section, it will be shown to what extent binding and elution at pH 4.5 are affected by changes in the loading time t_{load} when the Na^+ concentration remains at 50 mmol/L. Therefore, in contrast to the standard loading at 0.68 mL/min ($t_{load} = 110.3$ min), additional experiments with loadings of 75 $\text{mg}_{\text{bsAb}}/\text{mL}_{\text{resin}}$, where the sample was injected at 1.36 mL/min ($t_{load} = 55.2$ min), and at 0.34 mL/min ($t_{load} = 220.6$ min) were performed. The resulted chromatograms are shown in Figure 20.

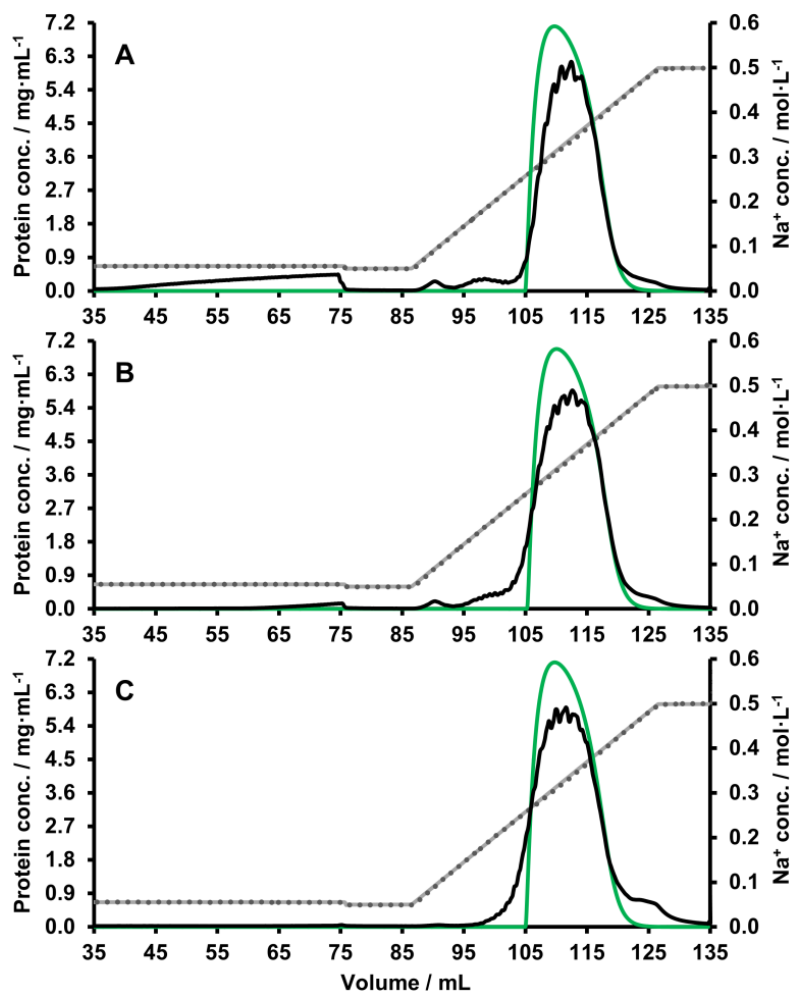


Figure 20. Comparison of salt gradient experiments performed at pH 4.5, where the sample bsAbY was injected at 50 mmol/L Na^+ with three different flow rates. The sample was injected at a flow rate of 1.36 mL/min (A), 0.68 mL/min (B), and 0.34 mL/min (C). The gray dots represent the experimental salt gradients (50 to 500 mmol/L Na^+), the gray lines represent the simulated salt gradients, the black lines represent the experimental bsAb concentrations and the green lines represent the simulated bsAb concentrations. This figure is already shown in a very similar form in the publication Seelinger et al.² (Part 2, 2022).

By doubling the flow rate used for loading to 1.36 mL/min (see Figure 20A), sample breakthrough is significantly higher. Although less sample is bound as a result, the pre-peak at the gradient start is quite pronounced. Instead of the peak shoulder, a second well-defined peak before the main elution peak is visible. Analysis by high-resolution CEX-HPLC showed that no charge variants are separated in these pre-peaks (data not shown). Interestingly, the main elution peak is as high as the other two main elution peaks (see Figure 20B/C), but it is narrower than the other two.

When the flow rate used for loading is halved to 0.34 mL/min (see Figure 20C), almost no breakthrough is observed. By doubling the loading time, the protein shows a better binding resulting in an increased DBC. The pre-peak and pre-shoulder are much less pronounced, the main elution peak is slightly larger, while many more later eluting proteins were formed. Analysis by SE-HPLC showed that the later eluting proteins are monomeric (data not shown). The increased amount of protein in the main elution peak did not cause the main elution peak to become taller, but only caused it to become broader. This also explains why the simulation does not describe the tip of the peak correctly.

Conclusively, it can be summarized that a higher flow rate leads to more breakthrough and leads to the formation of pre-peaks. On the other hand, a lower flow rate during loading massively reduces the breakthrough, leads to a significant reduction of the pre-peaks, whereas a clearly visible post-peak is formed.

3.7 Modeling the binding and elution behavior of bsAbX under high loading and overloading conditions using the Self-Association-SMA (SAS-SMA) model

3.7.1 Determination of non-linear model parameters under high loading and overloading conditions

Parts of section 3.7.1, including the subsections 3.7.1.1, 3.7.1.2, and 3.7.1.3, are also included in a similar or identical form in Seelinger et al.³ (DRAFT (submitted)).

In this work, a modified SAS-SMA model extended with an activity coefficient for the salt in solution γ_1 and a pH-dependent asymmetric activity coefficient for the protein in solution $\tilde{\gamma}_i$ was used. Thereby, the model contained three pH-dependent non-linear model parameters: The pH-dependent parameter $K_{p,i}$, which describes the pH-dependence of $\tilde{\gamma}_i$, the pH-dependent equilibrium constant of the dimerization process $K_{eq,2,i}/c$ and the pH-dependent shielding factor σ_i . The correct estimation of these

non-linear model parameters was essential to describe the binding and elution behavior of the sample bsAbX under high loading and overloading conditions. Therefore, the pH-dependent model parameters $K_{p,i}$, $K_{eq,2,i}/c$, and σ_i were simultaneously estimated, as described in section 2.2.5. The results are shown in the following section.

3.7.1.1 Determination of $K_{p,i}$, $K_{eq,2,i}/c$, σ_i and $k_{eff,i}$ values under high loading conditions

Linear salt gradient elution experiments at fixed pH performed under column loadings of 5 to 50 mg_{bsAb}/mL_{resin} were used to determine the non-linear model parameters. The salt gradients with loadings of 75 and 90 mg_{bsAb}/mL_{resin} were not used for determination of $K_{p,i}$, $K_{eq,2,i}/c$, and σ_i because overloading effects such as pre-shoulder formation could have distorted the values of the determined model parameters. The pH-dependent model parameters $K_{p,i}$, $K_{eq,2,i}/c$, σ_i , as well as the lumped parameter $k_{eff,i}$ were determined as described in section 2.2.5. The estimated values and corresponding standard deviations for $K_{p,i}$, $K_{eq,2,i}/c$, σ_i and $k_{eff,i}$ are listed in Table 23.

As can be seen in Table 23, for each linear salt gradient, different $k_{eff,i}$ values were determined for each loading. Both the determined $K_{p,i}$ and $K_{eq,2,i}/c$ values decrease with increasing pH. The evaluation of the pH-dependences of $K_{p,i}$ and $K_{eq,2,i}/c$ is shown in section 3.7.1.2. The determined σ_i values increase with increasing pH. The evaluation of the pH-dependence of σ_i is shown in section 3.7.1.3.

The chromatogram simulations of the runs performed at pH 4.5 and pH 6.3 are shown in Figure 21 and in Figure 22, respectively, which are presented as examples in this section.

The experimental and the corresponding simulated chromatograms shown for pH 4.5 are comparable to the corresponding chromatograms for pH 5.3. The experimental and simulated chromatograms for pH 5.3 are shown in Figure 35 in the figure appendix (see section 8). Similarly, the results shown for pH 6.3 are representative of the chromatograms for pH 7.0. The experimental and simulated chromatograms for the salt gradients at pH 7.0 are shown in Figure 36 in the figure appendix (see section 8).

Table 23: Determined SAS-SMA model parameters and $k_{eff,i}$ values for high loading conditions for sample bsAbX

pH / -	Batch Nr.	Load / mg·mL ⁻¹	Individually determined values			Globally determined values				Mean values	
			pH / - / ^{a)}	v_i / -	$k_{eff,i}$ / cm·s ⁻¹	$\frac{K_{eq,2,i}}{c}$ / -	$K_{p,i}$ / L·mol ⁻¹	σ_i / -	$q_{max,i}$ / mol·L ⁻¹	pH / - / ^{a)}	v_i / - / ^{d)}
4.5	3	5	4.49	18.14	$2.36 \cdot 10^{-5}$ $\pm 2.55 \cdot 10^{-7}$	42898 ± 2098	20841 \pm 1118	11.06 ± 0.40	$9.24 \cdot 10^{-3}$ $\pm 5.15 \cdot 10^{-5}$	4.49 ± 0.02 / ^{c)}	18.15 ± 0.16 / ^{d)}
	3	12	4.49	18.14	$2.85 \cdot 10^{-5}$ $\pm 1.17 \cdot 10^{-7}$						
	3	25	4.49	18.14	$2.26 \cdot 10^{-5}$ $\pm 2.36 \cdot 10^{-7}$						
	2	25	4.47	18.32	$2.25 \cdot 10^{-5}$ $\pm 1.54 \cdot 10^{-7}$						
	3	50	4.52	17.83	$6.03 \cdot 10^{-6}$ $\pm 4.59 \cdot 10^{-8}$						
	2	50	4.47	18.32	$6.10 \cdot 10^{-6}$ $\pm 5.38 \cdot 10^{-8}$						
	3	75	4.52	17.83	$2.30 \cdot 10^{-6}$ / ^{b)}						
	3	90	4.52	17.83	$1.65 \cdot 10^{-6}$ / ^{b)}						
5.3	3	5	5.26	12.46	$2.33 \cdot 10^{-5}$ $\pm 1.95 \cdot 10^{-7}$	19820 ± 369	9745 ± 269	18.23 ± 0.23	$8.80 \cdot 10^{-3}$ $\pm 1.12 \cdot 10^{-5}$	5.27 ± 0.01 / ^{c)}	12.43 ± 0.04 / ^{d)}
	3	12	5.26	12.46	$2.50 \cdot 10^{-5}$ $\pm 3.19 \cdot 10^{-7}$						
	3	25	5.26	12.46	$2.07 \cdot 10^{-5}$ $\pm 8.75 \cdot 10^{-8}$						
	2	25	5.28	12.38	$2.04 \cdot 10^{-5}$ $\pm 1.35 \cdot 10^{-7}$						
	2	50	5.28	12.38	$8.59 \cdot 10^{-6}$ $\pm 4.72 \cdot 10^{-8}$						
	3	75	5.26	12.46	$5.20 \cdot 10^{-6}$ / ^{b)}						
	2	90	5.28	12.38	$5.00 \cdot 10^{-6}$ / ^{b)}						
6.3	3	5	6.23	9.14	$2.39 \cdot 10^{-5}$ $\pm 3.91 \cdot 10^{-8}$	11277 ± 237	5140 ± 149	23.50 ± 0.17	$8.26 \cdot 10^{-3}$ $\pm 8.41 \cdot 10^{-6}$	6.22 ± 0.01 / ^{c)}	9.16 ± 0.03 / ^{d)}
	3	12	6.23	9.14	$2.66 \cdot 10^{-5}$ $\pm 4.77 \cdot 10^{-8}$						
	3	25	6.23	9.14	$2.31 \cdot 10^{-5}$ $\pm 2.97 \cdot 10^{-8}$						
	2	25	6.20	9.21	$1.55 \cdot 10^{-5}$ $\pm 8.13 \cdot 10^{-8}$						
	2	50	6.20	9.21	$8.41 \cdot 10^{-6}$ $\pm 3.84 \cdot 10^{-8}$						
	3	75	6.23	9.14	$7.45 \cdot 10^{-6}$ / ^{b)}						
7.0	3	5	6.91	7.63	$2.45 \cdot 10^{-5}$ $\pm 1.45 \cdot 10^{-7}$	7684 ± 206	3962 ± 146	26.69 ± 0.06	$7.86 \cdot 10^{-3}$ $\pm 2.48 \cdot 10^{-6}$	6.91 ± 0.00 / ^{c)}	7.64 ± 0.01 / ^{d)}
	3	12	6.91	7.63	$2.36 \cdot 10^{-5}$ $\pm 1.99 \cdot 10^{-7}$						
	3	25	6.90	7.65	$2.76 \cdot 10^{-5}$ $\pm 2.51 \cdot 10^{-7}$						
	3	50	6.90	7.65	$1.45 \cdot 10^{-5}$ $\pm 1.31 \cdot 10^{-7}$						

a) Corrected pH values. The corrected pH values were determined as described in section 2.2.2.5.2.

b) Estimated using the values for $K_{eq,2,i}/c$, $K_{p,i}$, and σ_i listed in this table, which were determined with the runs at loadings from 5 to 50 mg_{bsAb}/mL_{resin}.

c) Mean value of the corrected pH values from the runs with loadings from 5 to 50 mg_{bsAb}/mL_{resin}.

d) Mean value of the v_i values from the runs with loadings from 5 to 50 mg_{bsAb}/mL_{resin}.

As can be seen in Figure 21, Figure 35, Figure 22 and Figure 36, the elution peaks of the salt gradient runs performed with column loads of 5 to 50 $\text{mg}_{\text{bsAb}}/\text{mL}_{\text{resin}}$ could be precisely described by the SAS-SMA model for all pH values tested. The different types and amounts of dimers/multimers in batch 2 and batch 3 did seemingly not play a role in the determination of the non-linear model parameters $K_{p,i}$, $K_{eq,2,i}/c$, and σ_i . The elution profiles of both batches could be described with very good agreement by the simulation.

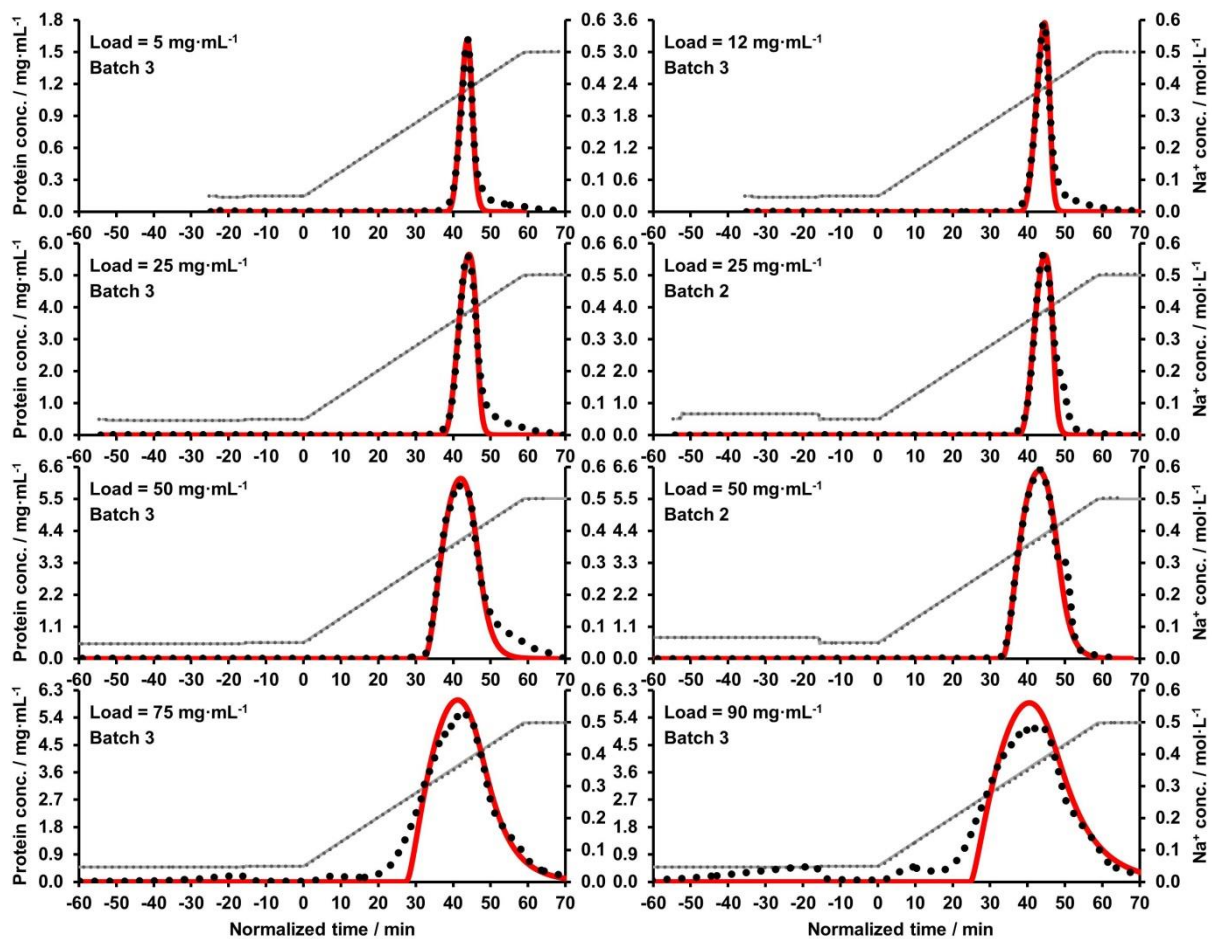


Figure 21. Salt gradient elutions of bsAbX at pH 4.5 used for estimation and verification of the model parameters $K_{p,i}$, $K_{eq,2,i}/c$, σ_i , and $k_{eff,i}$ by applying the SAS-SMA model. The black dots are experimental data and the red lines are simulated data. The time in minutes is normalized to the gradient start. The estimated $K_{p,i}$, $K_{eq,2,i}/c$, σ_i , and $k_{eff,i}$ values are listed in Table 23. Some of the data shown and illustrated in this figure are also included in Seelinger et al.³ (DRAFT (submitted)).

Figure 21 and Figure 35 show that for the linear salt gradients at pH 4.5 and 5.3, respectively, starting at a load of 75 $\text{mg}_{\text{bsAb}}/\text{mL}_{\text{resin}}$, complex high loading and

overloading effects like breakthroughs, pre-peaks and pre-shoulders occurred. These overloading phenomena made estimation of $K_{p,i}$, $K_{eq,2,i}/c$, and σ_i by inverse peak fitting unfeasible because they can lead to deviating and thus falsified values. This was the reason why these runs with loadings of $\geq 75 \text{ mg}_{\text{bsAb}}/\text{mL}_{\text{resin}}$ were excluded for the chromatogram fits for the determination of $K_{p,i}$, $K_{eq,2,i}/c$, and σ_i .

Even if overloading phenomena were not visible at first sight, the run at pH 6.3 with a loading of $75 \text{ mg}_{\text{bsAb}}/\text{mL}_{\text{resin}}$ was also excluded for the determination of $K_{p,i}$, $K_{eq,2,i}/c$, and σ_i (see Figure 22).

By using the estimated $K_{p,i}$, $K_{eq,2,i}/c$, and σ_i values listed in Table 23, only $k_{eff,i}$ was determined for the respective runs with column loadings of $\geq 75 \text{ mg}_{\text{bsAb}}/\text{mL}_{\text{resin}}$.

By subtracting the mass of protein that formed the breakthroughs, pre-peaks and pre-shoulders, the main peaks of the runs conducted at 75 and 90 $\text{mg}_{\text{bsAb}}/\text{mL}_{\text{resin}}$ could be well described at pH 4.5 and 5.3 (see Figure 21 and Figure 35). By using the full load, the entire elution profile at $75 \text{ mg}_{\text{bsAb}}/\text{mL}_{\text{resin}}$ could be very well described at pH 6.3 (see Figure 22).

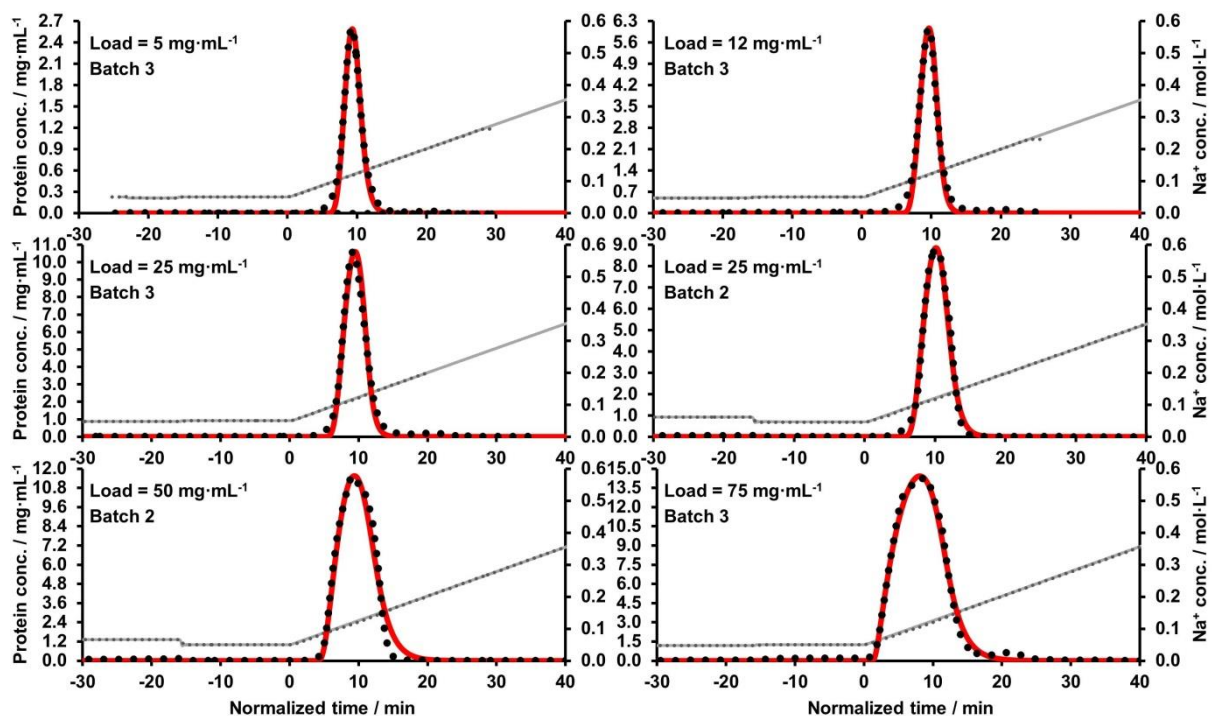


Figure 22. Salt gradient elutions of bsAbX at pH 6.3 used for estimation and verification of the model parameters $K_{p,i}$, $K_{eq,2,i}/c$, σ_i , and $k_{eff,i}$ by applying the SAS-SMA model. The black dots are experimental data and the red lines are simulated data. The time in minutes is normalized to the gradient start. The estimated $K_{p,i}$, $K_{eq,2,i}/c$, σ_i , and $k_{eff,i}$ values are listed in Table 23. Some of the data shown and illustrated in this figure are also included in Seelinger et al.³ (DRAFT (submitted)).

3.7.1.2 Empirical descriptions of the pH-dependence of $K_{p,i}$ and $K_{eq,2,i}/c$

The relevant parameters for description of protein-protein interactions are the pH-dependent parameters $K_{p,i}$ and $K_{eq,2,i}/c$, respectively. As shown in Table 23, both the estimated $K_{p,i}$ and $K_{eq,2,i}/c$ values decrease with increasing pH. As can be seen in Figure 23A, it was found that if both $K_{p,i}$ and $K_{eq,2,i}/c$ are plotted respectively over v_i^2 , then linear correlations are obtained in each case.

By setting the y-intercept of the straight line to zero, the following formula is obtained for $K_{p,i}$:

$$K_{p,i} = K_{p,i}^* \cdot v_i^2 \quad (42)$$

with the constant $K_{p,i}^*$, which corresponds to the slope of the straight line in Figure 23A and thus has a value of 63.243.

Likewise for $K_{eq,2,i}/c$, setting the y-intercept of the straight line to zero gives the following formula:

$$\frac{K_{eq,2,i}}{c} = \frac{K_{eq,2,i}^*}{c} \cdot v_i^2 \quad (43)$$

with the constant $K_{eq,2,i}^*/c$, which corresponds to the slope of the straight line in Figure 23A and thus has a value of 130.130.

By using the equations (42) and (43), the pH-dependence of $K_{p,i}$ and $K_{eq,2,i}/c$ is only described by the pH-dependent binding charge v_i (see equation (6)) and the constants $K_{p,i}^*$ and $K_{eq,2,i}^*/c$, respectively.

The change of $K_{p,i}$ and $K_{eq,2,i}/c$ over pH, calculated by equations (42) and (43), respectively, is shown in Figure 23B. It can be seen that the empirical functions describe the change of the experimental values for $K_{p,i}$ and $K_{eq,2,i}/c$ over their corresponding pH values very well, as shown by the dashed and solid lines for the calculated change of $K_{p,i}$ and $K_{eq,2,i}/c$, respectively.

The equations (42) and (43) were implemented into the SAS-SMA formalism, enabling the model to describe protein-protein interactions in a pH-dependent manner. The positive values for $K_{p,i}$ and $K_{eq,2,i}/c$ calculated with equations (42) and (43) resulted in simulated peaks that become broader and are shifted towards higher retention times. Representative for all high loading runs, this is demonstrated in Figure 24C, with a simulation of the linear salt gradient at pH 5.3 conducted at a

loading of 25 mg_{bsAb}/mL_{resin}. It can be seen, that the simulated peak is positioned on higher retention times compared to the experimental peak due to the calculated $K_{p,i}$ and $K_{eq,2,i}/c$ values, when a shielding factor σ_i of zero is used.

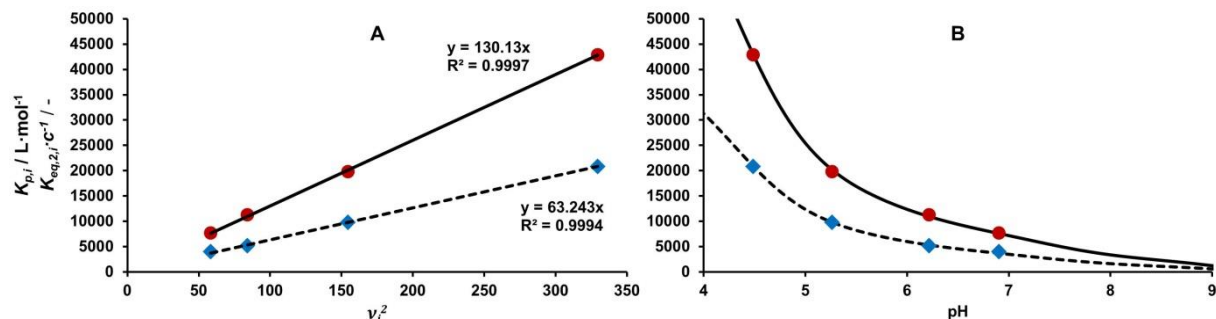


Figure 23. pH-dependence of $K_{p,i}$ and $K_{eq,2,i}/c$. **(A)** $K_{p,i}$ and $K_{eq,2,i}/c$ as functions of v_i^2 . The blue square data points represent the estimated $K_{p,i}$ values and the red circular data points represent the estimated $K_{eq,2,i}/c$ values, each plotted over their corresponding v_i^2 values, which are shown in their non-squared form v_i in Table 23. The dashed line represents a straight line describing the $K_{p,i}$ values and the solid line represents a straight line describing the $K_{eq,2,i}/c$ values. From the slopes of the straight lines with y-intercepts of zero, the values for the constants $K_{p,i}^*$ and $K_{eq,2,i}^*/c$ can be obtained with a value of 63.243 and 130.130, respectively. **(B)** $K_{p,i}$ and $K_{eq,2,i}/c$ as functions of pH. The blue square data points represent the estimated $K_{p,i}$ values and the red circular data points represent the estimated $K_{eq,2,i}/c$ values, each plotted over their corresponding pH values, which are shown in Table 23. The dashed line represents the change of $K_{p,i}$ over pH calculated by equation (42) and the solid line represents the change of $K_{eq,2,i}/c$ over pH calculated by equation (43). This figure is also included in a similar or identical form in Seelinger et al.³ (DRAFT (submitted)).

By setting the parameters $K_{p,i}$ and $K_{eq,2,i}/c$ to zero, the SAS-SMA model reduces to the SMA model. As can be seen in Figure 24A, the simulated peak is positioned at lower retention times than the experimental peak, when a shielding factor σ_i with a values of zero is used. Fitting the simulated peak to the experimental peak by varying the shielding factor σ_i , a negative value for σ_i is estimated, which is theoretically wrong and results in a poor agreement between simulated and experimental peak. This demonstrates that the SMA model is not able to describe anti-Langmuir behavior, whereas the SAS-SMA model describes the anti-Langmuirian elution behavior of the sample bsAbX pretty well (see Figure 24D).

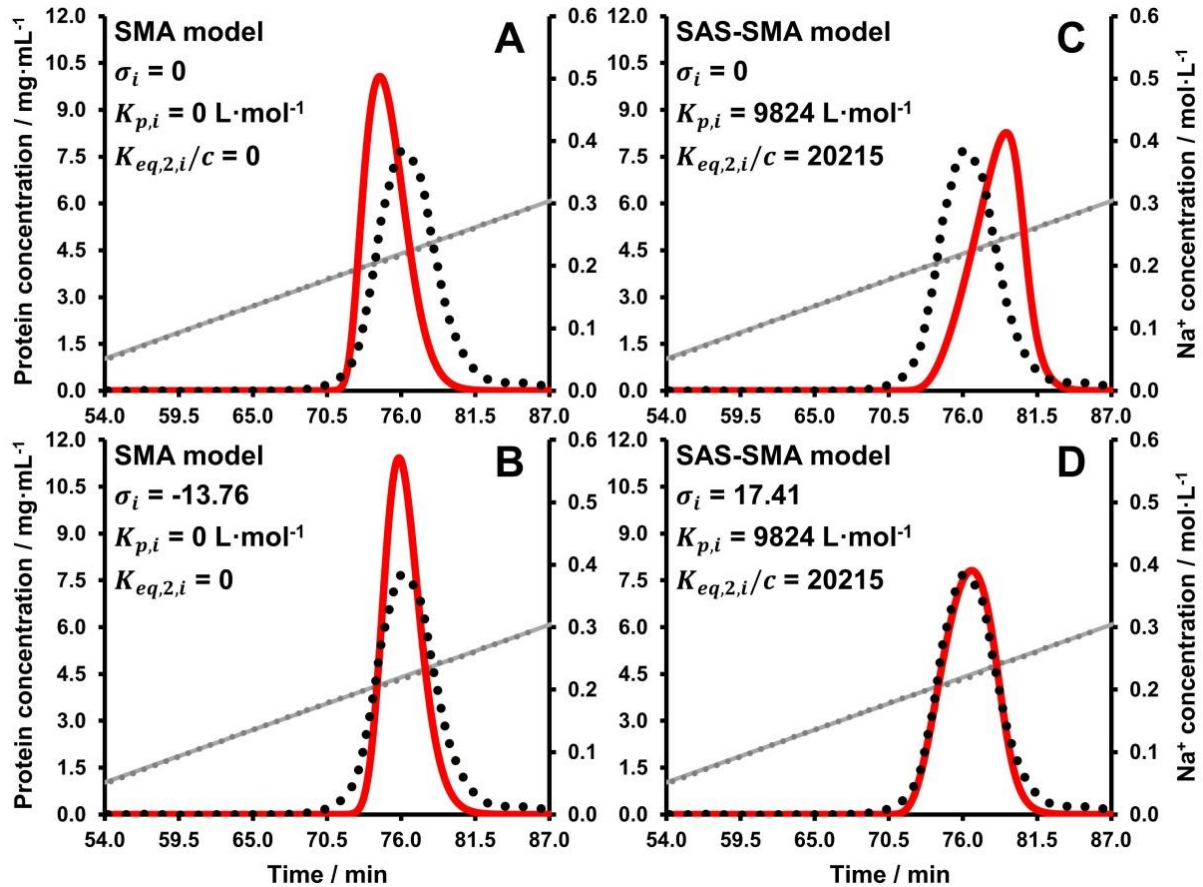


Figure 24. Comparison between the SMA model (A/B) and the SAS-SMA model (C/D) by chromatogram simulations of the linear salt gradient at pH 5.3 with a loading of $25 \text{ mg}_{\text{bsAb}}/\text{mL}_{\text{resin}}$ using the sample bsAbX. The black dots represent the experimental and the red lines the simulated protein concentrations. The gray dots represent the experimental and the gray lines the simulated Na^+ concentrations. For the simulations, a corrected pH of 5.26 and a $k_{\text{eff},i}$ of $2.07 \cdot 10^{-5} \text{ cm/s}$ was used. The SMA model (A/B) was computed with equation (30) and the SAS-SMA model (C/D) was computed with equation (29). The values for $K_{p,i}$ and $K_{eq,2,i}/c$ in (C) and (D) were calculated with equation (42) and (43) for a pH of 5.26. The value for σ_i in (B) was determined by inverse peak fitting. The value for σ_i in (D) was calculated with equation (44). The bsAb batch 3 was used for this experiment. Figure 24 is also included in a similar or identical form in Seelinger et al.³ (DRAFT (submitted)).

3.7.1.3 Semi-empirical description of the steric shielding factor's pH-dependence when using the SAS-SMA model

For describing the pH-dependence of σ_i , the fitted values for σ_i were plotted against pH, as shown in Figure 25A. As can be seen, the shielding factors σ_i are increasing with pH. The pH-dependence of σ_i was described with the following semi-empirical equation that was found during the project:

$$\sigma_i = m_i \cdot \frac{\Delta G_1^0}{RT} \cdot \frac{1}{\ln(10)} \cdot pH \cdot (v_{pH=0,i} - v_{pH,i}) \quad (44)$$

Here, σ_i is described as a function of the variable m_i , of mobile phase pH, and of the difference between a theoretical protein binding charge $v_{pH=0,i}$ at pH = 0 and the pH-dependent binding charge v_i calculated using equation (6). This semi-empirical equation has already been successfully used in almost identical form to describe the pH dependence of σ_i in the SMA model (see section 3.5.2, equation (40)) and only had to be extended by the variable m_i for use in the SAS-SMA model. As can be seen in Figure 25, the semi-empirical function with a value of 0.256 for m_i and a value of 37.829 for $v_{pH=0,i}$ describes the experimental values for σ_i plotted over their respective pH and v_i values with good agreement. In this work, no dependence of σ_i on column loading is observed.

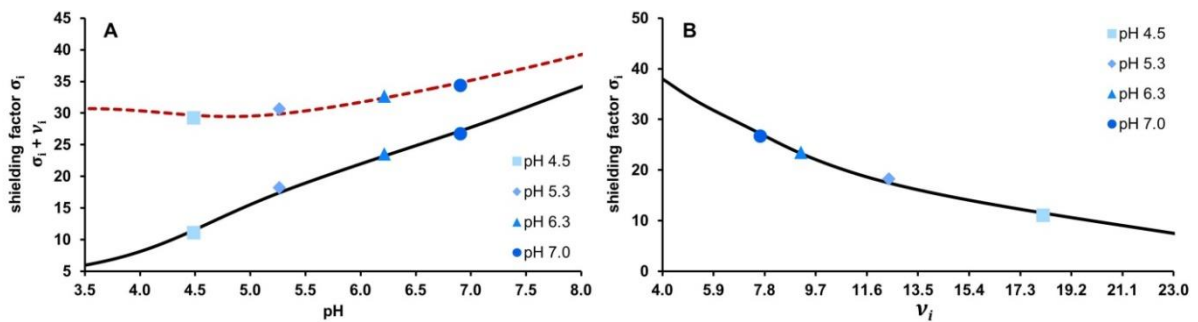


Figure 25. pH-dependence of σ_i and σ_i+v_i for bsAbX determined by applying the SAS-SMA model. (A) Semi-empirical description of the pH-dependence of σ_i . The data points display the estimated values for σ_i plotted over their corresponding pH values, as well as the sum of the estimated values for σ_i and their respective values for v_i plotted over their corresponding pH values. These values are listed in Table 23. The black solid line represents the change of σ_i over pH calculated by equation (44). The red dashed line represents the change of σ_i+v_i over pH determined by adding up the calculations with equation (44) and (6). (B) σ_i as a function of v_i . The data points display the estimated values for σ_i plotted over their corresponding v_i values that are listed in Table 23. The black solid line represents the change of σ_i over v_i calculated by equation (44) and (6). This figure is also included in a similar or identical form in Seelinger et al.³ (DRAFT (submitted)).

As shown in equation (41), the parameters σ_i and v_i dictate the pH-dependence of the theoretical maximal binding capacity $q_{max,i}$.⁴⁴ As can be seen in Table 23, $q_{max,i}$ decreases clearly from pH 4.5 to pH 7.0. The sum of σ_i and v_i (σ_i+v_i) decreases very

slightly from pH 3.7 to pH 4.8 (see Figure 25A), but then increases again significantly from pH 4.5 to pH ≥ 7.0 , which accounts for the pH-dependence of $q_{max,i}$ to a large extent.

3.7.2 Verification of the pH-dependent SAS-SMA model

3.7.2.1 Calculated change of pH-dependent model parameters over a linear pH gradient

Parts of this section 3.7.2.1 are also included in a similar or identical form in Seelinger et al.³ (DRAFT (submitted)).

The SAS-SMA model was modified by implementing the empirical equations for the pH-dependent non-linear model parameters $K_{p,i}$, $K_{eq,2,i}/c$, and σ_i (equation (42), (43), and (44), respectively) into the SAS-SMA formalism. With these extensions, the model includes pH-dependent linear model parameters ν_i as well as pH-dependent non-linear model parameters $K_{p,i}$, $K_{eq,2,i}/c$, σ_i , and $q_{max,i}$. The extended model is now capable of predicting non-linear adsorption and elution behavior when the mobile phase pH changes during the experiment, like in linear pH gradients.

A linear pH gradient from pH 4.5 to 9.3 in 51.2 CV was used as an example to visualize the change of the pH-dependent model parameters ν_i , $K_{p,i}$, $K_{eq,2,i}/c$, σ_i and $q_{max,i}$ (see Figure 26).

Figure 26 shows that the pH-dependent SAS-SMA model predicts a decreasing ν_i and an increasing σ_i over the applied linear pH gradient. The simulated $q_{max,i}$ remains approximately constant up to pH 4.8 and then decreases with increasing pH. Both $K_{p,i}$ and $K_{eq,2,i}/c$ decrease over the increasing linear pH gradient.

In Figure 26, the data points for ν_i , σ_i , $q_{max,i}$, $K_{p,i}$ and $K_{eq,2,i}/c$ are the individual values listed in Table 23. The data points were plotted at their respective pH values (see Table 23) into the linear pH gradient to confirm the simulation approach using the modified model and underlying parameter set.

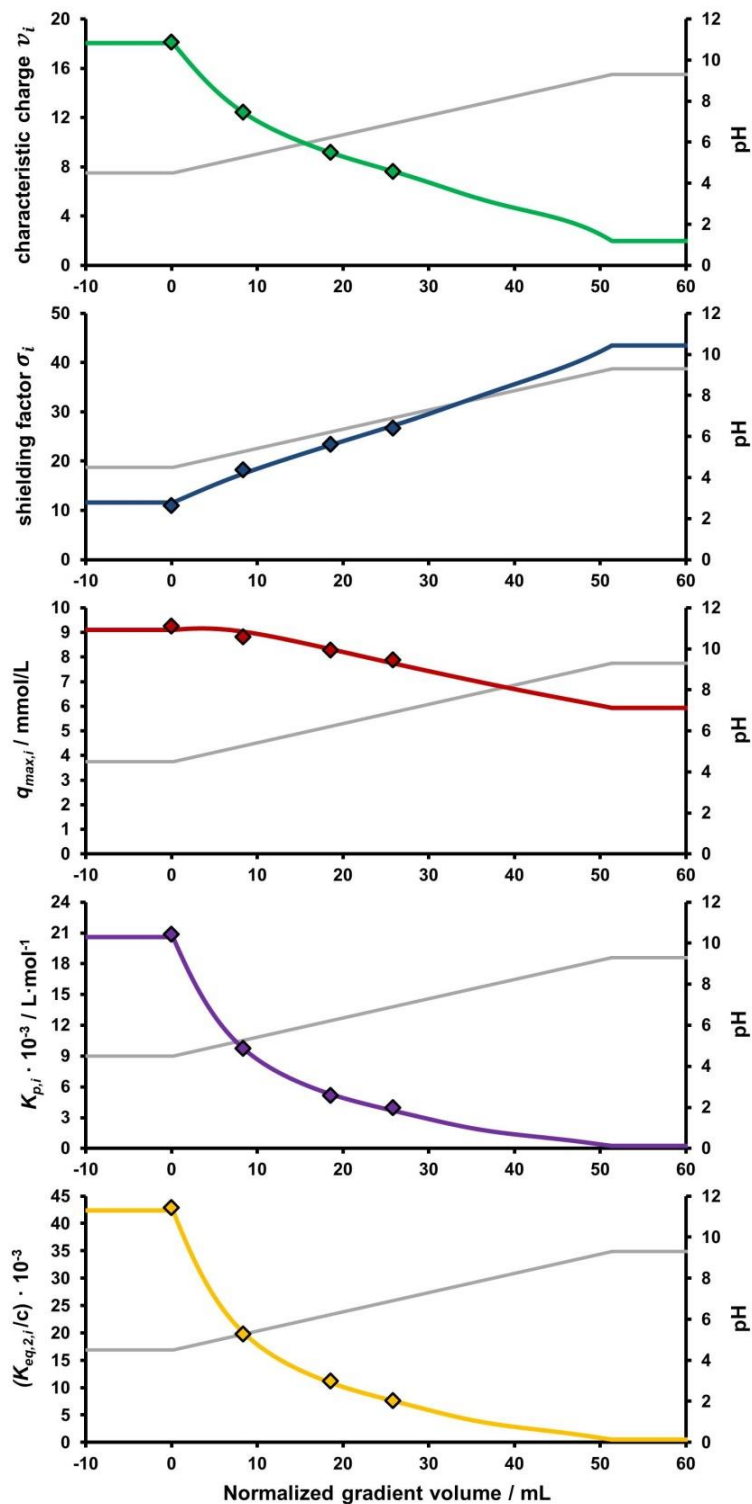


Figure 26. Simulated changes of the model parameters v_i , σ_i , $q_{max,i}$, $K_{p,i}$ and $K_{eq,2,i}/c$ for bsAbX over a linear pH gradient (pH 4.5 – 9.3) calculated by the pH-dependent SAS-SMA model. The data points for v_i , σ_i , $q_{max,i}$, $K_{p,i}$ and $K_{eq,2,i}/c$ are the values listed in Table 23, plotted at their corresponding pH values. The gradient volume in milliliters is normalized to the gradient start. This figure is also included in a similar or identical form in Seelinger et al.³ (DRAFT (submitted)).

3.7.2.2 Simulation of linear pH gradient elution under high loading and column overloading conditions

Parts of this section 3.7.2.2 are also included in a similar or identical form in Seelinger et al.³ (DRAFT (submitted)).

The pH-dependent SAS-SMA model was further verified by applying linear pH gradient elution experiments at three different fixed Na^+ concentrations (75, 120 and 200 mmol/L Na^+) and column loadings of 25, 50, 75 and 90 $\text{mg}_{\text{bsAb}}/\text{mL}_{\text{resin}}$. The used $k_{\text{eff},i}$ values are listed in Table 24. The resulted *in silico* chromatogram simulations are shown in Figure 27.

Table 24: $k_{\text{eff},i}$ values for bsAbX estimated with linear pH gradient experiments at high loading conditions

pH / -	$c(\text{Na}^+) / \text{mmol}\cdot\text{L}^{-1}$	Load / $\text{mg}\cdot\text{mL}^{-1}$	$k_{\text{eff},i} / \text{cm}\cdot\text{s}^{-1}$
4.50 – 9.30	75	25	$1.29\cdot 10^{-5}$
4.50 – 9.30	75	50	$5.58\cdot 10^{-6}$
4.50 – 9.30	75	75	$2.87\cdot 10^{-6}$
4.50 – 9.30	75	90	$2.78\cdot 10^{-6}$
4.50 – 8.25	120	25	$1.36\cdot 10^{-5}$
4.50 – 8.25	120	50	$5.52\cdot 10^{-6}$
4.50 – 8.25	120	75	$2.99\cdot 10^{-6}$
4.50 – 8.25	120	90	$2.94\cdot 10^{-6}$
4.50 – 8.25	200	25	$2.41\cdot 10^{-5}$
4.50 – 8.25	200	50	$1.25\cdot 10^{-5}$
4.50 – 8.25	200	75	$6.81\cdot 10^{-6}$

In Figure 27, it can be seen that the pH-dependent SAS-SMA model predicts the retentions and the peak shapes very well up to a load of 50 $\text{mg}_{\text{bsAb}}/\text{mL}_{\text{resin}}$. Accurate prediction of the peak shapes is based on the interplay between the pH-dependent model parameters v_i , σ_i , $K_{p,i}$ and $K_{\text{eq},2,i}/c$ which optimally adjust their values to the changing pH. This allows the correct simulation of anti-Langmurian elution behavior even within pH gradients.

As can be seen in Figure 27, at column loadings of 75 and 90 $\text{mg}_{\text{bsAb}}/\text{mL}_{\text{resin}}$, retention of the main elution peaks is well predicted at all Na^+ concentrations. The single-component simulation described the peak shape of the pH gradient at 200 mmol/L Na^+ with a loading of 75 $\text{mg}_{\text{bsAb}}/\text{mL}_{\text{resin}}$ very well. However, at 75 and 120 mmol/L Na^+ , complex elution profiles with overloading phenomena like breakthroughs and pre-shoulders can be seen for column loadings of

$\geq 75 \text{ mg}_{\text{bsAb}}/\text{mL}_{\text{resin}}$. By subtracting the amount of protein in the breakthrough from the the protein mass used in the simulation, the single-component simulation could at least predict the retention of the main elution peaks quite well with slight deviations in the description of the peak shape. The discrepancies here are mainly caused by the formed pre-shoulders. The observed overloading effects in the form of breakthrough and pre-shoulder formation at 75 and 120 mmol/L Na^+ were further investigated. The results are shown in the following chapter.

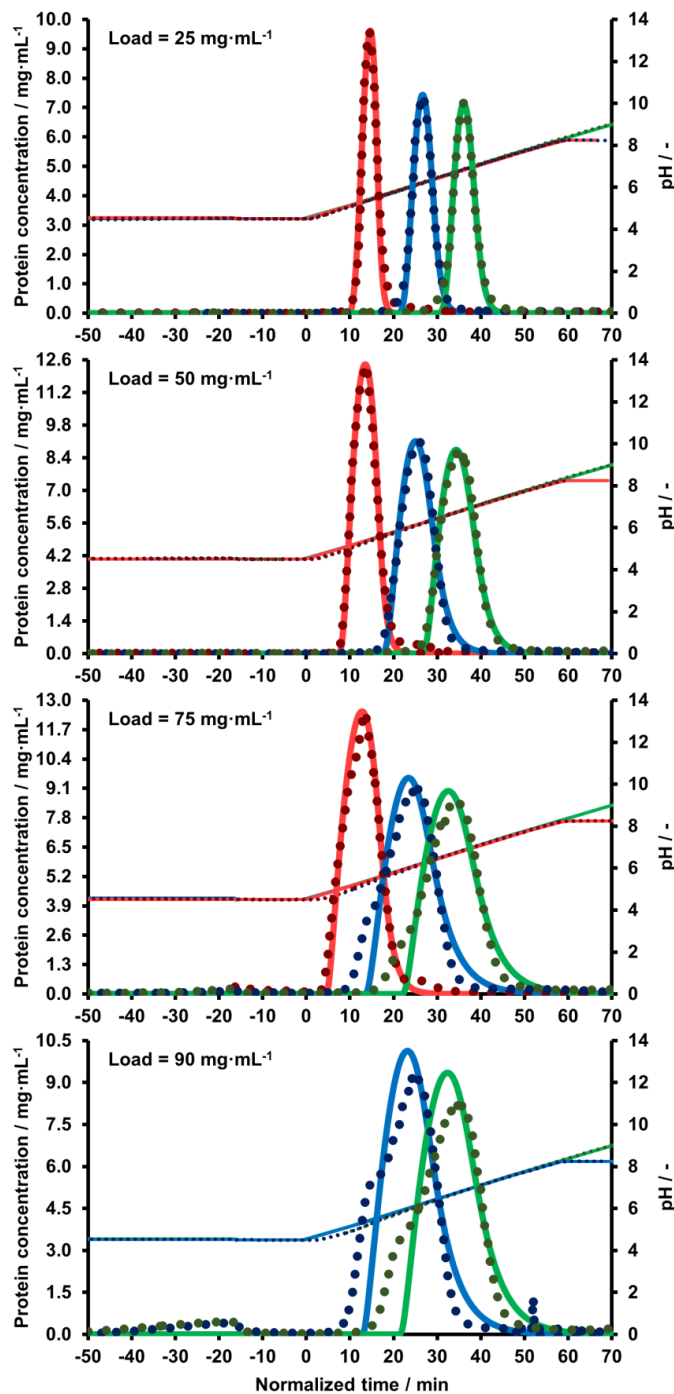


Figure 27. Linear pH gradient elution experiments performed at 75, 120 and 200 mmol/L Na^+ with loadings from 25 to 90 $\text{mg}_{\text{bsAb}}/\text{mL}_{\text{resin}}$ simulated by the pH-dependent SAS-SMA model using the sample bsAbX. The time in minutes is normalized to the gradient start. The dots display the experimental and the lines display the simulated data. The green data represents the runs with 75 mmol/L Na^+ , the blue data the runs with 120 mmol/L Na^+ , and the red data the runs with 200 mmol/L Na^+ . This figure is also included in a similar or identical form in Seelinger et al.³ (DRAFT (submitted)).

3.8 Investigation of complex high loading and overloading phenomena when using bsAbX

Parts of this section 3.8 may be also included in a similar or identical form in Seelinger et al.³ (DRAFT (submitted)).

Overloading phenomena such as breakthrough despite high binding strengths due to low pH and low Na⁺ concentrations and pre-shoulder formation were investigated using the linear pH gradient at 75 mmol/L Na⁺ with loadings of ≥ 75 mg_{bsAb}/mL_{resin}. For the experiments presented in this section, always the sample bsAbX batch 3 was used. First, it was tested whether different loading conditions such as an increased Na⁺ concentration during loading or whether a decreased flow rate during loading affect the binding at pH 4.5 and the following elution within the linear pH gradient (pH 4.5 to 9.3). The experiments performed are shown in Figure 28.

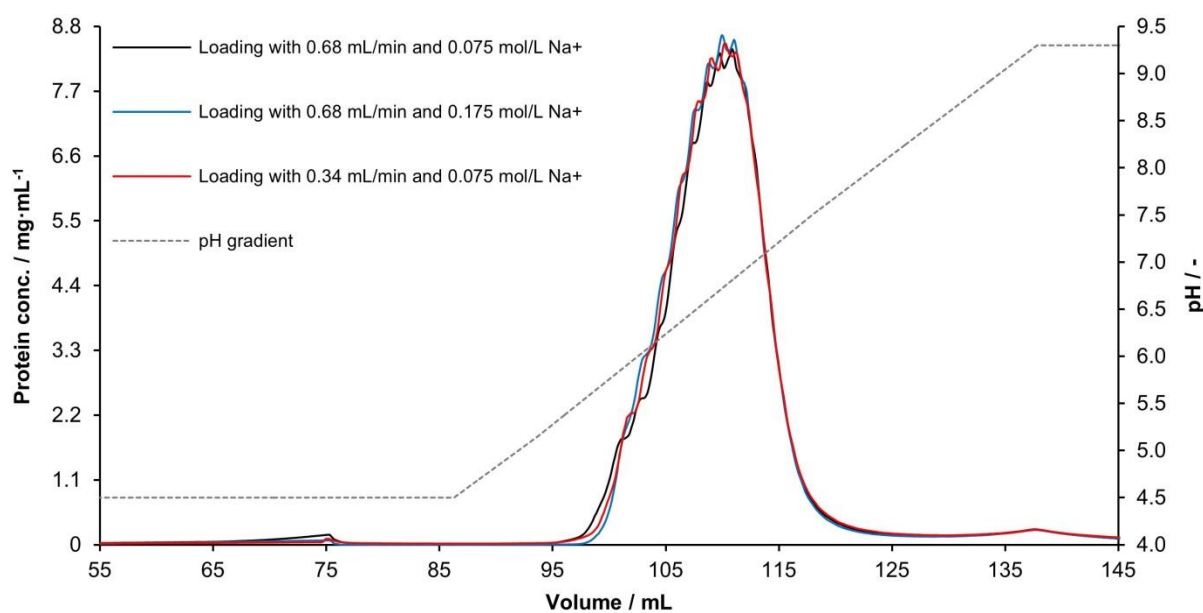


Figure 28. Overlay plot of linear pH gradients at 75 mmol/L Na⁺ with column loading of 75 mg_{bsAb}/mL_{resin} each performed with different loading conditions using the sample bsAbX batch 3. As noted in the legend of the figure, the sample was loaded onto the 1 mL column once at the standard conditions with 75 mmol/L Na⁺ and a flow rate of 0.68 mL/min, the sample was once loaded with an increased Na⁺ concentration of 175 mmol/L Na⁺ with a flow rate of 0.68 mL/min, and the sample was once loaded with 75 mmol/L Na⁺ with a reduced flow rate of 0.34 mL/min. Some of the data shown and illustrated in this figure may be included in Seelinger et al.³ (DRAFT (submitted)).

As can be seen, 75 mg bsAbX were loaded onto the 1 mL column once at the standard condition with 75 mmol/L Na⁺ and a flow rate of 0.68 mL/min, then the sample was loaded with an increased Na⁺ concentration of 175 mmol/L Na⁺ with a flow rate of 0.68 mL/min, and then the sample was loaded with 75 mmol/L Na⁺ with a reduced flow rate of 0.34 mL/min. It can be seen that at an increased Na⁺ concentration of 175 mmol/L and at a reduced flow rate of 0.34 mL/min, the breakthrough during loading was significantly reduced. However, these changes in loading conditions had little or even no effect on the elution within the gradient. The elution profiles within the gradient look almost the same for all three experiments. Only the peak areas of the experiments with changed loading conditions are slightly larger due to the reduced sample breakthrough (see Figure 28). The simulations looked similar for all three experiments (data not shown).

Furthermore, the charge variant distribution during sample breakthrough and gradient elution of the linear pH gradient at 75 mmol/L Na⁺ with a loading of 75 mg_{bsAb}/mL_{resin} was studied. In this experiment, the sample was loaded onto the 1 mL column in the normal manner at pH 4.5 with a Na⁺ concentration of 75 mmol/L by using a flow rate of 0.68 mL/min. Therefore, fractions were taken during the experiments to determine the distribution of pre-variants and main variants of bsAbX throughout the elution. For this purpose, the total bsAbX concentration in the fractions was first determined as described in section 2.2.3. Subsequently, the fractions were analyzed by CEX-HPLC, as described in section 2.2.1.2, to determine the species and proportions of the bsAbX charge variants in each fraction. Therefore, the charge variants of bsAbX were subdivided and classified into pre-variants and main variants, as shown in Figure 4. The concentrations of the pre-variants and main variants in each fraction could then be determined with the determined bsAbX concentrations and the determined proportions of pre-variants and main variants. The determined elution profiles of the bsAbX charge variants of the linear pH gradient at 75 mmol/L Na⁺ with a loading of 75 mg_{bsAb}/mL_{resin} are shown in Figure 29.

Figure 29 shows that the breakthrough always consists approximately of ~ 29% pre-variants and ~ 71% main variants. This means that the sample breaks through during loading exactly as it was injected. The individual CEX-HPLC analyses of the fractions from the breakthrough were always very comparable to the analysis shown in Figure 4. A separation or enrichment of charge variants in the breakthrough can thus be excluded. CEX-HPLC analyses of the fractions from the linear gradient show that the

pre-variants are enriched in the pre-shoulder, with the main variants also slightly eluting into the pre-shoulder. Subsequently, the pre-variants and main variants elute largely together, with the peak of the pre-variants merging in a dome shape into the main elution peak. The elution profiles shown in Figure 29 were not simulated.

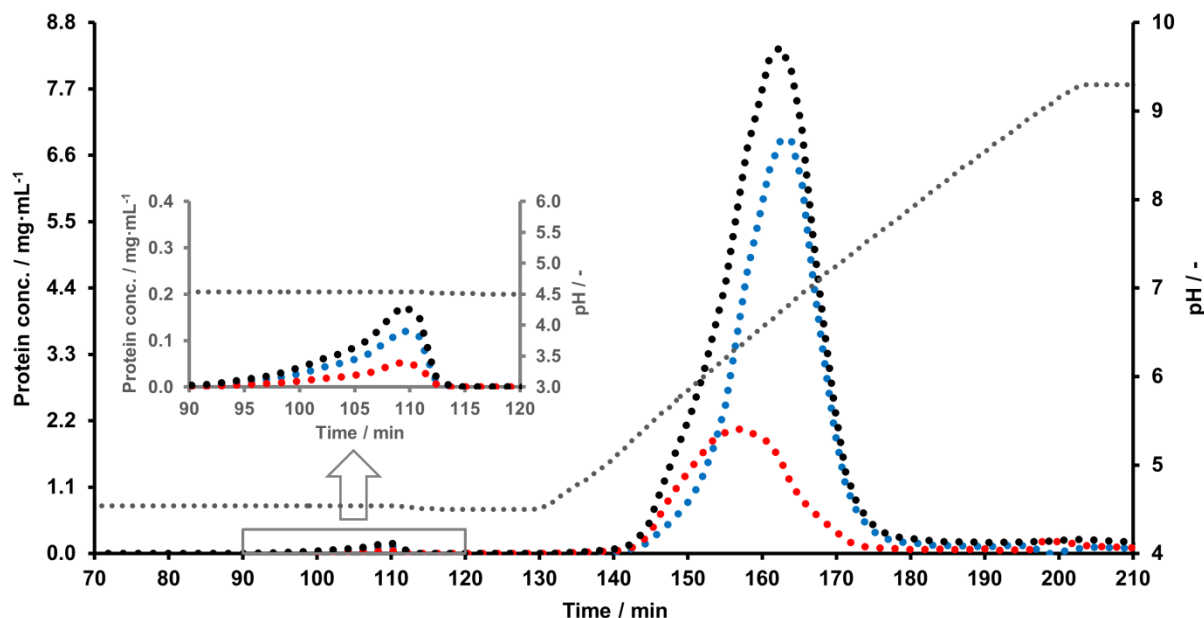


Figure 29. Elution of bsAbX (batch 3) charge variants in a linear pH gradient at 75 mmol/L Na⁺ with a column load of 75 mg_{bsAb}/mL_{resin}. The black dots represent the total bsAbX concentration, the blue dots represent the concentration of the main variant, the red dots represent the concentration of the pre-variants and the gray dots represent the mobile phase pH. Some of the data shown and illustrated in this figure may be included in Seelinger et al.³ (DRAFT (submitted)).

4 DISCUSSION

4.1 Size variants and charge variants heterogeneity of the bsAb samples

Parts of the section 4.1, particularly parts from subsection 4.1.1, have already been published in a similar or identical form in Seelinger et al.¹ (Part 1, 2022) and in Seelinger et al.² (Part 2, 2022). Parts of this section 4.1, particularly parts from subsection 4.1.2, are also included in a similar or identical form in Seelinger et al.³ (DRAFT (submitted)).

The most recombinant antibody products contain heterogeneous variants^{5,58,69,70,117,118} which differ in size^{58,70,119} or charge^{5,58,69,70,117,118} resulting in slightly different isoelectric pH values.⁵ If heterogeneous variants have a clear impact on the chromatographic purification step (e.g. formation of shoulders or multiple peaks⁵⁸), they have to be considered as individual species for mechanistic modeling studies.^{58,69,70} Therefore, it was necessary to determine whether the bsAb samples used contain different variants and, if present, whether these variants significantly affect the elution profiles, especially under high loading and overloading conditions. Based on these analyses, it was ultimately decided whether the samples used could be described using single-component simulations.

4.1.1 Size variants and charge variants heterogeneity of the sample bsAbY

The small amounts of dimers/multimers ($\leq 1\%$) and fragments ($\leq 9\%$) which were detected by SE-HPLC (see Figure 1A) are expected to have no or negligible impact on the preparative CEX elution profiles. However, analysis by CEX-HPLC showed that the sample bsAbY (see Figure 1B) consists of many different charge variants, with strongly distinct charge variants eluting between 22.2 to 30.0 mL (main variants) and weakly distinct charge variants eluting between 15.0 to 22.2 mL (pre-variants). The complex elution profile in CEX-HPLC shows that elution in preparative CEX experiments may result in the formation of asymmetric peaks or pre-shoulders, particularly because of the pre-variants (see Figure 1B). However, as can be seen in Figure 2, for the preparative linear salt gradient runs at pH 5.3 and pH 8.0 performed under low loading conditions (load $\leq 1 \text{ mg}_{\text{bsAb}}/\text{mL}_{\text{resin}}$), predominantly symmetric main elution peaks with only very weakly distinct pre-shoulders were observed (see Figure 2A/B). Analyses performed by CEX-HPLC showed that these small pre-shoulders are

indeed mainly formed by these pre-variants (e.g., linear salt gradient at pH 8 and 5 mg_{bsAb}/mL_{resin} (see Figure 14A/C). This was also the reason why these charge variants were grouped together as shown in Figure 1B. However, the just mentioned elution profiles at column loads of ≤ 1 mg_{bsAb}/mL_{resin} could be predicted with sufficient agreement using only one simulated variant (see Figure 2A/B). This was also the case for all other runs at ≤ 1 mg_{bsAb}/mL_{resin} including the linear pH and dual gradient elution experiments at low loading conditions.

Based on the results shown in Figure 1 and especially in Figure 2, the assumption was made that the size and charge variants of the bsAb sample could be modeled as one species. Modeling with only one variant and thus the use of single-component simulations reduces the experimental and time effort enormously, since the bsAbY sample can be used directly without prior isolation of variants, since only one data set has to be generated and only one set of model parameters has to be determined. However, it is also important to note that due to the very close elution of the individual variants, isolation of individual variants in sufficient quantities and high purity would have been practically impossible anyway.

However, the presence of the different charge variants can have a stronger influence under high loading and overloading conditions which may lead to discrepancies between experimental and simulated elution curves. As can be seen in section 3.5.1, the elution behavior of the bsAbY sample within linear salt gradients could be well described with single-component simulations until a column loading of 25 mg_{bsAb}/mL_{resin}, which was sufficient to determine the pH-dependence of the shielding factor σ_i . As can be seen in the sections 3.5.3.2 and 3.5.3.3, the elution behavior of the bsAbY sample in the linear pH gradients with 120 and 200 mmol/L Na⁺ and in all applied linear dual gradients could be described with outstanding precision with single-component simulations even up to a column loading of 75 mg_{bsAb}/mL_{resin}. Significant influences on the elution profiles of the sample bsAbY due to charge variant heterogeneity were found in this work only at pH values of ≥ 6 and especially at loadings of > 25 mg_{bsAb}/mL_{resin}. Affected by this were the salt gradients at pH ≥ 6.3 and the pH gradient at 75 mmol/L Na⁺, where the bsAbY sample eluted approximately between pH 6 to 9. Corresponding results, investigations and alternative multi-component simulations are shown in the respective sections.

4.1.2 Size variants and charge variants heterogeneity of the sample bsAbX

According to CEX-HPLC (see Figure 3B.1-3 and Figure 4), all 3 batches of bsAbX have a very distinctive, centrally positioned main variant flanked by much less distinctive side variants. Due to this dominant and centrally positioned main variant and the comparatively small amount of side variants, it was assumed that the different charge variants would not have a disturbing influence on the preparative CEX chromatography elution profiles. This assumption was confirmed during the work when low loading conditions ($\leq 1 \text{ mg}_{\text{bsAb}}/\text{mL}_{\text{resin}}$) and high loading conditions ($\leq 50 \text{ mg}_{\text{bsAb}}/\text{mL}_{\text{resin}}$) were applied. However, under overloading conditions ($\geq 75 \text{ mg}_{\text{bsAb}}/\text{mL}_{\text{resin}}$), it was found that the pre-variants of bsAbX were mainly responsible for the formation of complex peak shapes in the form of pre-shoulder formation and the formation of peak fronting. Corresponding studies are shown in section 3.8. The results shown in section 3.8 were also the reason why the sample bsAbX was divided into pre-variants and main variants as shown in Figure 4.

Analysis by SE-HPLC showed that batch 1, which was used for modeling in the linear range, consists of 98 % monomer (see Figure 3A.1). Due to the very high amount of monomer variant, it is clear that a negative influence due to fragments or dimers/multimers can be completely excluded for batch 1. However, the situation is different for batch 2 and batch 3. In both batches, an increased amount of dimers/multimers has been detected. Batch 2 contains ~ 11 % dimers/multimers and batch 3 contains ~ 8 %. Furthermore, the analyses by SE-HPLC also showed that the types of dimers/multimers are different in the two batches (see Figure 3A.2-3). This can also be seen in the chromatograms of the preparative runs at column loads of $\leq 1 \text{ mg}_{\text{bsAb}}/\text{mL}_{\text{resin}}$ (see Figure 5). However, when the amount of dimers/multimers was subtracted from the set loading of the single-component simulations, the main peaks could be described very well for both batches, which indicates that the increased amount of dimers/multimers have little or even no influence at low column loadings. It should be particularly noted that the $k_{eff,i}$ values for diluted conditions of $\leq 1 \text{ mg}_{\text{bsAb}}/\text{mL}_{\text{resin}}$, which are listed in Table 20, worked for both batches. This further confirms that the increased amount of dimers/multimers have little or even no influence at low column loadings. Based on the results discussed so far in this subsection, the assumption was made that the size and charge variants of the bsAbX sample could be modeled as one species. However, in LGE experiments performed under high loading and overloading conditions, the increased amount of

dimers/multimers could be a factor again, since an increased amount of dimers/multimers in these loading regions can lead to shifts of the main elution peaks and could significantly change or affect the peak shapes as a consequence of competitive binding and displacement effects.¹¹⁶ As can be seen in Figure 21, Figure 22, Figure 35, and Figure 36, where the chromatograms of the linear salt gradients performed under high loading and overloading conditions are shown, the elution profiles of batches 2 and 3 showed noticeable dimer/multimer peaks (see the post-shoulders) that indeed look different between the two batches. However, the increased amounts and the different types of dimers/multimers had no significant effect on the fitted non-linear model parameters (see Table 23), as can be seen from the fact that the same values for the non-linear model parameters could be used and determined for both batches at each pH tested. In addition, the agreement between simulated and experimental data for both batches was always of excellent precision up to a column loading of 50 mg_{bsAb}/mL_{resin} (partly also up to 75 mg_{bsAb}/mL_{resin}), by using single-component simulations, which is valid for both the linear salt and the linear pH gradients. Thus, the sample bsAbX could be described to a large extent very well with single-component simulations. The advantages of single-component simulations are already discussed in section 4.1.2. As for bsAbY, an isolation of individual size/charge variants in sufficient quantity and purity would have been almost impossible for bsAbX due to the close elution of these variants. Therefore, the individual variants could not be modeled separately; modeling the entire bsAbX sample with only one simulated variant and thus usage of single-component simulations was therefore the preferred option. However, the discrepancies in description of the experimental elution profiles by the single-component simulation which were observed under overloading conditions (≥ 75 mg_{bsAb}/mL_{resin}), are indeed most likely attributable to the heterogeneous composition of charge and size variants of the sample bsAbX (see for instance section 3.8). These discrepancies are discussed in the corresponding sections.

4.2 Modeling in the linear range of the adsorption isotherm

Parts of section 4.2 have already been published in a similar or identical form in Seelinger et al.¹ (Part 1, 2022). Parts of section 4.2 are also included in a similar or identical form in Seelinger et al.³ (DRAFT (submitted)).

A Yamamoto LGE approach^{96–98} was used, which was modified with a pH-dependent description of the protein binding charge v_i .⁵⁹ As a consequence of the pH-dependent v_i , also the linear model parameter $K_{eq,i}$ was described as a function of pH (see equation (5)).^{4,40,59} Several other publications^{1,59,70} demonstrated already the comparability between linear salt and linear pH gradient elution experiments when this modified Yamamoto LGE approach is applied. By using this approach, it was feasible to precisely describe the largest possible elution range for both antibodies bsAbY and bsAbX (see Figure 6) and thus to establish a stable basis for the following modeling under high loading and overloading conditions. By using the pH-dependent description of v_i based on a protein charge model established by Schmidt et al.⁵⁹, the applied model-based approach was completely described with pH-dependent model parameters ($v_i(pH)$ and $K_{eq,i}(pH)$) in the linear range of the adsorption isotherm. As shown in Figure 6C/F, both v_i and $\ln K_{eq,i}$ decrease with increasing pH for the two antibodies bsAbY and bsAbX, similar to what is already noted in previous publications for other proteins.^{1,40} Here, for the v_i and $\ln K_{eq,i}$ curves of both antibody samples bsAbY and bsAbX, it can be seen (see Figure 6C/F) that the strongest effect is observed between pH 4.0 and pH 5.5, while between pH 6.0 and pH 9.0 the decrease of v_i and $\ln K_{eq,i}$ is small. For bsAbY, the pH-dependence of $\ln K_{eq,i}$ follows exactly the pH-dependence of v_i , since $\Delta G_1^0/RT$ with a value of 0.93 is close to one (see equation (5)). For bsAbX, the pH-dependence of $\ln K_{eq,i}$ deviates very slightly from the pH-dependence of v_i , since $\Delta G_1^0/RT$ with a value of 1.17 differs somewhat more from one.

The $k_{eff,i}$ values are essential to properly describe the shape of the elution peaks. As can be seen in Table 20, at low loading conditions, different $k_{eff,i}$ values are determined for the linear salt and linear pH gradients with the steepest gradient slopes, as well as for the two dual gradients. These different $k_{eff,i}$ values reflect the pH- and salt concentration-dependence of the isotherm slope in the linear range of the adsorption isotherm.

Conclusively, the determined linear model parameters N_{AA} , $\Delta G_1^0/RT$, $\Delta G_i^0/RT$ (see Table 19) and the $k_{eff,i}$ values for low loading conditions (see Table 20) described the generated data sets with good agreement (see Figure 6). The model was now able to describe the elution behavior of the two bsAbs under low loading conditions and was furthermore ready for the following modeling in the non-linear range.

4.3 Langmuir and anti-Langmuir elution behavior under high loading and column overloading conditions

Parts of section 4.3 have already been published in a similar or identical form in Seelinger et al.¹ (Part 1, 2022) and in Seelinger et al.² (Part 2, 2022). Parts of section 4.3 are also included in a similar or identical form in Seelinger et al.³ (DRAFT (submitted)).

As shown, the sample bsAbY showed Langmuir elution behavior whereas the antibody sample bsAbX showed anti-Langmuir elution behavior under high loading and overloading conditions.

In CEX, the most proteins and especially antibodies show a Langmuirian behavior under high loading conditions.^{44,66} Khalaf et al.⁶⁶ investigated the elution behavior of six different proteins on polyelectrolyte brush type cation exchangers under high loading conditions. Two of these six proteins were monoclonal antibodies, which both showed common Langmuir elution behavior. The most widely used binding model in academia and industry³⁶, the SMA model⁴⁴, describes Langmuir behavior under high loading conditions. Langmuir behavior is described in the classical SMA model introduced by Brooks and Cramer by setting all activity coefficients to unity.⁴⁴ This shows that it is mostly sufficient for proteins which behave in a Langmuirian manner to calculate their IEC equilibrium purely by concentrations. Since all activity coefficients are set to unity, no aggregation, no multi-layer binding and no conformational changes are described.⁴⁴ This indicates that when proteins exhibit typical Langmuir behavior, it can usually be assumed that protein-protein interactions are generally not important. Moreover, the non-ideal behavior of the salt has been very often neglected in the literature,^{4,44} and the pH-dependence of the non-linear shielding factor σ_i has so far always been neglected.^{1,57} However, the data set shown in this work is exceptionally large and describes the entire elution range of the antibody bsAbY. Therefore, a SMA model modified with an activity coefficient for the salt in solution^{90,91} and with a pH-dependent steric shielding factor σ_i was applied, in order to precisely describe a broad range of salt concentrations and pH. As could be shown in this work, this model was largely able to accurately describe the elution behavior of bsAbY. The antibody bsAbY generally showed normal Langmuir behavior up to a loading of 25 mg_{bsAb}/mL_{resin}, sometimes also 50 mg_{bsAb}/mL_{resin}. From loadings of ≥ 50 mg_{bsAb}/mL_{resin}, unusual peak shapes caused by column overloading were observed in this work, which could no longer be explained by ordinary Langmuir

behavior. The complex overloading phenomena observed for bsAbY are discussed and explained in detail in section 4.5.

According to the literature, anti-Langmuir behavior as exhibited by the antibody bsAbX is a consequence of molecule-molecule interactions; in the case of proteins, this is referred to as protein-protein interactions.^{52,53,65,114,115,120} The association of molecules such as multi-layer binding on the stationary phase or the oligomerization of proteins (e.g. dimerization) can lead to anti-langmuir behavior.^{52,53,65,114,115,120} It is important to note, however, that to the best of the author's knowledge, anti-Langmuir behavior in proteins has so far only been observed for polypeptides, such as insulin⁵², glucagon-like peptide-1 (GLP-1) analogue⁵³, lysozyme⁶⁶, chymotrypsinogen A⁶⁶, and Goserelin⁶⁶. To the best of my knowledge, anti-Langmuir behavior has never been observed for an antibody before. To describe the anti-langmuir binding and elution behavior of the antibody bsAbX, Mollerup's SAS-SMA model^{52,53}, which describes self-association on the stationary phase surface in terms of self-dimerization, was used. This SAS-SMA model was extended by activity coefficients for the salt^{90,91} and the protein⁵² in solution and additionally described in a pH-dependent manner in both the linear and non-linear range. This ensured that the model could describe the complex high-loading elution behavior of bsAbX over a wide range of salt concentrations, protein concentrations, and pH. The antibody bsAbX generally showed complex high loading elution behavior in the form of anti-Langmuir behavior starting from a column loading of 5 mg_{bsAb}/mL_{resin}. Above 50 mg_{bsAb}/mL_{resin}, similar to bsAbY, additional complex overloading effects such as the formation of shoulders before and even after the main peaks, unexpected breakthrough, etc. were observed. The extent to which the model-based approach used was able to describe these complex high-loading and overloading phenomena is explained and discussed in the corresponding chapters (see e.g. section 4.7).

4.4 Modeling the binding and elution behavior of bsAbY in the non-linear range of the adsorption isotherm using a modified SMA model

4.4.1 Determination of the pH-dependent shielding factors σ_i

Parts of section 4.4.1 have already been published in a similar or identical form in Seelinger et al.¹ (Part 1, 2022) and in Seelinger et al.² (Part 2, 2022).

With the inverse peak fitting method utilized, the model parameters $k_{eff,i}$ and σ_i were determined simultaneously.

For the $k_{eff,i}$ values, additionally to the pH- and salt concentration-dependence, the dependence on the protein concentration of the isotherm slope is considered by the estimated $k_{eff,i}$ values.¹ For each linear salt gradient, decreasing values for $k_{eff,i}$ were determined with increasing column loadings, which most likely reflects the non-linear Langmuirian shape of the SMA adsorption isotherms.¹ Load-dependent $k_{eff,i}$ values allow a suitable description of the peak shapes observed under high loading and overloading conditions.

For the shielding factor σ_i , very similar values were estimated at each applied pH for column loadings from 5 to 25 mg_{bsAb}/mL_{resin} (50 mg_{bsAb}/mL_{resin} at pH 5.3). A loading-dependence for σ_i was not detected here, but a strong pH-dependence for σ_i was determined which will be discussed in detail in the following section 4.4.2.

From column loadings of ≥ 50 mg_{bsAb}/mL_{resin} (≥ 75 mg_{bsAb}/mL_{resin} at pH 5.3), σ_i values could no longer be determined, although other reasons were responsible for this at low pH values (pH ≤ 5.3) than at higher pH values (pH ≥ 6.3).

Thereby, at lower pH values of pH ≤ 5.3 , the unexpected phenomena due to high loading and overloading described in the results section (see section 3.5.1) are much more pronounced at pH 4.5 than at pH 5.3. Further studies showed that the described unexpected high loading phenomena at low pH, especially prominent at pH 4.5 (see section 3.6.2), are caused by hindered intraparticle mass transport^{1,2,73-77} and conformational changes of the bsAbY sample,^{1,2,11,78,80,81} which will be discussed in detail in section 4.5.2.

At higher pH values of pH ≥ 6.3 and column loadings of ≥ 50 mg_{bsAb}/mL_{resin}, further studies showed that the individual charge variants of the protein bsAbY affected the shape of the peaks in an unforeseen way.² Due to this multi-variant elution behavior, the elution peaks became unexpectedly narrow and tall, which affected both the σ_i values estimated by chromatogram fits and sometimes led to discrepancies between experimental and simulated data when the mean values $\bar{\sigma}_i$ were used. As shown in the respective results section (see section 3.6.1), the assumption of describing the bsAb's elution behavior with only one simulated variant is inadequate to predict the observed peak shapes caused by unexpected multi-component elution. The corresponding investigations and findings of this multi-component elution behavior

under high loading conditions and pH values greater than 6 are discussed in detail in section 4.5.1.

4.4.2 Semi-empirical description of the pH-dependent shielding factor σ_i in the SMA model

Parts of section 4.4.2 have already been published in a similar or identical form in Seelinger et al.¹ (Part 1, 2022).

As can be seen in Figure 10, the shielding factors σ_i determined for bsAbY are strongly increasing with increasing pH. Neglecting any effect of pH on the structure and stability of the protein and considering protonation/deprotonation reactions of the titratable amino acids only, the theoretical lower limit of σ_i should be reached at low pH values, when the protein reaches a maximum of positive charges.¹ The maximum value for σ_i is expected at high pH values, or more precisely at the pH values where the binding charge v_i is close to zero.¹ Between these two limits σ_i is a complex function of pH and reflects the deprotonation of acidic amino acids (generation of additional negative charges) and the basic amino acids (removal of positive charges).¹

In this work, the pH-dependence of σ_i is described using a semi-empirical formula (equation (40)), for which, remarkably, only one additional model parameter ($v_{pH=0,i}$) needs to be determined. Thereby, the parameter $v_{pH=0,i}$ theoretically describes the maximum binding charge at a pH value of 0. The semi-empirical function with an estimated $v_{pH=0,i}$ value of 47.54 describes the change of the experimental values for σ_i over their respective pH (Figure 10A) and v_i (Figure 10B) values very well, as shown by the calculated lines. As shown in Figure 10B the decrease of σ_i is a non-linear function of v_i . At higher pH values i.e., smaller v_i values the σ_i values decrease more strongly, than for larger v_i values. The σ_i - v_i dependence can be approximated by two linear relationships for low and high pH ranges with slopes of about -4 and -10. The transition region is at a pH value of about 6.0 to 6.5, where the amino acid histidine is predominantly deprotonating. Although additional negative charges strongly lower the binding charge v_i they contribute to a smaller extend to the change in σ_i compared to removed positive charges at higher pH.¹

In the classical SMA model⁴⁴, the shielding factor is considered as a strictly steric parameter that reduces the number of counterions available for exchange upon protein binding only by steric hindrance. However, this is no longer valid because, in

addition to steric hindrance, repulsive effects between the protein and the stationary phase surface⁷² as well as lateral protein-protein interactions at high surface protein densities¹²¹ may also have a significant contribution toward the steric factor. Furthermore effects like a pH-dependent change of the binding orientations of the protein^{122–124}, the conformation of the protein and the degree of oligomerization^{55,125–127} have to be considered. Moreover, the positive and negative surface areas of the protein were identified as key molecular descriptors in the quantitative structure–property relationship (QSPR) models of Ladiwala et al.⁷² for the shielding factor σ_i . A high positive charge of the protein lowers its steric factor σ_i where an increase of the negative surface area increases it. Both molecular descriptors depend on pH and consequently their contribution is also pH-dependent.⁷² Shi et al.⁵⁵ reported that pH-dependent conformational changes of their test protein bovine serum albumin (BSA) may lead to increased σ_i values. Bosma et al.⁶¹ and Bernau et al.¹²⁵ claimed that size exclusion effects may influence the magnitude of σ_i . Bernau et al.¹²⁵ argued that at pH values where proteins are more prone to aggregation a strong increase of σ_i is observed.

The aspects described show that the shielding factor σ_i is a complex parameter summing up several physicochemical characteristics of the target protein and the surface and ligand chemistry.¹ Non-steric protein-protein interactions of bound protein molecules are not per se neglected by this model.¹ For the therapeutic protein bsAbY no dependence of σ_i on column loading up to 50 mg_{bsAb}/mL_{resin} is observed. As already mentioned, deviations at higher loadings are predominantly caused by mass transport effects, conformational changes or multi-component effects, as discussed in section 4.5.2 and section 4.5.1. The importance of non-steric protein-protein interactions is only obtainable when these effects are minimized or explicitly considered in the model.

Since the pH-dependence of σ_i and ν_i is described, the pH-dependence of the maximal binding capacity $q_{max,i}$ is also described (see equation (41)). As the sum of σ_i and ν_i ($\sigma_i + \nu_i$) increases with increasing pH (see Figure 10A) the maximal binding capacity $q_{max,i}$ decreases. The data given in Table 21 show that $q_{max,i}$ decreases 2.3-fold when the mobile phase pH increases from 4.5 to 8.9. The strongest reduction of $q_{max,i}$ is between pH 4.5 and pH 6.0. These results demonstrate that $q_{max,i}$ becomes smaller the closer the pH value is to the IEP of the bsAb. This shows that the shielding of counterions described by σ_i has a larger effect on the value of $q_{max,i}$

than the stoichiometric exchange of counterions due to binding given by ν_i .¹ Shi et al.⁵⁵ also found a decreased $q_{max,i}$ at pH values close to the IEP. While Bosma et al.⁶¹ found no pH-dependence of $q_{max,i}$. Van der Wiel,¹²⁸ as well as Norde and Lyklema,¹²⁹ found also a dependence on pH but they determined a maximum in the binding capacity close to the IEP. These differently determined pH-dependences of $q_{max,i}$ could be an indication that the pH-dependence of $q_{max,i}$ strongly depends on the properties of the protein (e.g. shielding ability) and the ion exchange material (e.g. hydrophobicity⁶¹).¹

4.4.3 Verification of the pH-dependent SMA model

Parts of section 4.4.3 have already been published in a similar or identical form in Seelinger et al.¹ (Part 1, 2022) and in Seelinger et al.² (Part 2, 2022).

The results shown in this work demonstrate that constant values for σ_i , ν_i and $q_{max,i}$ should not be used when protein elution is described over an extended pH range. Hence, the determined parameters σ_i , ν_i and $q_{max,i}$ changed very strongly with pH. The pH-dependent models were validated with LGE experiments.

Thereby, the very good agreement between calculated σ_i values and determined σ_i values in Figure 10 proves that the pH-dependent SMA model is capable to describe salt gradient elution under high loading conditions at different pH values. The question was now how well the model can describe the elution within linear pH gradients. Figure 11 clearly shows how much the values of the parameters σ_i , ν_i and $q_{max,i}$ calculated with the pH-dependent SMA model vary over a pH gradient from pH 4.5 to 9.3. The functionality of these calculated pH-dependences was successfully demonstrated using simulated linear pH and dual gradient elutions experiments performed under high loading and overloading conditions using the sample bsAbY (see Figure 12 and Figure 13). Besides the correct description of peak retentions, especially the peak shapes were described very precisely for the most part. The agreement between simulated and experimental data at column loadings up to $75 \text{ mg}_{\text{bsAb}}/\text{mL}_{\text{resin}}$ is excellent for the most part. Kumar et al.³⁸ has already mentioned that when reviewing other papers, one often finds problems in describing peak shapes under high loading and overloading conditions. However, the pH-dependent SMA model developed and used during this work was able to describe the peak shapes precisely. It should be mentioned that neither pH gradients nor dual gradients were used for calibration of the binding model in the non-linear range of the

adsorption isotherm. Only the $k_{eff,i}$ values of the lumped rate model for the description of mass transfer were adjusted to the individual linear pH and dual gradients. As can be seen in Table 22, the $k_{eff,i}$ values of the individual linear pH and dual gradients decrease with increasing column loading, which presumably reflects the non-linear Langmuirian shape of the SMA adsorption isotherms at these high protein concentrations. This means, additionally to the pH- and salt-dependence, the dependence on the protein concentration of the isotherm slope is considered by these estimated $k_{eff,i}$ values. However, the accurate prediction of the peak shape within the linear pH gradients is most probably a consequence of the pH-dependent model parameters v_i and σ_i . In particular, as already stated by Saleh et al.,⁵⁷ the introduction of the pH-dependence of σ_i improves the ability of the model to predict experiments with changing pH carried out under high loading conditions. It is also noteworthy that the pH-dependent single-component SMA simulation is even capable of describing the observed double-peak formation (see Figure 12), however, with slight deviations in the shape description. Double-peak elution within linear pH gradients has already been observed by Briskot and co-workers.³⁶ Briskot et al.³⁶ used a CPA model which considers protein-protein interactions to describe this complex elution behavior. The double-peak elution behavior of a mAb in pH gradients can thus be partially described at high loading conditions (130 % of DBC) but fails at a load of 60 % of DBC. However, in this work, the supposedly more limited and simpler SMA model is also able to simulate this double-peak formation. As just mentioned, only the height of the maxima of the simulated elution profile and the experimental elution profile do not fully match (see Figure 12). At 75 mmol/L Na⁺, the protein eluted at higher pH values between pH 6 and pH 9. Further investigations showed that similar to the salt gradients, the charge variant distribution plays an important role at these higher pH values. Precise predictions of peak shapes are only possible with multi-component simulations. This means that the slight deviations in the description of the peak shapes were not a consequence of limitations of the pH-dependent SMA model. Moreover, it was a consequence of the fact that a simulation with only one variant was not sufficient to obtain optimal results. Further investigations and corresponding multi-component simulations of the pH gradients at 75 mmol/L Na⁺ are shown in section 3.6.1.2 and are discussed in section 4.5.1.2. Furthermore, under column loadings of 75 mg_{bsAb}/mL_{resin} and especially 90 mg_{bsAb}/mL_{resin}, overloading phenomena like sample breakthroughs were observed

as well as pre-shoulders and additional pre-peaks. These overloading phenomena were mainly caused by intraparticle diffusion effects⁷³⁻⁷⁷ and conformational changes^{11,78,80,81} of the sample bsAbY. Both hindered intraparticle diffusion and conformational changes were a consequence of high binding strengths due to low pH and low Na⁺ concentrations during sample loading. The reasons why these overloading phenomena occur and why the simulation cannot describe them are explained in section 4.5.2.

Conclusively, these results show that despite the relatively simplistic nature of the SMA mechanistic model, it can be used to predict protein elution over wide ranges of pH, salt concentrations and column loading. Especially, when the SMA model is extended with an activity coefficient for the salt in solution and with pH-dependent model parameters, as applied in this work.

4.5 Complex high loading and overloading phenomena when using bsAbY

4.5.1 High loading and column overloading phenomena at pH ≥ 6.0

Parts of section 4.5.1, including the subsections 4.5.1.1 and 4.5.1.2, have already been published in a similar or identical form in Seelinger et al.¹ (Part 1, 2022) and especially in Seelinger et al.² (Part 2, 2022).

In the results sections - section 3.5.1, section 3.5.3.2, and section 3.6 - it is shown that the applied model-based approach is partially unable to precisely predict bsAbY elution at high loading and overloading conditions when pH values of pH ≥ 6.0 were used. While the retention of the peaks could be well described, there were partial discrepancies in the simulation of the peak shapes for both the pH gradients and the salt gradients, similar to what was previously noted by Kumar and co-workers.³⁸ To find out if these discrepancies can be attributed to limitations of the SMA model or if there are other underlying reasons, the elution behavior of the protein sample bsAbY at high pH (pH ≥ 6.0) was thoroughly investigated (see section 3.6).

Analysis of the charge variant distribution of selected experiments showed that the elution of the individual charge variants plays a key role here. Competitive binding and multi-component elution of different variants can lead to complex peak shapes, which cannot be accurately described with a single-component simulation. The corresponding investigations and results from section 3.6 are discussed in the following sections 4.5.1.1 and 4.5.1.2.

4.5.1.1 bsAbY charge variants elution during linear salt gradients at pH 8.0

The distribution of bsAbY charge variants within the gradient elution of linear salt gradients at pH 8.0 and loadings of 5 and 75 mg_{bsAb}/mL_{resin} was investigated (see Figure 14). Thereby a clear difference can be seen: While the pre-variants and main variants were comparatively well separated at a loading of 5 mg_{bsAb}/mL_{resin} (Figure 14A/C), these variants eluted jointly at a loading of 75 mg_{bsAb}/mL_{resin} (Figure 14B/D). Normally, one would expect the stronger binding variants, which elute later, to displace the weaker binding variants. This is called the displacement effect, which occurs as a consequence of competitive binding between closely eluting components.¹¹⁶ This displacement effect should even enhance with increasing loadings, which may be recognized by the fact that the earlier eluting variant would always elute before the later eluting variant. However, this is definitely not the case here, as both variants elute jointly at a loading of 75 mg_{bsAb}/mL_{resin} (Figure 14B/D). This rather uncommon competitive binding behavior or respectively multi-component elution behavior leads to the fact that at a loading of 75 mg_{bsAb}/mL_{resin}, the main part of the peak was no longer influenced only by the main variants, as it was the case at 5 mg_{bsAb}/mL_{resin}. The main part of the peak at 75 mg_{bsAb}/mL_{resin} is influenced by all bsAbY charge variants, resulting in an unusually tall and narrow main elution peak. The result of this charge variant analysis explains why inverse fitting of the peaks at column loads of ≥ 50 mg_{bsAb}/mL_{resin} and pH ≥ 6.3 to determine σ_i was not feasible as shown in section 3.5.1. Additionally, these results demonstrate why discrepancies in the simulation of the bsAb's elution profiles within salt gradients with column loads of ≥ 50 mg_{bsAb}/mL_{resin} and pH ≥ 6.3 using the respective mean values $\bar{\sigma}_i$ were observed. This simultaneous elution between pre-variants and main variants changed the shape of the peaks at loadings of ≥ 50 mg_{bsAb}/mL_{resin} and pH ≥ 6.3 in such a way (uncommonly tall and narrow peaks) that the simulation could no longer describe the main peaks. However, when for the salt gradient at pH 8 and a loading of 75 mg_{bsAb}/mL_{resin}, the mass of pre-variants is subtracted from the total column load, the elution peak of the main variants is well described by the simulation (see Figure 14D). Despite simultaneous elution of pre-variants and main variants, the simulation describes the elution of the main variants at pH 8 and 75 mg_{bsAb}/mL_{resin} with very good agreement (see Figure 14D), as it is the case for non-simultaneous elution at 5 mg_{bsAb}/mL_{resin} (see Figure 14C).

Hence, the results in Figure 14C/D show that the elution of the main variants seems to be not affected by the co-elution of the pre-variants and that the σ_i values determined in section 3.5.1 were mainly influenced by the main variants. The tall and narrow peaks of the bsAb at pH 8.0 and $\geq 50 \text{ mg}_{\text{bsAb}}/\text{mL}_{\text{resin}}$ are caused mainly by a stacking of the peaks of the pre-variants and main variants. The peak shape of the main variants does not seem to be affected at all by the simultaneous elution of the pre-variants. To confirm this observation, the elution curves of the main variants of the linear salt gradient at pH 8.0 were fitted at column loadings of 5 and 75 $\text{mg}_{\text{bsAb}}/\text{mL}_{\text{resin}}$ (see Figure 14) by varying σ_i , using only the loading of the main variants for simulation (~81 % of the total load). For 5 $\text{mg}_{\text{bsAb}}/\text{mL}_{\text{resin}}$ a σ_i value of 118.75 and for 75 $\text{mg}_{\text{bsAb}}/\text{mL}_{\text{resin}}$ a σ_i value of 121.25 was determined (simulations not shown). These two estimated values are comparable to the mean $\bar{\sigma}_i$ with a value of 120.13 determined in section 3.5.1. These new fittings of the σ_i values only with the elution profiles of the main variants thus prove again clearly that the main variants have significantly influenced the determined σ_i values shown in section 3.5.1.

The results just discussed demonstrate that the discrepancies in simulating peak shapes of linear salt gradients at pH ≥ 6.3 performed with column loadings of $\geq 50 \text{ mg}_{\text{bsAb}}/\text{mL}_{\text{resin}}$ is not a consequence of limitations or shortcomings of the applied SMA model. It is a consequence of complex competitive binding and multi-component elution behavior. The elution profiles are clearly influenced by multi-component elution phenomena which could not be described for the complete elution profiles with only one simulated variant. Only the elution behavior of the main variants could be described, but with very good and convincing accuracy.

4.5.1.2 bsAbY charge variants elution during linear pH gradients at 75 mmol/L Na⁺

Complex binding and elution behavior was observed for the linear pH gradient elution experiments with fixed Na⁺ concentrations of 75 mmol/L, where the protein eluted within a pH range of pH 6 to pH 9. Thereby, the retention of the main elution peaks could be well described with the single-component simulations applying the pH-dependent descriptions of the linear and non-linear model parameters, however, discrepancies in the description of the peak shapes were observed under high loading conditions ($\geq 25 \text{ mg}_{\text{bsAb}}/\text{mL}_{\text{resin}}$). At column loadings of 75 and 90 $\text{mg}_{\text{bsAb}}/\text{mL}_{\text{resin}}$, even sample breakthrough is observed and the main part of the protein elutes as clear double-peaks. The breakthrough and pre-peaks indicate that the column was overloaded with bsAbY at these loading conditions (pH 4.5 and

75 mmol/L Na⁺). The breakthroughs and pre-peaks, despite high binding strengths due to low pH and low Na⁺ concentration, were a consequence of pH- and salt-dependent intraparticle diffusion effects^{73–77} and conformational changes^{11,78,80,81} of the bsAbY sample, which will be discussed in section 4.5.2. Since the applied model does not include a description for these types of overloading effects, breakthroughs and pre-peaks are not simulated. When the amount of protein in the breakthrough and the pre-peaks was subtracted from the mass of protein used in the simulation, the single-component simulation could predict the elution of the main elution peaks quite well (see Figure 12 and Figure 15). The single-component simulation was even capable of predicting the double-peak formation which is a consequence of the pH-dependent model parameters v_i and σ_i . However, the maxima of the simulated double-peaks are on the left side, while the experimental elution profiles each show a maximum on the right side. The analyses of the charge variant distribution at loadings of 50 and 90 mg_{bsAb}/mL_{resin} showed that the distribution of the pre-variants and main variants were not the main reason for the double-peak formation, but did influence the complex shape of the elution peak (see Figure 15). In contrast to the salt gradients at pH 8, the pre-variants and the main variants seem to have an influence on each other during the pH gradient experiments performed under high loading and overloading conditions. This could be a consequence of competitive binding and displacement effects.¹¹⁶ Displacement of the pre-variants by the more strongly binding main variants shifts the elution of the pre-variants to the peak front. The higher the loading, the lower the pH values at which the pre-variants elute within the linear pH gradient. As can be seen in Figure 15, the main variant peak (blue dots) still shows a shoulder, which is less pronounced compared to the single-component simulation (green line). The sum of the pre-variant peaks and the complex main variant peaks then also leads to complex bsAbY peaks, which can only be more precisely described with a multi-component simulation. Therefore, a multi-component model with two bsAbY species was used to predict the elution of the pre-variants and main variants. To do this, the pH-dependent v_i and σ_i parameters of the two variants were extended with factors, and these factors were then estimated. Therefore, the simulated elution profiles of the charge variants were directly fitted to the experimental elution profiles of the charge variants by varying the factors of v_i and σ_i , similar to what Rishawy et al.⁵⁸ and Saleh et al.⁵⁷ have already done in their work. Although this is a very rough description of the pH-dependent model parameters, it

worked at least for these pH-gradient runs. Therefore, a factor of 2.0 for σ_{pV} and of 0.98 for v_{pV} was determined for the pre-variant. For the main variant, a factor for σ_{MV} of 0.8 and a factor for v_{MV} of 1.00 was estimated. These results are in agreement with the findings of Saleh et al.,⁵⁷ who also found that the v_i values of mAb isoforms are quite similar, although the σ_i values differ greatly in some cases. The multi-component simulations computed with these values led to very good descriptions of the individual elution profiles of the pre-variants and main variants and the total bsAb concentration curve could now be described with very good agreement. While the single-component simulation can already predict the double-peak formation, the description of the elution profile of the total bsAb is significantly improved by the multi-component simulation (Figure 15, black line). The maxima of the multi-component simulation correctly match the maxima of the experimental elution profiles (see Figure 15).

The results shown in Figure 15 confirm the consideration that the discrepancies in simulating peak shapes of linear pH gradients performed under high loading conditions is not a consequence of limitations or shortcomings of the applied SMA model. It is a consequence of the simplification to describe the elution of the bsAbY with only one simulated variant. The elution profiles are clearly influenced by multi-component elution phenomena which could be confirmed by precise multi-component simulations using roughly estimated pH-dependent σ_i and v_i parameters. An application of the multi-component simulation method of Rischawy et al.⁵⁸ and Saleh et al.⁵⁷ for the entire high loading data set, however, was not possible. It would have been necessary to analyze all or at least a large part of the experiments performed at high loading conditions by CEX-HPLC. This would have meant far too much effort and was therefore not applicable. This method is therefore only an option in isolated cases, as shown with the pH gradients at 75 mmol/L Na⁺. Describing the entire bsAbY elution behavior using a single-component simulation still remains to be the best solution.

4.5.2 High loading and column overloading phenomena at pH \leq 5.3

Parts of section 4.5.2, including the subsections 4.5.2.1 and 4.5.2.2, have already been published in a similar or identical form in Seelinger et al.¹ (Part 1, 2022) and especially in Seelinger et al.² (Part 2, 2022).

At $\text{pH} \leq 5.3$ and column loadings of $\geq 50 \text{ mg}_{\text{bsAb}}/\text{mL}_{\text{resin}}$, complex high loading and column overloading phenomena like additional peaks, peak fronting, pre-shoulders, as well as unexpected sample breakthrough were observed. Separation of charge variants could be excluded by CEX-HPLC analyses, so other reasons must be behind it. Especially, the observation of strong sample breakthrough during loading was surprising since a high binding strength was expected at a low pH of 4.5 and a low Na^+ concentration of 50 mmol/L.

4.5.2.1 Influence of different Na^+ concentrations during loading on the sample breakthrough and the gradient elution

As already mentioned in the introduction (see section 1.2.3), some publications indicate that a high binding strength can significantly reduce the diffusion of the protein molecules into the ion exchanger beads which might explain observed overloading effects like unforeseen sample breakthrough.⁷³⁻⁷⁵ In particular, the salt concentration during loading has an impact on the binding strength and thereby influences the intraparticle diffusion.^{73,76,77} In addition, due to flexible linkers and additional domains, bsAbs can have a higher conformational flexibility than conventional mAbs and may generate molecular forms that bind with different binding affinities.^{11,78,80,81} Kimerer et al.⁸⁰ showed that the salt concentration during loading influences the conformation of their bsAb samples and demonstrated that lower Na^+ concentrations during loading led to the formation of stronger binding conformations.⁸⁰ Thereby, formation of additional peaks was observed by Kimerer and co-workers.⁸⁰ The tetravalent bsAb (bsAbY) used in this work has two additional CrossFab fragments added via linkers. Therefore, the tetravalent bsAb sample bsAbY could also form different conformations with different binding strengths at lower Na^+ concentrations, which might lead to peak fronting, peak shouldering, additional peaks, and could even affect breakthrough as well. Therefore, it was tested whether different Na^+ concentrations influence the binding and elution behavior of bsAbY.

4.5.2.1.1 Influence of different Na^+ concentrations during loading on the sample breakthrough

As shown in section 3.6.2.1, the effect of Na^+ concentration on binding was investigated by loading 75 mg bsAb onto the 1 mL column at Na^+ concentrations of 14.3, 50.0, 120.0, 200.0, and 250.0 mmol/L (see Figure 17). Thereby, it was

observed that when the Na^+ concentration was increased from 14.3 mmol/L Na^+ to 50.0 mmol/L Na^+ and then to 120 mmol/L Na^+ , the sample was progressively better bound by the column. At 200 mmol/L Na^+ , exactly as much protein was bound as at 120 mmol/L Na^+ . This means, the increase from 14.3 to 120/200 mmol/L Na^+ significantly increased the DBC of the column. Similar observations have been described by Harinarayan et al.⁷⁷ and can be explained by varying degrees of pore blocking,⁷⁷ by different surface diffusion rates,^{73–75} and pore diffusion rates,⁷⁵ all dependent on the binding affinity. This means that increasing the Na^+ concentration decreases the binding affinity, which promotes the transport of the protein into the chromatographic beads and ultimately leads to an increased DBC. An influence of conformation changes due to the different salt concentrations, as reported by Kimerer et al.⁸⁰ for other bsAbs could also play a role here. Indeed, the formation of stronger binding bsAb conformations at lower Na^+ concentrations, as observed by Kimerer and colleagues,⁸⁰ would further reduce intraparticle diffusion (pore and surface diffusion), as it would already be the case without conformation changes. Hence, it is possible that a combination of mass transport and reversible surface-induced conversion between differently strong binding molecular forms of the bsAbY are responsible for the observed breakthrough taking place at pH 4.5, especially at ≤ 50 mmol/L Na^+ .²

The applied model-based approach was not able to simulate the observed breakthroughs at low pH and Na^+ concentrations of ≤ 200 mmol/L (see Figure 18C.1-4). Since the breakthroughs at low pH and Na^+ concentrations of ≤ 200 mmol/L can be mainly attributed to hindered intraparticle diffusion, this is not a consequence of limitations of the binding model (SMA model) but of the mass transfer model (lumped rate model). Intraparticle diffusion is not considered in the applied lumped rate model⁷⁵ and thus cannot be described. A more comprehensive mass transfer model (e.g. general rate model (GRM)⁹⁹) should be considered for more accurate description. This more comprehensive mass transfer model should consider surface and pore diffusion, adsorption kinetics, and interconversion between different species. However, more comprehensive models such as the GRM are much more complex than the lumped rate model used and require the determination of significantly more model parameters.⁹⁹ The chosen lumped rate model is a simple and application-friendly model, which in most cases allowed simulations of outstanding quality in combination with the used binding models.

Interestingly, at a Na^+ concentration of 250.0 mmol/L Na^+ , the binding strength was reduced too much, which ultimately decreased the DBC significantly. This also explains the steep rise of the breakthrough curve after about 55 mg of loaded bsAb (see Figure 17). After a minor correction of the sample Na^+ concentration in the simulation from 250 to 261 mmol/L Na^+ , the model was able to describe the breakthrough with good agreement (see Figure 18C.5). This shows that breakthroughs due to decreased binding strength can be described quite well by the applied models.

4.5.2.1.2 Influence of different Na^+ concentrations during loading on the gradient elution

As shown by the results (see section 3.6.2.2), the Na^+ concentration during loading at a pH of 4.5 has a crucial effect on gradient elution. The lower the Na^+ ion concentration during loading, the lower the loadings where high loading and overloading phenomena occurred and the more pronounced these phenomena were (see Figure 18).

When the sample was loaded at 14.3 mmol/L Na^+ (see Figure 18A-C.1), additional peaks due to monomeric bsAb conformations were observed at all tested column loadings (25 to 75 $\text{mg}_{\text{bsAb}}/\text{mL}_{\text{resin}}$). The occurrence of bsAb conformations means that different monomeric bsAb forms are emerging, that bind with different binding strengths leading to the formation of peak-shoulders and additional peaks. While the single-component simulation was not able to describe this elution profiles correctly (see Figure A-C.1), a two-variant simulation was used to get a very good agreement between simulated and experimental data. Thereby the main elution peak and the post-peak were well-described. Only at overloading conditions (load = 75 $\text{mg}_{\text{bsAb}}/\text{mL}_{\text{resin}}$), the description of the simulated peak shape of the main peak deviates slightly from the experimental main peak. Interestingly, the same shielding factor σ_i could be used for the later eluting conformational variant as for the main variant. This confirms the SE-HPLC analyses, which showed that the later eluting conformations are monomeric.

When 25 mg bsAb were loaded with 50.0, 120.0, 200.0 and 250.0 mmol/L Na^+ , the elution peaks look almost identical and the simulation could describe all these peaks very well.

When 50 mg bsAbY were loaded with 120.0, 200.0 and 250.0 mmol/L Na^+ , the elution peaks look almost identical and the simulation could describe all these peaks

very well. In comparison, the elution peak where 50 mg bsAbY sample was loaded onto the column with 50.0 mmol/L Na⁺ was somewhat broader and lower because it had a very thin but high shoulder in the peak front, which occurs presumably as a consequence of conformational changes. However, the agreement of the single-component simulation with the main elution peak is still quite good when the determined mean value for pH 4.5 of the shielding factor $\bar{\sigma}_i$ was used.

When 75 mg bsAb were loaded, dome-shaped main elution peaks with fronting were observed in all cases. Additional peaks were observed when the sample was loaded with ≤ 50 mmol/L Na⁺, probably as a consequence of conformational changes. However, it can be observed that these high loading and overloading effects become less with higher Na⁺ concentration during loading and the simulation describes the main elution peaks better and better. For loadings with 120 and 200 mmol/L Na⁺ no additional peaks are seen anymore, only slight fronting and pre-shoulders are seen. At loading with 250 mmol/L Na⁺, no more high-loading phenomena are seen during gradient elution, and the simulation was able to describe the complete elution profile very well after correcting the Na⁺ loading concentration to 261 mmol/L Na⁺. These breakthroughs, frontings, pre-peaks, pre-shoulders, and post-peaks observed at column loadings of 75 mg_{bsAb}/mL_{resin} can be attributed to hindered intraparticle mass transfer and likely to the reversible surface-induced generation of various bsAb conformations that bind with different adsorption affinities^{11,78,80}. In the case of the tetravalent bsAb used in this work, this seems to occur mainly at strong binding conditions (low pH and low salt) and high column loadings (≥ 75 mg_{bsAb}/mL_{resin}). Interestingly, Kimerer et al.¹¹ also found for their bivalent bsAbs that lower Na⁺ concentrations during loading favored the formation of additional peaks. Thereby, species were formed that eluted later which was similarly observed in this work with sample loading at 14.3 mmol/L Na⁺. The observations of Kimerer and colleagues,¹¹ that lower Na⁺ ion concentrations during loading lead to additional peaks due to conformation changes of bsAbs can thus be confirmed in this work. However, in this work, earlier eluting monomeric conformations (pre-peaks) and later eluting monomeric conformations (post-peaks) were detected. Due to the fact, that the pre-peaks, the pre-shoulders, as well as the post-peaks occurred due to these bsAb-specific conformations, extending the single-component simulation to a multi-component simulation by manually adjusting the v_i values and areas of the individual peaks already improves the description of these complex elution profiles,

as shown in Figure 19 for the salt gradients with loading at 14.3 mmol/L Na⁺. However, this is a rather simplified approach. It would be better to extend the classical SMA model to describe multi-state binding mechanistically, as already shown by Kimerer et al.,^{11,78} as well as by Diedrich and co-workers.⁶⁷ Correct description of the fronting, the additional peaks and the pre-shoulders would then also improve the description of the main peaks.

4.5.2.2 Influence of different flow rates (loading times) during loading on the sample breakthrough and the the gradient elution

Kimerer et al.¹¹ already showed that besides Na⁺ concentration, residence time and hold time can also influence the formation of different bsAb conformations. This means that the longer the bsAb sample is bound by the column, the more these reversible surface-catalyzed conformational changes occur. In this work, the loading time t_{load} was varied for this purpose by varying the flow rate used for loading. Thereby, the results shown in section 3.6.2.3 demonstrate that a prolonged loading time leads to increased conversion of early eluting monomeric species into monomeric species with higher binding affinities. The longer the loading time, the less breakthrough is seen and the more later binding conformational variants of the bsAbY sample are seen (see Figure 20). This is consistent with the observations of Kimerer et al.,¹¹ who found that a hold time of 60 min after loading resulted in more pronounced later eluting peaks and less pronounced earlier eluting peaks. The findings by Kimerer et al.¹¹ and this work demonstrate that the time in which the sample binds or is bound has a significant effect on the subsequent elution profile, at least if the protein undergoes conformational changes. However, in this work, these earlier eluting peaks appear only at overloading conditions ($\geq 75 \text{ mg}_{bsAb}/\text{mL}_{resin}$). Later eluting peaks were already detectable at $25 \text{ mg}_{bsAb}/\text{mL}_{resin}$, and were particularly pronounced after loadings at 14.3 mmol/L Na⁺. In Kimerer et al.,¹¹ formation of multiple peaks is observed even at low loading conditions.

The simulation was able to describe retention of the main peaks for the three experiments with the different loading times, but peak shape, breakthrough, pre-peaks, and pre-shoulders could not or only partially be described (see Figure 20). As noted previously, description of these overloading phenomena would require a multi-state SMA model in combination with a more comprehensive mass transfer model. Such a model-based approach, however, would be significantly more complicated than the combination of SMA model and lumped rate model used in this work.

4.6 Modeling the binding and elution behavior of bsAbX in the non-linear range of the adsorption isotherm using a modified SAS-SMA model

4.6.1 Determination of the pH-dependent non-linear model parameters $K_{p,i}$, $K_{eq,2,i}/c$, and σ_i

Parts of section 4.6.1 are also included in a similar or identical form in Seelinger et al.³ (DRAFT (submitted)).

The pH-dependent model parameters $K_{p,i}$, $K_{eq,2,i}/c$, σ_i , as well as the lumped parameter $k_{eff,i}$, determined as described in section 2.2.5, are listed in Table 23 along with their corresponding standard deviations. As can be seen, the standard deviations of each parameter, determined from the five best fits, are comparatively small. This proves that the fits performed are very robust and stable. This means that for the best curve fits, very similar values were always determined. A so-called overestimation, which could be recognized by strongly fluctuating values, can thus be excluded. By using the determined model parameters listed in Table 23, all linear salt gradients could be described very well by the simulation, except for the runs at pH 4.5 and 5.3 with column loadings of $\geq 75 \text{ mg}_{\text{bsAb}}/\text{mL}_{\text{resin}}$. In these experiments, high loading and overloading phenomena such as unexpected breakthrough despite high binding strengths, additional peaks, peak fronting, and pre-shoulders were detected. Since these overloading phenomena at $\text{pH} \leq 5.3$ are very similar to those of bsAbY, it is quite possible that the overloading phenomena observed for bsAbX are also caused by slow intraparticle transport⁷³⁻⁷⁷ and conformational changes of the bsAb sample.^{11,78,80,81} Furthermore, competitive binding and displacement effects of the bsAb's charge variants could also play a role here, like it was observed for the pH gradient at 75 mmol/L Na^+ using the protein sample bsAbY (see sections 3.8 and 4.7). The single-component simulation was not able to predict the breakthroughs, the pre-peaks, and the peak-shoulders. However, by subtracting the mass of protein that formed the breakthroughs, pre-peaks and pre-shoulders, at least the main elution peaks of the runs conducted at 75 and 90 $\text{mg}_{\text{bsAb}}/\text{mL}_{\text{resin}}$ could be well described by the applied single-component simulation (see Figure 21 and Figure 35). To simulate these overloading phenomena, the mass transfer model has to be extended or has to be replaced by a more comprehensive model (e.g. GRM⁹⁹) to enable the description of intraparticle diffusion. Furthermore, the SAS-SMA model has to be extended to describe multi-state binding, as already done by Kimerer et

al.^{11,78} and Diedrich et al.⁶⁷ for the SMA and SD models. Moreover, the simulation has to be extended to describe multi-component elution.^{2,57,58} While these changes would most likely improve the quality of the chromatogram simulations, they would significantly increase the complexity of the overall modeling approach, which probably makes it unattractive for industrial applications.

With the $k_{eff,i}$ values estimated under high loading and overloading conditions (see Table 23), the load-dependence of the isotherm slope is now considered in addition to the pH- and salt-dependence. Thereby, the non-linear sigmoidal⁶⁵ slope of the SAS-SMA adsorption isotherms is reflected, which allows a suitable description of the peak shapes observed under high loading and overloading conditions.

The estimated pH-dependent model parameters $K_{p,i}$, $K_{eq,2,i}/c$, and σ_i are discussed in the following two sections.

4.6.2 Empirical descriptions of the pH-dependent parameters $K_{p,i}$ and $K_{eq,2,i}/c$

Parts of section 4.6.2 are also included in a similar or identical form in Seelinger et al.³ (DRAFT (submitted)).

With the pH-dependent values for $K_{p,i}$ listed in Table 23, an empirical correlation could be established. (see equation (42)). By using a determined value of 63.243 for the constant $K_{p,i}^*$ in equation (42), positive values are calculated for $K_{p,i}$ in the described pH range (see Figure 23). Positive values for $K_{p,i}$ mean that water-protein interactions outweigh protein-protein interactions in the mobile phase⁹⁵, which indicates that self-dimerization occurs on the stationary phase and not in the mobile phase.⁶⁵ With the pH-dependent values for $K_{eq,2,i}/c$ an empirical correlation could be derived (see equation (43)). By using a determined value of 130.130 for the constant $K_{eq,2,i}^*/c$ in equation (43), likewise, positive values for $K_{eq,2,i}/c$ are calculated in the described pH range (see Figure 23). Positive values for $K_{eq,2,i}/c$ demonstrate that self-dimerization on the resin surface is predicted. It can be seen in Figure 23 that the calculated values for both $K_{p,i}$ and $K_{eq,2,i}/c$ decrease with increasing pH. A reduction in the values of both parameters with increasing pH indicates that self-dimerization on the resin surface becomes weaker with increasing pH.

The calculated positive values for $K_{p,i}$ and $K_{eq,2,i}/c$ lead to the prediction of increased binding capacities by the SAS-SMA model, as can be seen from the fact

that with a σ_i value of zero the simulated peaks are shifted towards higher retention times compared to the simulated peak calculated by the SMA model. (see Figure 24).

4.6.3 Semi-empirical description of the pH-dependent shielding factor σ_i in the SAS-SMA model

Parts of section 4.6.3 are also included in a similar or identical form in Seelinger et al.³ (DRAFT (submitted)).

The shielding factors σ_i determined for bsAbX are increasing with pH (see Figure 25). As already discussed in section 4.4.2, the shielding factor σ_i is a complex parameter that, in addition to steric hindrance⁴⁴, is influenced by repulsive effects⁷², by lateral protein-protein interactions¹²¹, different binding orientations of the protein^{122–124}, different conformations of the protein and the degree of oligomerization^{55,125–127}, etcetera. The σ_i values determined for bsAbX are lower than those determined for bsAbY, however, the change of σ_i over pH for bsAbX is quite comparable to that of bsAbY. This is also shown by the fact that for both antibodies and thus also for both models (SMA and SAS-SMA model) almost the same semi-empirical equations can be used to describe the pH-dependences of the shielding factors σ_i . The semi-empirical equation (44), which was used in the SAS-SMA model, only had to be extended by the variable m_i compared to equation (40), which was used in the SMA model. This means, with m_i and $v_{pH=0,i}$, only two parameters must be determined to describe the pH-dependence of σ_i . The semi-empirical function with estimated values of 0.256 and 37.829 for m_i and $v_{pH=0,i}$, respectively, describes the change of the experimental values for σ_i over their respective pH (Figure 25A) and v_i (Figure 25B) values very well, as shown by the solid lines. As can be seen in Figure 10B, the decrease of σ_i is a non-linear function of v_i . At smaller v_i values (i.e. higher pH) the σ_i values decrease more strongly, than for larger v_i values, similar as it was the case with bsAbY (compare with Figure 10B). The transition region is at a pH value of about 5.0 to 5.5.

As it is the case for bsAbY, the theoretical maximal binding capacity $q_{max,i}$ of bsAbX is also pH-dependent. For bsAbX, the maximal binding capacity $q_{max,i}$ increases marginally between pH 3.7 to pH 4.8, since the sum of σ_i and v_i (σ_i+v_i) decreases slightly in this range with increasing pH (see Figure 25A). The decrease in σ_i+v_i from pH 3.7 to pH 4.8 occurs because in this pH range v_i is dominant compared to σ_i and

decreases strongly here (see Figure 6). From pH 4.8 to pH > 8.0, $q_{max,i}$ decreases significantly because $\sigma_i + \nu_i$ increases (see Figure 25A). The data given in Table 23 show that $q_{max,i}$ decreases 1.2-fold when the mobile phase pH increases from 4.5 to pH 7.0. These results demonstrate that $q_{max,i}$ overall decreases as the pH approaches the IEP (~ 8.6) of bsAbX. As with bsAbY, the results for bsAbX thus show that the shielding of counterions described by σ_i has generally a larger effect on the value of $q_{max,i}$ than the stoichiometric exchange of counterions due to binding given by ν_i . However, in the case of bsAbX $q_{max,i}$ is not as strongly dominated by σ_i as is the case for bsAbY. This supports the conclusion drawn in section 4.4.2 that the pH-dependence of $q_{max,i}$ is strongly dependent on, among other things, the properties of the protein (e.g. shielding capacity).

4.6.4 Verification of the pH-dependent SAS-SMA model

Parts of section 4.6.4 are also included in a similar or identical form in Seelinger et al.³ (DRAFT (submitted)).

The results shown in this work demonstrate that constant values for σ_i , ν_i , $q_{max,i}$, $K_{p,i}$ and $K_{eq,2,i}/c$ should not be used when protein elution is described over a broad pH range. Thereby, the very good agreement between calculated and determined σ_i values in Figure 25, as well as the very good agreement between calculated and determined $K_{p,i}$ and $K_{eq,2,i}/c$ values in Figure 23 demonstrate that the pH-dependent SMA model is capable to predict salt gradient elution under high loading conditions at different pH values. This is also shown in Figure 24D, where the pH-dependent SAS-SMA model was able to describe the salt gradient elution at pH 5.3 with a loading of 25 mg_{bsAb}/mL_{resin} with very good agreement. The question was now how well the model can describe the elution within linear pH gradients. Figure 26 shows how the calculated model parameters ν_i , σ_i , $q_{max,i}$, $K_{p,i}$ and $K_{eq,2,i}/c$ change over a linear pH gradient from pH 4.5 to 9.3. The model parameters ν_i , σ_i , as well as $q_{max,i}$ behave quite similarly to those in the SMA model, and their pH-dependences do not show any significant differences. However, it is interesting to investigate the behavior of the non-linear model parameters $K_{p,i}$ and $K_{eq,2,i}/c$, which account for the protein-protein interactions. Both parameters, $K_{p,i}$ and $K_{eq,2,i}/c$, decrease over the increasing linear pH gradient, whereby it is noticeable that both parameters drop sharply in value up to a pH of 5.6 and then decrease significantly less in value with increasing pH. This

clearly shows that especially at low pH values ($\text{pH} < 5.6$) the protein-protein interactions on the resin surface are strongest.

The $k_{eff,i}$ values of the lumped rate mass transfer model were adjusted individually for each pH gradient. As can be seen in Table 24, for each linear pH gradient, decreasing values for $k_{eff,i}$ were determined with increasing column loadings from 25 to 90 $\text{mg}_{\text{bsAb}}/\text{mL}_{\text{resin}}$, thereby reflecting the non-linear slope of adsorption isotherms at these high column loadings.

In Figure 12, it can be seen that the pH-dependent SAS-SMA model predicts the retentions and the peak shapes very well up to a load of 50 $\text{mg}_{\text{bsAb}}/\text{mL}_{\text{resin}}$. Accurate prediction of the peak shapes is based on the interplay between the pH-dependent model parameters v_i , σ_i , $K_{p,i}$ and $K_{eq,2,i}/c$ which optimally adjust their values to the changing pH. This allows the correct simulation of anti-Langmuirian elution behavior even within pH gradients. These simulations again demonstrate the importance of describing the pH-dependence of non-linear parameters (σ_i , $q_{max,i}$, $K_{p,i}$ and $K_{eq,2,i}/c$) when pH gradient elutions must be simulated under high loading conditions.

At column loadings of 75 and 90 $\text{mg}_{\text{bsAb}}/\text{mL}_{\text{resin}}$, retention of the main elution peaks is well described at all Na^+ concentrations. At a column loading of 75 $\text{mg}_{\text{bsAb}}/\text{mL}_{\text{resin}}$, the prediction of the peak shape at 200 mmol/L Na^+ is still very good, however, slight deviations can be seen at 120 and 75 mmol/L Na^+ which is mainly caused by the formed pre-shoulders. At a column loading of 90 $\text{mg}_{\text{bsAb}}/\text{mL}_{\text{resin}}$, the deviations at 120 and 75 mmol/L Na^+ are even more noticeable, mainly due to the more pronounced pre-shoulders and the clear breakthrough. The breakthroughs occurred because of the binding at pH 4.5 and are a consequence of hindered intraparticle diffusion⁷³⁻⁷⁷ due to high binding affinities, as shown in section 3.8 and discussed in section 4.7. The pre-shoulders were a consequence of enrichment of the pre-variants on the peak front, as a consequence of competitive binding and displacement effects, as shown in section 3.8 and discussed in section 4.7. Since the combination of lumped rate mass transfer model and single-component SAS-SMA model is not capable to describe such phenomena, these shoulders and breakthroughs could not be described.

In conclusion, the results demonstrate that the relatively simple lumped rate and SAS-SMA models were able to describe complex anti-Langmuirian high loading elution behavior and partially also overloading elution behavior over wide ranges of pH, salt concentrations and column loading. This demonstrates the tremendous capabilities of

the model, especially, when the SAS-SMA model is extended with an activity coefficient for the salt in solution, with an activity coefficient for the protein in solution, and with pH-dependent model parameters, as applied in this work.

4.7 Complex high loading and overloading phenomena when using bsAbX

Parts of section 4.7 are also included in a similar or identical form in Seelinger et al.³ (DRAFT (submitted)).

By using bsAbX, complex high loading and overloading phenomena in the form of breakthrough despite high binding strengths and pre-shoulders were investigated with the linear pH gradients at 75 mmol/L Na⁺ with column loadings of $\geq 75 \text{ mg}_{\text{bsAb}}/\text{mL}_{\text{resin}}$. Here, the sample was loaded onto the column at pH 4.5 with 75 mmol/L Na⁺. Breakthrough was also observed for the salt gradients at pH ≤ 5.3 , where the sample was loaded with 50 mmol/L Na⁺, when $\geq 75 \text{ mg}$ of bsAbX were loaded onto the 1 mL column. This means, despite high binding affinities due to the low pH and low Na⁺ concentrations, these breakthroughs occurred. As seen in Figure 29, no enrichment or separation of charge variants was observed in the breakthrough from the pH gradient with 75 mmol/L Na⁺ with a loading of $75 \text{ mg}_{\text{bsAb}}/\text{mL}_{\text{resin}}$. The analyses by CEX-HPLC showed an identical pattern of charge variants between the analysis of the bsAbX sample which was used for injection and the analyses of the samples from the breakthrough fractions. This means that the sample broke through as it was loaded onto the column, an enrichment of individual charge variants could not be determined. Hence, the breakthrough did not occur because of competitive binding and displacement effects,¹¹⁶ because, if weaker-binding charge variants were displaced by stronger-binding charge variants, an enrichment of weaker-binding charge variants should have been observed in the breakthrough. As shown in Figure 28, additional linear pH gradient elution experiments at 75 mmol/L Na⁺ were performed with loadings of $75 \text{ mg}_{\text{bsAb}}/\text{mL}_{\text{resin}}$, where the sample was loaded onto the column once at an increased Na⁺ concentration of 175 mmol/L and once at a halved flow rate of 0.34 mL/min. The increased Na⁺ concentration and the doubled loading time significantly reduced the breakthrough in each case. This proves that the breakthroughs of the antibody bsAbX at low pH and low Na⁺ concentrations, as with bsAbY, occurred due to hindered intraparticle diffusion and possibly also due to conformational changes of the antibody sample. In any case, to describe breakthroughs at low pH, one would need to apply a more comprehensive but also

significantly more complex mass transfer model such as the GRM,⁹⁹ which is able to describe hindered surface diffusion, hindered pore diffusion and also pore blocking.² While the increased Na⁺ concentration and doubled loading time each significantly decreased sample breakthrough, they had very little or even no effect on the elution within the gradient (see Figure 28). However, Figure 29 shows that the formation of the pre-shoulder is due to an enrichment of the pre-variants. This enrichment of pre-variants most likely occurs only under overloading conditions and is presumably a consequence of competitive binding and displacement between the individual charge variants. This means, while competitive binding and variant displacement play no role in the formation of the breakthroughs, the situation is different for the elution within the gradients. According to Golshan-Shirazi and Guiochon,¹¹⁶ displacement effects only occur under high loading and overloading conditions, whereby in this work, these pre-shoulders as a consequence of charge variant displacement are only seen under overloading conditions. These complex multi-component elution profiles and the influence of the individual charge variants on each other due to competitive binding¹¹⁶ and displacement effects¹¹⁶ thus explain why the single-component simulation could not describe these bsAbX gradient elution profiles completely under overloading conditions. However, a description of the elution profiles using multi-component simulation was not possible. The use of variant-specific v_i , σ_i , $K_{p,i}$ and $K_{eq,2,i}/c$ values led neither to meaningful combinations of parameter values nor to robust fits. The determination of four different pH-dependent variables probably led to a so-called overestimation. As explained in section 4.1.2, it was not possible to isolate the pre-variants and main variants in sufficient amounts and purity, since the two variants always eluted too closely together. Thus, a separate modeling of both variants was not possible. The use of single-component simulations was unavoidable and mostly led to excellent predictions of the bsAbX elution profiles.

4.8 Conclusion

Parts of section 4.8 have already been published in a similar or identical form in Seelinger et al.¹ (Part 1, 2022) and in Seelinger et al.² (Part 2, 2022). Parts of section 4.8 are also included in a similar or identical form in Seelinger et al.³ (DRAFT (submitted)).

The modified SMA and SAS-SMA models presented in this work include pH-dependent linear (v_i and $K_{eq,i}$) and pH-dependent non-linear (σ_i , $K_{p,i}$ and $K_{eq,2,i}/c$)

model parameters. Thereby, the models are modified by the addition of simple empirical equations to predict the non-linear model parameters σ_i , $q_{max,i}$, $K_{p,i}$ and $K_{eq,2,i}/c$ as functions of pH. As also written in Seelinger et al.,¹ to the best of the authors' knowledge, this is the first scientific work in which the pH dependence of the steric shielding factor σ_i has been described and consequently implemented into the SMA model, as well as now also into the SAS-SMA model.^{1,3} Since the non-linear model parameters $K_{p,i}$ and $K_{eq,2,i}/c$ were also described as a function of pH in the SAS-SMA model, both the SAS-SMA model and the SMA model are each fully described in a pH-dependent manner.¹⁻³ These fully pH-dependent SMA and SAS-SMA models could accurately predict linear salt, linear pH and linear dual gradient elution experiments performed under high loading and even overloading conditions. Due to the applied activity coefficients and the pH-dependent descriptions, both models were able to precisely predict the elution behavior of the therapeutic bsAbs over wide ranges of pH, salt-, and protein concentrations. The pH-dependent SMA model was able to describe the Langmuir's elution behavior of bsAbY under high loading conditions with the highest precision and for the most part also under overloading conditions. The SAS-SMA model was able to accurately describe the anti-Langmuir elution behavior of bsAbX under high loading and partially also under overloading conditions. The results shown in this work demonstrate the importance of considering pH-dependence in both the linear and non-linear range of the adsorption isotherm.

It is shown in this work that empirical extensions of mechanistic models can be an effective tool to improve the predictive power of a model. The benefit of empirically described pH-dependences of non-linear model parameters like the shielding factor σ_i is mainly the improved description of the elution peaks observed during pH and dual gradients. It was even possible to predict the formation of double-peaks using a single-component simulation.

The SMA and SAS-SMA models used in this work are both comparatively simple and have largely fixed formalisms due to their mechanistic nature. The observations of other publications^{36,38,43}, which often claim limitations in the non-linear range for stoichiometric models could not be found at all for the applied SMA and SAS-SMA models. As demonstrated in this work, effects like multi-component elution, intraparticle mass transport, and presumably bsAb conformational flexibility greatly impact the formation of complex elution profiles when high loading and overloading

conditions are applied. Interestingly, the therapeutic bsAbs used in this work show a combination of several of these phenomena responsible for the complex elution profiles. It could be shown that most of the observed discrepancies between simulated and experimental data were not caused by fundamental limitations of the SMA and SAS-SMA models. Rather, a too simple mass transfer model, the modeling with only one simulated variant, the neglect of multi-state binding as a consequence of multiple bsAb conformations etcetera were responsible for the observed discrepancies. However, this could only be found out thanks to extensive analyses and investigations. If necessary, the model-based approaches could be further modified to also describe the observed overloading phenomena. Extending the simple lumped rate mass transfer model to account for hindered intraparticle diffusion or even replacing the lumped rate model with an extended mass transfer model that includes surface and pore diffusion, as well as incorporating the kinetics of conformational changes of the bound protein into the models, may allow to describe the reported high loading and overloading phenomena at lower pH values ($\text{pH} \leq 5.3$). Activity coefficients for salt-salt and protein-protein interactions on the surface¹³⁰ could be added to the models. The SAS-SMA model could be extended to describe higher self-oligomerization such as three-layer binding.^{66,114,115} The used modeling approaches could be generally extended from single-component systems to multi-component systems.^{2,57,58} Or at least one could change the description of some further selected experiments from single-component simulation to multi-component simulation. For instance in section 3.6.1.2, it was already shown with the antibody bsAbY that the change from single-component simulation to multi-component simulation significantly improved the description of the bsAbs elution profile. Only with a multi-component simulation, competitive binding and displacement effects can be accurately described, which were responsible for complex peak shapes like pre-shoulder formation. Furthermore, extending the SMA and SAS-SMA models to describe multi-state binding, as already shown by Kimerer et al.^{11,78} and Diedrich et al.⁶⁷ for SD/SMA models, could help to simulate the shown additional peaks and pre-shoulders which occurred due to conformational changes of the bsAbs. In section 3.6.2.2, it was shown that an extension to a two-variant simulation by manually adjusting the binding charge of the later eluting variant resulted in a good description of a two-peak formation due to conformational changes of the bsAb. (see Figure 19). However, it must be considered that these extensions and modifications just

mentioned would most probably increase the predictive ability of the model, but also would increase the complexity of the model-based approach and would increase the effort required for it.

Due to the simplicity of the applied models and their fixed formalisms, as well as the straightforward methods for parameter determination, the applicability of the approach shown in this dissertation in industrial projects is very well conceivable. To make this approach even more attractive for use in the industry, a smaller process parameter space and less laborious batch experiments could be very well used to reduce the necessary effort and to save time.¹

5 SUMMARY

The binding and elution behavior of two therapeutic bispecific monoclonal antibodies (bsAbs) on the strong cation exchange resin POROS™ XS is investigated and modeled over broad ranges of pH, salt concentrations, and column loadings. One of the two bsAbs exhibits common Langmuir elution behavior under high loading and column overloading conditions, whilst the other bsAb exhibits uncommon anti-Langmuir elution behavior as a consequence of multi-layer binding on the stationary phase surface. The frequently used Steric Mass Action (SMA) model modified with an activity coefficient for the salt in solution is used to simulate the Langmuirian elution behavior. A Self-Association Steric Mass Action (SAS-SMA) model extended with two activity coefficients for the protein and salt in solution is applied to describe the anti-Langmuir elution behavior. The SAS-SMA model is able to describe self-dimerization on the resin surface and thus can predict anti-Langmuir elution behavior. The binding models are each combined with a lumped rate model to describe mass transfer inside the chromatography column.

To apply these models for describing protein elution over wide ranges of pH, the pH-dependences of all model parameters, including the linear and especially the non-linear model parameters, are investigated, described, and implemented into the binding models. Therefore, extensive data sets were generated that consist of linear gradient elution experiments comprising a pH range from pH 4.5 to 8.9 and column loadings from 0.5 to 90.0 mg_{bsAb}/mL_{resin}. The modeling results of both antibodies show that the pH of the mobile phase has a strong influence on the non-linear model parameters, thus valuable process insights can be gained by interpretation of these results. An increasing buffer pH leads to an increase in binding sites shielded by the antibodies, whilst self-dimerization on the resin surface becomes less with increasing pH. Empirical correlations describing the non-linear model parameters as functions of pH are established and implemented into the SMA and SAS-SMA formalisms. The functionality of these modified pH-dependent binding models is verified with linear salt, pH and dual gradient elution experiments using single-component simulations. Most of these experiments can be accurately predicted under high loading and overloading conditions, whereby especially the peak shapes are well-described. Slight discrepancies between the simulated and experimental data can be observed

for some of these experiments, especially when they were performed under overloading conditions.

In this dissertation, it is clearly shown that these discrepancies are not primarily a consequence of limitations of the SMA and SAS-SMA models. At lower pH values ($\text{pH} \leq 5.3$), overloading phenomena such as protein breakthrough during the loading phase, additional peaks, and peak-shoulders occur. The outcomes of additional experiments in which the antibodies were loaded onto the column with different counterion concentrations and loading times show that intraparticle diffusion effects and conformational changes of the bsAbs are responsible for these overloading phenomena at low pH. The applied lumped rate mass transfer model is not adequate here since it cannot describe hindered intraparticle transport and should be extended to consider these effects. Additional peaks and peak shoulders due to bsAb conformations can only be predicted by describing multi-state binding, which is shown in this dissertation for one case by a simple extension to a multi-component simulation. Furthermore, it is shown that the description of complex peak shapes arising due to competitive binding and multi-component elution of the antibodies' charge variants cannot be adequately predicted using single-component simulations. However, an extension of the model to a simple multi-component system consisting of two charge variants enables accurate prediction of some of these complex elution profiles.

6 REFERENCES

4. Kluters S: *Modeling of pH and solvent modulated chromatography for the purification of biopharmaceuticals*, 2016
5. Khawli LA, Goswami S, Hutchinson R, Kwong ZW, Yang J, Wang X, Yao Z, Sreedhara A, Cano T, Tesar D, Nijem I, Allison DE, Wong PY, Kao Y-H, Quan C, Joshi A, Harris RJ, Motchnik P: Charge variants in IgG1: Isolation, characterization, in vitro binding properties and pharmacokinetics in rats. *mAbs* 2(6): 613–24, 2010. doi:10.4161/mabs.2.6.13333
6. van Beers MMC, Bardor M: Minimizing immunogenicity of biopharmaceuticals by controlling critical quality attributes of proteins. *Biotechnology journal* 7(12): 1473–84, 2012. doi:10.1002/biot.201200065
7. Wang S, Chen K, Lei Q, Ma P, Yuan AQ, Zhao Y, Jiang Y, Fang H, Xing S, Fang Y, Jiang N, Miao H, Zhang M, Sun S, Yu Z, Tao W, Zhu Q, Nie Y, Li N: The state of the art of bispecific antibodies for treating human malignancies. *EMBO molecular medicine* 13(9): e14291, 2021. doi:10.15252/emmm.202114291
8. Chames P, van Regenmortel M, Weiss E, Baty D: Therapeutic antibodies: successes, limitations and hopes for the future. *British journal of pharmacology* 157(2): 220–33, 2009. doi:10.1111/j.1476-5381.2009.00190.x
9. Fekete S, Gassner A-L, Rudaz S, Schappler J, Guillaume D: Analytical strategies for the characterization of therapeutic monoclonal antibodies. *TrAC Trends in Analytical Chemistry* 42: 74–83, 2013. doi:10.1016/j.trac.2012.09.012
10. Marichal-Gallardo PA, Alvarez MM: State-of-the-art in downstream processing of monoclonal antibodies: process trends in design and validation. *Biotechnology progress* 28(4): 899–916, 2012. doi:10.1002/btpr.1567
11. Kimerer LK, Pabst TM, Hunter AK, Carta G: Chromatographic behavior of bivalent bispecific antibodies on cation exchange columns. I. Experimental observations and phenomenological model. *Journal of chromatography. A* 1601: 121–32, 2019. doi:10.1016/j.chroma.2019.04.012

12. Garber K: Bispecific antibodies rise again. *Nat Rev Drug Discov* 13(11): 799–801, 2014. doi:10.1038/nrd4478
13. Mahlangu J, Oldenburg J, Paz-Priel I, Negrier C, Niggli M, Mancuso ME, Schmitt C, Jiménez-Yuste V, Kempton C, Dhalluin C, Callaghan MU, Bujan W, Shima M, Adamkewicz JI, Asikanius E, Levy GG, Kruse-Jarres R: Emicizumab Prophylaxis in Patients Who Have Hemophilia A without Inhibitors. *The New England journal of medicine* 379(9): 811–22, 2018. doi:10.1056/NEJMoa1803550
14. Mullard A: Bispecific antibody pipeline moves beyond oncology. *Nat Rev Drug Discov* 16(10): 666–8, 2017. doi:10.1038/nrd.2017.187
15. Sedykh SE, Prinz VV, Buneva VN, Nevinsky GA: Bispecific antibodies: design, therapy, perspectives. *Drug design, development and therapy* 12: 195–208, 2018. doi:10.2147/DDDT.S151282
16. DiGiandomenico A, Keller AE, Gao C, Rainey GJ, Warrener P, Camara MM, Bonnell J, Fleming R, Bezabeh B, Dimasi N, Sellman BR, Hilliard J, Guenther CM, Datta V, Zhao W, Gao C, Yu X-Q, Suzich JA, Stover CK: A multifunctional bispecific antibody protects against *Pseudomonas aeruginosa*. *Science translational medicine* 6(262): 262ra155, 2014. doi:10.1126/scitranslmed.3009655
17. Brinkmann U, Kontermann RE: The making of bispecific antibodies. *mAbs* 9(2): 182–212, 2017. doi:10.1080/19420862.2016.1268307
18. NISONOFF A, WISSLER FC, LIPMAN LN: Properties of the major component of a peptic digest of rabbit antibody. *Science (New York, N.Y.)* 132(3441): 1770–1, 1960. doi:10.1126/science.132.3441.1770
19. NISONOFF A, Rivers MM: Recombination of a mixture of univalent antibody fragments of different specificity. *Archives of Biochemistry and Biophysics* 93(2): 460–2, 1961. doi:10.1016/0003-9861(61)90296-X
20. Mullard A: FDA approves first bispecific. *Nat Rev Drug Discov* 14(1): 7, 2015. doi:10.1038/nrd4531
21. Przepiorka D, Ko C-W, Deisseroth A, Yancey CL, Candau-Chacon R, Chiu H-J, Gehrke BJ, Gomez-Broughton C, Kane RC, Kirshner S, Mehrotra N, Ricks TK, Schmiel D, Song P, Zhao P, Zhou Q, Farrell AT, Pazdur R: FDA Approval: Blinatumomab. *Clinical cancer research an official journal of the*

- American Association for Cancer Research* 21(18): 4035–9, 2015. doi:10.1158/1078-0432.CCR-15-0612
22. Passariello M, Yoshioka A, Takahashi K, Hashimoto S, Rapuano Lembo R, Manna L, Nakamura K, Lorenzo C de: Novel Bi-Specific Immuno-Modulatory Tribodies Potentiate T Cell Activation and Increase Anti-Tumor Efficacy. *IJMS* 23(7): 3466, 2022. doi:10.3390/ijms23073466
 23. Zhang Z, Luo F, Cao J, Lu F, Zhang Y, Ma Y, Zeng K, Zhang L, Zhao H: Anticancer bispecific antibody R&D advances: a study focusing on research trend worldwide and in China. *Journal of hematology & oncology* 14(1): 124, 2021. doi:10.1186/s13045-021-01126-x
 24. Wu Y, Yi M, Zhu S, Wang H, Wu K: Recent advances and challenges of bispecific antibodies in solid tumors. *Experimental hematology & oncology* 10(1): 56, 2021. doi:10.1186/s40164-021-00250-1
 25. Antonarelli G, Giugliano F, Corti C, Repetto M, Tarantino P, Curigliano G: Research and Clinical Landscape of Bispecific Antibodies for the Treatment of Solid Malignancies. *Pharmaceuticals (Basel, Switzerland)* 14(9), 2021. doi:10.3390/ph14090884
 26. Strube J, Grote F, Josch JP, Ditz R: Process Development and Design of Downstream Processes. *Chemie Ingenieur Technik* 83(7): 1044–65, 2011. doi:10.1002/cite.201100017
 27. Sanchez Reyes G: *Separation and characterization of antibody-based protein variants in column chromatography for the production of biopharmaceuticals*, 2022. doi:10.11588/HEIDOK.00030762
 28. Hanke AT, Ottens M: Purifying biopharmaceuticals: knowledge-based chromatographic process development. *Trends in biotechnology* 32(4): 210–20, 2014. doi:10.1016/j.tibtech.2014.02.001
 29. Kimerer LK, Pabst TM, Hunter AK, Carta G: Chromatographic behavior of bivalent bispecific antibodies on hydrophobic interaction chromatography columns. *Journal of chromatography. A* 1617: 460836, 2020. doi:10.1016/j.chroma.2019.460836
 30. Manzke O, Tesch H, Diehl V, Bohlen H: Single-step purification of bispecific monoclonal antibodies for immunotherapeutic use by hydrophobic interaction chromatography. *Journal of Immunological Methods* 208(1): 65–73, 1997. doi:10.1016/s0022-1759(97)00129-4

31. Ansaldi DA, Lester P: *Separation of polypeptide monomers.*, 2003
32. Osberghaus A, Hepbildikler S, Nath S, Haindl M, Lieres E von, Hubbuch J: Determination of parameters for the steric mass action model--a comparison between two approaches. *Journal of chromatography. A* 1233: 54–65, 2012. doi:10.1016/j.chroma.2012.02.004
33. Hunt B, Goddard C, Middelberg AP, O'Neill BK: Economic analysis of immunoabsorption systems. *Biochemical Engineering Journal* 9(2): 135–45, 2001. doi:10.1016/S1369-703X(01)00136-X
34. Rolandi PA: The Unreasonable Effectiveness of Equations: Advanced Modeling For Biopharmaceutical Process Development. In: *Proceedings of the 9th International Conference on Foundations of Computer-Aided Process Design*, Elsevier, 2019, pp 137–150. doi:10.1016/B978-0-12-818597-1.50023-0
35. Roush D, Asthagiri D, Babi DK, Benner S, Bilodeau C, Carta G, Ernst P, Fedesco M, Fitzgibbon S, Flamm M, Griesbach J, Grosskopf T, Hansen EB, Hahn T, Hunt S, Insaïdoo F, Lenhoff A, Lin J, Marke H, Marques B, Papadakis E, Schlegel F, Staby A, Stenvang M, Sun L, Tessier PM, Todd R, Lieres E von, Welsh J, Willson R, Wang G, Wucherpfennig T, Zavalov O: Toward in silico CMC: An industrial collaborative approach to model-based process development. *Biotechnology and bioengineering* 117(12): 3986–4000, 2020. doi:10.1002/bit.27520
36. Briskot T, Hahn T, Huuk T, Wang G, Kluters S, Studts J, Wittkopp F, Winderl J, Schwan P, Hagemann I, Kaiser K, Trapp A, Stamm SM, Koehn J, Malmquist G, Hubbuch J: Analysis of complex protein elution behavior in preparative ion exchange processes using a colloidal particle adsorption model. *Journal of chromatography. A* 1654: 462439, 2021. doi:10.1016/j.chroma.2021.462439
37. Babi DK, Griesbach J, Hunt S, Insaïdoo F, Roush D, Todd R, Staby A, Welsh J, Wittkopp F: Opportunities and challenges for model utilization in the biopharmaceutical industry: current versus future state. *Current Opinion in Chemical Engineering* 36: 100813, 2022. doi:10.1016/j.coche.2022.100813
38. Kumar V, Leweke S, Heymann W, Lieres E von, Schlegel F, Westerberg K, Lenhoff AM: Robust mechanistic modeling of protein ion-exchange

- chromatography. *Journal of Chromatography A* 1660: 462669, 2021. doi:10.1016/j.chroma.2021.462669
39. Creasy A, Barker G, Yao Y, Carta G: Systematic interpolation method predicts protein chromatographic elution from batch isotherm data without a detailed mechanistic isotherm model. *Biotechnology journal* 10(9): 1400–11, 2015. doi:10.1002/biot.201500089
40. Kluters S, Wittkopp F, Jöhnck M, Frech C: Application of linear pH gradients for the modeling of ion exchange chromatography: Separation of monoclonal antibody monomer from aggregates. *Journal of separation science* 39(4): 663–75, 2016. doi:10.1002/jssc.201500994
41. Creasy A, Barker G, Carta G: Systematic interpolation method predicts protein chromatographic elution with salt gradients, pH gradients and combined salt/pH gradients. *Biotechnology journal* 12(3), 2017. doi:10.1002/biot.201600636
42. Creasy A, Reck J, Pabst T, Hunter A, Barker G, Carta G: Systematic Interpolation Method Predicts Antibody Monomer-Dimer Separation by Gradient Elution Chromatography at High Protein Loads. *Biotechnology journal* 14(3): e1800132, 2019. doi:10.1002/biot.201800132
43. Briskot T, Hahn T, Huuk T, Hubbuch J: Protein adsorption on ion exchange adsorbers: A comparison of a stoichiometric and non-stoichiometric modeling approach. *Journal of chromatography. A* 1653: 462397, 2021. doi:10.1016/j.chroma.2021.462397
44. Brooks CA, Cramer SM: Steric mass-action ion exchange: Displacement profiles and induced salt gradients. *AIChE J.* 38(12): 1969–78, 1992. doi:10.1002/aic.690381212
45. Ståhlberg J, Jönsson B, Horváth C: Theory for electrostatic interaction chromatography of proteins. *Anal. Chem.* 63(17): 1867–74, 1991. doi:10.1021/ac00017a036
46. Ståhlberg J, Jönsson B: Influence of charge regulation in electrostatic interaction chromatography of proteins. *Anal. Chem.* 68(9): 1536–44, 1996. doi:10.1021/ac9509972
47. Ståhlberg J: Retention models for ions in chromatography. *Journal of Chromatography A* 855(1): 3–55, 1999. doi:10.1016/S0021-9673(99)00176-4

48. Oberholzer MR, Lenhoff AM: Protein Adsorption Isotherms through Colloidal Energetics. *Langmuir* 15(11): 3905–14, 1999. doi:10.1021/la981199k
49. Guélat B, Khalaf R, Lattuada M, Costioli M, Morbidelli M: Protein adsorption on ion exchange resins and monoclonal antibody charge variant modulation. *Journal of chromatography. A* 1447: 82–91, 2016. doi:10.1016/j.chroma.2016.04.018
50. Kopaciewicz W, Rounds MA, Fausnaugh J, Regnier FE: Retention model for high-performance ion-exchange chromatography. *Journal of Chromatography A* 266: 3–21, 1983. doi:10.1016/S0021-9673(01)90875-1
51. Velayudhan A, Horváth C: Preparative chromatography of proteins. *Journal of Chromatography A* 443: 13–29, 1988. doi:10.1016/S0021-9673(00)94779-4
52. Mollerup JM: A Review of the Thermodynamics of Protein Association to Ligands, Protein Adsorption, and Adsorption Isotherms. *Chem. Eng. Technol.* 31(6): 864–74, 2008. doi:10.1002/ceat.200800082
53. Mollerup JM: Adsorption Isotherms. In: *Preparative chromatography for separation of proteins*, edited by Staby A, Rathore AS, Ahuja S, Hoboken, New Jersey, Wiley, 2017, pp 11–79. doi:10.1002/9781119031116.ch2
54. Hunt S, Larsen T, Todd RJ: Modeling Preparative Cation Exchange Chromatography of Monoclonal Antibodies. In: *Preparative chromatography for separation of proteins*, edited by Staby A, Rathore AS, Ahuja S, Hoboken, New Jersey, Wiley, 2017, pp 399–427. doi:10.1002/9781119031116.ch13
55. Shi Q, Zhou Y, Sun Y: Influence of pH and ionic strength on the steric mass-action model parameters around the isoelectric point of protein. *Biotechnology progress* 21(2): 516–23, 2005. doi:10.1021/bp049735o
56. Borg N, Brodsky Y, Moscariello J, Vunnum S, Vedantham G, Westerberg K, Nilsson B: Modeling and robust pooling design of a preparative cation-exchange chromatography step for purification of monoclonal antibody monomer from aggregates. *Journal of chromatography. A* 1359: 170–81, 2014. doi:10.1016/j.chroma.2014.07.041
57. Saleh D, Wang G, Müller B, Rischawy F, Kluters S, Studts J, Hubbuch J: Straightforward method for calibration of mechanistic cation exchange

- chromatography models for industrial applications. *Biotechnology progress* 36(4): e2984, 2020. doi:10.1002/btpr.2984
58. Rischawy F, Saleh D, Hahn T, Oelmeier S, Spitz J, Kluters S: Good modeling practice for industrial chromatography: Mechanistic modeling of ion exchange chromatography of a bispecific antibody. *Computers & Chemical Engineering* 130: 106532, 2019. doi:10.1016/j.compchemeng.2019.106532
59. Schmidt M, Hafner M, Frech C: Modeling of salt and pH gradient elution in ion-exchange chromatography. *Journal of separation science* 37(1-2): 5–13, 2014. doi:10.1002/jssc.201301007
60. Yang T, Sundling MC, Freed AS, Breneman CM, Cramer SM: Prediction of pH-dependent chromatographic behavior in ion-exchange systems. *Anal. Chem.* 79(23): 8927–39, 2007. doi:10.1021/ac071101j
61. Bosma JC, Wesselingh JA: pH dependence of ion-exchange equilibrium of proteins. *AIChE J.* 44(11): 2399–409, 1998. doi:10.1002/aic.690441108
62. Ribeiro JM, Sillero A: An algorithm for the computer calculation of the coefficients of a polynomial that allows determination of isoelectric points of proteins and other macromolecules. *Computers in biology and medicine* 20(4): 235–42, 1990
63. Ribeiro JM, Sillero A: A program to calculate the isoelectric point of macromolecules. *Computers in biology and medicine* 21(3): 131–41, 1991
64. Mollerup JM, Hansen TB, Frederiksen SS, Staby A: Thermodynamic Modeling of Chromatographic Separation. *Advances in chromatography* 48(48): 57–97, 2010. doi:10.1201/9781420084542-c2
65. Koch J, Scheps D, Gunne M, Boscheinen O, Hafner M, Frech C: Mechanistic modeling and simulation of a complex low and high loading elution behavior of a polypeptide in cation exchange chromatography. *Journal of separation science*, 2022. doi:10.1002/jssc.202200098
66. Khalaf R, Coquebert de Neuville B, Morbidelli M: Protein adsorption in polyelectrolyte brush type cation-exchangers. *Journal of chromatography. A* 1471: 126–37, 2016. doi:10.1016/j.chroma.2016.10.024
67. Diedrich J, Heymann W, Leweke S, Hunt S, Todd R, Kunert C, Johnson W, Lieres E von: Multi-state steric mass action model and case study on complex high loading behavior of mAb on ion exchange tentacle resin.

- Journal of chromatography. A* 1525: 60–70, 2017. doi:10.1016/j.chroma.2017.09.039
68. Huuk TC, Hahn T, Doninger K, Griesbach J, Hepbildikler S, Hubbuch J: Modeling of complex antibody elution behavior under high protein load densities in ion exchange chromatography using an asymmetric activity coefficient. *Biotechnology journal* 12(3), 2017. doi:10.1002/biot.201600336
69. Kumar V, Leweke S, Lieres E von, Rathore AS: Mechanistic modeling of ion-exchange process chromatography of charge variants of monoclonal antibody products. *Journal of chromatography. A* 1426: 140–53, 2015. doi:10.1016/j.chroma.2015.11.062
70. Lee YF, Jöhnck M, Frech C: Evaluation of differences between dual salt-pH gradient elution and mono gradient elution using a thermodynamic model: Simultaneous separation of six monoclonal antibody charge and size variants on preparative-scale ion exchange chromatographic resin. *Biotechnology progress* 34(4): 973–86, 2018. doi:10.1002/btpr.2626
71. Guélat B, Ströhlein G, Lattuada M, Delegrange L, Valax P, Morbidelli M: Simulation model for overloaded monoclonal antibody variants separations in ion-exchange chromatography. *Journal of chromatography. A* 1253: 32–43, 2012. doi:10.1016/j.chroma.2012.06.081
72. Ladiwala A, Rege K, Breneman CM, Cramer SM: A priori prediction of adsorption isotherm parameters and chromatographic behavior in ion-exchange systems. *Proceedings of the National Academy of Sciences of the United States of America* 102(33): 11710–5, 2005. doi:10.1073/pnas.0408769102
73. Khanal O, Kumar V, Schlegel F, Lenhoff AM: Estimating and leveraging protein diffusion on ion-exchange resin surfaces. *Proceedings of the National Academy of Sciences of the United States of America* 117(13): 7004–10, 2020. doi:10.1073/pnas.1921499117
74. Feller BE, Kellis JT, Cascão-Pereira LG, Robertson CR, Frank CW: The role of electrostatic interactions in protease surface diffusion and the consequence for interfacial biocatalysis. *Langmuir the ACS journal of surfaces and colloids* 26(24): 18916–25, 2010. doi:10.1021/la103080a
75. Wesselingh JA, Bosma JC: Protein ion-exchange adsorption kinetics. *AIChE J.* 47(7): 1571–80, 2001. doi:10.1002/aic.690470710

76. Dziennik SR, Belcher EB, Barker GA, Lenhoff AM: Effects of ionic strength on lysozyme uptake rates in cation exchangers. I: Uptake in SP Sepharose FF. *Biotechnology and bioengineering* 91(2): 139–53, 2005. doi:10.1002/bit.20503
77. Harinarayan C, Mueller J, Ljunglöf A, Fahrner R, van Alstine J, van Reis R: An exclusion mechanism in ion exchange chromatography. *Biotechnology and bioengineering* 95(5): 775–87, 2006. doi:10.1002/bit.21080
78. Kimerer LK, Pabst TM, Hunter AK, Carta G: Role of configurational flexibility on the adsorption kinetics of bivalent bispecific antibodies on porous cation exchange resins. *Journal of chromatography. A* 1655: 462479, 2021. doi:10.1016/j.chroma.2021.462479
79. Ma Z, Whitley RD, Wang N-HL: Pore and surface diffusion in multicomponent adsorption and liquid chromatography systems. *AIChE J.* 42(5): 1244–62, 1996. doi:10.1002/aic.690420507
80. Kimerer LK, Pabst TM, Hunter AK, Carta G: Chromatographic behavior of bivalent bispecific antibodies on cation exchange columns. II. Biomolecular perspectives. *Journal of chromatography. A* 1601: 133–44, 2019. doi:10.1016/j.chroma.2019.04.013
81. Kimerer LK, Niu B, Pabst TM, Zhai W, Hunter AK, Carta G: Chromatographic and adsorptive behavior of a bivalent bispecific antibody and associated fragments. *Journal of chromatography. A* 1648: 462181, 2021. doi:10.1016/j.chroma.2021.462181
82. Frederiksen SS: *Computer aided development and optimisation of chromatographic separations*. Dissertation, Technical University of Denmark, 2004
83. Mollerup JM: Applied thermodynamics: A new frontier for biotechnology. *Fluid Phase Equilibria* 241(1-2): 205–15, 2006. doi:10.1016/j.fluid.2005.12.037
84. Mollerup JM, Hansen TB, Kidal S, Staby A: Quality by design--thermodynamic modelling of chromatographic separation of proteins. *Journal of Chromatography A* 1177(2): 200–6, 2008. doi:10.1016/j.chroma.2007.08.059
85. Yamamoto S: Electrostatic Interaction Chromatography Process for Protein Separations: Impact of Engineering Analysis of Biorecognition Mechanism

- on Process Optimization. *Chem. Eng. Technol.* 28(11): 1387–93, 2005. doi:10.1002/ceat.200500199
86. Gerstner JA, Bell JA, Cramer SM: Gibbs free energy of adsorption for biomolecules in ion-exchange systems. *Biophysical Chemistry* 52(2): 97–106, 1994. doi:10.1016/0301-4622(94)00006-9
87. Pedersen L, Mollerup J, Hansen E, Jungbauer A: Whey proteins as a model system for chromatographic separation of proteins. *Journal of chromatography. B, Analytical technologies in the biomedical and life sciences* 790(1-2): 161–73, 2003. doi:10.1016/s1570-0232(03)00127-2
88. Bose K, Clark AC: pH effects on the stability and dimerization of procaspase-3. *Protein science a publication of the Protein Society* 14(1): 24–36, 2005. doi:10.1110/ps.041003305
89. Hebditch M, Kean R, Warwicker J: Modelling of pH-dependence to develop a strategy for stabilising mAbs at acidic steps in production. *Computational and structural biotechnology journal* 18: 897–905, 2020. doi:10.1016/j.csbj.2020.03.002
90. Davies CW: 397. The extent of dissociation of salts in water. Part VIII. An equation for the mean ionic activity coefficient of an electrolyte in water, and a revision of the dissociation constants of some sulphates. *J. Chem. Soc.:* 2093, 1938. doi:10.1039/jr9380002093
91. Debye P, Hückel E: Zur Theorie der Elektrolyte. *Physikalische Zeitschrift*(9): 185–206, 1923
92. Archer DG, Wang P: The Dielectric Constant of Water and Debye-Hückel Limiting Law Slopes. *Journal of Physical and Chemical Reference Data* 19(2): 371–411, 1990. doi:10.1063/1.555853
93. Samson E, Lemaire G, Marchand J, Beaudoin JJ: Modeling chemical activity effects in strong ionic solutions. *Computational Materials Science* 15(3): 285–94, 1999. doi:10.1016/S0927-0256(99)00017-8
94. *J.F. Pankow, Aquatic Chemistry Concepts, Lewis Publishers, 1994, 1994*
95. Nfor BK, Noverraz M, Chilamkurthi S, Verhaert PDEM, van der Wielen LAM, Ottens M: High-throughput isotherm determination and thermodynamic modeling of protein adsorption on mixed mode adsorbents. *Journal of chromatography. A* 1217(44): 6829–50, 2010. doi:10.1016/j.chroma.2010.07.069

96. Yamamoto S, Nakanishi K, Matsuno R, Kamijubo T: Ion exchange chromatography of proteins-predictions of elution curves and operating conditions. II. Experimental verification. *Biotechnology and bioengineering* 25(5): 1373–91, 1983. doi:10.1002/bit.260250516
97. Yamamoto S, Nakanishi K, Matsuno R, Kamikubo T: Ion exchange chromatography of proteins-prediction of elution curves and operating conditions. I. Theoretical considerations. *Biotechnology and bioengineering* 25(6): 1465–83, 1983. doi:10.1002/bit.260250605
98. Yamamoto S, Nakanishi K, Matsuno R: *Ion exchange chromatography of proteins*, New York, Dekker, 1988
99. Schmidt-Traub H, Schulte M, Seidel-Morgenstern A (eds): *Preparative chromatography*, 2nd ed., Weinheim, Germany, Wiley-VCH, 2012
100. GLUECKAUF E, COATES JI: Theory of chromatography; the influence of incomplete equilibrium on the front boundary of chromatograms and on the effectiveness of separation. *J. Chem. Soc.:* 1315–21, 1947. doi:10.1039/jr9470001315
101. Ingham J: *Chemical Engineering Dynamics: An Introduction to Modelling and Computer Simulation*, 3rd ed., Weinheim, Wiley-VCH, 2008
102. Steinebach F: *Multi-Column Chromatography for Continuous Integrated Biomanufacturing*, 2017. doi:10.3929/ETHZ-A-010866618
103. Pirrung SM, Da Parruca Cruz D, Hanke AT, Berends C, van Beckhoven RFWC, Eppink MHM, Ottens M: Chromatographic parameter determination for complex biological feedstocks. *Biotechnology progress* 34(4): 1006–18, 2018. doi:10.1002/btpr.2642
104. Wu Y, Simons J, Hooson S, Abraham D, Carta G: Protein and virus-like particle adsorption on perfusion chromatography media. *Journal of chromatography. A* 1297: 96–105, 2013. doi:10.1016/j.chroma.2013.04.062
105. Guo J, Carta G: Unfolding and aggregation of monoclonal antibodies on cation exchange columns: effects of resin type, load buffer, and protein stability. *Journal of chromatography. A* 1388: 184–94, 2015. doi:10.1016/j.chroma.2015.02.047

106. Neuville BC de, Lamprou A, Morbidelli M, Soos M: Perfusive ion-exchange chromatographic materials with high capacity. *Journal of chromatography. A* 1374: 180–8, 2014. doi:10.1016/j.chroma.2014.11.066
107. Klein C, Schaefer W, Regula JT: The use of CrossMAb technology for the generation of bi- and multispecific antibodies. *mAbs* 8(6): 1010–20, 2016. doi:10.1080/19420862.2016.1197457
108. Klein C, Schaefer W, Regula JT, Dumontet C, Brinkmann U, Bacac M, Umaña P: Engineering therapeutic bispecific antibodies using CrossMAb technology. *Methods (San Diego, Calif.)* 154: 21–31, 2019. doi:10.1016/j.ymeth.2018.11.008
109. Schweiger S, Jungbauer A: Scalability of pre-packed preparative chromatography columns with different diameters and lengths taking into account extra column effects. *Journal of chromatography. A* 1537: 66–74, 2018. doi:10.1016/j.chroma.2018.01.022
110. Kröner F, Hubbuch J: Systematic generation of buffer systems for pH gradient ion exchange chromatography and their application. *Journal of chromatography. A* 1285: 78–87, 2013. doi:10.1016/j.chroma.2013.02.017
111. Urbansky ET, Schock MR: Understanding, Deriving, and Computing Buffer Capacity. *J. Chem. Educ.* 77(12): 1640, 2000. doi:10.1021/ed077p1640
112. Marcoline FV, Furth J, Nayak S, Grabe M, Macey RI: Berkeley Madonna Version 10-A simulation package for solving mathematical models. *CPT: pharmacometrics & systems pharmacology* 11(3): 290–301, 2022. doi:10.1002/psp4.12757
113. Nelder JA, Mead R: A Simplex Method for Function Minimization. *The Computer Journal* 7(4): 308–13, 1965. doi:10.1093/comjnl/7.4.308
114. Mihlbachler K, Kaczmariski K, Seidel-Morgenstern A, Guiochon G: Measurement and modeling of the equilibrium behavior of the Tröger's base enantiomers on an amylose-based chiral stationary phase. *Journal of Chromatography A* 955(1): 35–52, 2002. doi:10.1016/S0021-9673(02)00228-5
115. Mihlbachler K, Jesús MA de, Kaczmariski K, Sepaniak MJ, Seidel-Morgenstern A, Guiochon G: Adsorption behavior of the (+/-)-Tröger's base enantiomers in the phase system of a silica-based packing coated with amylose tri(3,5-dimethyl carbamate) and 2-propanol and molecular

- modeling interpretation. *Journal of Chromatography A* 1113(1-2): 148–61, 2006. doi:10.1016/j.chroma.2006.02.001
116. Golshan-Shirazi S, Guiochon G: Theoretical explanation of the displacement and tag-along effects. *Chromatographia* 30(11-12): 613–7, 1990. doi:10.1007/BF02269733
117. Kaschak T, Boyd D, Lu F, Derfus G, Kluck B, Nogal B, Emery C, Summers C, Zheng K, Bayer R, Amanullah A, Yan B: Characterization of the basic charge variants of a human IgG1: effect of copper concentration in cell culture media. *mAbs* 3(6): 577–83, 2011. doi:10.4161/mabs.3.6.17959
118. Vlasak J, Ionescu R: Heterogeneity of monoclonal antibodies revealed by charge-sensitive methods. *Current pharmaceutical biotechnology* 9(6): 468–81, 2008. doi:10.2174/138920108786786402
119. Lu C, Liu D, Liu H, Motchnik P: Characterization of monoclonal antibody size variants containing extra light chains. *mAbs* 5(1): 102–13, 2013. doi:10.4161/mabs.22965
120. Mollerup JM: Modelling oligomer formation in chromatographic separations. *Journal of chromatography. A* 1218(49): 8869–73, 2011. doi:10.1016/j.chroma.2011.05.097
121. Xu W, Regnier FE: Protein–protein interactions on weak-cation-exchange sorbent surfaces during chromatographic separations. *Journal of Chromatography A* 828(1-2): 357–64, 1998. doi:10.1016/s0021-9673(98)00641-4
122. Dimer F, Hubbuch J: 3D structure-based protein retention prediction for ion-exchange chromatography. *Journal of chromatography. A* 1217(8): 1343–53, 2010. doi:10.1016/j.chroma.2009.12.061
123. Dimer F, Petzold M, Hubbuch J: Effects of ionic strength and mobile phase pH on the binding orientation of lysozyme on different ion-exchange adsorbents. *Journal of Chromatography A* 1194(1): 11–21, 2008. doi:10.1016/j.chroma.2007.12.085
124. Zhou J, Tsao H-K, Sheng Y-J, Jiang S: Monte Carlo simulations of antibody adsorption and orientation on charged surfaces. *The Journal of chemical physics* 121(2): 1050–7, 2004. doi:10.1063/1.1757434
125. Bernau CR, Jäpel RC, Hübbers JW, Nölting S, Opdensteinen P, Buyel JF: Precision analysis for the determination of steric mass action parameters

- using eight tobacco host cell proteins. *Journal of chromatography. A* 1652: 462379, 2021. doi:10.1016/j.chroma.2021.462379
126. Vermeer AW, Norde W: The Thermal Stability of Immunoglobulin: Unfolding and Aggregation of a Multi-Domain Protein. *Biophysical Journal* 78(1): 394–404, 2000. doi:10.1016/S0006-3495(00)76602-1
127. Fink AL, Calciano LJ, Goto Y, Kurotsu T, Palleros DR: Classification of acid denaturation of proteins: intermediates and unfolded states. *Biochemistry* 33(41): 12504–11, 1994. doi:10.1021/bi00207a018
128. van der Wiel JP: *Continuous recovery of bioproducts by adsorption*. Dissertation, Delft University of Technology, 1989
129. Norde W, Lyklema J: The adsorption of human plasma albumin and bovine pancreas ribonuclease at negatively charged polystyrene surfaces. *Journal of Colloid and Interface Science* 66(2): 257–65, 1978. doi:10.1016/0021-9797(78)90303-X
130. Raje P, Pinto NG: Combination of the steric mass action and non-ideal surface solution models for overload protein ion-exchange chromatography. *Journal of Chromatography A* 760(1): 89–103, 1997. doi:10.1016/S0021-9673(96)00812-6

OWN PUBLICATIONS:

1. Seelinger F, Wittkopp F, von Hirschheydt T, Hafner M, Frech C: Application of the Steric Mass Action formalism for modeling under high loading conditions: Part 1. Investigation of the influence of pH on the steric shielding factor. *Journal of chromatography. A* 1676: 463265, 2022. doi:10.1016/j.chroma.2022.463265
2. Seelinger F, Wittkopp F, von Hirschheydt T, Frech C: Application of the Steric Mass Action formalism for modeling under high loading conditions: Part 2. Investigation of high loading and column overloading effects. *Journal of chromatography. A* 1676: 463266, 2022. doi:10.1016/j.chroma.2022.463266
3. Seelinger F, Wittkopp F, von Hirschheydt T, Frech C: Anti-Langmuir elution behavior of a bispecific monoclonal antibody in cation exchange chromatography: Mechanistic modeling using a pH-dependent Self-Association Steric Mass Action isotherm. DRAFT (submitted)

7 TABULAR APPENDIX

Table 25: Composition of buffer solutions for the application of linear salt gradients from 50 to 500 mmol/L Na⁺ at pH 4.5

Buffer	Ingredients	Concentrations
Buffer A for salt gradient elution at pH 4.5 with 50 mmol/L Na⁺	Succinic acid	8.32 mmol/L
	Acetic acid	6.10 mmol/L
	MES H ₂ O	13.80 mmol/L
	MOPSO	16.31 mmol/L
	NaOH	9.80 mmol/L
	NaCl	40.20 mmol/L
	In ultrapure water, pH 4.5	
Buffer B for salt gradient elution at pH 4.5 with 500 mmol/L Na⁺	Succinic acid	8.32 mmol/L
	Acetic acid	6.10 mmol/L
	MES H ₂ O	13.80 mmol/L
	MOPSO	16.31 mmol/L
	NaOH	12.90 mmol/L
	NaCl	487.10 mmol/L
	In ultrapure water, pH 4.5	

Table 26: Composition of buffer solutions for the application of linear salt gradients from 50 to 500 mmol/L Na⁺ at pH 5.3

Buffer	Ingredients	Concentrations
Buffer A for salt gradient elution at pH 5.3 with 50 mmol/L Na⁺	Succinic acid	8.46 mmol/L
	Acetic acid	4.80 mmol/L
	MES H ₂ O	10.86 mmol/L
	MOPSO	15.42 mmol/L
	HEPES	3.16 mmol/L
	TAPS	2.00 mmol/L
	CHES	1.36 mmol/L
	NaOH	17.90 mmol/L
	NaCl	32.10 mmol/L
	In ultrapure water, pH 5.3	
Buffer B for salt gradient elution at pH 5.3 with 500 mmol/L Na⁺	Succinic acid	8.46 mmol/L
	Acetic acid	4.80 mmol/L
	MES H ₂ O	10.86 mmol/L
	MOPSO	15.42 mmol/L
	HEPES	3.16 mmol/L
	TAPS	2.00 mmol/L
	CHES	1.36 mmol/L
	NaOH	21.30 mmol/L
	NaCl	478.70 mmol/L
	In ultrapure water, pH 5.3	

Table 27: Composition of buffer solutions for the application of linear salt gradients from 50 to 500 mmol/L Na⁺ at pH 6.3

Buffer	Ingredients	Concentrations
Buffer A for salt gradient elution at pH 6.3 with 50 mmol/L Na⁺	Succinic acid	8.63 mmol/L
	Acetic acid	3.17 mmol/L
	MES H ₂ O	7.18 mmol/L
	MOPSO	14.30 mmol/L
	HEPES	7.12 mmol/L
	TAPS	4.51 mmol/L
	CHES	3.06 mmol/L
	NaOH	27.30 mmol/L
	NaCl	22.70 mmol/L
	In ultrapure water, pH 6.3	
Buffer B for salt gradient elution at pH 6.3 with 500 mmol/L Na⁺	Succinic acid	8.63 mmol/L
	Acetic acid	3.17 mmol/L
	MES H ₂ O	7.18 mmol/L
	MOPSO	14.30 mmol/L
	HEPES	7.12 mmol/L
	TAPS	4.51 mmol/L
	CHES	3.06 mmol/L
	NaOH	30.50 mmol/L
	NaCl	469.50 mmol/L
	In ultrapure water, pH 6.3	

Table 28: Composition of buffer solutions for the application of linear salt gradients from 35 to 500 mmol/L Na⁺ at pH 7.0

Buffer	Ingredients	Concentrations
Buffer A for salt gradient elution at pH 7.0 with 35 mmol/L Na⁺	Succinic acid	8.75 mmol/L
	Acetic acid	2.03 mmol/L
	MES H ₂ O	4.60 mmol/L
	MOPSO	13.52 mmol/L
	HEPES	9.88 mmol/L
	TAPS	6.26 mmol/L
	CHES	4.25 mmol/L
	NaOH	33.30 mmol/L
	NaCl	1.70 mmol/L
	In ultrapure water, pH 7.0	
Buffer B for salt gradient elution at pH 7.0 with 500 mmol/L Na⁺	Succinic acid	8.75 mmol/L
	Acetic acid	2.03 mmol/L
	MES H ₂ O	4.60 mmol/L
	MOPSO	13.52 mmol/L
	HEPES	9.88 mmol/L
	TAPS	6.26 mmol/L
	CHES	4.25 mmol/L
	NaOH	36.95 mmol/L
	NaCl	463.05 mmol/L
	In ultrapure water, pH 7.0	

Table 29: Composition of buffer solutions for the application of linear salt gradients from 25 to 500 mmol/L Na⁺ at pH 8.0

Buffer	Ingredients	Concentrations
Buffer A for salt gradient elution at pH 8.0 with 25 mmol/L Na⁺	Succinic acid	4.46 mmol/L
	Acetic acid	0.20 mmol/L
	MES H ₂ O	0.46 mmol/L
	MOPSO	6.20 mmol/L
	HEPES	6.92 mmol/L
	TAPS	4.38 mmol/L
	CHES	2.98 mmol/L
	NaOH	21.65 mmol/L
	NaCl	3.35 mmol/L
	In ultrapure water, pH 8.0	
Buffer B for salt gradient elution at pH 8.0 with 500 mmol/L Na⁺	Succinic acid	4.46 mmol/L
	Acetic acid	0.20 mmol/L
	MES H ₂ O	0.46 mmol/L
	MOPSO	6.20 mmol/L
	HEPES	6.92 mmol/L
	TAPS	4.38 mmol/L
	CHES	2.98 mmol/L
	NaOH	23.37 mmol/L
	NaCl	476.63 mmol/L
	In ultrapure water, pH 8.0	

Table 30: Composition of buffer solutions for the application of linear salt gradients from 25 to 500 mmol/L Na⁺ at pH 8.5

Buffer	Ingredients	Concentrations
Buffer A for salt gradient elution at pH 8.5 with 25 mmol/L Na⁺	Succinic acid	4.30 mmol/L
	Acetic acid	0.46 mmol/L
	MES H ₂ O	1.05 mmol/L
	MOPSO	5.07 mmol/L
	HEPES	7.45 mmol/L
	TAPS	4.01 mmol/L
	CHES	3.92 mmol/L
	NaOH	24.40 mmol/L
	NaCl	0.60 mmol/L
	In ultrapure water, pH 8.5	
Buffer B for salt gradient elution at pH 8.5 with 500 mmol/L Na⁺	Succinic acid	4.30 mmol/L
	Acetic acid	0.46 mmol/L
	MES H ₂ O	1.05 mmol/L
	MOPSO	5.07 mmol/L
	HEPES	7.45 mmol/L
	TAPS	4.01 mmol/L
	CHES	3.92 mmol/L
	NaOH	25.78 mmol/L
	NaCl	474.22 mmol/L
	In ultrapure water, pH 8.5	

Table 31: Composition of buffer solutions for the application of linear salt gradients from 25 to 500 mmol/L Na⁺ at pH 8.9

Buffer	Ingredients	Concentrations
Buffer A for salt gradient elution at pH 8.9 with 25 mmol/L Na⁺	Succinic acid	3.44 mmol/L
	Acetic acid	0.18 mmol/L
	MES H ₂ O	0.42 mmol/L
	MOPSO	3.94 mmol/L
	HEPES	6.56 mmol/L
	TAPS	3.53 mmol/L
	CHES	3.45 mmol/L
	NaOH	21.25 mmol/L
	NaCl	3.75 mmol/L
	In ultrapure water, pH 8.9	
Buffer B for salt gradient elution at pH 8.9 with 500 mmol/L Na⁺	Succinic acid	3.44 mmol/L
	Acetic acid	0.18 mmol/L
	MES H ₂ O	0.42 mmol/L
	MOPSO	3.94 mmol/L
	HEPES	6.56 mmol/L
	TAPS	3.53 mmol/L
	CHES	3.45 mmol/L
	NaOH	22.26 mmol/L
	NaCl	477.74 mmol/L
	In ultrapure water, pH 8.9	

Table 32: Composition of buffer solutions for the application of linear pH gradients from pH 4.50 to 8.25 at 50 mmol/L Na⁺

Buffer	Ingredients	Concentrations
Buffer A for pH gradient elution at 50 mmol/L Na⁺ (pH 4.50)	Succinic acid	8.32 mmol/L
	Acetic acid	6.10 mmol/L
	MES H ₂ O	13.80 mmol/L
	MOPSO	16.31 mmol/L
	NaOH	10.50 mmol/L
	NaCl	39.50 mmol/L
	In ultrapure water, pH 4.50	
Buffer B for pH gradient elution at 50 mmol/L Na⁺ (pH 8.25)	Succinic acid	8.97 mmol/L
	MOPSO	12.13 mmol/L
	HEPES	14.83 mmol/L
	TAPS	9.39 mmol/L
	CHES	6.38 mmol/L
	NaOH	47.84 mmol/L
	NaCl	2.16 mmol/L
	In ultrapure water, pH 8.25	

Table 33: Composition of buffer solutions for the application of linear pH gradients from pH 4.50 to 8.25 at 75 mmol/L Na⁺

Buffer	Ingredients	Concentrations
Buffer A for pH gradient elution at 75 mmol/L Na⁺ (pH 4.50)	Succinic acid	8.86 mmol/L
	Acetic acid	5.29 mmol/L
	MES H ₂ O	15.57 mmol/L
	MOPSO	15.58 mmol/L
	NaOH	11.03 mmol/L
	NaCl	63.97 mmol/L
	In ultrapure water, pH 4.50	
Buffer B for pH gradient elution at 75 mmol/L Na⁺ (pH 8.25)	Succinic acid	8.21 mmol/L
	MOPSO	13.51 mmol/L
	HEPES	15.01 mmol/L
	TAPS	9.84 mmol/L
	CHES	6.40 mmol/L
	NaOH	48.43 mmol/L
	NaCl	26.57 mmol/L
	In ultrapure water, pH 8.25	

Table 34: Composition of buffer solutions for the application of linear pH gradients from pH 4.50 to 9.30 at 75 mmol/L Na⁺

Buffer	Ingredients	Concentrations
Buffer A for pH gradient elution at 75 mmol/L Na⁺ (pH 4.50)	Succinic acid	8.44 mmol/L
	Acetic acid	5.52 mmol/L
	MES H ₂ O	12.64 mmol/L
	MOPSO	13.12 mmol/L
	NaOH	10.67 mmol/L
	NaCl	64.33 mmol/L
	In ultrapure water, pH 4.50	
Buffer B for pH gradient elution at 75 mmol/L Na⁺ (pH 9.30)	Succinic acid	8.63 mmol/L
	MOPSO	9.55 mmol/L
	HEPES	17.89 mmol/L
	TAPS	9.63 mmol/L
	CHES	9.41 mmol/L
	NaOH	58.57 mmol/L
	NaCl	16.43 mmol/L
	In ultrapure water, pH 9.30	

Table 35: Composition of buffer solutions for the application of linear pH gradients from pH 4.50 to 8.25 at 100 mmol/L Na⁺

Buffer	Ingredients	Concentrations
Buffer A for pH gradient elution at 100 mmol/L Na⁺ (pH 4.50)	Succinic acid	8.83 mmol/L
	Acetic acid	5.00 mmol/L
	MES H ₂ O	15.74 mmol/L
	MOPSO	15.50 mmol/L
	NaOH	11.17 mmol/L
	NaCl	88.83 mmol/L
	In ultrapure water, pH 4.50	
Buffer B for pH gradient elution at 100 mmol/L Na⁺ (pH 8.25)	Succinic acid	8.16 mmol/L
	MOPSO	13.38 mmol/L
	HEPES	15.14 mmol/L
	TAPS	9.88 mmol/L
	CHES	6.34 mmol/L
	NaOH	48.59 mmol/L
	NaCl	51.41 mmol/L
In ultrapure water, pH 8.25		

Table 36: Composition of buffer solutions for the application of linear pH gradients from pH 4.50 to 9.30 at 100 mmol/L Na⁺

Buffer	Ingredients	Concentrations
Buffer A for pH gradient elution at 100 mmol/L Na⁺ (pH 4.50)	Succinic acid	7.02 mmol/L
	Acetic acid	6.48 mmol/L
	MES H ₂ O	12.17 mmol/L
	MOPSO	11.47 mmol/L
	NaOH	10.07 mmol/L
	NaCl	89.93 mmol/L
	In ultrapure water, pH 4.50	
Buffer B for pH gradient elution at 100 mmol/L Na⁺ (pH 9.30)	Succinic acid	9.71 mmol/L
	MOPSO	9.13 mmol/L
	HEPES	16.44 mmol/L
	TAPS	8.85 mmol/L
	CHES	8.69 mmol/L
	NaOH	57.93 mmol/L
	NaCl	42.07 mmol/L
In ultrapure water, pH 9.30		

Table 37: Composition of buffer solutions for the application of linear pH gradients from pH 4.50 to 8.25 at 120 mmol/L Na⁺

Buffer	Ingredients	Concentrations
Buffer A for pH gradient elution at 120 mmol/L Na⁺ (pH 4.50)	Succinic acid	8.72 mmol/L
	Acetic acid	4.90 mmol/L
	MES H ₂ O	16.93 mmol/L
	MOPSO	13.18 mmol/L
	NaOH	11.23 mmol/L
	NaCl	108.77 mmol/L
	In ultrapure water, pH 4.50	
Buffer B for pH gradient elution at 120 mmol/L Na⁺ (pH 8.25)	Succinic acid	7.95 mmol/L
	MOPSO	14.74 mmol/L
	HEPES	14.19 mmol/L
	TAPS	9.54 mmol/L
	CHES	6.47 mmol/L
	NaOH	48.65 mmol/L
	NaCl	71.35 mmol/L
	In ultrapure water, pH 8.25	

Table 38: Composition of buffer solutions for the application of linear pH gradients from pH 4.50 to 8.25 at 150 mmol/L Na⁺

Buffer	Ingredients	Concentrations
Buffer A for pH gradient elution at 150 mmol/L Na⁺ (pH 4.50)	Succinic acid	7.81 mmol/L
	Acetic acid	5.49 mmol/L
	MES H ₂ O	16.19 mmol/L
	MOPSO	12.00 mmol/L
	NaOH	10.85 mmol/L
	NaCl	139.15 mmol/L
	In ultrapure water, pH 4.50	
Buffer B for pH gradient elution at 150 mmol/L Na⁺ (pH 8.25)	Succinic acid	8.56 mmol/L
	MOPSO	14.11 mmol/L
	HEPES	13.24 mmol/L
	TAPS	9.15 mmol/L
	CHES	5.67 mmol/L
	NaOH	48.28 mmol/L
	NaCl	101.72 mmol/L
In ultrapure water, pH 8.25		

Table 39: Composition of buffer solutions for the application of linear pH gradients from pH 4.50 to 8.25 at 200 mmol/L Na⁺

Buffer	Ingredients	Concentrations
Buffer A for pH gradient elution at 200 mmol/L Na⁺ (pH 4.50)	Succinic acid	7.47 mmol/L
	Acetic acid	5.50 mmol/L
	MES H ₂ O	16.44 mmol/L
	MOPSO	10.54 mmol/L
	NaOH	10.80 mmol/L
	NaCl	189.20 mmol/L
	In ultrapure water, pH 4.50	
Buffer B for pH gradient elution at 200 mmol/L Na⁺ (pH 8.25)	Succinic acid	8.69 mmol/L
	MOPSO	14.46 mmol/L
	HEPES	12.49 mmol/L
	TAPS	8.84 mmol/L
	CHES	5.48 mmol/L
	NaOH	48.25 mmol/L
	NaCl	151.75 mmol/L
	In ultrapure water, pH 8.25	

Table 40: Composition of buffer solutions for the application of linear pH gradients from pH 4.50 to 8.25 at 250 mmol/L Na⁺

Buffer	Ingredients	Concentrations
Buffer A for pH gradient elution at 250 mmol/L Na⁺ (pH 4.50)	Succinic acid	7.92 mmol/L
	Acetic acid	4.80 mmol/L
	MES H ₂ O	16.50 mmol/L
	MOPSO	11.38 mmol/L
	NaOH	11.11 mmol/L
	NaCl	238.89 mmol/L
	In ultrapure water, pH 4.50	
Buffer B for pH gradient elution at 250 mmol/L Na⁺ (pH 8.25)	Succinic acid	8.51 mmol/L
	MOPSO	14.24 mmol/L
	HEPES	13.17 mmol/L
	TAPS	8.99 mmol/L
	CHES	5.77 mmol/L
	NaOH	48.57 mmol/L
	NaCl	201.43 mmol/L
In ultrapure water, pH 8.25		

Table 41: Composition of buffer solutions for the application of linear pH gradients from pH 4.50 to 8.25 at 300 mmol/L Na⁺

Buffer	Ingredients	Concentrations
Buffer A for pH gradient elution at 300 mmol/L Na⁺ (pH 4.50)	Succinic acid	7.95 mmol/L
	Acetic acid	4.68 mmol/L
	MES H ₂ O	16.97 mmol/L
	MOPSO	11.00 mmol/L
	NaOH	11.23 mmol/L
	NaCl	288.77 mmol/L
	In ultrapure water, pH 4.50	
Buffer B for pH gradient elution at 300 mmol/L Na⁺ (pH 8.25)	Succinic acid	8.35 mmol/L
	MOPSO	14.61 mmol/L
	HEPES	13.10 mmol/L
	TAPS	9.10 mmol/L
	CHES	5.64 mmol/L
	NaOH	48.70 mmol/L
	NaCl	251.30 mmol/L
	In ultrapure water, pH 8.25	

Table 42: Composition of buffer solutions for the application of linear anti-parallel dual gradients with increasing linear salt gradient from 50 to 350 mmol/L Na⁺ and decreasing linear pH gradient from pH 6.30 to 5.10

Buffer	Ingredients	Concentrations
Buffer A for anti-parallel dual gradient elution (50 mmol/L Na⁺ and pH 6.3)	Succinic acid	7.92 mmol/L
	Acetic acid	5.04 mmol/L
	MES H ₂ O	5.10 mmol/L
	MOPSO	1.76 mmol/L
	NaOH	23.63 mmol/L
	NaCl	26.37 mmol/L
	In ultrapure water, pH 6.3	
Buffer B for anti-parallel dual gradient elution (350 mmol/L Na⁺ and pH 5.1)	Succinic acid	5.82 mmol/L
	Acetic acid	4.23 mmol/L
	HEPES	4.53 mmol/L
	NaOH	12.75 mmol/L
	NaCl	337.25 mmol/L
	In ultrapure water, pH 5.1	

Table 43: Composition of buffer solutions for the application of linear parallel dual gradients with increasing linear salt gradient from 80 to 300 mmol/L Na⁺ and increasing linear pH gradient from pH 5.20 to 7.50

Buffer	Ingredients	Concentrations
Buffer A for parallel dual gradient elution (80 mmol/L Na⁺ and pH 5.2)	Succinic acid	5.99 mmol/L
	Acetic acid	6.13 mmol/L
	MOPSO	5.00 mmol/L
	NaOH	13.77 mmol/L
	NaCl	66.23 mmol/L
	In ultrapure water, pH 5.2	
Buffer A for parallel dual gradient elution (300 mmol/L Na⁺ and pH 7.5)	Succinic acid	21.50 mmol/L
	MES H ₂ O	7.85 mmol/L
	HEPES	8.61 mmol/L
	NaOH	55.84 mmol/L
	NaCl	244.16 mmol/L
	In ultrapure water, pH 7.5	

8 FIGURE APPENDIX

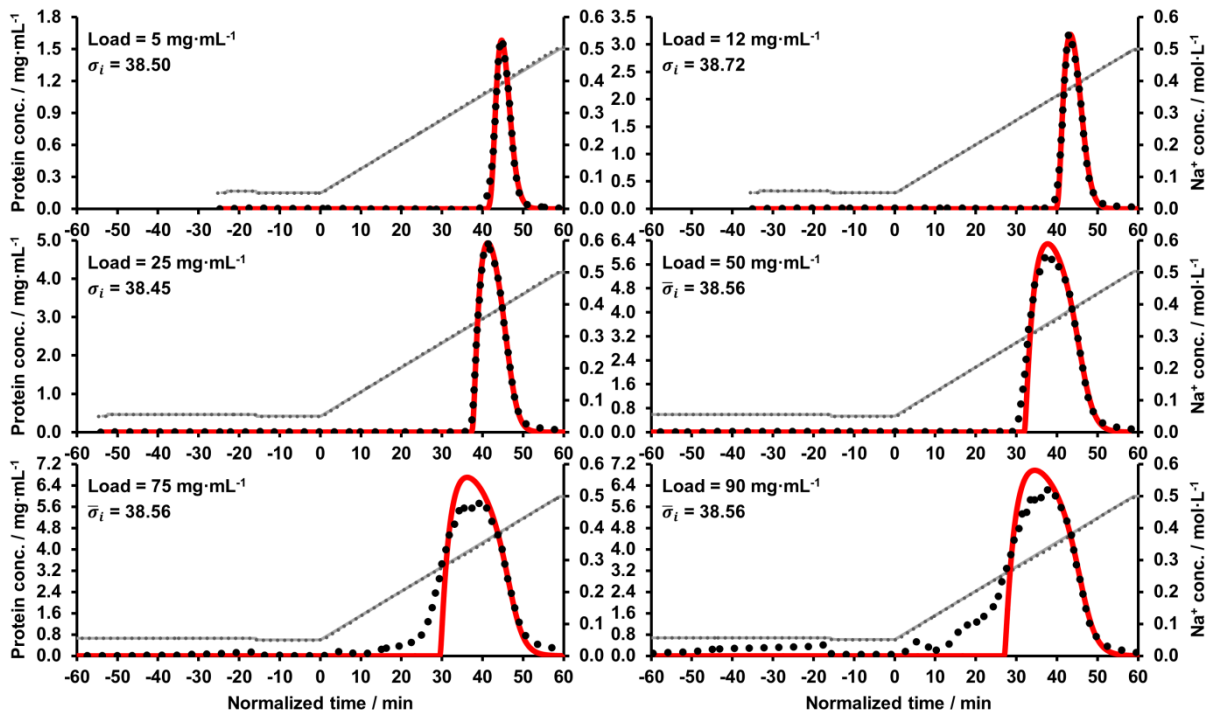


Figure 30. Salt gradient elutions of bsAbY at pH 4.5 used for estimation and verification of the steric shielding factor (σ_i) values by applying the SMA model. The black dots are experimental data and the red lines are simulated data. The time in minutes is normalized to the gradient start. At pH 4.5, highly similar values for σ_i were determined by inverse peak fitting for column loads of 5, 12, and 25 $\text{mg}_{\text{bsAb}}/\text{mL}_{\text{resin}}$. At column loads of 50, 75, and 90 $\text{mg}_{\text{bsAb}}/\text{mL}_{\text{resin}}$, a mean value $\bar{\sigma}_i$ was used for the chromatogram simulations. The applied fitted σ_i values, the mean values $\bar{\sigma}_i$ and the $k_{eff,i}$ values are listed in Table 21. Some of the data shown and illustrated in this figure are already published in Seelinger et al.¹ (Part 1, 2022) and in Seelinger et al.² (Part 2, 2022).

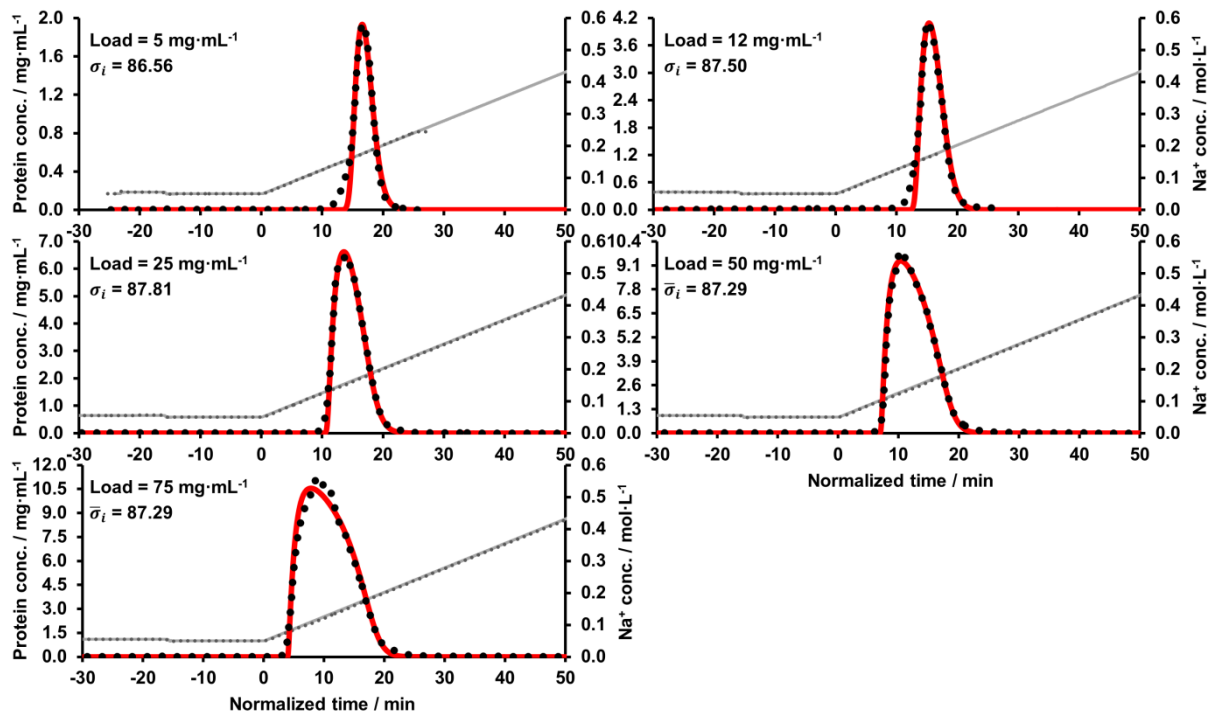


Figure 31. Salt gradient elutions of bsAbY at pH 6.3 used for estimation and verification of the steric shielding factor (σ_i) values by applying the SMA model. The black dots are experimental data and the red lines are simulated data. The time in minutes is normalized to the gradient start. At pH 6.3, highly similar values for σ_i were determined by inverse peak fitting for column loads of 5, 12, and 25 $\text{mg}_{\text{bsAb}}/\text{mL}_{\text{resin}}$. At column loads of 50 and 75 $\text{mg}_{\text{bsAb}}/\text{mL}_{\text{resin}}$, a mean value $\bar{\sigma}_i$ was used for the chromatogram simulations. The applied fitted σ_i values, the mean values $\bar{\sigma}_i$ and the $k_{eff,i}$ values are listed in Table 21. Some of the data shown and illustrated in this figure are already published in Seelinger et al.¹ (Part 1, 2022) and in Seelinger et al.² (Part 2, 2022).

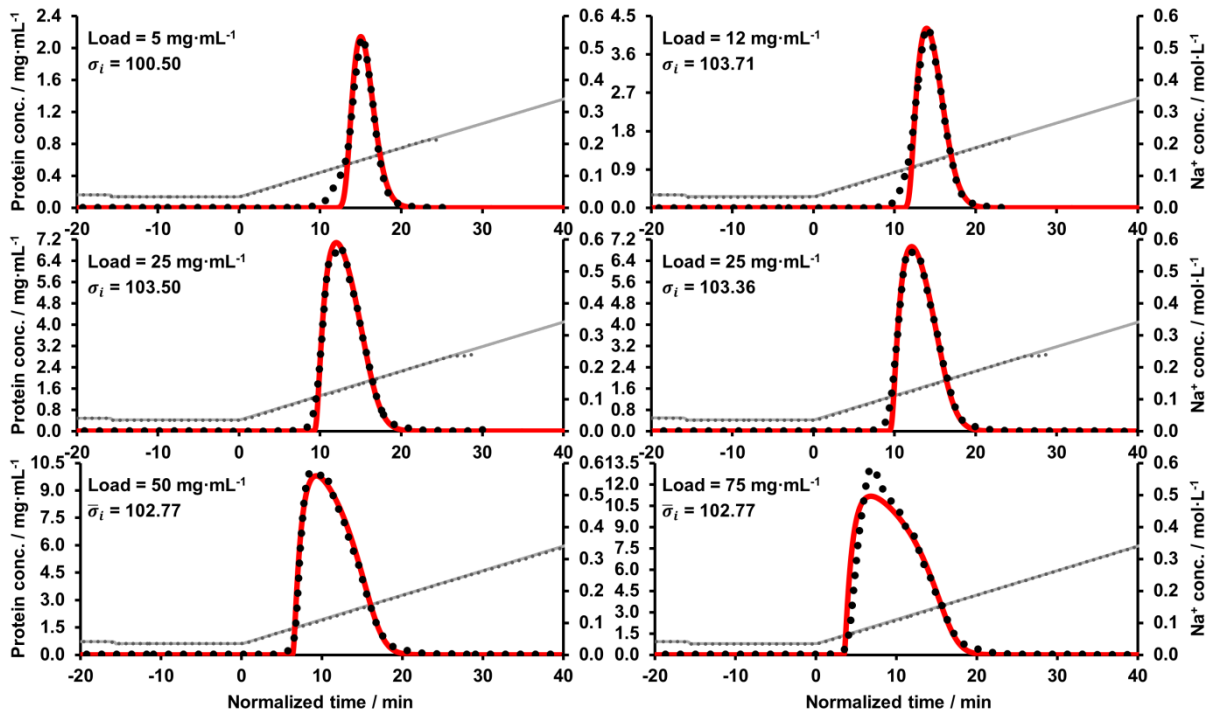


Figure 32. Salt gradient elutions of bsAbY at pH 7.0 used for estimation and verification of the steric shielding factor (σ_i) values by applying the SMA model. The black dots are experimental data and the red lines are simulated data. The time in minutes is normalized to the gradient start. At pH 7.0, highly similar values for σ_i were determined by inverse peak fitting for column loads of 5, 12, and 25 $\text{mg}_{\text{bsAb}}/\text{mL}_{\text{resin}}$. At column loads of 50 and 75 $\text{mg}_{\text{bsAb}}/\text{mL}_{\text{resin}}$, a mean value $\bar{\sigma}_i$ was used for the chromatogram simulations. The applied fitted σ_i values, the mean values $\bar{\sigma}_i$ and the $k_{\text{eff},i}$ values are listed in Table 21. Some of the data shown and illustrated in this figure are already published in Seelinger et al.¹ (Part 1, 2022) and in Seelinger et al.² (Part 2, 2022).

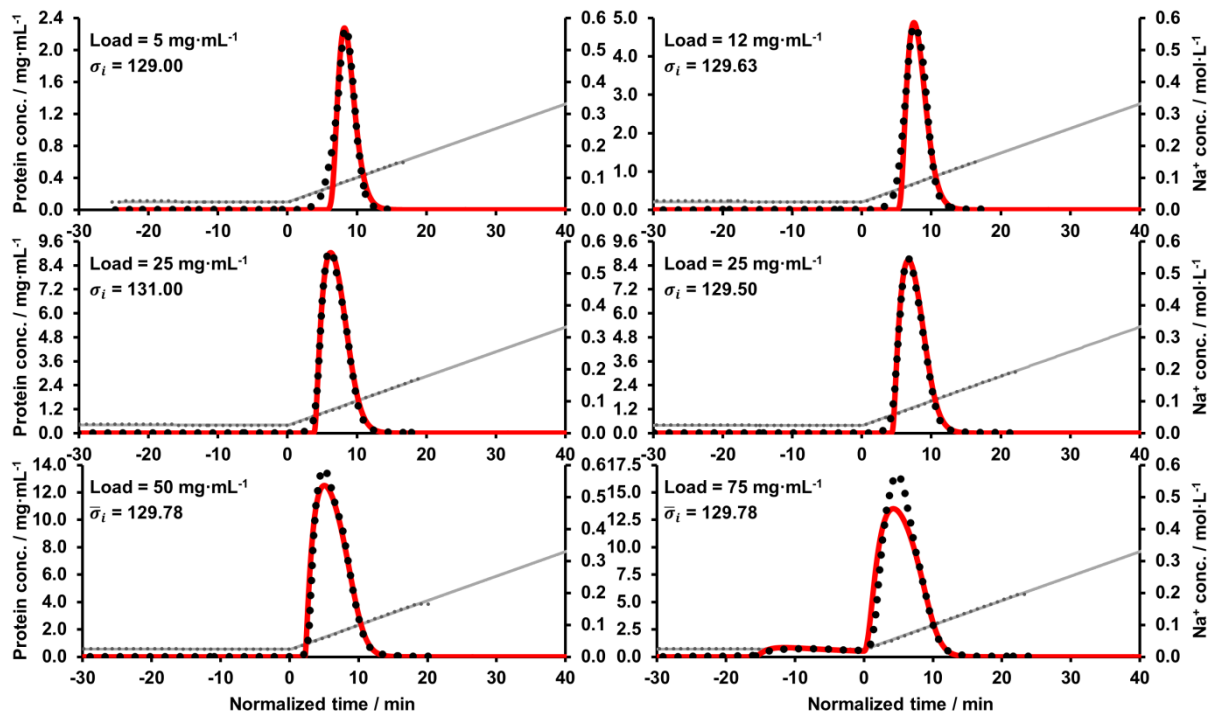


Figure 33. Salt gradient elutions of bsAbY at pH 8.5 used for estimation and verification of the steric shielding factor (σ_i) values by applying the SMA model. The black dots are experimental data and the red lines are simulated data. The time in minutes is normalized to the gradient start. At pH 8.5, highly similar values for σ_i were determined by inverse peak fitting for column loads of 5, 12, and 25 $\text{mg}_{\text{bsAb}}/\text{mL}_{\text{resin}}$. At column loads of 50 and 75 $\text{mg}_{\text{bsAb}}/\text{mL}_{\text{resin}}$, a mean value $\bar{\sigma}_i$ was used for the chromatogram simulations. The applied fitted σ_i values, the mean values $\bar{\sigma}_i$ and the $k_{eff,i}$ values are listed in Table 21. Some of the data shown and illustrated in this figure are already published in Seelinger et al.¹ (Part 1, 2022) and in Seelinger et al.² (Part 2, 2022).

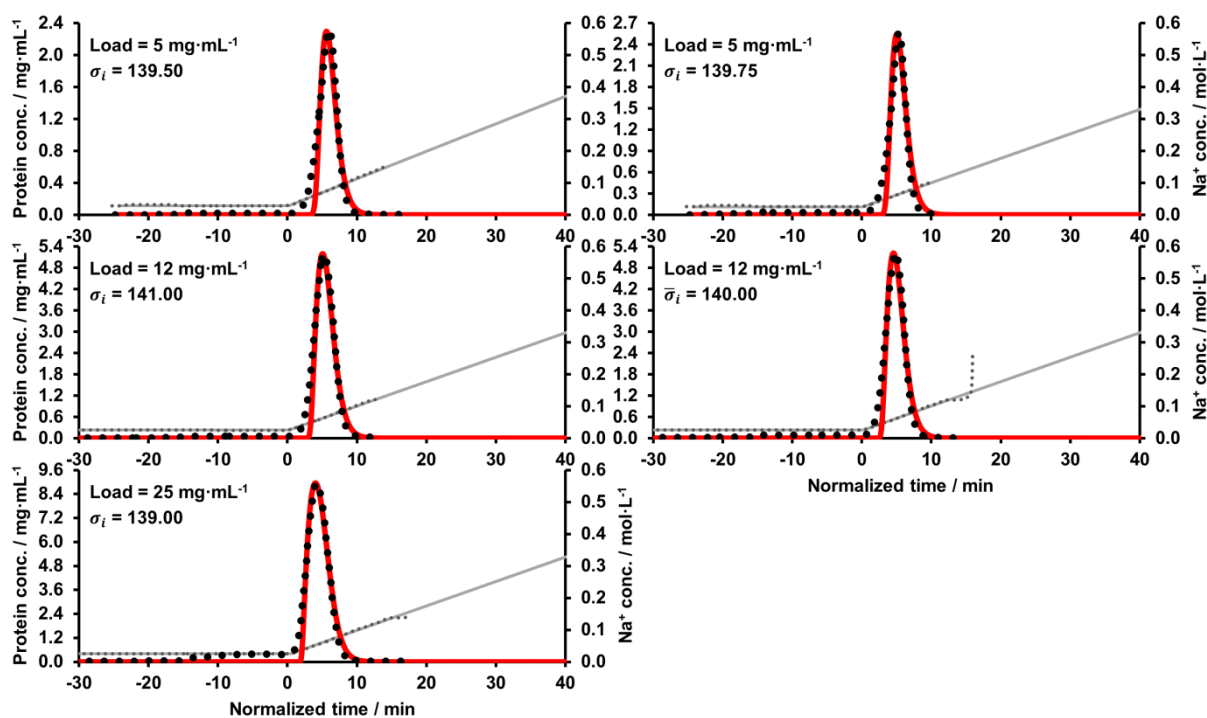


Figure 34. Salt gradient elutions of bsAbY at pH 8.9 used for estimation and verification of the steric shielding factor (σ_i) values by applying the SMA model. The black dots are experimental data and the red lines are simulated data. The time in minutes is normalized to the gradient start. At pH 8.9, highly similar values for σ_i were determined by inverse peak fitting for column loads of 5, 12, and 25 $\text{mg}_{\text{bsAb}}/\text{mL}_{\text{resin}}$. The applied fitted σ_i values and the $k_{eff,i}$ values are listed in Table 21. Some of the data shown and illustrated in this figure are already published in Seelinger et al.¹ (Part 1, 2022) and in Seelinger et al.² (Part 2, 2022).

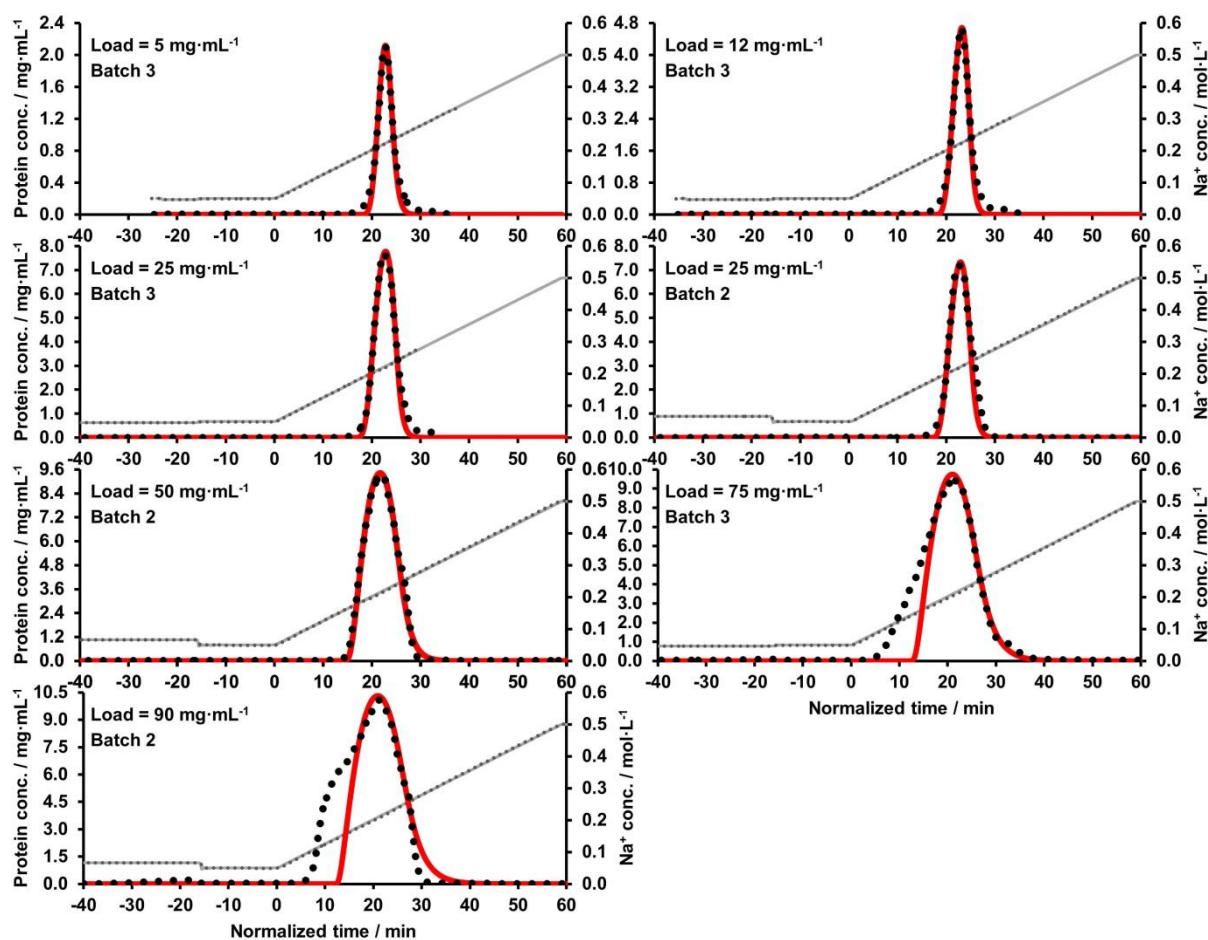


Figure 35. Salt gradient elutions of bsAbX at pH 5.3 used for estimation and verification of the model parameters $K_{p,i}$, $K_{eq,2,i}/c$, σ_i , and $k_{eff,i}$ by applying the SAS-SMA model. The black dots are experimental data and the red lines are simulated data. The time in minutes is normalized to the gradient start. The estimated $K_{p,i}$, $K_{eq,2,i}/c$, σ_i , and $k_{eff,i}$ values are listed in Table 23. Some of the data shown and illustrated in this figure may also be included in Seelinger et al.³ (DRAFT (submitted)).

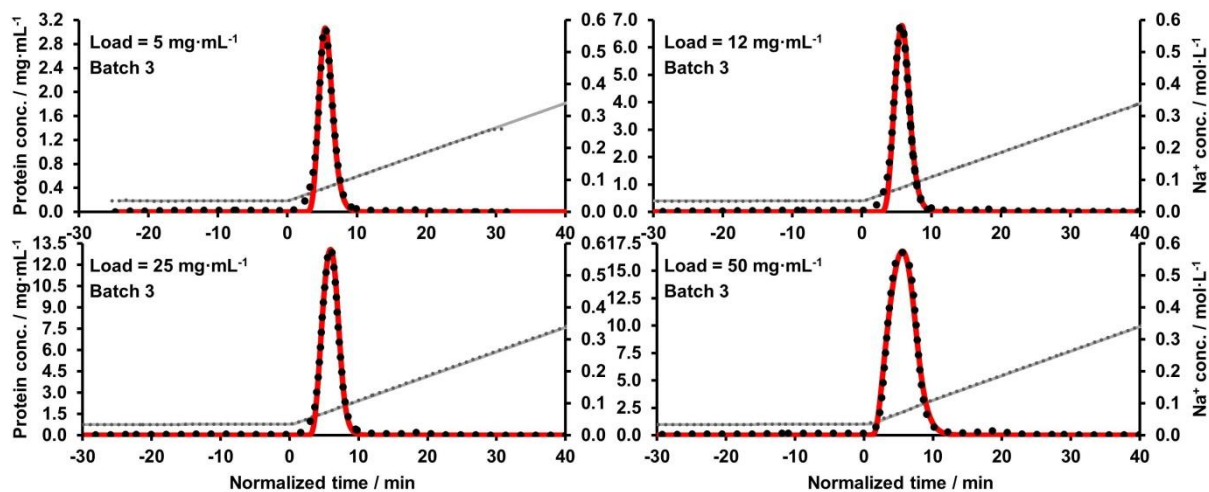


Figure 36. Salt gradient elutions of bsAbX at pH 7.0 used for estimation and verification of the model parameters $K_{p,i}$, $K_{eq,2,i}/c$, σ_i , and $k_{eff,i}$ by applying the SAS-SMA model. The black dots are experimental data and the red lines are simulated data. The time in minutes is normalized to the gradient start. The estimated $K_{p,i}$, $K_{eq,2,i}/c$, σ_i , and $k_{eff,i}$ values are listed in Table 23. Some of the data shown and illustrated in this figure may also be included in Seelinger et al.³ (DRAFT (submitted)).

9 LIST OF TABLES

Table 1: List of chemicals	27
Table 2: List of electronic devices.....	28
Table 3: List of software.....	29
Table 4: List of columns used for analytical chromatography	30
Table 5: Composition of buffer solution used as running buffer for determination of dead volumes, porosities and axial dispersion coefficient (D_{ax}).	31
Table 6: Composition of buffer solution used as salt tracer for determination of dead volumes and porosities.....	32
Table 7: Composition of buffer solution for determination of the exclusion factors $k_{d,i}$	32
Table 8: Buffer solution at pH 4.5 with 7.5 mmol/L Na^+ used for dilution of the bsAbY sample with 140 mmol/L Na^+ to a Na^+ concentration of 14.3 mmol/L.....	36
Table 9: Composition of buffer solution for analytical SE-HPLC.....	37
Table 10: Composition of buffer solutions for the application of linear pH gradients at 30 mmol/L Na^+ in CEX-HPLC	37
Table 11: Composition of buffer solutions for the application of linear pH gradients at 60 mmol/L Na^+ in CEX-HPLC	38
Table 12: Composition of CIP solution using a high NaCl concentration.....	38
Table 13: Composition of CIP solution using a NaOH concentration of 200 mmol/L	38
Table 14: Composition of CIP solution using a high NaOH concentration of 1000 mmol/L.....	39
Table 15: Composition of storage solution used for storage of preparative CEX and analytical CEX-HPLC columns	39
Table 16: Set of experiments used for modeling of bsAbY elution and bsAbX elution at low loading conditions (load = 0.5 $\text{mg}_{\text{bsAb}}/\text{mL}_{\text{resin}}$).....	48
Table 17: pK_{ai} values of amino acids used for modeling	54
Table 18: Dead volumes, column parameters, resin parameters, exclusion factors ($k_{d,i}$) and axial dispersion coefficient (D_{ax}).....	56
Table 19: Determined thermodynamic model parameters and determined number of amino acids N_{AA}	65
Table 20: Determined $k_{eff,i}$ values for low loading conditions (load $\leq 1 \text{ mg}_{\text{bsAb}}/\text{mL}_{\text{resin}}$).....	65

Table 21: Determined SMA model parameters and $keff,i$ values for high loading and overloading conditions for the sample bsAbY.....	69
Table 22: $keff,i$ values for sample bsAbY estimated with linear pH and dual gradient elution experiments at high loading and overloading conditions.....	78
Table 23: Determined SAS-SMA model parameters and $keff,i$ values for high loading conditions for sample bsAbX.....	96
Table 24: $keff,i$ values for bsAbX estimated with linear pH gradient experiments at high loading conditions	105
Table 25: Composition of buffer solutions for the application of linear salt gradients from 50 to 500 mmol/L Na ⁺ at pH 4.5	158
Table 26: Composition of buffer solutions for the application of linear salt gradients from 50 to 500 mmol/L Na ⁺ at pH 5.3	159
Table 27: Composition of buffer solutions for the application of linear salt gradients from 50 to 500 mmol/L Na ⁺ at pH 6.3	160
Table 28: Composition of buffer solutions for the application of linear salt gradients from 35 to 500 mmol/L Na ⁺ at pH 7.0	161
Table 29: Composition of buffer solutions for the application of linear salt gradients from 25 to 500 mmol/L Na ⁺ at pH 8.0	162
Table 30: Composition of buffer solutions for the application of linear salt gradients from 25 to 500 mmol/L Na ⁺ at pH 8.5	163
Table 31: Composition of buffer solutions for the application of linear salt gradients from 25 to 500 mmol/L Na ⁺ at pH 8.9	164
Table 32: Composition of buffer solutions for the application of linear pH gradients from pH 4.50 to 8.25 at 50 mmol/L Na ⁺	165
Table 33: Composition of buffer solutions for the application of linear pH gradients from pH 4.50 to 8.25 at 75 mmol/L Na ⁺	166
Table 34: Composition of buffer solutions for the application of linear pH gradients from pH 4.50 to 9.30 at 75 mmol/L Na ⁺	167
Table 35: Composition of buffer solutions for the application of linear pH gradients from pH 4.50 to 8.25 at 100 mmol/L Na ⁺	168
Table 36: Composition of buffer solutions for the application of linear pH gradients from pH 4.50 to 9.30 at 100 mmol/L Na ⁺	169
Table 37: Composition of buffer solutions for the application of linear pH gradients from pH 4.50 to 8.25 at 120 mmol/L Na ⁺	170

Table 38: Composition of buffer solutions for the application of linear pH gradients from pH 4.50 to 8.25 at 150 mmol/L Na ⁺	171
Table 39: Composition of buffer solutions for the application of linear pH gradients from pH 4.50 to 8.25 at 200 mmol/L Na ⁺	172
Table 40: Composition of buffer solutions for the application of linear pH gradients from pH 4.50 to 8.25 at 250 mmol/L Na ⁺	173
Table 41: Composition of buffer solutions for the application of linear pH gradients from pH 4.50 to 8.25 at 300 mmol/L Na ⁺	174
Table 42: Composition of buffer solutions for the application of linear anti-parallel dual gradients with increasing linear salt gradient from 50 to 350 mmol/L Na ⁺ and decreasing linear pH gradient from pH 6.30 to 5.10	175
Table 43: Composition of buffer solutions for the application of linear parallel dual gradients with increasing linear salt gradient from 80 to 300 mmol/L Na ⁺ and increasing linear pH gradient from pH 5.20 to 7.50	176

10 LIST OF FIGURES

Figure 1. Analysis of the bsAbY sample by SE-HPLC and CEX-HPLC.....	58
Figure 2. Linear salt gradient elution experiments with the sample bsAbY performed under low loading conditions.	59
Figure 3. Analysis of the bsAbX sample by SE-HPLC and CEX-HPLC.....	60
Figure 4. Analysis of sample bsAbX batch 3 by CEX-HPLC and subdivision of the sample into pre-variants and main variants.	61
Figure 5. Linear salt gradient elution experiments with the sample bsAbX performed under low loading conditions.	62
Figure 6. Modeling in the linear range of the adsorption isotherm.	64
Figure 7. Elution behavior of bsAbY and bsAbX (batch 3) under high loading and overloading conditions.	66
Figure 8. Salt gradient elutions of bsAbY at pH 5.3 used for estimation and verification of the steric shielding factor (σ_i) values by applying the SMA model.	70
Figure 9. Salt gradient elutions of bsAbY at pH 8.0 used for estimation and verification of the steric shielding factor (σ_i) values by applying the SMA model.	71
Figure 10. pH-dependence of σ_i and σ_i+vi (bsAbY).	75
Figure 11. Simulated changes of vi , σ_i and $q_{max,i}$ for bsAbY over a linear pH gradient (pH 4.5 – 9.3) calculated by the pH-dependent SMA model.....	76
Figure 12. Linear pH gradient elution experiments performed at 75, 120 and 200 mmol/L Na ⁺ with increasing loadings from 25 to 90 mg _{bsAb} /mL _{resin} , performed with the sample bsAbY and simulated by the pH-dependent SMA model.	79
Figure 13. Dual gradient elution experiments with high column loads of 25 and 50 mg _{bsAb} /mL _{resin} , performed with sample bsAbY and simulated by the pH-dependent SMA model.....	80
Figure 14. Elution of bsAbY charge variants in linear salt gradients at pH 8.0.	82
Figure 15 Comparison between single- and multi-component simulations of the pH gradient runs at 75 mmol/L Na ⁺ performed under high loading and overloading conditions using the sample bsAbY.....	84
Figure 16. Comparison between experimental and simulated data from the salt gradient runs at pH 4.5 performed with increasing loadings from 5 to 90 mg _{bsAb} /mL _{resin} using sample bsAbY.	87

Figure 17. Overlay plot of different sample loadings performed at different Na ⁺ concentrations using sample bsAbY.....	88
Figure 18. Comparison between experimental and simulated data of the salt gradient runs performed at pH 4.5 where the sample bsAbY was injected at different Na ⁺ concentrations.	90
Figure 19. Multi-component simulations of the linear salt gradient runs at pH 4.5 where the sample bsAbY was injected with 14.3 mmol/L Na ⁺	92
Figure 20. Comparison of salt gradient experiments performed at pH 4.5, where the sample bsAbY was injected at 50 mmol/L Na ⁺ with three different flow rates.....	93
Figure 21. Salt gradient elutions of bsAbX at pH 4.5 used for estimation and verification of the model parameters Kp,i , $Keq,2,ic$, σ_i , and $keff,i$ by applying the SAS-SMA model.....	97
Figure 22. Salt gradient elutions of bsAbX at pH 6.3 used for estimation and verification of the model parameters Kp,i , $Keq,2,ic$, σ_i , and $keff,i$ by applying the SAS-SMA model.....	98
Figure 23. pH-dependence of Kp,i and $Keq,2,ic$. (A) Kp,i and $Keq,2,ic$ as functions of $vi2$	100
Figure 24. Comparison between the SMA model (A/B) and the SAS-SMA model (C/D) by chromatogram simulations of the linear salt gradient at pH 5.3 with a loading of 25 mg _{bsAb} /mL _{resin} using the sample bsAbX.....	101
Figure 25. pH-dependence of σ_i and σ_i+vi for bsAbX determined by applying the SAS-SMA model.....	102
Figure 26. Simulated changes of the model parameters vi , σ_i , $qmax,i$, Kp,i and $Keq,2,ic$ for bsAbX over a linear pH gradient (pH 4.5 – 9.3) calculated by the pH-dependent SAS-SMA model.....	104
Figure 27. Linear pH gradient elution experiments performed at 75, 120 and 200 mmol/L Na ⁺ with loadings from 25 to 90 mg _{bsAb} /mL _{resin} simulated by the pH-dependent SAS-SMA model using the sample bsAbX.	106
Figure 28. Overlay plot of linear pH gradients at 75 mmol/L Na ⁺ with column loading of 75 mg _{bsAb} /mL _{resin} each performed with different loading conditions using the sample bsAbX batch 3.....	107
Figure 29. Elution of bsAbX (batch 3) charge variants in a linear pH gradient at 75 mmol/L Na ⁺ with a column load of 75 mg _{bsAb} /mL _{resin}	109

Figure 30. Salt gradient elutions of bsAbY at pH 4.5 used for estimation and verification of the steric shielding factor (σ_i) values by applying the SMA model. ..	177
Figure 31. Salt gradient elutions of bsAbY at pH 6.3 used for estimation and verification of the steric shielding factor (σ_i) values by applying the SMA model. ..	178
Figure 32. Salt gradient elutions of bsAbY at pH 7.0 used for estimation and verification of the steric shielding factor (σ_i) values by applying the SMA model. ..	179
Figure 33. Salt gradient elutions of bsAbY at pH 8.5 used for estimation and verification of the steric shielding factor (σ_i) values by applying the SMA model. ..	180
Figure 34. Salt gradient elutions of bsAbY at pH 8.9 used for estimation and verification of the steric shielding factor (σ_i) values by applying the SMA model. ..	181
Figure 35. Salt gradient elutions of bsAbX at pH 5.3 used for estimation and verification of the model parameters Kp,i , $Keq,2,ic$, σ_i , and $keff,i$ by applying the SAS-SMA model.....	182
Figure 36. Salt gradient elutions of bsAbX at pH 7.0 used for estimation and verification of the model parameters Kp,i , $Keq,2,ic$, σ_i , and $keff,i$ by applying the SAS-SMA model.....	183

11 CURRICULUM VITAE

PERSONAL DATA

Name: Felix Seelinger
Date of birth: 28.05.1991
Place of birth: Speyer
Father: Dr. med. Matthias Seelinger
Mother: Petra Seelinger

SCHOOL CAREER

08/2002 – 06/2007 Georg-Friedrich-Kolb Schulzentrum Realschule, Speyer
Mittlere Reife (Middle School Degree)
Final grade: 2.0 (good)

08/2007 – 03/2010 Nikolaus-von-Weis Gymnasium, Speyer
Fachhochschulreife (University Entrance Qualification)
Final grade: 2.7 (satisfactory)

UNIVERSITY CAREER

03/2011 – 02/2015 Hochschule Mannheim – Mannheim University of Applied Sciences
Biotechnology (Bachelor of Science)
Final grade: 2.0 (good)

03/2015 – 07/2017 Hochschule Mannheim – Mannheim University of Applied Sciences
Biotechnology-Bioprocess Development (Master of Science)
Final grade: 1.2 (with distinction)

28.02.2018 Acceptance as a doctoral candidate at the Medical Faculty Mannheim of the Ruprecht-Karls-University Heidelberg (Dr. sc. hum. (Doctor of Human Sciences))

PUBLICATIONS:

Niu J., Arentshorst M., **Seelinger F.**, Ram A. F., Ouedraogo J. P. (2016). A set of isogenic auxotrophic strains for constructing multiple gene deletion mutants and parasexual crossings in *Aspergillus niger*. *Arch. Microbiol.* 198 861–868.

Seelinger F., Wittkopp F., von Hirschheydt T., Hafner M., Frech C. (2022). Application of the Steric Mass Action formalism for modeling under high loading conditions: Part 1. Investigation of the influence of pH on the steric shielding factor. *J. Chrom. A*

Seelinger F., Wittkopp F., von Hirschheydt T., Frech C. (2022). Application of the Steric Mass Action formalism for modeling under high loading conditions: Part 2. Investigation of high loading and column overloading effects. *J. Chrom. A*

Seelinger F., Wittkopp F., von Hirschheydt T., Frech C. (DRAFT (submitted)). Anti-Langmuir elution behavior of a bispecific monoclonal antibody in cation exchange chromatography: Mechanistic modeling using a pH-dependent Self-Association Steric Mass Action isotherm.

SCIENTIFIC CONFERENCES:

Seelinger F., Frech C. (06/2021). Modeling and simulation of uncommon antibody elution behavior under high load conditions in cation exchange chromatography by using a modified SMA isotherm. PREP Symposium, Online; Presentation.

Frech C., **Seelinger F.** (07/2021). Modeling and simulation of antibody elution behavior under high load conditions in cation exchange chromatography by using a modified SMA Isotherm. Recovery Conf. series – 4th Mini Modelling Workshop, Online; Presentation.

Seelinger F., Wittkopp F., von Hirschheydt T., Frech C. (05/2022). Modeling and simulation of the elution behavior of a bispecific antibody in cation exchange chromatography by using a pH-dependent Self-Association Steric Mass Action (SAS-SMA) model. PREP Symposium, Baltimore (USA); Poster presentation.

12 ACKNOWLEDGEMENT

First of all, I would like to thank Prof. Dr. Mathias Hafner for the supervision of my doctoral thesis and the organizational support.

Special acknowledgments go to Prof. Dr. Christian Frech for this unique opportunity as well as for his support, his advice and his contribution to my work during my time at the Institute for Biochemistry at the Mannheim University of Applied Sciences.

I would also like to thank Dr. Felix Wittkopp and Dr. Thomas von Hirschheydt from Roche Diagnostics GmbH (Penzberg, Germany) for their support throughout the entire project.

Thanks also go to Christiane Koch and Elke Gebauer for their extensive support in the laboratory and to Andrea Bentz for her organizational support.

I would also like to thank my former doctoral colleagues Dr. Gabriela Sánchez Reyes, Carolin Stange, Jonas Koch, and Jan Hedrich.

Many thanks also to all the students I supervised or co-supervised during my time at the Institute for Biochemistry. Here I would like to thank Kim, Sandor, Clemens, Thomas, Jochen, Dominik, Pierre, Manuel, Tamara, Nadine, Jonas A., Karen and Rita.

I also want to thank my best friends Robert, Martin, Ugur, Marco, and Strauß.

I would also like to thank my Parents Petra Seelinger and Dr. Matthias Seelinger, my Aunt Monika Beck, my Uncle Norbert Beck, and my Grandma Gustl Seelinger.

Last but not least I would like to thank Grandma Duddie and my beloved Yoda. I will never forget you.

*„Der Schlüssel zum Erfolg ist Kameradschaft und der Wille,
alles für den anderen zu geben.“
Friedrich „Fritz“ Walter*